Finite Element simulation of methods for improving tissue ultrasound backscatter coefficient estimation

George Thomas West

A thesis presented for the degree of

Doctor of Philosophy

Department of Radiotherapy and Imaging,
The Institute of Cancer Research,
Sutton, UK

Department of Mechanical Engineering,
Imperial College London,
London, UK

Declaration of Originality

I declare that the content of this thesis is my own work, performed under supervision from Dr. Emma Harris, Dr. Peter Huthwaite, Professor Jeffrey Bamber and Professor Michael Lowe.

George West

September 28, 2023

Abstract

This thesis will describe the efforts to generate Finite Element simulations of methods to improve the accuracy and reliability of backscatter coefficient methods (BSC). BSC measurements are a promising diagnostic tool in tissue characterisation, but are limited by corrections for attenuation and diffraction. To investigate this, simulation models were developed and analysed to investigate the sources of variability in BSC estimation, to make it a more clinically applicable tool for the investigation of tissue state. Computational models mimicking attenuation of ultrasound by soft tissue mimicking materials were shown to accurately reproduce the frequency dependent attenuation coefficients of the materials, providing a tool with which attenuation corrections can be generated in silico. In addition, the development of mathematical and simulation methods were shown to generate reliable and accurate simulations of BSC estimation. Results of the subsequent analysis revealed how the diffraction correction affected the quality of BSC estimates under different conditions. In addition, an algorithm was developed to segment backscattered echoes based on their spatial wave coherence. This algorithm was shown to be capable of segmenting coherence outliers embedded in incoherent scattering media, improving the resulting BSC estimate through omitting regions of a simulated tissue mimicking material that did not align with the conditions required for accurate evaluation of the BSC.

Acknowledgements

I would firstly like to acknowledge my supervisors Dr. Emma Harris, Dr. Peter Huthwaite, Professor Jeffrey Bamber and Professor Michael Lowe for their assistance in both the production of this thesis and the work of which it is comprised. Their encouragement, insight and scientific curiosity were a constant source of motivation, and I thank them all deeply for their help throughout my research, particularly for their continued patience with my *idiosyncratic* approach to aspects of scientific research and organisation.

I would also like to thank my family and friends for their care and attention, my parents and sister for their love and encouragement, both Barney Walsh and Rosie McClean for their support in matters both emotional and culinary, and P.Q. for their unwavering loyalty in all endeavours.

In addition, I would like to acknowledge past and present members of the Ultrasound department at the Institute of Cancer Research and the Non-Destructive Evaluation department at Imperial College. Your friendship and willingness to offer assistance was invaluable throughout the course of my studies. A particular thanks goes to Dr. Stewart Haslinger for his assistance in formulating the mathematics that underpins this work.

Contents

List of Figures

List of Tables

Symbols

i	Imaginary unit
r	Position vector to point in field
r'	Position vector to point on source
f	Frequency
ω	Angular frequency
c	Speed of sound
λ	Wavelength
k	Wavenumber
ρ	Mass density
Z_i	Acoustic impedance
$T_{i,j}$	Interface transmission coefficient
$\alpha(\omega)$	Attenuation coefficient
α_0	Attenuation constant
b	Power law index of frequency dependent attenuation coefficient
e_s	Echo A-line from a scatterer
e_p	Echo A-line from a planar reflector
P_i	Unperturbed incident pressure field
P_s	Scattered pressure field
R_p	Planar reflector amplitude reflection coefficient
R	Reflection coefficient of scattering body

R_s	Standard deviation of reflection coefficient in medium populated by diffuse scattering bodies
R_m	Mean reflection coefficient of diffuse scattering medium
σ	Correlation length of amplitude reflection coefficient of the scattering medium
κ_A	Area concentration of scattering bodies in diffuse scattering medium
$g(\omega)$	Backscatter frequency behaviour of a medium based on spatial variation in amplitude reflection coefficient
Υ	Angle of backscatter for assessment of sub wavelength targets
a	Half-width of line source
Φ	Velocity potential of source
$\hat{\Phi}$	Geometric velocity potential
A_Φ	Magnitude of Gaussian approximated velocity potential
$U(\omega)$	Velocity amplitude of source
$T(\omega)$	Transmit frequency characteristics of source
$G(\omega)$	Receive frequency characteristics of receiver
$f(k,x)$	Source directivity function
Y_{LAM}	Last axial maximum of simulated unfocused source
Y_A	Arbitrary axial distance to a point past the last axial maximum of a simulated unfocused source
Y_∞	Arbitrary axial distance to a point in the far field of a simulated unfocused source
D_i	Diffraction correction corresponding to method 'i'

Q	Maximum spatial lag evaluated as a percentage of receive aperture width
Ω	Solid angle subtended by receive aperture at the centre of the cylinder
$\mathbf{M}$	Finite element mass matrix
$\mathbf{C}_D$	Finite element damping matrix
$\mathbf{K}$	Finite element stiffness matrix
$\mathbf{F}$	Finite element force matrix
$\mathbf{U}$	Finite element degree of freedom matrix
δt	Finite element time step
δx	Finite element spatial discretisation
γ	Damping constant
μ_{BS}	Backscatter coefficient
$S_i(\omega)$	Backscattered power spectrum from sample
$S_p(\omega)$	Backscattered power spectrum from planar reflector
$R(m)$	Spatial Correlation function
m	Spatial lag
N	Maximum spatial lag
n_i	Data point for correlation calculation
H_i^j	'i'th order Hankel function of the 'j'th kind
J_i	'i'th order Bessel function of the first kind

Chapter 1

Introduction

In the field of oncology, quantitative imaging approaches attempt to both predict and assess tumour responses to treatment. Backscatter coefficient (BSC) measurements have proven sensitivity to microstructural changes in tissues, and present a non-invasive alternative to biopsy in measuring the efficacy of treatments for patients. BSC measurements however, are limited in their accuracy by the associated diffraction and attenuation corrections[1], and even in highly controlled cases, have shown to be variable in their accuracy between different transducers and methodologies[2]. This thesis will explore the sources of variability found within BSC measurements, in an attempt to improve their reliability, and make the BSC a more clinically useful imaging biomarker for cancer response to therapy. To investigate sources of variability, a simulation based approach will be proposed, as this allows flexible variation in the acoustic properties of the simulated media, reproducibility in results and the ability to compute gold standards for quantities such as attenuation or backscatter coefficient based on the simulation properties. The estimation of these quantities from the simulation can be compared to this gold standard to investigate sources of error in the measurement. The aim of this thesis will be to develop and validate a model of ultrasound propagation through tissue, which can be used to simulate a BSC measurement and thereby investigate methods to improve the experimental measurement of the BSC. Results chapter 3 will validate a method by which ultrasound attenuation by soft tissue can be modelled. Results

chapter 4 will validate a method to simulate scattering from a simulated soft tissue like material. Chapters 5 and 6 will then simulate BSC estimation experiments on this scattering model to investigate the sources of error in estimation of the BSC.

1.1 Motivation

The variability in tumours is a hallmark of cancer, in both initial presentation and progression [3]. For this reason, accurate and reliable imaging is essential not only in diagnosis, but also the assessment of response to therapy. The current clinical standard (tumour shrinkage) assesses changes to tumour dimension as a measure of progression or response, typically through CT or MRI imaging [4]. This approach is firstly limited in a technical sense by the accuracy of measurement (how accurately one can measure volume, particularly in the case of irregularly shaped tumours). The second limitation is biological, due to the fact that tumour volume lags behind the biological and functional changes within the tumour that accompany response to therapy [5][6]. It is for this reason that reliable imaging biomarkers of treatment response are of interest in oncology, as they could allow both the design of customised treatment plans for predicted response based on the presented morphology, as well as more adaptive treatment plans based on continuous assessment of changes to the tumour environment [7]. Adaptive therapy approaches confer multiple benefits to the patient, due to the potential increase in efficacy of the treatment from informed treatment selection, and the reduction in the associated side effects of treatment [8]. In regards to the first point, mathematical models have indicated that treatment resistant phenotypes arise in small numbers in untreated tumours, reflecting a biological cost of resistance which reduces the energy available for proliferation [8]. In the absence of treatment, the population of resistant cells will continue to lag, whereas the introduction of a therapy to which one sub population is resistant will naturally change this imbalance. Monitoring of treatment response to identify the effect of treatment on the tumour structure and identify cell death is therefore imperative to ensure not only that there is response to therapy,

but also to ensure that - where treatment insensitivity presents itself - the treatment plan can be altered to fully eradicate the disease. The secondary benefit concerns the general well-being of the patient. Monitoring the effect of treatment can allow changes to the treatment plan to minimise unnecessary exposure to chemotherapeutic agents or radiation, providing both greater quality and reduced cost of care.

In order to realise adaptive therapy approaches, imaging biomarkers are required that can be reliably related to the tumour structure - and the associated changes therein - to allow the functional changes of the tumour such as cell death to be monitored throughout the progression of the treatment course. Currently, imaging biomarkers proposed for this purpose include – but are not limited to - diffusion weighted MRI [9][10][11], dynamic contrast enhanced MRI [12][13], magnetic resonance spectroscopy [14][15], positron emission tomography [16], ultrasound strain elastography [17][18], ultrasound attenuation measurements [19][20] and ultrasound backscatter characterisation [21][22][23][20]. Whilst these methodologies all have their benefits, the price, portability, real-time imaging capability and non-ionising nature of ultrasound based approaches make them an attractive option for imaging. Typically, ultrasound (US) is considered qualitatively, where the scattering from tissue structures is used to provide a non-invasive, non-ionising image of a patient or biological sample. The scattering from interfaces between tissues or structures larger than the imaging wavelength generates specular echoes that are used in qualitative investigation of patient tissues. Scattering from structures smaller, and separated by distances smaller than the wavelength constitute speckle, which is often perceived as a noisy detriment to the quality of US images, yet it is a type of US image texture, and relation of the image texture to the tissue microstructure – and associated tissue condition – make it a candidate for assessment of treatment response. In addition to texture analysis of B-mode images [24], the quantification of echo strength in terms of the frequency dependence the ultrasound backscatter coefficient (BSC) [25][26][27][28] can provide information about the sizes of sub-resolution and sub-wavelength scattering structures. Together, B-mode texture

and BSC spectral analysis form the basis of backscatter quantitative ultrasound (QUS), whereby the 'brightness' of scattering images (B-mode) is supplemented by the quantification of tissue properties through the analysis of the associated wave propagation or scattering properties.

This thesis will investigate the factors associated with accurate and reliable measurement of the scattering behaviour of soft tissues, in an attempt to improve upon current analysis approaches. To do so, a simulation based approach will be used. This approach will allow modelling of the physical phenomena associated with scattering, allowing us to investigate the properties of wave propagation in soft tissue like materials, improving upon BSC estimates and subsequently improving tissue characterisation for the monitoring of cancer.

1.2 Quantitative Ultrasound Approaches and Theory

This section will briefly describe the theoretical framework for, and the subsequent applications of QUS approaches in the characterisation of tissue. Firstly a brief description will be provided of the imaging metrics associated with large scale fluctuations in the bulk wave propagation properties of tissue, before considering - in more depth - the biomarkers associated with subwavelength fluctuations that generate scattering effects. The first category of QUS approaches concerns the quantification of the acoustic properties of the tissue concerned with bulk wave propagation on a larger scale. In this category we include the sound speed, stiffness and attenuation.

Sound speed measurements of biological tissues have shown promise in detection of breast masses [29][30], where it has been proposed that the lesions are distinguishable from surrounding breast tissue by their (higher) sound speed and attenuation values [31]. Sound speed imaging has also found application in the liver, where it has been used to differentiate healthy livers from those afflicted by a variety of liver diseases

[32][33][19][34]. Sound speed imaging is performed using both pulse echo [35] and tomographical techniques [36].

Stiffness of cancerous tissues is a potentially useful biomarker for tumour imaging, due to the relationship between the changes caused by the tumour development to the extracellular matrix and the associated increase in bulk elastic modulus relative to the surrounding tissue [37][38]. Stiffness measurements often overlap with sound speed measurements when assumptions of linear wave propagation and absence of dispersion are made, which leads to similar tumour models being investigated. Investigations into tissue stiffness also consider breast masses [39][40][41] and liver tissue [42][43][44] for the identification of disease.

Ultrasound attenuation measurements of normal and diseased tissue also revealed differences in attenuation (as compared to healthy liver) due to non-alcoholic fatty liver disease [45][46][47] and cancer [19], as well as breast masses [48][49].

We now consider the nature of backscattering from tissue. Scattering can be defined as the change in direction, phase or amplitude (or all of the above) of a propagating wave as a result of a spatial inhomogeneity in the acoustic impedance of the medium through which the wave propagates. It is the inhomogeneity that causes ultrasonic waves to be scattered from tissues back to an imaging device to generate B-mode images, or for analysis to generate QUS estimates of the tissue property. The scatterers within human tissue may be separated into two categories. The first is specular scatterers, formed of acoustic inhomogeneities much larger than the imaging wavelength. Within biological structures, this could be indicative of a tissue boundary, or a boundary within a tissue that possesses differing properties due to disease or damage. Identification of these regions form the primary visual cues in clinical, qualitative ultrasound, where tissue boundaries delineating tissue boundaries are used for the identification of organs, or specific tissue regions. The second category is diffuse scatterers, much smaller, and separated by distances smaller than the wavelength of the insonification, which present in B-mode images as a fine, granular 'speckle' pattern. Speckle texture is seen as an

image-degrading artifact by some authors, who wish to remove it to improve visual image quality [50][51]. Other authors treat speckle as a feature for use in tracking, particular in echocardiography [52][53][54]. In the field of QUS the relationship between the microstructure of materials and the resultant speckle texture is investigated to analyse the state of a tissue, allowing disease progression or treatment response to be assessed. This thesis is concerned with the latter, and hence we will treat speckle textures as useful image features, and analyse their properties to determine the state of the tissue from they are generated.

Soft-tissue scatterers are typically either modelled as discrete, weak, sub-wavelength, scatterers [55][25][56][57] or as local acoustic impedance fluctuations in a tissue described by an inhomogeneous continuum model [56][58][59]. A discussion of these two models will be considered in section 1.3.3. The quantification of scattering for tissue characterisation is separable into two modes of analysis. The first is the spectral quantification of scattered power, which provides information on the sub-resolution scatterer size and number density. The second is the analysis of the envelope amplitude statistics of echoes, which provides information on the spatial distribution of sub-resolution scatterers. The former constitutes a frequency domain analysis of backscattered power and subsequent calculation of the BSC, where the spectrum of backscattered echoes are normalised by the incident intensity and the properties of this normalised spectrum analysed to reveal details pertaining to the tissue structure, which will form the primary focus of this thesis.

1.2.1 The Backscatter Coefficient

The BSC is defined as measure of scattered intensity in the backward direction (toward the source of the ultrasound) per unit volume per unit solid angle normalised to the incident intensity [60]. It quantifies the strength of backscattered echoes and their frequency dependence from a sample, from which microstructural properties such as scatterer size, number density and individual scatterer acoustic impedance relative to

surrounding media can be estimated. BSC approaches have been shown to be sensitive to tissue and cell changes caused by therapy [61][62][63][64][65], presenting a promising tool for treatment monitoring. Other successful applications of BSC methods include the findings that BSC was a strong indicator of malignancy in ocular [66] and breast tumours[67][68], detection of cancer in excised lymph nodes [22][69], determination of radiotherapy response in breast tumours [70][71] and predictive modelling of response to chemotherapy [72][73].

A typical experimental method by which one computes the BSC is outlined in figure 1.1. One first acquires the backscattered data from the sample to be investigated, before performing the appropriate signal processing to gate and window the signal at the depth of the region of interest within the sample. At this point, the signal is translated into the Fourier domain by way of a Fourier transform to give a spectral representation of the backscattering from the region. At this point, averaging is typically performed over a spatial region of the insonified tissue to smooth out statistical fluctuations that occur due to interference of scattered wavefront from scatterers separated by distances smaller than the lateral imaging resolution. The average is then normalised by a calibration spectrum acquired from a reference scatterer. This is typically performed using the same device (and settings) to correct for the frequency dependent electro-acoustic and acousto-electric transducer responses. This spectrum is then diffraction corrected to account for geometrical effects typical to the combined geometry of the source and receive apertures, the relative geometry of the sample and reference scatterers, and focusing effects. The aim of this is to eliminate the dependence of the source and receive aperture sizes on the measurement of the backscattered power. The diffraction correction considers the geometrical extents of the aperture, the sampled gate length, and the distance to the sample to consider wave spreading effects on emit and received intensity. The final step is to perform an attenuation correction, whereby the signal loss due to absorption and scattering in the path between emission and reception are corrected for. Since diffraction effects, tissue absorption and tissue scattering are all

frequency dependent effects, they have a direct impact on the BSC (which is expressed in the frequency domain), and hence the quality of these corrections is directly relatable to the quality of the BSC estimate. These two corrections are vitally important in computation of the BSC, and this thesis will explore both in greater depth to investigate sources of error within BSC measurements.

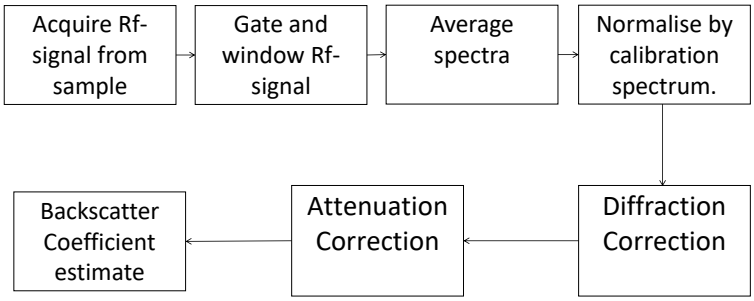

Figure 1.1: BSC flow diagram outlining the required steps in order to compute a BSC estimate. 'Rf' refers to the radio-frequency output signal output by the imaging device.

1.2.1.1 Diffraction corrections

The diffraction correction is an attempt to codify the emit and receive characteristics of the source used in the investigation. As mentioned, the typical manner of quantifying such a correction is through the use of a well defined scatterer, such as a planar reflector or reference phantom (illustrated in figure 1.2), which is substituted for the sample. These two methods are the most common, although recent efforts have been made to propose an *in situ*, spherical reference scatterer [74]. The planar reflector method assumes that the reflector is much larger than the beamwidth, and therefore approximates to an infinite surface, from which wave energy is scattered back to the source (scaled by the reflection coefficient of the plane). This method is commonly derived for use with single element sources [28][26][25][75][56][76][49][77], but examples with array systems also exist [78]. The reference phantom method takes a well characterised phantom (in sound speed, attenuation coefficient and BSC) and uses the backscattered spectrum as

the reference. This method is typically used with array systems [79]. The advantage of the reference phantom method is that there is no need for a geometrical correction to the normalisation spectrum to account for the diffraction, as the assumed geometry of the scatterers in the phantom and sample are hypothesised to be similar. This is in contrast to the planar reflector method, where the geometry of the reflector is different to the scatterers. The disadvantage of the reference phantom method is that the quality of the BSC estimate is limited by the accuracy to which the BSC of the reference phantom can be determined (which is determined either through model based calculation based on the average properties of the phantom or through measurement by another technique such as a planar reflector substitution method), and relies on the sound speed and attenuation of the sample to be similar to that of the reference [80][81].

The disadvantages of the planar reflector method are the sensitivity to reflector positioning and angle, and there is still question within the literature as to the most ideal positioning in the case of an unfocused source. This issue was discussed by Chen et al. [75], and is covered further in chapter 5

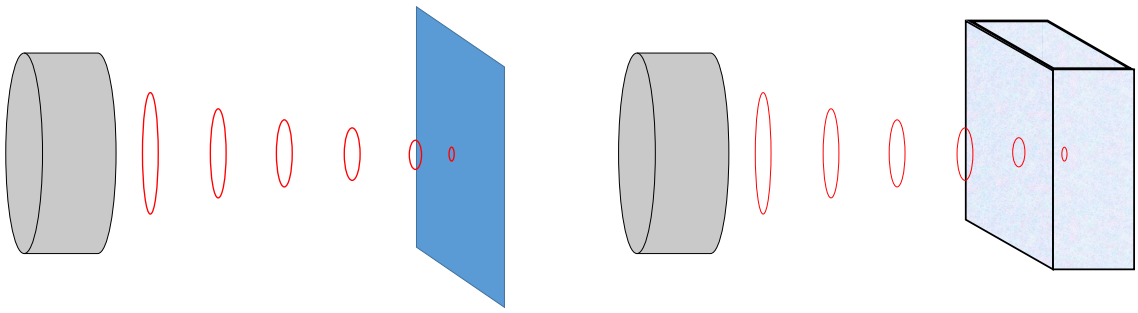

(a) (b)

Figure 1.2: Illustration of the planar reflector (figure 1.2a) and reference phantom substitution (figure 1.2b) methods. The source (pictured in grey), insonifies (red) the chosen reference scatterer and measures the backscattered spectrum, for normalisation of the backscattered spectrum acquired from the unknown sample.

1.2.1.2 Attenuation Correction

Whilst attenuation of ultrasound by a tissue is itself a biomarker of tissue state [45][46][47], it is also an important step in computation of the BSC. The attenuation correction attempts to reduce the impact of intervening, attenuative tissue layers (see figure 1.3) on the measurement of backscattered power from a region of interest (ROI). Soft tissues typically attenuate ultrasound (primarily through absorption mechanisms) with a linear frequency dependency, hence they will impact on the quality of spectral approaches to measure backscatter. To compute the attenuation of a signal between the surface and the ROI within the tissue some investigators estimate the tissue attenaution of thin layers iteratively down to the surface of the ROI, before summing over these values [25], whilst others assign attenuation coefficient values to distinct tissues based on measured values from separate experiments [82], whilst more recent methods have attempted simultaneously estimate attenuation and backscattering coefficient values using a linear least squares method [80].

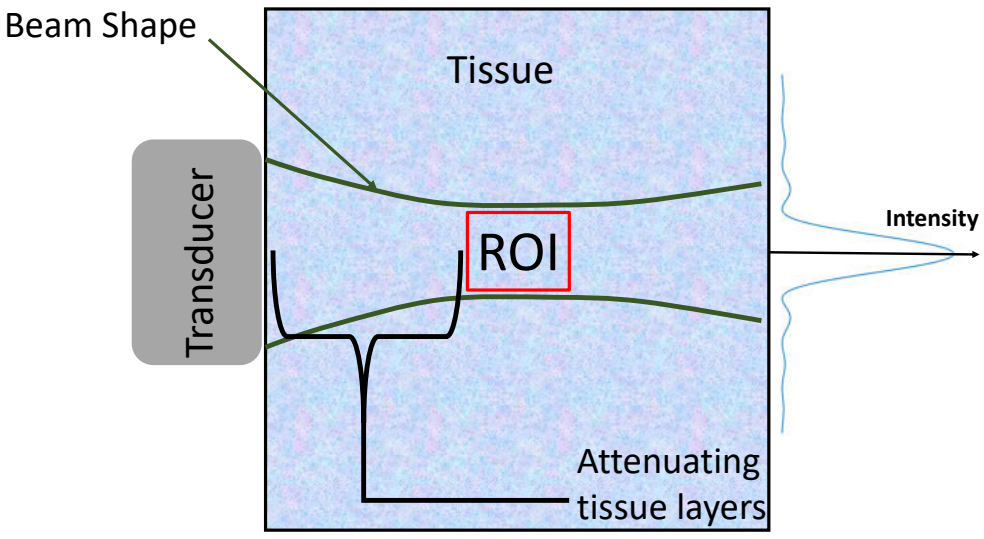

Figure 1.3: Illustration of the problem of attenuation. Attenuating tissue layers between the US device and the region of interest (ROI) alter both the propagating intensity, and the frequency characteristics of the beam, leading to frequency dependent underestimates in the BSC if not corrected for.

1.2.1.3 Methods for estimation of the BSC

One of the first attempts to encode the spectral scattering characteristics of materials was performed by Holaseck et al. [83], who attempted to record the frequency content of echoes, displaying the images for a set of bandwidths to highlight the potential for US based investigation into tissues based on the relative scattering contributions at different frequencies. This work was then developed by later authors into the BSC as it recognised today, where the spectral scattering behaviour is quantified to investigate scatterer properties.

The first method to estimate the BSC was performed using a planar reflector substitution method was published by Sigelmann and Reid [26], whose expression estimates the backscattered power from randomly positioned scatterers insonified by a single-element planar transducer. They assumed a fully developed speckle pattern (through the assumption that the scattered phase was uniformly distributed through all the phase angles). Later, Bamber et al. [28] independently used this same methodology to estimate the back scatter cross section from a cylindrical tissue sample. The equation used for this estimation was

$$\mu_s(\omega) = \frac{S_i(\omega)}{S_p(\omega)} \frac{4\alpha R_p^2}{\Omega e^{-4\alpha r} \left(e^{\alpha c \tau} - e^{-\alpha c \tau}\right)}. \tag{1.1}$$

Here, μ_S corresponds to the BSC, S_i to the backscattered spectrum from the unknown sample at angular frequency ω, S_p to the equivalent spectrum for the planar reflector (which has amplitude reflection coefficient R_p), α is the attenuation coefficient of the sample, r is the cylinder radius, c is the sound speed in the cylinder, Ω is the solid angle subtended by the transducer face at the centre of the cylinder and τ is the duration of the temporal gate. This equation approximates the directivity at the depth of the sample and planar reflector to a rectangular function, which is supposed to cancel when the ratio of the reflected powers is calculated for the sample and reference reflector.

A later work published by Nicholas et al. [76] also used the substitution method to

derive the BSC giving another expression, developing on the work of Sigelmann ad Reid and Bamber et al. to incorporate the directivity of the source in their expression. The beam directivity was measured through the measuring the receive spectra from echoes acquired by scanning a small steel ball across the beam width placed in the acoustic field at a specific wavelength (λ_0). Their final expression takes the form:

$$\mu_s(\omega) = \frac{S_i(\omega)}{S_p(\omega)} \frac{2\eta R_p^2 x^2}{\beta^2 A} \left(\frac{\lambda_0}{\lambda}\right)^2 \frac{2\alpha}{e^{-2\alpha x_1}\left(1 - e^{-\alpha c \tau}\right)}. \tag{1.2}$$

The additional components included in this expression are the transmission coefficient of the interface of the water and tissue (β), the area of the transducer face A, the wavelength of interest (λ) and the depth of the ROI within the cylinder (x_1).

Continuing this work, D'Astous and Foster [49][84], were the first to consider the estimation of BSC values using focused sources. Through assumption of a uniform angular differential scattering coefficient throughout the solid angle subtended by the transducer, they included the effect of transducer geometry through incorporation of the half angle of the transducer subtended at the focus to give the expression

$$\mu_s(\omega) = \frac{S_i(\omega)}{S_p(\omega)} \frac{R_p^2}{2\pi(1 - cos(\Omega))} \frac{2\alpha}{e^{-2\alpha x_1} - e^{-2\alpha x_2}}, \tag{1.3}$$

where the anterior and posterior depths of the temporal gate are x_1 and x_2 respectively.

An additional method was also developed by Ueda and Ozawa [77][57], who used a boundary integral wave approach under the first order Born approximation and assumed a Gaussian beam profile at the focal plane to give an expression for a weakly focused source:

$$\mu_s(\omega) = \frac{S_i(\omega)}{S_p(\omega)} \frac{e^{-4\alpha d} R_p^2 k^2 a^2}{8\pi d\left(1 + (ka^2/4w_0)^2\right)}. \tag{1.4}$$

Here k refers to the wavenumber of the ultrasound. The additional terms described

here include the distance to the centre of the temporal gate (w_0), the spatial extent of the gate (d), and the radius of the source (a).

Insana et al. [56][85] used a volumetric wave integral wave equation (also under the first order Born approximation) and incorporated the effect of windowing the receive data into their expression to yield:

$$\mu_s(\omega) = \frac{S_i(\omega)}{S_p(\omega)} \frac{1.45 w_0^2 R_p^2}{4 A_0 d} e^{-4\alpha(w_0 + d/2)}. \tag{1.5}$$

Within this expression, an inconsistency was discovered (by a factor of 16 in the definition of the reflection coefficient of the planar reflector) by Lavarello [2], hence the above expression should be amended through multiplication by a factor of 16.

Concluding the process of BSC estimation using single element sources, a mirror image approach, accompanied by a more detailed description of the transmitter directivity pattern (in reference [75]) was used by Chen et al. [79] to develop another equation for estimating the BSC, notable in that it permits the use of the planar reflector at a different distance than that to the region of interest, deriving the equation

$$\mu_s(\omega) = \frac{S_i(\omega)}{S_p(\omega)} \frac{2.17 R_p^2 w_0^2}{A_0 d} |e^{-iG_p}(J_0(G_p) + iJ_1(G_p)) - 1| e^{-4\alpha(w - w_0)}. \tag{1.6}$$

Here, J_m corresponds to the m^{th} order Bessel function and G_p the focusing gain of the source, defined as $G_p = ka^2/2w_0$.

The planar reflector method was also extended to incorporate the use of array transducers by Insana et al. [78] who considered the beam directivity function of a variety of aperture designs, providing a general expression:

$$\mu_s(\omega) = \frac{S_i(\omega)}{S_p(\omega)} \frac{2}{3 d B_H(0,0)} \left(\frac{\lambda w_0^2 R_p}{2A} \right)^2 e^{4[\alpha - \alpha_0]d}, \tag{1.7}$$

for which the directivity function (B_H) is specific to the array type.

Finally, the reference phantom method (RPM) developed by Yao et al. [86] used a well characterised reference phantom (of known attenuation coefficient, sound speed and BSC) to generate the normalisation spectrum. The backscattered energy from a particular depth used to correct the source diffraction effects. The measurement equation took the form

$$\mu_S(\omega) = \frac{S_i(\omega)}{S_p(\omega)}\mu_R(\omega). \tag{1.8}$$

Where μ_R is the BSC of the reference phantom. The advantage of this approach is that no explicit knowledge of the transducer beam pattern or transmit receive properties of the instrument are required. The disadvantage (as discussed previously) is that the quality of the sample BSC is related directly to the quality of the estimation of μ_R. A summary of the mentioned equations and methods for BSC estimation are outlined in table 1.1.

Table 1.1: Table listing the authors and their respective equations for computing estimates of the BSC using a variety of sources. For simplicity, only the diffraction term (excluding the power ratio and attenuation correction) of the equation has been included.

Author(s)	Diffraction term of equation	Source type	Beam shape assumptions
Sigelmann and Reid[26] Bamber[28]	$\frac{4R_p}{\Omega}$	Single element, planar	Uniform directivity within beam diameter.
Nicholas[76]	$\frac{2\eta R_p^2}{\beta^2 A}\left(\frac{\lambda_0}{\lambda}\right)^2$	Single element, planar	Directivity pattern computed from steel ball.
D'Astous and Foster[49]	$\frac{R_p^2}{2\pi(1-cos(\theta_T))}$	Single element, focused	Narrow, beam at focus
Ueda and Ozawa[77]	$\frac{R_p k^2 a^2}{8\pi d(1+(ka^2/4w_0)^2)}$	Single element, weakly focused or planar	Gaussian beam at the focal plane
Insana et al.	$\frac{1.45R_p^2}{A_0 d}$	Single element, weakly focused	Beam narrower than scattering volume

Chen et al.[79]	$\frac{2.17R_p^2w_0^2}{A_0d}\times$ $\lvert e^{-iG_p}(J_0(G_p)+ iJ_1(G_p))-1\rvert$	Single element, weakly focused or planar	Directivity function computed numerically[75]
Insana et al.[78]	$\frac{2}{3dB_H(0,0)}\left(\frac{\lambda w_0^2R_p}{2A}\right)^2$	Array transducer	Specific to array design
Yao et al.[86]	$\mu_R(\omega)$	Array transducer	None

1.2.2 Factors limiting clinical application of the BSC

Comparisons between the methods listed above have been reported in the literature, both explicitly, using the same equipment and samples [2] and through interlaboratory comparisons, where different authors used the method typical to their lab [87][88][89]. A notable first was conducted by Madsen et al. [88] who performed an interlaboratory investigation into BSC estimates. Laboratories returned BSC estimates based on their own experimental and analysis methodologies based on tissue-mimicking samples. Methodologies included both the reference phantom and planar-reflector substitution methods. BSC estimates differed by as much as an order of magnitude. More recently, Wear et al. [90] repeated the experiment across 8 laboratories in much the same way, finding multiple orders of magnitude difference between the laboratories. Anderson et al. [89] performed a two-laboratory study using glass beads as the scatterers and compared BSC estimates to Faran [91] scattering theory revealing agreement to scattering theory within 14% and much greater interlab agreement than previously observed. Additional studies with tissue mimicking and agar-glass bead phantoms [92][93] and in vivo studies [94] also improved on previous results, indicating increased reliability between estimates, and promise for clinical applicability. These studies typically either analyse phantom based, or small *in vivo* samples, which - while useful - are simpler cases than the end goal of clinical BSC estimation. For this reason, ongoing research

is still required to bring BSC practices into the clinical sphere. Studies performing analysis of the same sample using different methods of BSC estimation and different single element transducers has been performed, which highlights some of the

1.3 A simulation based approach to BSC estimation

To investigate the factors associated with the quality of BSC estimation, a simulation based approach is proposed. The advantages of simulation based approaches are two-fold. Firstly, they allow the generation of idealised samples whereby individual factors (such as the effect of attenuation, diffraction or scatterer strength and structure) can be investigated in isolation with a known ground truth. Secondly, they allow highly repeatable tests to be performed, with the ability to measure wave propagation properties in a manner not possible in a physical experiment (for example, measuring wave propagation within a sample). Limitations to the approach are their idealised nature. Tissues are complex, and we are limited by both our ability to measure their acoustic properties and organisation, as well as our ability to model the wave propagation physics. Naturally, assumptions are required, specific to both the simulation type and the simulated tissue. Nonetheless, a simulation based approach is proposed, based on the use of the Finite Element method, a powerful tool for full-wave simulation, the details of which are expanded upon below.

1.3.1 US simulation concepts and examples

With the advent of computer based simulations, initial interest in the field of QUS pertained to the simulation of B-mode images to investigate more deeply the nature of scattering from soft tissues. The simulations were combined with theoretical analysis to mitigate the uncertainties associated with the particular imaging device on the measurements acquired from the tissue [95]. One of the early examples of this was the simulations constructed by Bamber et al. [95] who employed a convolutional approach

to combine the characteristics of the simulated transducer (the impulse response, or point spread function) with the scattering properties of the simulated tissue structure. Through application of the Born approximation, this allows a fictitious tissue to be conceptualised as a collection of point scatterers, whose scattering characteristics combined with the imaging characteristics of the system will generate the resulting image. This approach was expanded and developed upon, in a number of works simulating – in particular – the nature of B-mode speckle for both the investigation into the masking of small lesions [84] and the investigation of speckle texture as a function of scatterer number density [96]. Field II [97][98], is an example of such a simulation approach is still widely used within QUS to this day [99][100][101] that also uses the impulse response method to compute the backscattering from a collection of discrete, sub wavelength scattering bodies. Field II calculates the convolution using a semi-analytical approach to generate Rf-data corresponding to the expected scattering response. The limitation to such an approach is that the computation of impulse responses does not allow for certain mechanisms. The concept of structure within materials is unavailable using a simulation platform such as Field II, due to the fact that the explicit wave propagation is not computed for the full path length from the simulated device to the scattering body and back. This means that regions of acoustical property changes (such as stiffness or sound speed) are not tractable. For this reason, tissue boundaries, or large specular scatterers are not available to be simulated as well as they may be for temporal based methods. It is for this reason that attempts to compute a BSC estimate for a cloud of discrete scatterers using Field II relied on a point scatter to compute the diffraction correction required for the absolute measurement to be made [99]. So too are other mechanisms, such as multiple scattering (due to the application of the Born approximation in the convolutional approach) or frequency dependent attenuation unavailable to a convolutional approach.

An alternative to the use of impulse response functions is the use of full-wave approaches. These methods employ discretisation of the simulation domain, computing

the solutions to the appropriate wave equation at each discretisation point within the grid. Placing a source of acoustic energy within the simulation domain, the solving of such equations with evolving time will then allow simulation of a wave propagating through a domain, based on the initial disturbance. The exact methods by which this is achieved varies between methodologies, but for simplicity we will consider the finite difference, finite element and psuedospectral approaches.

The propagation of an acoustic wave through a non-dispersive medium is governed by the inhomogeneous wave equation, which we may represent as

$$\frac{1}{c_0^2}\frac{\partial^2 P_i(\bar{r},t)}{\partial t^2} - \nabla^2 P_i(\bar{r},t) = \frac{2\Delta c(\bar{r})}{c_0^3}\frac{\partial^2 P_i(\bar{r},t)}{\partial t^2} - \frac{1}{\rho_0}\nabla[\Delta\rho(\bar{r})]\cdot\nabla P_i(\bar{r},t). \tag{1.9}$$

If we consider a simulation domain in which a pressure inhomogeneity is present (due to the simulation of a source of ultrasonic energy), then the computation of the solution to this equation at each discretised point within the domain can be represented through the approximation of the time and spatial operators by finite differences. In a given domain governed by variable q, we may express the differential of our wavefunction as a forward finite difference in the form:

$$\nabla_q f(q) \simeq \frac{f(q+\delta q) - f(q)}{\delta q}. \tag{1.10}$$

Other differences, such as the backward or central difference methods are also possible, which mimic the approach described herein, albeit using the 'backward' data point $f(q-\delta q)$ in the backward case, and both the 'forward' and 'backward' data point in the central case. Similarly, second order differential operators can be represented using the form:

$$\nabla_q^2 f(q) \simeq \frac{f(q+2\delta q) - 2f(q+\delta q) + f(q)}{(\delta q)^2}. \tag{1.11}$$

This constitutes a differential approach to solution of the wave equation.

Given the natural oscillatory nature of solutions to the wave equation, the use of a Fourier series instead of a Taylor series is logical. This forms the basis of a "spectral" method, whereby an approximation of the function at the grid points is found using a finite sum of sinusoidal basis functions. The wave field is decomposed into terms of varying wavenumber: superposing plane waves to generate the field. This reduces the density of grid points required down to the Nyquist limit of the shortest wavelength required in modelling, easing computational demand. In addition, spectral truncation error scales on the order of N^{-N} [102], which represents a faster convergence in accuracy than that exhibited by the FD approach. An example of a package utilising a spectral methodology is that of K-wave, based a k-space pseudo-spectral method [102]. This method contains an explicit solution factor within the temporal derivative that permits accurate solutions with a time step larger than would be achieved with a standard difference method, whilst the spatial grid separation is reduced using Fourier basis functions. The Fourier basis is well suited to calculation of spatial derivatives by transforming to and from Fourier space, allowing use of Fast Fourier transform routines in runtime calculations.

The finite element approach to the solution of such problems differs from this computation mathematically through the approximation of the solution over the domain by a family of functions with piecewise definitions between each element[103]. The piecewise functions link the nodes within the finite element mesh, with the piecewise functions defined by the material property of the element that shaped by these nodes. Finite element schemes can be divided into two camps, the explicit and implicit. The implicit variety attempts to solve time independent problems, where the model is in static equilibrium and we wish to solve the system of partial differential equations (PDEs) to investigate the distribution of a certain quantity over a certain domain. An example of a use for such analysis would be used for assessing the strain applied to a section of an object placed under a stress. Explicit methods attempt to describe the

temporal evolution of a quantity, through solving iteratively for the evolution of a field that locally is described by the PDEs of the physical system. An example of this could be the propagation of a pressure disturbance in a material as a result of an applied impulse to the system. Within this thesis, we are considering the propagation of acoustic waves, so we will concern ourselves with the explicit finite element methods, and the appropriate examples it attempts to simulate. We may summarise the finite element method within the following steps:

1. Discretisation: the process by which the simulation domain is restructured into a collection of elements.

2. Property assignment: The application of the material properties to the discretised elements determines the associated effect of application of a certain impulse. For example, the assignment of an element's density or wave speed will dictate the resulting pressure distribution that passes through it as a result of an incident pressure disturbance.

3. Assembly: Connecting the elements through the domain completes the formation of the finite element model in its stationary state.

4. Initial loading: Application of known initial conditions constitutes the formation of the problem to be solved. The initial pressure disturbance in the case of a wave simulation propagates through the model based on the material properties defined earlier.

5. Solution: iterated calculation of the evolving disturbance then models the evolution of the system based on the initial conditions.

6. Analysis: The recorded values of the measured quantity can then be extracted from the simulation results to present the answer to the question posed by the simulation.

The formulation of the specific FE approach used within Pogo has been described by Huthwaite[104], and FE more broadly in other works[103][105]. Here, a short overview will be presented based on reference [104]. In the case of acoustic wave propagation, the governing matrix equation for the system may be expressed as:

$$M\ddot{U} + C\dot{U} + KU = F, \tag{1.12}$$

where the matrices M, C and K correspond to the mass, damping and stiffness values of the elements within the model. F constitutes a vector of forces applied at each degree of freedom within the model. The vector U corresponds to the value for each degree of freedom within the model (stress and strain or pressure, depending on whether an acoustic or elastic simulation are considered), with $\dot{U}$ and $\ddot{U}$ corresponding to the first and derivatives of the degree of freedom with respect to time. Pogo utilises a finite difference scheme to step through the temporal evolution of an acoustic propagation problem, which on consultation with equations (1.3.1) and (1.3.1), yields the explicit relation:

$$M\frac{U(t+\delta t) - 2U(t) + U(t-\delta t)}{\delta t^2} + C\frac{U(t+\delta t) - U(t-\delta t)}{2\delta t} + KU(t) = F. \tag{1.13}$$

Rearranging for the next time step gives

$$U(t+\delta t) = \left(M\frac{1}{\delta t^2} + C\frac{1}{2\delta t}\right)^{-1}\left[F + \left(C\frac{1}{2\delta t} - M\frac{1}{\delta t^2}\right)U(t-\delta t) + \left(M\frac{2}{\delta t^2} - K\right)U(t)\right], \tag{1.14}$$

which is then computed for a specified degree of freedom for the given time step.

1.3.2 Selection of Simulation Package

In comparing the relative methods, the finite element method appears to be the most promising for the task of simulation of ultrasound images, particularly with respect to simulating scatterers below the resolution limit due to the adaptive meshing capabilities. This will become pertinent when assessing the ultrasound backscatter characteristics of the tissue under simulation, due to the size of the details the model will need to include. Simulating with a grid of uniform, high density could prove a severe challenge for a FD or pseudo-spectral method, and an analytical methodology such as that employed by Field II appears inappropriate due to the requirements on attenuation and diffraction corrections. We reject frequency domain solutions due to the size of the matrices required to be inverted in performing such routines, instead opting for a time domain solution of the propagation. The free meshing ability of a finite element could prove useful in adapting the mesh around structures within the tissue, and the freedom to alter the physical parameters of individual or small groups of elements could prove useful in quantitative ultrasound investigation of the tissue under consideration. Finally, the novelty of this approach in utilising a FE approach to model soft tissue is seen as a benefit, as the literature offers limited examples in this area.

1.3.3 Modelling soft tissue wave propagation and scattering

It is important to consider the nature of the scatterers present within soft tissues that generate the observed scattering behaviour. This section will discuss the proposed theoretical models to describe them.

Wave propagation in soft biological tissues is assumed to be governed by the mass density and compressibility (which dictate the wave speed) and the relaxation losses (which determine the absorption characteristics) [106]. Sub-wavelength spatial fluctuations in the compressibility generate monopole scattering bodies, and density fluctuations generate dipole scattering bodies [107] that generate diffuse scattering, leading to the formation of image speckle. Fluctuations in tissue density have been shown to

be smaller than the variations in compressibility [108][109][58] (although research into quantification of the relative contributions to scattering are ongoing [110]), leading to the discarding of the angular variation in amplitude of scattering from individual scatterers forming the scattering medium, and the assumption that diffuse scattering is typically considered as being due to a modulation in the compressibility in preference to density. Even in some cases where this assumption is not made literally (through the direct comparison of the relative magnitude of the fluctuations), the expression of scattering strength via the impedance, and assumption of angular independence in scattering constitutes a weak assumption that compressibility is the source of the impedance mismatch of the scatterer relative to the rest of the tissue medium [25]. An often used additional assumption is that of tissue as being weak scattering [57][58][25], which allows the application of the Born approximation. This results in the description of the scattered field as being a summation over a set of radiators, equal in radiating amplitude to that of the unperturbed field. This assumption relies on the number density, and individual scattering amplitude of the population of scatterers to be low. The mathematical benefit of applying the Born approximation in such a way is to limit the scattering mechanisms to consider only singular scattering events, and to not consider perturbation to the propagating wave field due to scattering events. Additional assumptions in the formulation of scattering theories incorporate the concept of stationary behaviour, or weak stationary behaviour. This simply assumes that the scattering sites within tissues are either completely stationary, or their movement can be attributed to a movement of the sample (i.e. the scattering sites do not move within the reference frame of the sample).

As mentioned previously, an inhomogeneous tissue medium is modelled in one of two ways [107]. The first is the inhomogeneous continuum model, whereby the tissue is modelled as a continuously varying (in acoustic property) medium, with fluctuations in the acoustic impedance generating the scattering. To describe such a model, we require the definition of correlation functions that relate the acoustic properties at different

points in the medium over characteristic length scales. These length scales dictate the size of the scattering body being approximated, and the degree of fluctuation relative to the rest of the medium dictating the scattering strength. Examples of this include gaussian and exponential models of medium fluctuation [56][58][59][111].

The second model describes the tissue as a homogeneous background medium, populated by finite sized inhomogeneities that generate the associated scattering behaviour. These scatterers are typically modelled as spheres [57][25][56][111], although attempts to model tissue scattering as being due to cylindrical vessels [55] have been proposed. It is worth noting the crossover in cited literature between these two schools of thought, with many authors comparing both discrete and continuous models on their acquired data. We may also note that, from Chivers' mathematical review of the inhomogeneous continuum and discrete models of tissue [107], and from results within the above cited works that inhomogeneous continuum and discrete models produce similar results in predicted scattered intensity, and that they appear to differ in their descriptions of relative contributions of coherent and incoherent components of scattering [107].

1.4 Thesis structure and aims

The aims of this thesis are to generate simulation models within which the factors affecting the accuracy of BSC estimates can be evaluated. These factors are attenuation, diffraction correction and scattering wave coherence. The first factor will be investigated through construction of a simulation model within which the attenuation of ultrasound by soft tissue like materials can be modelled. The production of such a model would allow investigation into the effect of attenuation on the accuracy of BSC estimates by providing a framework within which ultrasound attenuation can be applied to a scattering simulation, and the effect on the resulting BSC estimate evaluated. To investigate diffraction effects, scattering models will be developed, and the effect of different source designs (with the associated diffraction correction) on the estimation of the BSC will be evaluated. Finally, the spatial coherence of backscattered wave energy

will be analysed, to determine how the spatial wave coherency of backscattered echoes affects the estimation of BSC values.

This thesis will be structured as follows. Firstly, a broad methodology chapter will describe some of the terms and methods used to generate the FE models, as well as some of the methodology used in analysing their output. The aim of this chapter is to give the reader a broad overview of the methods and some of the terminology that will be common to the respective chapters. The specific details of the models that form the basis of each result will be further discussed within the respective results chapter.

Chapter 3 will be concerned with attenuation of ultrasonic energy. Simulations of ultrasound attenuation by soft tissue like materials using the finite element method will be presented. The results will include arbitrary and human-like models to test the suitability of the Finite Element method to simulate attenuation, and by extension, produce attenuation corrections for the measurement of the BSC. This chapter will aim to develop a simulation based approach to the computation of attenuation corrections for BSC estimation methods.

Chapter 4 will describe the development of mathematical methods for 2D BSC estimation, and of a simulation tool that mimics a BSC measurement experiment using the planar reflector substitution method. The first section of this chapter will include the derivation of equations to calculate the BSC from 2D simulation models (based on the backscattered spectra and the normalisation spectrum) and an equation quantifying the expected BSC value measured from a collection of circular scatterers lying on a 2D plane. The second section of this chapter will detail the development of the approach for simulating a BSC experiment using the FE method. This will include design of the scattering medium, the reference reflector, and the requisite analysis required to compute the BSC estimate, which is then compared to the aforementioned mathematics for validation. This chapter will form the proof of concept for the simulation approach, which will be used in later chapters to investigate the physics of BSC estimation to assess sources of error and unreliability. The aim of this chapter is to develop a simulation

based approach for the investigation of diffuse scattering from a soft tissue like material. This will facilitate investigation into the factors that affect the quality of BSC estimates.

Chapter 5 will explore how the approach developed in chapter 4 was used to test the accuracy of the planar reflector substitution method. The investigation was primarily concerned with assessing the accuracy of the approach as a function of the position of the planar reflector within the beam axis for a variety of different simulated apertures. This chapter explores the concept of the diffraction correction, and assesses how the nature of the diffraction correction affects the accuracy of BSC estimates, providing insight into best practice for measuring the BSC using the planar reflector method. The aim of this chapter is to formalise the approach of the planar reflector method in BSC estimation, to advise best practice in the use of unfocused sources in computing the BSC.

Chapter 6 will explore the effect of spatial wave coherence of backscattered waves on the quality of BSC estimation from a diffuse scattering medium. The aim of this work was to investigate the effect of highly incoherent and highly coherent backscattered wave contributions from tissue like models to assess their effects on BSC estimation accuracy. Within this chapter models were constructed with varying degrees of coherence, and the coherence analysed with respect to the BSC. This chapter details the development of a coherence segmentation algorithm which attempts to filter backscattered data based on coherence characteristics in order to improve the accuracy of BSC estimates. The aim of this chapter is to investigate the effect of coherence and tissue structure on the quality of BSC estimates, to allow improvements in BSC estimates through coherence segmentation.

These findings will be collated and discussed in chapter 7, in which the results will be discussed, and ideas for future work presented. Overarching conclusions will then be presented in chapter 8.

Chapter 2

Methodology

This chapter will outline briefly the analysis and Finite Element (FE) methods terms and approaches used. This is to provide a basis for understanding the terminology and methods used later in this thesis. Terms and convepts are expressed in general terms, with the precise details and variations explored in future chapters. The structure of this chapter is as follows: section 2.1 will explore the design of the FE models, and the associated concepts, section 2.2 will outline the approach taken for the analysis of the results of the simulations.

2.1 FE Methods

This section will detail the general methods and parameters used to generate the FE models that form the basis of this thesis. All FE simulations were performed using the FE package Pogo, developed at Imperial College [104]. The Pogo models were constructed using a combination of generic and Pogo specific Matlab [112] functions, and all analysis was performed using Matlab. After constructing the FE Models, the time domain computations were calculated on a GeForce GTX 1080 Ti graphics card.

The models presented in chapter 3 varied in size, with the lowest frequency model occupying $0.511\,MB$ of memory, requiring $18\,s$ to complete the simulation and the largest occupying $5.94\,GB$ of memory, requiring $245\,s$ to complete the simulation.

The models presented in chapters 4, 5 and 6 occupied $2.32\,GB$ of memory, and required $152\,s$ to complete the simulation.

2.1.1 Mesh Parameters

For the entirety of this thesis, structured meshes were used. This constitutes a discretisation of the simulation domain into a regular array of elements of characteristic length δx. For wave propagation simulation, the level of domain discretisation (also referred to as the mesh fineness), is required to be at least one tenth of a wavelength to maintain numerical stability in the simulation. For the time domain element of the simulation, the maximum time step (δt) is described by the courant value (C), a numerical expression of the Courant-Friedrichs-Lewy condition for the solution of partial differential equations. Broadly, this condition requires that the information propagation through the mesh cannot progress more than one mesh length in one mesh timestep. In the case of wave propagation problems, the wave speed (c) dictates the rate of the transfer of information, and the courant value must ensure that the product of the wave speed and time step does not exceed the mesh discretisation length. This may be expressed by the inequality

$$C = \frac{c\delta t}{\delta x} < 1. \tag{2.1}$$

Throughout this thesis, the mesh discretisation will be expressed as a function of the wavelength of the centre frequency of the excitation. For a model containing elements that possess a wave speed c, an excitation of centre frequency f_0 will lead to the propagation of a wave of wavelength λ_0. The mesh discretisation will be expressed as a function of this wavelength (i.e. $\delta x = \lambda_0/20$ would be expressed as 20 elements per wavelength). Whilst no simulations will be mono-chromatic, the linearity of the FE routine will allow us to consider only the frequency component of interest. The time step will be expressed through the courant value.

2.1.2 Element selection

The elements used within this thesis were either triangular or square acoustic elements. These elements possess one degree of freedom (pressure) and were arranged in a regular grid of points for both ease of mesh manipulation, simplicity, and to minimise spurious numerical reflections that can occur with unstructured meshes where the element size is allowed to vary. The models are constructed through selecting the size of domain required and the characteristic length, and a grid is formed of the element positions. The elements possess one spatial property (their size) and three acoustic properties (sound speed, mass density and attenuation parameter). Acoustic elements were selected as this thesis will focus on the longitudinal wave propagation and scattering properties of tissue, and will not discuss the shear properties.

2.1.3 Principle of scattering within meshes

Two types of scattering body are considered within this thesis. The first of which is a 2D equivalent of a planar reflector (or line reflector). To simulate line reflectors (which are used to compute normalisation spectra for BSC measurements), the edge of the FE mesh was used. The nodes lying on the edge of the FE model possess a pressure degree of freedom, and since they are not connected only to nodes within the model and each other, they form a sound soft acoustic boundary, which reflects incident pressure waves without phase change or energy loss. In chapters 2, 3 and 4, an infinite line reflector was modelled using the boundary edge, which reflects energy back to the source of the pressure disturbance. To simulate microstructural soft tissue scatterers, elements within the mesh were designated as scatterers, and their acoustic properties were altered relative to the rest of the model to generate an acoustic impedance between the selected element and the background medium. A study into this approach is included in Chapter 2. In chapters 2 and 3, random scatterer distributions are generated through randomly selecting the positions of the scatterers for each simulation, generating statistically independent scattering distributions for each simulation. In chapter 4, the position of

the scatterers is set, then laterally translated (relative to the beam axis), to mimic lateral scanning of a source across a sample.

2.1.4 Absorbing regions

To simulate small regions of a large (or infinite domain), it is useful to design absorbing regions adjacent to the edge of the simulation domain. This prevents reflections from the edges of the model (when not desired) and simulates wave propagation within an infinite 2D plane. The absorbing boundaries used within Pogo employ the stiffness reduction method [113], whereby damping is increased gradually while reducing the stiffness of elements adjacent to the model boundary. The damping employed in Pogo is mass proportional, which introduces a real exponential decay into the solution of the inhomogeneous acoustic wave equation (for more details, see Chapter 1). The material damping attenuates the incident pressure waves and the accompanying reduction in stiffness reduces numerical reflections caused by the addition of an imaginary part to the wavenumber of the propagating wave.

2.1.5 Dimensionality Considerations

This thesis considers simulations relating to the nature of ultrasonic backscattering from soft tissue like materials. For this reason, we require subwavelength scatterers, which in return requires a finely discretised mesh. For this reason, large simulation domains (spatially) will generate models requiring substantial memory and processing requirements, which are time intensive to run, due to both hardware limitations, and the number of calculations required to compute wave propagation over a large distance on a finely discretised mesh. For these reasons, the FE models presented here are in 2D. It has been shown that simulating wave propagation and scattering problems in 2D is an efficient strategy for investigating complex problems [114], as they can capture all the wave propagation and scattering mechanisms with reduced processing power and shorter runtimes. The conclusions of such experiments are qualitative, and would

require conceptually 'scaling up' a dimension to generate quantitative 3D answers, but the results of 2D experiments can be useful in their ability to investigate and thereby influence 3D practices.

2.1.6 Source and Receiver Design

To generate the plane wave sources as described in results chapter 3, nodes covering the full width of the model were simultaneously excited by the same signal such that they all coherently emitted a pressure wave of the same frequency, of the same number of cycles. Since the nodes on the edge of the model radiate only into a half plane, to generate a uniform plane wave across the width of the model, the amplitude of the excitation applied to these nodes was half that of the others.

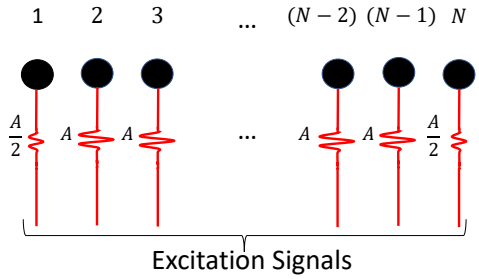

Figure 2.1: Illustration of amplitude variation approach used for generating infinite plane waves from line source. Nodes 1 and N correspond to nodes on the edge of the model, for which the amplitude of excitation was set to half ($A/2$) that for the other nodes (A).

To generate focused sources as used in chapters 4, 5 and 6, a line of nodes (the number of which depends on the width of the source designed) was selected perpendicular to the desired beam axis, on which the excitation signal was applied. A time delay profile was applied to the signals from each node to simulate a (spatially) curved source of pressure waves, mimicking the field emitted by a single element, focused transducer (figure 2.2), or a linear array with a focusing delay applied across the array elements. In all cases, the radius of curvature was set to be $5\,cm$. In receive mode, the backscattered pressure was recorded at each of the source nodes and time delayed with the same

profile. This method was selected in preference to placing the nodes in a physical arc as it permitted the use of a regular grid.

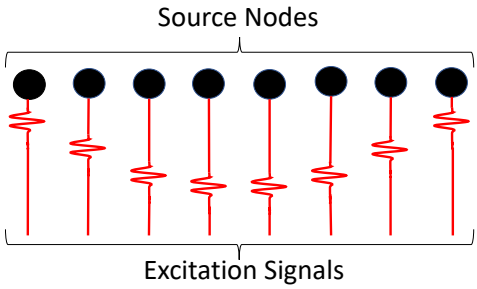

Figure 2.2: Illustration of time delayed signal approach for generating focusing from line source.

Where an unfocused source was used (as in chapter 5), a finite number of nodes was selected. The same excitation (without any time delay) was applied to each nodes to simulate an unfocused, single element source, or a linear array with no delay profile in emit or receive modes. For all the sources used within this thesis, a sinusoidal 3-cycle, Hanning windowed pulse was used as the excitation applied to the nodes, with an excitation amplitude of 100 Pa used in all cases besides the edge nodes of the plane wave sources described previously. It should be noted that since Pogo is a linear FEM solver [115], the absolute amplitude of the pressure waves used is not relevant to the simulations presented within this thesis.

2.2 Analysis Methodology

This section will briefly detail the three analysis routines performed on the results of the FE simulations. These include computation of the BSC, the amplitude envelope and the coherence

2.2.1 BSC Calculations

To compute the BSC from the simulations, the backscattered data from the simulation is beamformed according to the receive profile of the simulated receiver and summed to

generate a receive RF-line. The scattered line is then gated onto a depth of interest and windowed, with the spectrum computed from the Fourier transform of the windowed signal. For BSC estimates we require many spectra to be averaged, to smooth out statistical fluctuations that occur due to scattering, so the mean of the acquired spectra is computed to generate the final BSC estimate. Variations on this approach are found in chapters 4, 5 and 6, within which further details on the approach are included.

2.2.2 Amplitude envelope Calculations

B-mode images are formed of pixel values of brightness corresponding to the unsigned scattering amplitude of scattering from a region. To construct B-mode images from the FE simulations, the matrix of received signals across the simulated receiver is beam-formed according to the receive delay profile (mimicking reception at a single element receiver), and summed to generate a single RF (radio freqeuncy) line. From this line, the amplitude envelope is then found by computing the absolute value of the Hilbert transform of the RF line (as shown in figure 2.3). In chapter 4, the Rayleigh statistics of this amplitude envelope are computed and compared to scattering theory. In chapter 6, he value of the envelope is used as a pixel value within the B-mode images. The axial position of a given pixel is calculated using the time of flight to a given depth and the lateral positions were computed based on the relative position of the centre of the source to the centre of the simulated mesh.

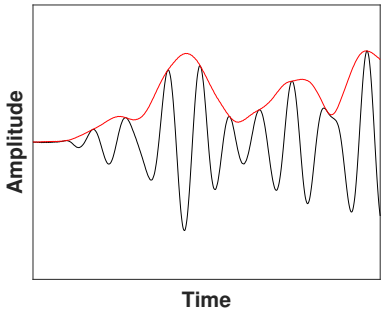

Figure 2.3: Illustration of a beamformed received scattering line (black), and the associated envelope (red) used to provide pixel values for the b-mode images and statistical analysis.

2.2.3 Coherence Calculation

In chapter 4, the spatial coherence function as a function of lag ($R(m)$) across the wavefront of the echoes received from a scatterer are computed using the equation

$$R(m) = \frac{1}{N-m} \sum_{i=1}^{N-m} \frac{\sum_{n=n_1}^{n_2} s_i(n) s_{i+m}(n)}{\sqrt{\sum_{n=n_1}^{n_2} s_i^2(n) \sum_{n=n_1}^{n_2} s_{i+m}^2(n)}}. \tag{2.2}$$

Where s_j corresponds to the received pressure signal at receiver j, m corresponds to the spatial lag between receivers, and n corresponds to the index of a samples within the received signals within the analysis kernel defined by n_2 and n_1. Parameterisations of this function are then computed to investigate the coherence characteristics of the simulations in chapters 5 and 6.

Chapter 3

An investigation into attenuation correction using the Finite Element Method

A previous iteration of the work presented in the following chapter is published in conference proceedings for the 2021 IEEE International Ultrasonics Symposium [116].

3.1 Introduction

This chapter will explore attenuation of ultrasound by soft tissue like materials. The aim of this investigation will be to develop a simulation based tool capable of calculating the attenuation losses of an ultrasound wave passing through a section of tissue mimicking the properties of an *in vivo* sample. To do so, a Finite Element (FE) approach will be developed to construct models, through which the absorption of propagating ultrasound waves will be measured. The approach of this chapter will be to simulate an attenuation measurement experiment on a sample of known attenuation coefficient and thickness, and to compare the values calculated from the simulation to the input parameters. The measure of success of the approach will then be through comparison of the values derived from the results of the simulation to the input parameters. This study will develop confidence and provide proof of concept for the FE approach. If successful, the possible applications of this tool could be: to compute attenuation corrections *in silico* (in cases where an experimental attenuation correction would be difficult to acquire), to test the accuracy of attenuation coefficient estimation algorithms (by providing ground truth values of attenuation against which to compare the output from the algorithm) or as a first step in development of an FE model containing both attenuating regions and scattering regions, to develop a tool by which BSC estimation algorithms could be investigated.

Knowledge of the attenuation coefficient of human soft tissue may be used as a tool for the diagnosis of disease such as cancer, either directly where the attenuation coefficient of the tissue plays the role of a diagnostic metric, or indirectly where the path length attenuation is used for calculation of the backscatter coefficient (BSC). In the former, quantification of the value, and relative spatial variation of the attenuation coefficient may be used as a biomarker for tissue state. For example, attenuation coefficient has been used as a metric for the quantification of hepatic steatosis [117] and fat content [118][45][46][47] in liver. Attenuation coefficient can also be an indication of tissue state for pathologies such as breast cancer [119][48][49].

In the latter, ultrasound attenuation measurements are required to acquire accurate estimates of quantitative ultrasound (QUS) biomarkers such as the BSC. Since the BSC is a measure of backscattered power, the energy loss in the path between the source and depth of interest is required to make depth-independent measurements of the BSC. Since the BSC is typically expressed as a function of frequency, the presence of frequency dependent attenuation will affect the quality of measurement not only in measuring the absolute value of the BSC but also any parameterisation based on the frequency dependence. Ultrasound attenuation is a result of both absorption and scattering mechanisms. The first of these converts the incident wave energy into heat, whilst the second redirects beam energy away from the current acoustic path. The energy loss associated with the absorption is more substantial than scattering in soft tissues [120][121], with absorption being attributed to 80% of ultrasonic attenuation by soft tissues [122]. The dominance of absorption mechanisms highlights the need for attenuation corrections when assessing tissue scattering behaviour (since the energy loss in the propagating wave pulse due to absorption is significant relative to the total backscattered power). It also partially explains the relatively low power to noise ratio associated with the measurement of ultrasonic backscattering (as opposed to transmission measurements). The absorption of ultrasound by soft tissue like materials typically varies with a linear dependence on the frequency [123]. Specific tissue attenuation coefficient values are typically expressed in the form of a power law, with frequency exponents ranging from around 0.8 to 1.5 [124]. The microstructural explanation for the absorption is typically explained using relaxation processes, distributed over a range of frequencies [123], but the exact mechanisms by which this occurs are not well understood.

Ultrasound attenuation of slab-like samples are typically measured through use of transmission substitution techniques, particularly for weakly attenuating materials. To perform such a measurement two transducers are positioned facing each other, aligned by their beam axes and one is treated as a source, and the other a receiver. The

difference in the received spectra with and without the sample present are then used to compute the attenuation coefficient of the sample as a function of frequency. Similarly to the BSC, corrections for factors such as the electro-mechanical emission and reception properties of the device used, material boundary reflections and the diffraction field of the source and receiver can bias the estimates of attenuation measurements.

Where attenuation measurements are computed for intact samples (i.e. they have not been prepared in a slab), algorithmic approaches compute the attenuation from different scattering depths within the sample. Three principal algorithms for the computation of attenuation coefficient are the spectral difference, spectral log difference and spectral shift methods. The spectral difference method compares the power of frequency components at different depths to estimate the local attenuation coefficient [86]. The spectral log difference method computes the slope of the fitted line of the log ratio of the power spectra from the shallowest and deepest sections of the region of interest, as a function of depth [125]. The spectral shift method models the receive spectra as Gaussian in shape, and computes the shift in centre frequency of the receive spectra as a function of depth to obtain the attenuation coefficient [120]. Comparisons between the spectral-shift and log-spectral difference methods have been performed in simulation by Kuc [126], who observed that the results of application of both algorithms to a simulated data set produced distributions of attenuation coefficient estimates that were statistically indistinguishable for longer windows. For shorter window sizes, the frequency shift estimates were observed to exhibit more accuracy. They recommend the log-spectral difference since it does not require the assumption of a Gaussian pulse, which allows it to be employed in cases where non-linear propagation is present [126]. The accuracy and precision of the algorithms were also shown to be strongly dependent on the size and homogeneity of the ROI [127]. A limitation of the spectral shift technique is that it does not correct for diffraction effects, owing to the need for corrections to be developed. In an attempt to generate diffraction free (i.e. plane wave) estimates of attenuation, axial beam translation has also been proposed [128], whereby

the translation of the source and receiver is used to maintain a fixed distance between the transducer aperture and the depth of interest within the sample. Such an approach requires a water stand-off to provide a coupling medium within which the transducer can be translated, which is challenging to implement in a clinical setting [129].

Due to the difficulty in computing the attenuation corrections using through transmission methods or the axial beam translation method in a clinical scenario, one solution to allow the calculation of the BSC in a clinic would be to compute attenuation corrections using a simulation based approach. If patient specific FE models could be generated using the patient geometry and estimates of their tissue acoustic properties, total attenuation (and diffraction values) could be computed using the FE method, and subsequently provide correction spectra for the estimation of system independent BSC values. In addition, development of simulation models that mimic the attenuation of ultrasound by soft tissue like materials generates a controlled environment within which algorithms and methods for attenuation coefficient and BSC estimation can be investigated, which would allow investigation into the effects that can improve or diminish the quality of BSC estimates.

To investigate this, this chapter will consider the simulation of attenuation by soft tissue using the FE method. Presented are idealised models of tissue sections insonified using infinite plane waves, firstly with materials of arbitrary properties, and then a simplified tissue model containing layers of skin, fat, and muscle. Comparison of the attenuation coefficient measurements to the input simulation values for the acoustic properties and attenuating region lengths will then be used to test the accuracy of the simulation. If successful, it is hoped that these results will present a case for the use of patient specific finite element models to compute attenuation corrections, which could subsequently allow accurate BSC measurements to be made in vivo. In addition, this would also provide proof of concept for a simulation tool within which the effects of different attenuation correction algorithms on a BSC estimate could be tested. Since attenuation correction constitutes significantly to the accuracy of BSC estimation [1],

a simulation based approach could provide an environment within which to test the effect of different attenuation correction methods on BSC estimates under different - highly controlled - conditions.

3.2 Methods

This section will describe the design of the FE models used to simulate the attenuation of ultrasound by soft tissue, and the subsequent analysis. Firstly, a description of the FE methodology will presented, followed by a description of the model parameters used in the simulations. The method by which the results were extracted from the simulations will be outlined, followed by the theoretical models against which the results were compared.

3.2.1 The Multi-Band Finite Element Method

Due to the lack of understanding into the microstructural mechanism by which ultrasound absorption occurs, it is more feasible to utilise empirical bulk measurements of attenuation coefficients in the formulation of an attenuation simulation. The reason for this is three-fold: the structures and/or structural interfaces that generate ultrasonic absorption are not known, their associated relaxation times are not known, and the simulation of a material possessing multiple relaxation parameters as a function of frequency is challenging computationally. For these reasons, we will consider bulk attenuation measurements of soft tissues, considering average attenuation over length scales greater than the wavelength, as opposed to considering the relaxation parameters on the sub-wavelength scale due to the tissue microstructure. In addition, the simulation of frequency dependent attenuation within the FE method is simplified by dividing the frequency range into a set of narrow frequency bands, over which the attenuation coefficient is presumed to be constant. Explicit simulation of the frequency dependence on a broadband scale complicates the FE formulation, to no added benefit, as we will wish to analyse the attenuation characteristics at distinct frequencies regardless. Based on these arguments, the multi-band finite element (MBFE) approach is proposed [130]. The MBFE approach models frequency *independent* attenuation over multiple narrowband solutions, which can then be combined to generate a broadband solution with the desired frequency dependence of attenuation (or dispersion). This approach has been

successfully used to model attenuation and dispersion in high-density polyethylene pipe (HDPE) [130]. This chapter will present a novel use of the method in simulating the frequency dependence of attenuation in human soft-tissue.

To implement the MBFE method, multiple simulations are performed, each of which use a different centre frequency of transmitted ultrasound, covering the range of frequencies over which the attenuation modelling is required. For each simulation, the attenuation parameters of the material(s) are set according to the attenuation coefficient value at the centre frequency of the simulation, and the narrowband results are combined at the end to generate the broadband solution. A flowchart outlining the process is shown in figure 3.1.

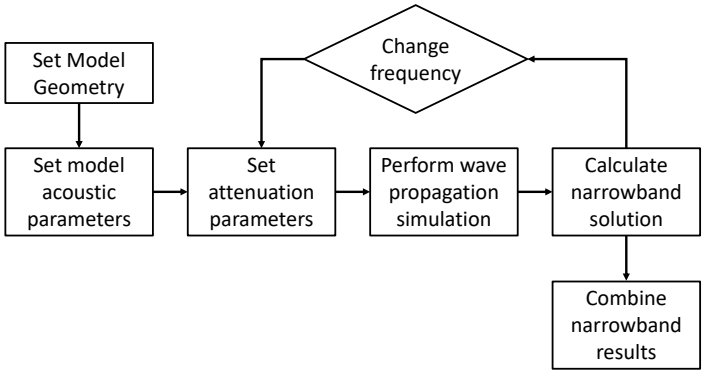

Figure 3.1: Flowchart explaining the design of the MBFE models.

As discussed in chapter 2, the finite element simulation solves for the displacement matrix of the nodes within the domain ($\mathbf{U}$) based on the mass, stiffness and damping matrices ($\mathbf{K}$, $\mathbf{M}$ and $\mathbf{C}_D$ respectively) based on the differential equation:

$$\mathbf{F} = \mathbf{K}\mathbf{U} + \mathbf{C}_D\dot{\mathbf{U}} + \mathbf{M}\ddot{\mathbf{U}}. \tag{3.1}$$

The time (t) dependent harmonic solution to one dimensional (x) form of equation (3.1) is $U(x,t) = e^{i(kx-\omega t)}$, where k is the wavenumber and ω is the angular frequency. Through the use of mass proportional damping, we may express the damping matrix as

$$\mathbf{C}_D = \gamma \mathbf{M}, \tag{3.2}$$

where γ is a constant of dimension $[time]^{-1}$. Substituting equation (3.2) and the harmonic solution allows the rewriting of equation with a complex density term:

$$\rho \to \rho \left(1 + i\frac{\gamma}{\omega}\right), \tag{3.3}$$

which in turn produces a complex wavenumber, that we may express as:

$$k' \propto \sqrt{\frac{\rho(1 + \frac{i\gamma}{\omega})}{E}}, \tag{3.4}$$

where E is the material stiffness. In the weak damping limit ($\gamma \ll \omega$), $\Re(k) \gg \Im(k)$ and

$$\Re(k') \propto \sqrt{\frac{\rho}{E}} \tag{3.5}$$

and

$$\Im(k') \propto i\Re(k')\frac{\gamma}{2\omega} \tag{3.6}$$

by Taylor expansion. Reapplying the assumption of weak damping to apply a linear, real dispersion relation, substitution of equations (3.5) and (3.6) into the harmonic solution produces

$$u(x,t) = e^{i(kx-\omega t)}e^{-\frac{\gamma}{2c}x}, \tag{3.7}$$

where the original harmonic solution is attenuated by an exponentially decaying amplitude envelope proportional to a damping parameter (γ) and the wave speed (c). From dimensional arguments we can consider γ as the rate of amplitude decay with respect

to time, which combined with the wave speed generates a rate of amplitude decay with respect to distance. This form of the equation illustrates clearly how errors in the wave propagation velocity result in errors in the resulting attenuation.

In a strongly damped case ($\gamma \sim \omega$) the damping introduces a non-negligible contribution to the real part of the stiffness matrix, introducing wave velocity errors in homogeneous model sections, and changes to scattering behaviour at the boundary of model inhomogeneities. To prevent these undesired scattering events (to generate absorbing regions), stiffness reduction methods [131] can be employed, but it will be shown that the level of damping required for simulation of human soft tissue should not require such measures. These methods are however employed in the boundary regions to minimise reflections back into the model. For a more complete description of mass proportional damping and stiffness reduction methods, consider the referenced work by Pettit et al. [131].

3.2.2 Effect of mesh refinement and Courant value on attenuation estimates

To ensure convergence of the numerical solution, an initial test was performed to assess the effect of mesh refinement and Courant value on the attenuation generated within the simulation. Sound speed errors are known to be exacerbated by small Courant values and coarse meshes [132], both of which will result in overestimation of the attenuation coefficient when compared to the input value of the material simulated. Therefore, we expect to observe a convergence of the results onto the theoretical value with increasing mesh refinement and Courant value. To test this hypothesis, a simple two-phase model (pictured in figure 3.2) was constructed with properties detailed in table 3.1. The mesh refinement for this model was varied from 10 to 100 elements per wavelength in an increment of 1, with a Courant value of 0.5 for the investigation into discretisation, and the Courant value was varied from 0.01 to 0.5 in increments of 0.01 for the time step investigation. The maximum value of the Courant value for stable numerical wave

propagation is 1. Values over 0.5 were not considered such that the results maintained a high level of temporal resolution, even for coarse mesh refinement values.

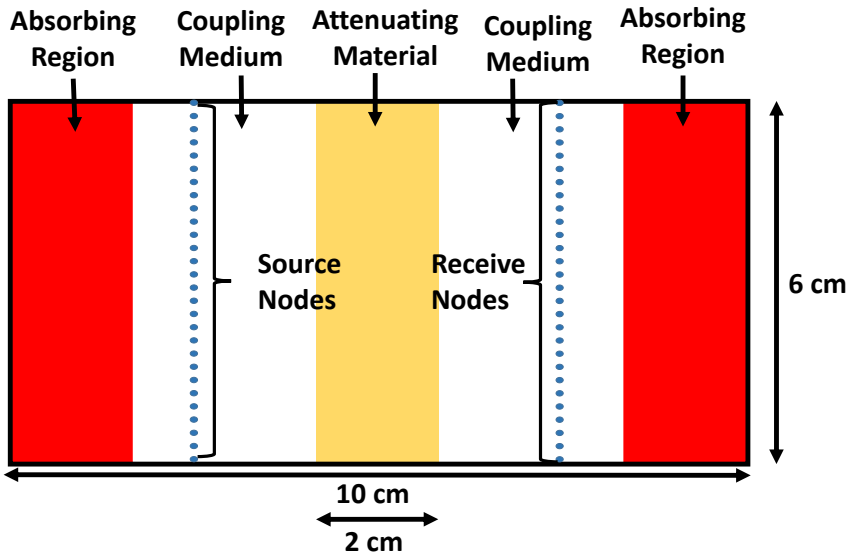

Figure 3.2: Schematic of model 1: Through transmission model simulation model. The source and receive nodes mimic ultrasonic transducers emitting and receiving a plane wave that passes through the attenuating section of the model. Figure not to scale.

Table 3.1: Acoustic properties of the materials used in test model.

	Properties		
Material	ρ $(kg\,m^{-3})$	**c** (ms^{-1})	α $(Np\,m^{-1})$
Coupling Medium	1000	1500	0
Attenuating material	1000	1500	5

This model imitates a through transmission attenuation experiment, whereby the wave passing through the sample was compared to a reference signal which propagates through the same distance of un-attenuating coupling medium. Within the context of the FE simulations, this constitutes a model partially populated by elements with zero attenuation to form the background coupling medium and other elements with non-zero attenuation to mimic soft tissue. A three cycle Hann tone burst centred on 1 MHz was applied to source nodes covering the full width of the domain. This generates a plane wave that passes through the attenuating region(s), thus negating the need to

account for the diffraction field of the source. Based on the width of the attenuating region ($2\,cm$) and the attenuation constant ($5\,Np\,m^{-1}$), the expected attenuation is $0.1\,Np$. The attenuation value was arbitrarily selected, but is of comparable decay rate to the attenuation of a $1\,MHz$ source of ultrasound energy passing through human subcutaneous fat. The convergence of the result was shown to be for around 50 elements per wavelength and a Courant value of 0.5, which was used for all subsequent simulations. The nature of the convergence is shown in figure 3.5.

3.2.3 Acoustic impedance matched models

Two models were developed to test the ability of the MBFE method to simulate ultrasound absorption with attenuating sections that are matched by acoustic impedance (possessing the same sound speed and mass density) to the coupling medium. The first applied a linear frequency dependence of attenuation to a 2 cm region within the centre of the model (as per figure 3.2), with the properties outlined in table 3.2. Simulations were performed using centre frequencies of excitation of $0.5\,MHz$ to $10\,MHz$ with an increment of $0.5\,MHz$. For each simulation, the mesh was constructed using a refinement of 50 elements per wavelength. In all cases, a 3 cycle Hann windowed excitation was applied to the source nodes. The lowest frequency models occupied $0.511\,MB$ of memory, requiring $18\,s$ to simulate the wave propagating across the full length of the model. The highest frequency models occupied $5.94\,GB$ of memory, requiring $245\,s$ to complete the simulation.

Table 3.2: The material properties used in the acoustic impedance matched model 1. The attenuation properties were modelled in a power law of the form $\alpha = \alpha_0 f^b$, where f is the frequency in MHz.

	Properties			
Material	ρ $(kg\,m^{-3})$	c (ms^{-1})	α_0 $(Np\,m^{-1}MHz^{-b})$	b
Coupling Medium	1000	1500	0	0
Attenuating Material 1	1000	1500	5	1

The second model was comprised of two adjacent 1 cm attenuating regions with attenuation coefficients of frequency dependency 1.2 and 1.5 respectively. This is outlined in figure 3.3 and in table 3.3. The same centre frequencies and mesh refinements were used with these models.

Table 3.3: The attenuating properties of the materials used in the acoustic impedance matched model 2.

	Properties			
Material	ρ $(kg\,m^{-3})$	c (ms^{-1})	α_0 $(Np\,m^{-1}MHz^{-b})$	b
Coupling Medium	1000	1500	0	0
Attenuating Material 1	1000	1500	2	1.2
Attenuating Material 2	1000	1500	1	1.5

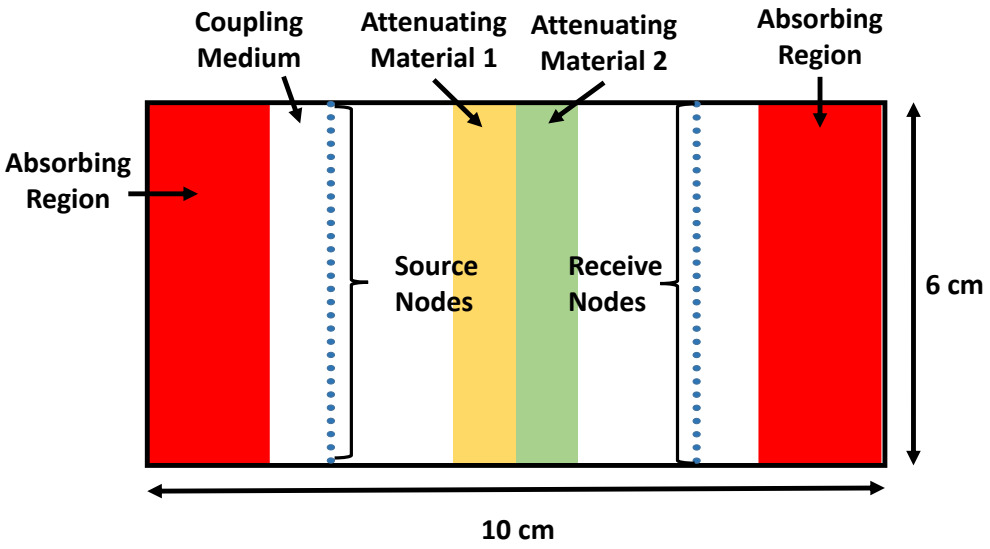

Figure 3.3: Schematic of model 2: Three phase through-transmission model simulation. The frequency dependence of attenuation within the regions at the center of the model were differed to test the flexibility of the model to multiple materials. Figure not to scale.

3.2.4 Human model

To extend the complexity of the simulations, a third model was designed that incorporated variations in sound speed and density within the model. The FE model was constructed using published data on skin, muscle and fat thickness, sound speed, density and bulk attenuation to simulate the propagation of ultrasound through layers in soft tissue (as shown in figure 3.4). The data for the skin and fat thicknesses were taken from references [133] and [134] respectively, with the properties of density, sound speed and attenuation coefficient taken from the database of The Foundation for Research on Information Technologies in Society (ITIS) [135]. The receiver nodes were placed inside the muscle layer to compute the transmitted energy through the skin and fat layers.

The distance labeled as path length (d) through the coupling medium (as shown in table 3.4) corresponds to the distance from the source nodes and the coupling medium-skin interface. The same distance in the muscle corresponds to the distance between the receive nodes and the fat-muscle interface. For the skin and fat entries, d corresponds

to the thickness of the layer.

Table 3.4: The acoustic propagation properties of the materials used in the human model. References for the original source of the property values are: human skin mass density[124][136], sound speed[124][137][138] and attenuation constant[124], fat mass density[136][124], sound speed[137][124] and attenuation constant[136] and muscle density[124][136], sound speed[124][137][138][139][140] and attenuation constant[138][124][140].

	Properties				
Material	ρ $(kg\,m^{-3})$	c (ms^{-1})	α_0 (m^{-1})	b	d (m)
Coupling Medium	1000	1500	0	0	3e-2
Human Skin	1109	1624.0	21.158	1.000	1e-3
Human Subcutaneous Fat	911	1440.2	4.3578	1.086	2e-2
Human Muscle	1090	1558.4	7.1088	1.089	5e-3

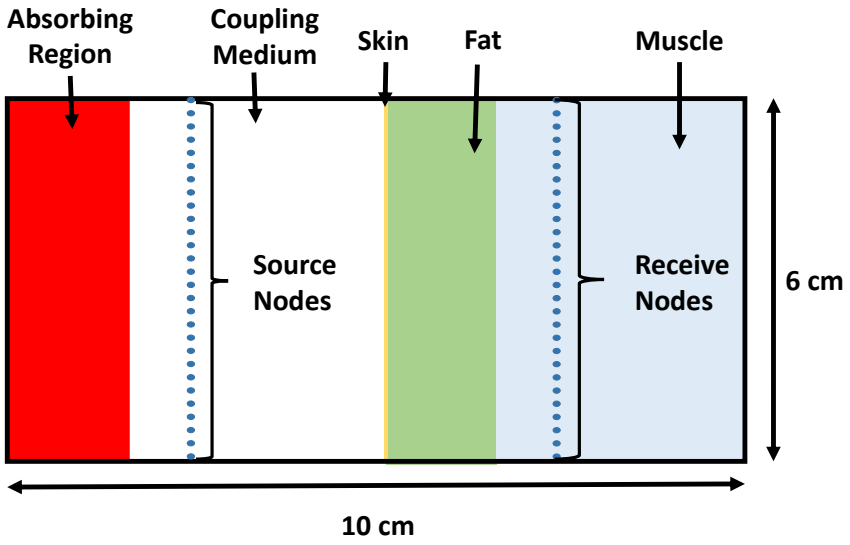

Figure 3.4: Schematic of model 3: Four phase model containing published properties and dimensions for human skin (yellow), fat (green) and muscle (blue), with a coupling medium (white). Figure not to scale.

3.2.5 Analysis Methodology

The propagating wave passing through the attenuating material was recorded at the receive nodes in all cases, and summed across the receive nodes to give a single time trace. The signal was then gated based on the expected arrival time calculated from the distance between the source and receive nodes and the model wave speed(s), with a gate length equal to that of the initial excitation applied to the source, and centred on the expected arrival time at the receive nodes. A Hanning window was then applied to the gated data and the result Fourier transformed to give a receive power spectrum. For each attenuating model, a conjugate model was developed without any attenuating elements present to provide a reference power spectrum. The same method of analysis was applied to this reference spectrum. To compute the total attenuation, the spectral log-difference method was employed, where the attenuation value in $N\,p$ is given by the natural logarithm of the ratio of the spectra from the attenuating and non-attenuating simulations. Defining the attenuated receive power spectrum as $S_a(f)$ and the unattenuated reference power spectrum as $S_r(f)$, we hypothesise that the two are linked by the equation

$$S_a(f) = S_r(f) \prod_i^N e^{-\alpha(f)_i x_i}, \tag{3.8}$$

where α_i and x_i represent the attenuation coefficient and thickness of the 'i'th layer of 'N' attenuating layers respectively. By computing the natural logarithm of the ratio of S_a and S_r, and expressing the attenuation coefficient with a power law ($\alpha(f) = \alpha_0 f^b$) the resulting line will take the form:

$$-log\left(\frac{S_a(\omega)}{S_r(\omega)}\right) = \sum_i^N \alpha_{0,i} f^{b_i} x_i. \tag{3.9}$$

For models 1 and 2, $N = 1$ and $N = 2$ respectively. Polynomial fitting of the log spectral difference generates estimates for $\alpha_{0,i}$ and b_i respectively, where x_i was treated as a known variable. This equation was used to compute the theoretical total attenuation

for models 1 and 2.

In model 3, the introduction of impedance mismatches between materials means that the reflection coefficients were also required to compute the energy less due to boundary reflections. To do so, the acoustic impedance of material 'i' (Z_i) was calculated using the sound speed (v_i) and mass density (ρ_i) using equation $Z_i = v_i\rho_i$. From this the power transmission coefficient at the boundary between material i and j were computed using the formula

$$T_{i,j} = 1 - \left(\frac{Z_j - Z_i}{Z_i + Z_j}\right)^2. \tag{3.10}$$

The inclusion of reflection as a loss mechanism requires equation 3.8 to be altered to

$$S_a(f) = S_r(f) \prod_i^N e^{-\alpha(f)x_i} \prod_i^{N-1} T_{i,i+1}, \tag{3.11}$$

and equation 3.9 to

$$-log\left(\frac{S_a(\omega)}{S_r(\omega)}\right) = \sum_i^N \alpha_{0,i} f^{b_i} x_i - \sum_i^{N-1} log(T_{i,i+1}). \tag{3.12}$$

Now treating the reflection coefficients and layer thicknesses as known values, a polynomial fit allows estimates of the values of $\alpha_{0,i}$ and b_i to be made. This equation was used to compute the theoretical attenuation coefficients for model 3.

All polynomial fitting was performed using the Matlab curve fitting toolbox, where custom equations were designed using the known values, leaving the values of $\alpha_{0,i}$ and b_i as parameters against which the fitting was performed. The uncertainty in the extracted fit parameters is characterised through the 95% confidence interval within the curve fitting toolbox, the full width of which is reported here as a measure of the uncertainty in the calculated values for $\alpha_{0,i}$ and b_i. The fitting employed a non-linear least squares approach, with the solver set to compute a maximum of 10^6 function evaluations and 10^6 max iterations.

3.3 Results

The results of the investigation into the relationship between the mesh refinement and the total attenuation is shown in figure 3.5a. Between 10 and 40 elements per wavelength, there was a general overestimation of the attenuation, which can be attributed to the sound speed errors caused by the sub-optimal spatial discretisation. The convergence onto the theoretical value is monotonic for the cases of 10 to 23 elements per wavelength, implying that the mesh refinement is the dominating factor in the overestimation of the attenuation in this range. Closer agreement to the theoretical value was observed for mesh refinement values of around 50 elements per wavelength. Beyond 50 elements per wavelength, under and overestimates were observed in the estimated attenuation, implying that a form of numerical noise is now contributing to deviations. The fluctuations between over and underestimates were observed to increase as the mesh was discretised more finely, with a slight bias towards overestimation. Due to the increased number of calculations required in the simulation of a wave propagation over a fixed distance using an increasingly finer grid, we can hypothesise that the numerical error is proportional to the number of time step calculations per simulation. The best tradeoff between the underestimation due to sound speed errors and the random variation appeared to be at around 50 elements per wavelength, which was used in the subsequent simulations.

From figure 3.5b, smaller deviations from the expected value were observed than from the investigation into mesh refinement. From the general trend of the relationship, it can be concluded that the larger Courant values provided the most accurate reproduction of the expected total attenuation. From these observations, the mesh refinement and courant values were subsequently set to be 50 (λ^{-1}) and 0.5 respectively. The commonality between the mesh refinement and the courant value is the effect on the number of calculations required. Increasing the number of elements per wavelength, or reducing the courant value has the effect of increasing the number of calculations to compute the propagation of a wave between a fixed physical distance. The increase in

error with increasing mesh refinement or decreasing courant value, suggests that this methodology could be prone to numerical errors, which become more pronounced in their effect as the number of computations is increased.

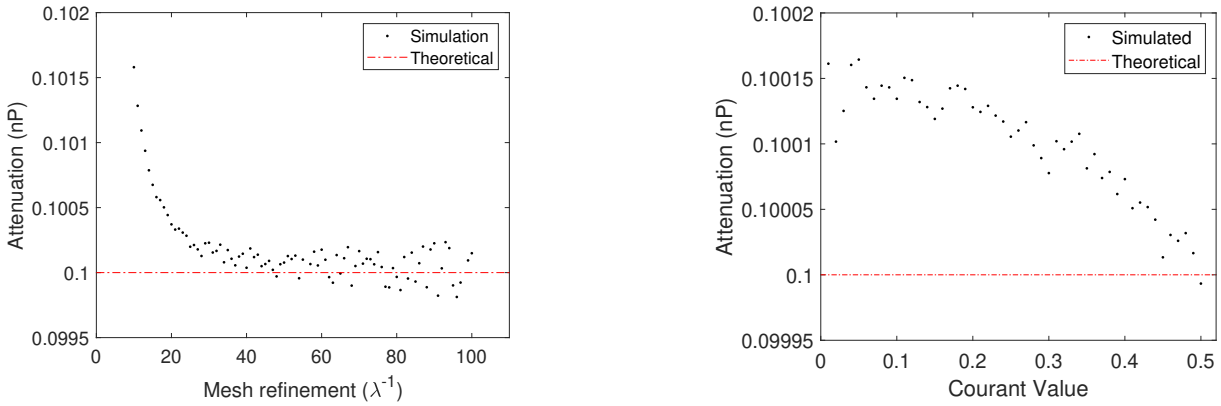

(a) (b)

Figure 3.5: Measured attenuation as a function of mesh fineness (3.5a) and courant value (3.5b). Mesh refinement indicates the number of mesh elements per (centre) wavelength.

The results for model 1 are shown in figure 3.6, with the extracted fit parameters shown in table 3.5. The theoretical attenuation (α_T) was computed using the right hand side of equation (3.9) to give:

$$\alpha_T(f) = x\alpha_0\, f, \tag{3.13}$$

where $x = 0.02\,m$ is the thickness of the attenuating region. A high level of agreement was observed between the theoretical and measured attenuation, reproducing both the linear frequency dependence and the absolute values within the fitting uncertainties (as shown in table 3.5). The percentage error was computed based on the percentage difference between the theoretical and measured attenuation values. A positive error corresponds to the FE method overestimating the attenuation and a negative error to an underestimation. The lowest accuracy was observed at the higher frequency end of the spectrum. This correlates with the mesh refinement observations, the greater

number of time steps results in a greater deviation in attenuation from the desired characteristics. Since the approach appears to be biased towards overestimates of attenuation, it logically follows that the higher frequencies, for which the number of time steps is greatest, would be most likely to generate overestimates of attenuation.

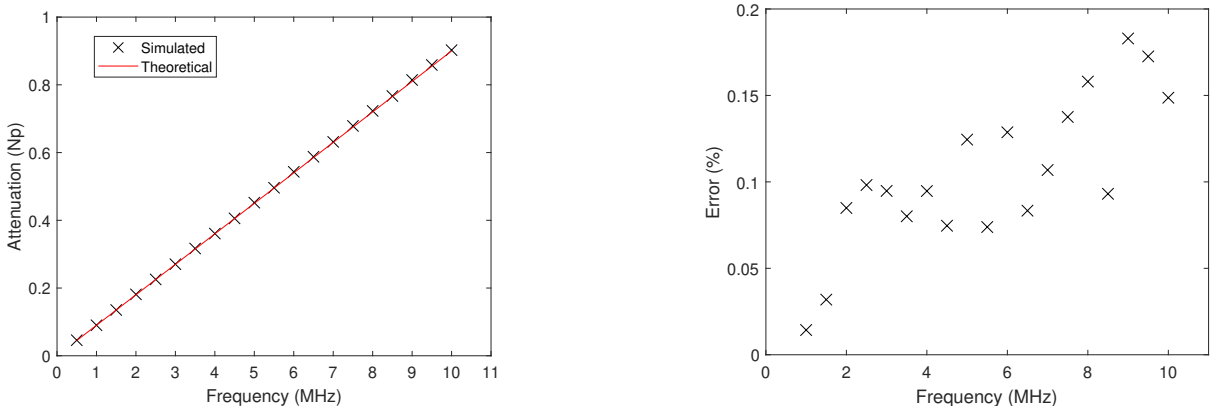

(a) (b)

Figure 3.6: Comparison of attenuation estimated from simulations to expected (theoretical) value for model 1. Figure 3.6a shows the results, with the percentage error shown in figure 3.6b

Table 3.5: Results for model 1. Input values are the mesh properties used for the construction of the properties, and the fit values are the result of the parameterisation of the best fit line. Uncertainties ($\pm$) correspond to the 95% confidence width as reported by the fitting tool. The SSE is the sum of squared errors between the fit line and the data.

Parameter	Input Value	Fit Value
α_0 $(Np\,m^{-1}MHz^{-1})$	5	5 ± 0.002
b	1.00	1.00 ± 0.02
SSE (Np^2)	N/A	6×10^{-7}

The results of model 2 are shown in figure 3.7 and table 3.6. The theoretical attenuation (α_T) was computed using the right hand side of equation (3.9) to give:

$$\alpha_T(f) = x\left(\alpha_{0,1}f^{1.2} + \alpha_{0,2}f^{1.5}\right), \tag{3.14}$$

where $x = 0.01\,m$ is the thickness of the attenuating regions. As in model 1, the higher percentage errors were observed for the higher frequencies, with a stronger correlation between frequency (and therefore damping) and the percentage error than observed with model 1.

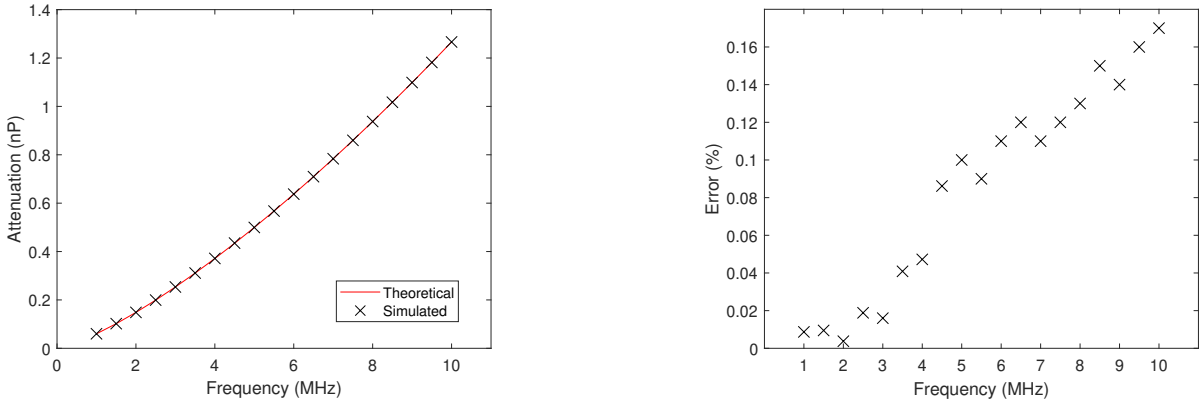

(a) (b)

Figure 3.7: Comparison of attenuation estimated from simulation to expected (theoretical) value for model 2.

Table 3.6: Results for model 2. $\alpha_{0,i}$ and and b_i are the attenuation constant and frequency exponent of the 'i'th attenuating layer respectively.

Parameter	Input Value	Fit Value
$\alpha_{0,1}$ $(Np\,m^{-1}MHz^{-1})$	2	$2.0115 \pm 1 \times 10^{-4}$
$\alpha_{0,2}$ $(Np\,m^{-1}MHz^{-1})$	1	$0.9996 \pm 1 \times 10^{-3}$
b_1	1.2	1.198 ± 0.003
b_2	1.5	1.501 ± 0.025
SSE (Np^2)	N/A	7×10^{-7}

The results of model 3 are shown in figure 3.8 and table 3.7. The theoretical attenuation (α_T) was computed using the right hand side of equation (3.12) to give:

$$\alpha_T(f) = \alpha_0^{skin} f^{b_{skin}} d_{skin} + \alpha_0^{fat} f^{b_{skin}} d_{skin} + \alpha_0^{muscle} f^{b_{muscle}} d_{muscle} - \sum_i^2 log(T_{i,i+1}), \quad (3.15)$$

where the three elements of T correspond to the transmission coefficients of the coupling medium-skin, skin-fat, and the fat-muscle interfaces. Conversely, the errors for this model were seen to be greatest for the lower frequencies, with a general reduction in error magnitude with increasing frequency. The error at $0.5\,MHz$ corresponds to a propagation wavelength in skin of $\sim 3.2mm$, so the error could be attributed to phase cancellation between the main pulse and a reverberation within the skin layer. The amplitude of this reverberation would be small relative to the main pulse, due to both attenuation in the skin layer and the weak reflection coefficients between the skin-muscle and skin-water interfaces. As such, it would be expected to be generate a weak effect, but could be significant in comparison to the numerical errors present. Evidence towards this hypothesis are the significant reduction in error with increasing frequency. As the frequency is increased, the wavelength of propagation within the skin will reduce and the reverberation echo will no longer interfere with the main pulse. Considering table 3.7, it was observed that the fitting approach was able to reproduce the input parameters within the 95% confidence intervals for all the attenuation constants and frequency dependencies.

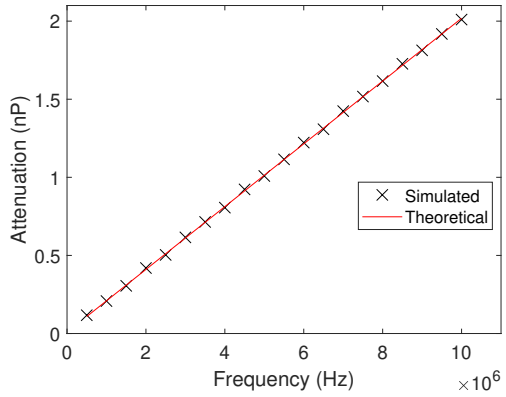

(a)

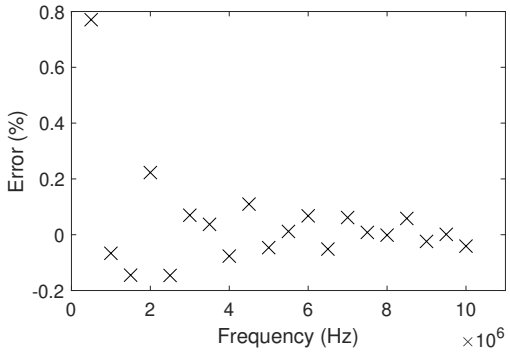

(b)

Figure 3.8: Comparison of attenuation measured by simulation to expected (theoretical) value for model 3. Pictured are the measured attenuation 3.8a and the percentage error 3.8b.

Table 3.7: Results for model 3

Parameter	Input Value	Fit Value
$\alpha_0^{skin}(Np\,m^{-1}MHz^{-1})$	21.158	$21.156 \pm 2 \times 10^{-3}$
$\alpha_0^{fat}(Np\,m^{-1}MHz^{-1})$	4.3578	$4.3576 \pm 1 \times 10^{-4}$
$\alpha_0^{muscle}(Np\,m^{-1}MHz^{-1})$	7.1088	$7.1087 \pm 1 \times 10^{-4}$
b_{skin}	1.000	1.000 ± 0.002
b_{fat}	1.086	1.085 ± 0.003
b_{muscle}	1.0890	1.080 ± 0.010
SSE (Np^2)	N/A	5×10^{-5}

3.4 Discussion

The multi-band finite element method was shown to be able to accurately reproduce the frequency dependence of attenuation for models of arbitrary material combinations (models 1 and 2) and also for a model based on real human soft tissue properties. These examples show that the method can effectively model the bulk properties on a narrow-band scale, which can then be recombined to compute the broadband attenuation.

The mesh refinement investigation model indicate that the attenuation estimates are best performed using a mesh discretisation with at least 20 elements per the centre wavelength of the simulation. The acoustic properties of a biological sample are difficult to compute on such a small scale length, which will naturally place a limit on the accuracy of the input parameters to the simulation. The observed optimal accuracy of the attenuation estimate at 50 elements per wavelength is an important, positive result, as it permits the possibility that sub-wavelength scatterers could be included into these models without the requirement for local mesh refinement. This consideration implies that models with greater complexity, containing both bulk attenuation and scattering from sub-wavelength scattering bodies (such as those that would contribute to speckle production) could be constructed using the MBFE approach. This optimal result deviates from the results obtained by Egerton et al. [130], who used 20 elements per wavelength, but direct comparison of accuracy is unavailable, as the authors were both simulating a different material type, and reported the attenuation through computation of the pulse width (by incorporation of attenuative and dispersive mechanisms), rather than computation of the attenuation value as has been described in this chapter. Dispersion effects are quoted as being negligible for soft tissues over the clinical range of ultrasound frequencies, so were not considered [124]. Other examples within the literature include the work of Brandner et al. [141], who developed a time domain finite element approach using a fractional derivative approach to computation of attenuation in breast tissue. The approach requires a more involved FE mathematical formulation than the use of mass proportional damping presented here. This may

explain their use of 2 elements per wavelength in the mesh design, as the increased complexity of the governing equations will incur greater computational cost than the approach of adapting the mass matrix to generate the attenuative behaviour. Whilst it is not possible to qualitatively apply the observations made here to other simulation packages, wave speed errors are associated with sparser grids [132], and as such, it is possible that this approach may result in systematic overestimation of the attenuation if the same effect of wave speed propagation is observed.

At the high mesh discretisation value, the increase in attenuation error observed has been hypothesised to be a cumulative increase in error with the number of time steps required in the simulation model. If this hypothesis is correct, then we would expect models with greater spatial dimensions to report greater attenuation errors as the wave is required to propagate over a greater distance (which for a fixed mesh refinement constitutes a greater number of elements). In a real, physical experiment, the signal to noise ratio will be reduced for regions of interest separated from the source (and by extension the receiver) where the path length in the attenuating material is increased, we will observe increased measurement errors for deeper lying regions of interest. Thus, we expect to see reductions in accuracy of the attenuation correction and BSC for these regions. However, the errors presented in this simulation approach are appreciably smaller than those observed in comparisons of attenuation measurement algorithms[127] (where variances of 25% were observed), which suggests that implementation of this approach would not be a limiting factor in the study of attenuation corrections or investigations.

Comparing models 1 and 2, we first note that the attenuation values are approximately equal for the two simulations, with the power law generating slightly higher attenuation at higher frequencies for model 2 compared to model 1. The uncertainties in fit parameters and SSE were larger for model 2 compared to model 1. The increase in uncertainties could be attributed to the increased dimensionality of the fitting procedure (4 fitted parameters instead of 2), which would result in a greater probability of

finding local minima, and/or a broadening of the global minimum region in the fitting procedure. The greater SSE value is apparent when we compare figures 3.6b and 3.7b. In figure 3.6b, there appears to be a correlation between frequency (and attenuation value) and percentage error. This correlation is stronger in figure 3.7b. The increase in frequency (and accompanying number of elements in the model) will result in a greater number of time steps, which has been hypothesised to contribute to an overestimation in attenuation as compared to the input value. Both figures 3.6b and 3.7b suggest that increasing the damping parameter in the model results in an increase in observed percentage error.

Considering the results of model 3, greater errors uncertainties were reported by the fitting approach. This could be attributed to the increased dimensionality of the fitting (using the same arguments as already presented). The increased SSE could be attributed to both the increase in parameter uncertainty, as well as the introduction of impedance mismatches into the model. The results indicate that the model was accurately able to reproduce the attenuation reflection characteristics across the full frequency range, suggesting that this methodology could be used for the simulation of attenuation corrections for models where large scale (on the order of multiple wavelengths) sound speed and density variations are present. This model features the soft tissue material with the greatest expected attenuation of ultrasound (skin [124]), so the reduced accuracy as compared to models 1 and 2 could be as a result of this, but the observation of accuracy is encouraging, as this model has accurately considered the limiting high attenuation case.

3.4.1 Limitations

The notable limitations to the application of the investigations presented here are the dimensionality of the simulations and the modelling of the source. The simulations presented here are 2D, neglecting the elevational propagation dimension to facilitate more lightweight simulations of wave propagation to be constructed. To present a

fully compelling case for the use of the tool with models mimicking real samples would naturally require the introduction of this third dimension. Nonetheless, the approach presented here does contain all the same physical mechanisms as would be used in a 3D model, and as such, should be scalable by dimension. The second limitation is in the source modelling. The approach of generating infinite plane waves neglects the need for diffraction correction of the results, which simplifies the consideration, but does not allow us to consider the attenuation combined with diffractive effects. Infinite plane sources are not realistic, and as such implementation of finite aperture widths and/or emit and receive focusing would be required to make the results more realistic.

Additionally, no attempts were made to incorporate effects of non-linear wave propagation into the simulation. Non-linear effects can result in generation of harmonics and excess deposition of energy in tissue [142], and hence are relevant to the attenuation of a finite amplitude wave. These effects were neither computed by the FE package (since Pogo is a linear FE solver), nor were the effects modelled through specific alteration of the linear solutions in the MBFE method. Non-linear effects were not considered as an effect of interest, and hence the FE tool was not developed to include these (as that would represent a substantial task). No consideration was given to altering the linear solutions to include non-linearity as the results would be specific to the incident pressure disturbance, and would not substantially improve the scope of these results.

Limitations of implementing this approach to generate attenuation corrections for real physical samples are the dependence on the approach to the availability of published tissue properties. Knowledge of the ultrasound propagation properties of a sample are important across all QUS modalities, since the wave propagation within the sample needs to be computed to infer the diffraction field within the source (as an example, consider the investigation into the sensitivity of the reference phantom method for diffraction correction on sound speed differences between the phantom and sample [143]). If this approach were to be used to generate attenuation corrections for real samples, it would require accurate knowledge of the bulk attenuation properties of

the sample in order to compute the appropriate attenuation correction for a specific emit/receive aperture.

In future work, it is hoped that these models can be increased in complexity and dimensionality, reflecting the inhomogeneity of real human tissue, to allow simulations of ultrasound propagation through patient specific models. Through this it is intended that patient specific attenuation corrections can be made to assist clinicians in using ultrasound for cancer progression tracking, by providing the corrections necessary to apply quantitative ultrasound approaches to tissue samples *in vivo* where performing a physical experiment to compute the correction is not possible.

3.5 Conclusion

This chapter has presented simulations of acoustic attenuation of plane wave signals in a plane wave model using the MBFE method to generate a broadband solution with sets of narrowband results. These results have presented accurate reproduction of the input parameters in all cases, suggesting that the approach could be used to simulate the attenuation of ultrasonic waves for use in the development of attenuation coefficient estimation algorithms or for generating attenuation corrections for estimation of the BSC of a tissue sample. The convergence of the attenuation behaviour with respect to mesh dicretisation was observed to have two facets. Sound speed underestimates caused by mesh refinement effects for simulations using < 20 elements per wavelength were observed that generated a monotonic overestimate of attenuation that was shown to decrease as the mesh was refined up to ~ 20 elements per wavelength. Continued mesh discretisation beyond this condition did not result in improvement, instead resulting in noisy behaviour which was observed to increase in magnitude as the number of elements exceeded 50 elements per wavelength. The convergence testing implied that mesh refinements of around 50 elements per wavelength results in the optimal trade-off between these effects in the simulation of attenuation effects using this approach.

With regards to the time step, a smaller variation in the measured attenuation was observed as the time step was varied when compared to the variation due to mesh discretisation. The optimal time step for accurate attenuation calculation was observed where a Courant value of 0.5 was applied.

Simulations of linear and power law frequency dependent attenuation experiments were constructed in acoustically impedance matched models, reproducing the expected attenuation to a high degree of accuracy through fitting of the measured attenuation, with errors $< 0.2\%$ observed over a frequency range of $0.5\,MHz$ to $10\,MHz$. The error in the estimated attenuation was found to be correlated to the strength of damping. Simulations of a human-like model comprised of layers of soft tissue materials were presented, with the estimated attenuation values over the same frequency range measured

as below 0.8%. A greater error was observed for the lowest frequency value ($0.5MHz$) which was hypothesised to be due to thin layer effects within the skin. High levels of agreement were observed using this model, with the non-linear fitting reproducing the input parameters within the 95% confidence width for all of the attenuation parameters.

Chapter 4

An investigation into BSC estimation using focused sources

The contents of this chapter have been submitted in manuscript form to Ultrasonic Imaging for consideration of publication.

4.1 Introduction

An obstacle to translating BSC estimation techniques into a clinical scenario is the problem of reproducibility between different methods or transducers. Many studies have been performed to investigate this. A notable first was conducted by Madsen et al. [88] who performed an interlaboratory investigation into BSC estimates. Laboratories returned BSC estimates based on their own experimental and analysis methodologies, and their own transducers based on distributed tissue-mimicking samples. Methodologies included both the reference phantom and planar-reflector substitution methods. BSC estimates differed by as much as an order of magnitude. More recently, Wear et al. [90] repeated the experiment across 8 laboratories in much the same way, finding multiple orders of magnitude difference between the laboratories. Anderson et al. [89] performed a two-laboratory study using glass beads as the scatterers and compared BSC estimates to Faran [91] scattering theory revealing agreement to scattering theory within 14% and much greater interlab agreement than previously observed. Additional studies with tissue mimicking and agar-glass bead phantoms [92][93] and in vivo studies [94] also improved on previous results, indicating increased reliability between estimates, and promise for clinical applicability. Similar studies have been performed considering more specific aspects of the BSC estimation process, including intermethod and interdevice [2][144] investigations. Based on the cited work it is clearly a long standing, and ongoing interest of the scientific community to investigate the conditions under which reproduceable and accurate BSC values can be obtained, to make the BSC a more clinically useful measure of tissue microstructure by determining the best conditions and methodology for BSC estimation.

This chapter will present a computational tool with which to perform this type of investigation, the advantages of which are threefold. Firstly, simulations offer flexibility in experimental design. One is not limited by the transducers available or the ability to accurately construct phantoms with specific properties. Secondly, simulations offer the opportunity to "switch off" certain physical effects such as attenuation, thereby isolating

different factors, and the knowledge that the desired parameters (sound speed, mass density, number density of scatterers, reflection coefficient of scatterers) can be input precisely, giving a trustworthy and error free ground truth for the BSC (unlike a physical experiment where the ground truth BSC must be estimated from the estimated scatterer properties and number density). Simulation based approaches have been used within the field of QUS for investigations into B-mode image texture [96][95][145], to investigate analysis parameters in investigation of US images [146] , and direct simulations of backscatter via both tissues [99] and red blood cells [147][148][149], as well as examples using the finite element method in the field of non-destructive evaluation [150][114][151]. Within the literature, tissue backscatter simulation has been performed by Shieh et al. [99], using Field II [98][152], a US image simulation tool based on impulse response of point scatterers. Whilst these results were promising, the limitation of this approach is that it does not capture all the physical mechanisms of scattering. Computation of the impulse response for point scatterers negates the possibility of multiple scattering and does not easily permit the construction of structure within the models. For this reason, Shieh et al. were unable to construct a reference plane reflector, and used a point scatterer to construct a spherical reference scatterer for the normalisation spectrum [99], which is an uncommon method within the BSC literature. Additionally, Field II [98][152] does not permit modelling of frequency dependence of attenuation, nor regional variation in sound speed or mass density, preventing it from being able to simulate tissue layers. By contrast, these factors are implementable in a FE framework. Due to the memory and time penalties associated with performing a 3D simulation, the FE models presented here are in 2D. It has been shown that simulating wave propagation and scattering problems in 2D is an efficient strategy for investigating complex problems [114], as they can capture all the wave propagation and scattering mechanisms with reduced processing power and shorter runtimes. The conclusions of such experiments are qualitative, and would require conceptually 'scaling up' a dimension to generate quantitative 3D answers, but the results of 2D experiments can be useful in their ability

to investigate and thereby influence 3D practices [114]. The simulations presented here model scattering from an idealised tissue-like region normalised by the spectrum from a reference reflector. The BSC estimate for the simulated collection of scattering bodies was then compared to a theoretical model. Since theoretical backscattering models are typically derived in 3D, this work will also present new derivations of backscatter equations into 2D. These will be used to both validate the 2D simulations and provide mathematical tools which other 2D simulations can be analysed by, facilitating greater throughput of simulations (due to the reduced runtime of lower dimensional simulations) and hence broader investigation into tissue backscattering. The reduction of model size is particularly useful in the simulation of a BSC experiment, where multiple beam lines are required to average over the statistical fluctuations in backscattered wave energy due to interference [1] (hence we require many simulations), and fine mesh discretisation is required to simulate tissue scattering contributions (leading to memory intensive simulations).

This chapter is structured as follows, section 4.2.1 will outline the mathematical framework for the construction of a 2D BSC measurement experiment, including both the theoretical computation of the BSC for an ensemble of identical scatterers based on their number density and individual scattering coefficient and the measurement equation that will generate a BSC estimate from the backscattered spectra from a sample and a reference reflector. The design of the scatterers in the FE model will be discussed in section 4.2.2.1, followed by the construction and testing of the BSC models in sections 4.2.2.5 and 4.2.2.6. To test the BSC models, two variables were altered: the backscattering properties of the simulated sample, and the focusing strength of the simulated source. The calculated BSC estimates were then compared to the theoretically derived BSC estimate for the simulation (which was calculated analytically), and additionally the amplitude envelope statistics were assessed to compare its behaviour to scattering theory [96][153][154] to provide further assurance of the validity of the model behaviour. This work provides proof of concept for this FE simulation approach, with

the future aim of using it to improve the reproducibility, accuracy and understanding of the factors affecting BSC measurement.

4.2 Methods

4.2.1 Derivations

This section is comprised of rederivations of fundamental BSC equations based on the approach of Ueda et al. [27][155], a novel effort to rederive the referenced works in a reduced dimensionality, to allow lightweight simulations to be constructed with similar underlying concepts. The two referenced works derive a mathematical framework for determining the BSC using the planar reflector substitution method for a material populated with weak sub-wavelength scattering bodies. Their mathematical approach was selected because - under appropriate assumptions - it was shown to reduce to results derived by other authors, unifying the different expressions [27].

4.2.1.1 Notation Convention

In all cases, primed coordinates correspond to those associated with the sound source and unprimed co-ordinates within the scattering area. For example the vector $\bar{r}'$ is on the source aperture, whilst $\bar{r}$ is within the scattering area. So too, the integral over l' is over the source aperture, and A is over the scattering area.

4.2.1.2 Density and Sound Speed Scattering Formulations

To begin, we define a pressure wave incident on an inhomogeneous medium with background density ρ_0 and sound speed c_0 with local density and sound speed fluctuations of $\Delta\rho(\bar{r})$ and $\Delta c(\bar{r})$ respectively. Its wavefunction ($P_i(\bar{r},t)$) will be a solution of the inhomogeneous wave equation[27].

$$\frac{1}{c_0^2}\frac{\partial^2 P_i(\bar{r},t)}{\partial t^2} - \nabla^2 P_i(\bar{r},t) = \frac{2\Delta c(\bar{r})}{c_0^3}\frac{\partial^2 P_i(\bar{r},t)}{\partial t^2} - \frac{1}{\rho_0}\nabla[\Delta\rho(\bar{r})]\cdot\nabla P_i(\bar{r},t). \tag{4.1}$$

We first take the Born approximation[156], assuming that all scattered pressure waves ($P_s(\bar{r},t)$) from the inhomogeneities received at the transducer (with co-ordinates de-

noted $\bar{r}'$) will be equivalent to sources defined by wavefunction $Q(\bar{r},t)$. These wavefronts will diverge spatially according to distance and wavenumber (k) as $1/\sqrt{k|\bar{r}-\bar{r}'|}$, with a constant Γ related to the full-space Green's function. This gives:

$$P_s(\bar{r}',t) = \Gamma \int_A dA \, \frac{Q\left(\bar{r}, t - \frac{|\bar{r}-\bar{r}'|}{c_0}\right)}{\sqrt{k|\bar{r}-\bar{r}'|}} \tag{4.2}$$

We can express the time-dependent incident field as the inverse Fourier transform of its frequency representation, and substitute the relation between the velocity potential (Φ) and pressure $P_i(\bar{r},\omega) = -\rho_0 \frac{\partial \Phi(\omega,\bar{r})}{\partial t}$, giving

$$P_i(\bar{r},t) = \mathscr{F}^{-1}\left[P_i(\bar{r},\omega)\right] = -\mathscr{F}^{-1}\left[\rho_0 \frac{\partial}{\partial t}\Phi(\omega,\bar{r})\right]. \tag{4.3}$$

Separating the velocity potential into the frequency dependent velocity amplitude of the source and the velocity potential of the system ($\Phi(\omega) = U(\omega)\hat{\Phi}(\omega)$) and assuming $\Phi(\omega)$ is time harmonic we may then write

$$P_i(\bar{r},t) = \frac{1}{2\pi}\int_{-\infty}^{\infty} d\omega \; (i\omega)\rho_0 U(\omega)\hat{\Phi}(\omega,\bar{r})e^{i\omega t}. \tag{4.4}$$

Now setting $Q(\bar{r},t)$ equal to the right hand side of equation (4.1), we first consider the case where the scatterer at $\bar{r}$ is a sound speed fluctuation, i.e. $\Delta\rho = 0$, $\Delta c \neq 0$. On substitution of (4.4) into equation (4.1), we then find

$$Q(\bar{r},t) = \frac{2\Delta c(\bar{r})\rho_0}{2\pi c_0^3}\int_{-\infty}^{\infty} d\omega \; (i\omega)^3 \hat{\Phi}(\omega,\bar{r})U(\omega)e^{i\omega t}. \tag{4.5}$$

Substituting this into equation (4.2) gives

$$P_s(\bar{r}',t) = \int_A dA \left(\frac{\Gamma}{\sqrt{k|\bar{r}-\bar{r}'|}}\frac{2\Delta c(\bar{r})\rho_0}{c_0^3}\frac{1}{2\pi}\int_{-\infty}^{\infty} d\omega \; (i\omega)^3\hat{\Phi}(\omega,\bar{r})U(\omega)e^{i\omega(t-\frac{|\bar{r}-\bar{r}'|}{c_0})}\right). \tag{4.6}$$

The A-line received by the aperture (treating it as a single element) $e_s(t)$ will be the integration of the scattered wave over the receive aperture:

$$e_s(t) = \int_{l'} dl' \; P_s(\bar{r}', t), \tag{4.7}$$

which, on substitution into equation (4.6) gives

$$e_s(t) = \int_{l'} dl' \int_A dA \int_{-\infty}^{\infty} d\omega \left(\frac{\Gamma}{2\pi\sqrt{k|\bar{r} - \bar{r}'|}} \frac{2\Delta c(\bar{r})\rho_0}{c_0^3} (i\omega)^3 \hat{\Phi}(\omega, \bar{r}) U(\omega) e^{i\omega(t - \frac{|\bar{r} - \bar{r}'|}{c_0})} \right). \tag{4.8}$$

Defining the velocity potential as

$$\hat{\Phi}(\omega, \bar{r}) = \int_{l'} dl' \; g_{2D}(r, k), \tag{4.9}$$

where

$$g_{2D}(r, k) = -\frac{i}{4} H_0^{(2)}(kr) \tag{4.10}$$

and $H_0^{(2)}(kr)$ is the zero order Hankel function of the second kind. First assuming that we are in the spatial far field of the infinite line source we may take the asymptotic limit of the right hand side of (4.10) to produce

$$g_{2D}(r, k) \lim_{kr >> 1} = \frac{-i}{4} \sqrt{\frac{2}{\pi kr}} e^{-i(kr - \pi/4)}. \tag{4.11}$$

In this limit (with substitution in our co-ordinate system), the velocity potential becomes

$$\hat{\Phi}(\omega, \bar{r}) = \frac{-i}{4} \sqrt{\frac{2}{\pi}} \int_{l'} dl' \; \frac{e^{-i(k|\bar{r} - \bar{r}'| - \pi/4)}}{\sqrt{k|\bar{r} - \bar{r}'|}}. \tag{4.12}$$

Comparing equations (4.12) and (4.2) we can see that the constant $\Gamma = \frac{-ie^{i\pi/4}}{4}\sqrt{\frac{2}{\pi}}$. Combining the source and receive characteristics into a single variable ($T(\omega) = U(\omega)G(\omega)$) and noting that the integral over l' in equation (4.8) will resemble equation (4.12) we may write an equation describing the frequency response of the medium as received at

the source:

$$E_s(\omega) = G(\omega)\mathscr{F}\left[e_s(t)\right] = -G(\omega)\int_A dA\ \frac{2\Delta c(\bar{r})}{c_0^3}\rho_0\omega^3\hat{\Phi}^2(\omega,\bar{r}). \tag{4.13}$$

Substituting in the reflection coefficient as a function of position ($R(\bar{r}) = \frac{\Delta c(\bar{r})}{2c_0}$), the acoustic impedance ($Z_0 = c_0\rho_0$) and a linear dispersion relation ($\omega = c_0 k$), we arrive at the equation describing the scattered field due to a distribution of velocity fluctuations.

$$E_s(\omega) = -4iT(\omega)Z_0 k\int_A dA\ R(\bar{r})[k\hat{\Phi}(\omega,\bar{r})]^2. \tag{4.14}$$

Now considering a density fluctuation, the source function can be expressed as

$$Q(\bar{r},t) = -\frac{1}{\rho_0}\nabla[\Delta\rho(\bar{r})]\cdot\nabla\frac{1}{2\pi}\int_{-\infty}^{\infty}d\omega\ (i\omega)\rho_0(U(\omega)\hat{\Phi}(\omega))e^{i\omega t}. \tag{4.15}$$

Which on substitution into equation (4.2) gives

$$P_s(\bar{r}',t) = \int_A dA\ \frac{\Gamma}{\sqrt{k|\bar{r}-\bar{r}'|}}\frac{1}{\rho_0}\nabla[\Delta\rho(\bar{r})]\cdot\nabla\left[\frac{1}{2\pi}\int_{-\infty}^{\infty}d\omega\ (i\omega)\rho_0(U(\omega)\hat{\Phi}(\omega))e^{i\left(\omega t-\frac{|\bar{r}-\bar{r}'|}{c_0}\right)}\right]. \tag{4.16}$$

Once again, the receive echo will be the integral over the transducer (as in equation (4.7)). The integral over the transducer again introduces a factor of $\hat{\Phi}(\omega,\bar{r})$. Notating this echo as $e_p(t)$ gives:

$$e_p(t) = -\frac{1}{2\pi}\int_A dA\ \int_{-\infty}^{\infty}d\omega\ \hat{\Phi}(\omega))\nabla\left[\frac{\Delta}{\rho_0}\rho(\bar{r})\right]\cdot\nabla\left[(i\omega)\rho_0(U(\omega)\hat{\Phi}(\omega))e^{i\omega t}\right]. \tag{4.17}$$

Now assuming that the medium is a combination of discrete blocks, we may write

$$\nabla\left[\frac{\Delta\rho}{\rho_0}\right] = \frac{\Delta\rho_j}{\rho_0}\hat{N}_j\delta(\bar{r}-\bar{r_j}), \tag{4.18}$$

where $\hat{N}_j$ is the vector normal to the scattering block, and $\bar{r}_j$ is its position. If we

arrange these blocks parallel to the beam axis, to form a line reflector, the integral over the area of the scattering domain A reduces to a line integral over line reflector (since we disregard any later reflections) with surface normal $\hat{N}$. If we define this surface normal as $\hat{j}$ equation (4.16) becomes

$$E_p(\omega) = G(\omega).\mathscr{F}e_p(t) = i\omega\rho_0 T(\omega)\int_{-\infty}^{\infty} dx\ [R(\bar{r})\hat{\Phi}(\omega,\bar{r})\frac{\partial}{\partial y}\hat{\Phi}(\omega,\bar{r})], \tag{4.19}$$

where we have expressed the scattered amplitude spectrum from a line reflector in terms of its reflection coefficient, the medium properties and the velocity potential characteristics of the source. Equations (4.14) and (4.19) will later be used to derive the mathematical formulation for the substitution method, from which the backscatter coefficient will be extracted.

4.2.1.3 Incoherent Scattered Signal Derivation

Considering first a monopole source of sound waves at position $\bar{r}$ measured at $\bar{r}'$, the measured intensity (in the asymptotic limit $k|\bar{r}-\bar{r}'|$) will be

$$I(\bar{r}) = \frac{|P_{AS}|^2}{(2\rho_0 c_0)}, \tag{4.20}$$

where the asymptotic amplitude will be given by

$$P_{AS} = B\sqrt{\frac{2}{\pi k|\bar{r}-\bar{r}'|}}, \tag{4.21}$$

where B is the amplitude of the scattered wave. The power received at a distance of radius $|\bar{r}-\bar{r}'|$ will be given by:

$$W = \frac{2|B|^2}{kc_0\rho_0}. \tag{4.22}$$

Considering now the incident field on position $\bar{r}$, we first write this as the time derivative of the vector potential of the source Φ'

$$I(\bar{r}) = \frac{|\rho_0 \frac{\partial}{\partial t}\Phi'|^2}{2\rho_0 c_0} \tag{4.23}$$

and assuming Φ' is time harmonic:

$$I(\bar{r}) = \frac{|i\omega\rho_0\Phi'|^2}{2\rho_0 c_0}, \tag{4.24}$$

the power scattered by the elemental area on which this intensity is incident will be

$$W = 2\pi I \mu_{BS} \Delta s \tag{4.25}$$

where μ_{BS} is the BSC of the scattering element. To conserve energy, equation (4.22) must equal (4.25), which allows us to compute B for a given backscatter coefficient and velocity potential.

$$|B|^2 = \frac{k\pi\rho_0^2\omega^2|\Phi'|^2\mu_{BS}\Delta s}{2} \tag{4.26}$$

The echo amplitude received at the transducer from the scatterer at $\bar{r}$ will be given by

$$E_s(\omega, \bar{r}) = T(\omega)B\int_{l'} dl' \frac{e^{ik|\bar{r}-\bar{r}'|}}{\sqrt{k|\bar{r}-\bar{r}'|}} \tag{4.27}$$

Substituting our definition of $\hat{\Phi}$ from equation (4.12):

$$E_s(\omega, \bar{r}) = -ie^{i\pi/4}4\sqrt{\frac{\pi}{2}}T(\omega)B\hat{\Phi}(\omega, \bar{r}). \tag{4.28}$$

The incoherent scattered power spectrum will then be given by the echo spectrum from each scatterer squared, integrated over the whole sample under interrogation (A):

$$S_i(\omega) = \int_A dA\ |E_s(\omega, \bar{r})|^2 = 8\pi|T(\omega)|^2 \int_A dA\ |B\hat{\Phi}|^2. \tag{4.29}$$

Assuming weak and singular scattering only, we assume that $|\hat{\Phi}|$ is unchanged in the axial direction over the gate length d we consider. This produces a factor of d and reduces the double integral to a single, lateral integral. In addition, we substitute equation (4.26), whilst assuming the magnitude of the velocity potentials Φ' and $\hat{\Phi}$ are equivalent:

$$S_i(\omega) = 4\pi^2\omega^2\rho_0^2\mu_{BS}|T(\omega)|^2kd\int_{-\infty}^{infty} dy|\hat{\Phi}|^4. \tag{4.30}$$

Now applying the ansatz

$$\hat{\Phi}(k,x,y) = A_\Phi e^{-ik(y+\frac{x^2}{2y_0})}f(k,x) \tag{4.31}$$

where $f(k,x)$ is the directivity of the source, given by

$$f(k,x) = e^{-\frac{x^2}{\sigma_B^2}}, \tag{4.32}$$

equation (4.30) becomes

$$S_i(\omega) = 4\pi^2\omega^2\rho_0^2\mu_{BS}|T(\omega)|^2kd\int_{-\infty}^{\infty} dx\ |A_\Phi|^4 e^{-\frac{4x^2}{\sigma_B^2}}. \tag{4.33}$$

The identity

$$\int_{-\infty}^{\infty} dq e^{-(\chi^2q^2+i\tau q)} = \frac{\sqrt{\pi}}{\chi}e^{-\frac{\tau^2}{4\chi^2}} \tag{4.34}$$

simplifies (4.33) into

$$S_i(\omega) = 2\pi^2\omega^2\rho_0^2\mu_{BS}|T(\omega)A_\Phi^2|^2kd\sigma_B\sqrt{\pi} \tag{4.35}$$

which describes the backscattered power spectrum received from an ensemble of small, weak, monopole scatterers as a function of the BSC and the source properties.

4.2.1.4 Plane Reflector Signal Derivation

Starting from equation (4.19), we substitute the ansatz from (4.31), and notice that only the phase changes in the $\hat{j}$ direction, hence the derivative will simply extract a factor of ik. Defining

$$A_E = \omega \rho_0 T(\omega) \tag{4.36}$$

for simplicity, we find

$$E(\omega) = ikA_E R_p A_\Phi^2 e^{-2iky} \sqrt{\frac{\pi}{\frac{2}{\sigma_B^2} + \frac{ik}{y_0}}}. \tag{4.37}$$

Taking the magnitude squared of this expression will give

$$S_p(\omega) = k^2 |A_E A_\Phi^2|^2 R_p^2 \frac{\pi}{\sqrt{\left(\frac{2}{\sigma_B^2}\right)^2 + (\frac{k}{y_0})^2}} \tag{4.38}$$

Substituting equation (4.36) for A_E, the resulting equation for the plane reflector signal will be

$$S_p(\omega) = \frac{k y_0 \omega^2 \rho_0^2 |T(\omega) A_\Phi^2|^2 R_p \pi}{\sqrt{(1 + (\frac{2y_0}{k\sigma_B^2})^2)}} \tag{4.39}$$

4.2.1.5 The Measurement Equation

Taking the ratio of (4.35) and (4.39) and rearranging for μ_{BS} gives

$$\mu_{BS} = \frac{S_i(\omega)}{S_p(\omega)} \frac{1}{2\pi\sqrt{\pi}} \frac{y_0 R_p/(d\sigma_B)}{\sqrt{(1 + (\frac{2y_0}{k\sigma_B^2})^2)}}. \tag{4.40}$$

If we make the substitution $\sigma_B = \sqrt{8} y_0/ka$, the resulting equation is

$$\mu_{BS} = \frac{S_i(\omega)}{S_p(\omega)} \frac{1}{2\pi\sqrt{8\pi}} \frac{R_p ka/d}{\sqrt{(1 + (\frac{ka^2}{4y_0})^2)}}, \tag{4.41}$$

which can be seen as the typical form of an experimental substitution method backscatter experiment, where the backscattered signal $S_i(\omega)$ is compared to a reference signal $S_p(\omega)$, with a factor concerned with the geometry of the problem. $S_i(\omega)$ and $S_p(\omega)$ refer to two finite element simulations, one with a diffuse scattering medium present, and one with a planar reflector present. These are compared using (4.41) to compute an estimate for the BSC.

4.2.1.6 Theoretical Backscatter Coefficient

Starting with equation (4.14), we once again apply the ansatz in equation (4.31) and square the magnitude to find the receive power spectrum:

$$S(\omega) = 16Z_0^2k^2|U(\omega)|^2 \int\int dA_1 dA_2 \, \overline{R(\bar{r_1})R(\bar{r_2})} \times [k^2\Phi(\omega,\bar{r_1})\Phi^*(\omega,\bar{r_1})]^2, \tag{4.42}$$

where the bar indicates the average. Using a weak scattering assumption, and hence that the incident field is unchanged significantly by the scattering medium, the behaviour of the integrand is dominated by the spatial variation in the reflection coefficient. If $|r_1 - r_2| << \sigma$ (where σ is the correlation length of the amplitude reflection coefficient of the medium) then

$$\overline{R(\bar{r_1})R(\bar{r_2})} = \overline{R^2(\bar{r})}, \tag{4.43}$$

and if $|\bar{r_1} - \bar{r_2}| >> \sigma$ then

$$\overline{R(\bar{r_1})R(\bar{r_2})} = [\overline{R(\bar{r})}]^2. \tag{4.44}$$

Combining these limiting cases gives

$$\overline{R(\bar{r_1})R(\bar{r_2})} = R_s^2\kappa(\bar{r_1} - \bar{r_2}) + R_m^2, \tag{4.45}$$

and the following relations may be found:

$$R_s^2 = \overline{R^2(\bar{r})} - \overline{R(\bar{r})}^2 \tag{4.46}$$

$$R_m = R_0 \kappa_v \tag{4.47}$$

$$R_m(\bar{r}) = \overline{R(\bar{r})} \tag{4.48}$$

where R_s and R_m are the standard deviation and mean of $R(\bar{r})$ respectively and $\kappa(\bar{r_1} - \bar{r_2})$ is the autocorrelation function of the amplitude reflection coefficient of the material. For an ensemble of discrete scattering bodies with amplitude reflection coefficient relative to background of R_0, area concentration κ_A and number density n, the following statements also hold:

$$R_s^2 = R_0^2(\kappa_A - \kappa_A^2) \tag{4.49}$$

$$R_m = R_0 \kappa_A \tag{4.50}$$

$$\kappa_A = n\sigma^2 \tag{4.51}$$

Applying this to equation (4.42) gives a coherent component S_c, (a reflection due to the mean behaviour of the medium) and an incoherent component S_i (due to the ensemble of individual scattering bodies within the medium), with the total scattering $S(\omega)$ being the sum of these contributions. We can define them as

$$S_c(\omega) = 16 Z_0^2 k^2 |U(\omega)|^2 \left| \int_A dA \; R_m k^2 \Phi(\omega, \bar{r_1}) \Phi^*(\omega, \bar{r_1}) \right|^2 \tag{4.52}$$

and

$$S_i(\omega) = 16Z_0^2 k^2 |U(\omega)|^2 \int\int dA_1 dA_2 \; R_s \kappa(\bar{r_1} - \bar{r_2}) \times [k^2 \Phi(\omega, \bar{r_1}) \Phi^*(\omega, \bar{r_1})]^2. \quad (4.53)$$

Focusing on the incoherent component, we rewrite as

$$S_i(\omega) = 16Z_0^2 |U(\omega)|^2 k^6 R_s^2 A_\Phi^4 g(\omega) \quad (4.54)$$

where $g(\omega)$ is the frequency response of the medium based on the spatial variation of the amplitude reflection coefficient. To solve $g(\omega)$ we first define a new set of co-ordinates:

$$\begin{aligned} s_1 &= x_1 - x_2, \quad s_2 = x_1 + x_2 \\ u_1 &= y_1 - y_2, \quad u_2 = y_1 + y_2 \end{aligned} \quad (4.55)$$

Defining $g(\omega)$ as

$$g(\omega) = \frac{d}{4} \int_{-\infty}^{\infty} \int_{-\infty}^{\infty} ds_1 du_1 \; \kappa(s_1, u_1) h(s_1) e^{i2ku_1} \quad (4.56)$$

and

$$h(s_1) = 4 \int_{-\infty}^{\infty} ds_2 \; f\left(k, \frac{s_1 + s_2}{2}, y_0\right) f^*\left(k, \frac{s_1 - s_2}{2}, y_0\right) \quad (4.57)$$

we now assume that the correlation coefficient of the medium varies much more rapidly than the velocity potential (i.e. all the scattering bodies see the same field), which corresponds to $h(s_1)$ only being evaluated at $s_1 = 0$:

$$S_i(\omega) = 16Z_0^2 |U(\omega)|^2 k^6 R_s^2 d \int_{-\infty}^{\infty} \int_{-\infty}^{\infty} ds_1 du_1 \; \left(\kappa(s_1, u_1) \left[\int_{-\infty}^{\infty} ds_2 \; |A_\Phi^4 f(k, s_2, y_0)|^4 \right] e^{i2ku_1} \right). \quad (4.58)$$

This further simplifies on substitution of $|A_\Phi^4 f(k)^4|$ for $|\Phi|^4$ (using equation (4.31))

$$S_i(\omega) = 16Z_0^2|U(\omega)|^2k^6R_s^2d\int_{-\infty}^{\infty} ds_2\ |\Phi|^4 \int_{-\infty}^{\infty} ds_1du_1\ \kappa(s_1,u_1)e^{i2ku_1}. \tag{4.59}$$

Comparing equations (4.30) and (4.59) gives an expression for a theoretical BSC value (μ_{BS}^T) based only on the properties of the medium.

$$\mu_{BS}^T(\omega) = \frac{4k^3R_s^2}{\pi^2}\int_{-\infty}^{\infty} ds_1du_1\ \kappa(s_1,u_1)e^{-i2ku_1}. \tag{4.60}$$

Defining a new co-ordinate system

$$s_1 = \gamma\sigma_x cos(\theta) \tag{4.61}$$

$$u_1 = \gamma\sigma_x sin(\theta) \tag{4.62}$$

$$ds_1du_1 = \gamma\sigma_x\sigma_w d\gamma d\theta \tag{4.63}$$

converts (4.60) into

$$\mu_{BS}^T(\omega) = \frac{4k^3R_s^2\sigma^2}{\pi^2}\int_{-\infty}^{\infty} d\gamma\ \gamma\kappa(\gamma)\int_{-\pi}^{\pi} d\theta\ e^{-2ik\gamma\sigma_w sin(\theta)}. \tag{4.64}$$

Applying the identity

$$J_n(\gamma) = \frac{1}{2\pi}\int_{-\pi}^{\pi} d\chi\ e^{-i(\gamma sin(\chi sin(\chi)-\eta\chi))} \tag{4.65}$$

results in

$$\mu_{BS}^T(\omega) = \frac{8k^3R_s^2\sigma^2}{\pi}\int_{-\infty}^{\infty} d\gamma\ \gamma\kappa(\gamma)J_0(2k\gamma\sigma_w). \tag{4.66}$$

To find the backscatter coefficient for a collection of circular scattering bodies we take the intersection area of two circles of radius equal to the correlation length of the

reflection coefficient of the material (σ) based on the dimensionless spatial lag $\gamma = \frac{r}{\sigma}$. The normalised intersection area of two circles is given by

$$\kappa(\gamma) = \begin{cases} \frac{1}{\pi}\left(2cos^{-1}(\frac{\gamma}{2}) - \frac{\gamma}{2}\sqrt{4-\gamma^2}\right) & : \ 0 < \gamma \leq 2 \\ 0 & : \ 0 > \gamma > 2 \end{cases} \tag{4.67}$$

The backscatter coefficient will hence be

$$\mu_{BS}^{T}(\omega) = \frac{16k^3R_s^2\sigma^2}{\pi}\int_0^2 d\gamma \ \gamma J_0(2k\gamma\sigma)\left(2cos^{-1}\left(\frac{\gamma}{2}\right) - \frac{\gamma}{2}\sqrt{4-\gamma^2}\right). \tag{4.68}$$

which is evaluated numerically for comparison with BSC estimates evaluated using the FEM described in the next section.

4.2.2 Finite Element Methods

The following section describes the design of the FE models used to simulate a BSC estimation experiment. Firstly, the design of the individual scatterers will be explained, followed by the design of the BSC models and the analysis methodology. The ultimate test of the approach was to compare a simulated BSC estimate to a theoretically derived value from the mesh properties. To achieve this, simulations were performed and the BSC coefficient estimate computed using equation (4.41). The accuracy of the approach was then assessed through comparison of the BSC estimate to that computed from equation (4.68). This was then repeated whilst altering simulation parameters to test the accuracy of the methodology in differing conditions. The two parameters altered were the BSC of the simulated scattering region and the focusing strength of the source used to insonify the scattering region. The former was altered through changing the number density of scatterers. This was varied to test the accuracy of the tool to simulate different tissue types, from one sparsely populated by scatterers and possessing a low BSC value, up to a condition where there are sufficient scatterers to generate a fully developed speckle pattern and a greater BSC value. The second parameter was

controlled by changing the source aperture width whilst maintaining the same focal depth. This was altered to test the accuracy of the tool to generate accurate BSC estimates with a range of sources.

4.2.2.1 Scatterer Design Models

Initial experimentation was performed to design weak, monopole scatterers matching those described in section 4.2.1.6. To do so, the properties of the FE mesh were locally varied and the resulting scattering distribution compared to Faran scattering theory [91]. The simulation parameters are listed in table 4.1. Weak, monopole scattering was achieved by applying a small sound speed fluctuation to element(s) within the mesh relative to the rest of the domain (whilst maintaining a homogeneous mass density throughout the whole domain). The mesh was set to be highly discretised spatially to model small scatterers and the Courant value set for high temporal resolution to prioritise accuracy over run-time. Three configurations were tested: square scattering bodies formed of single elements, square scattering bodies formed of four elements, and a heptagonal scattering body formed of 7 tessellated triangular elements (see figure 4.1). Square elements were tested as they generate a simple, regular grid of points which is simple to mesh. This was compared to a triangular meshed case, which more closely maps the perimeter of the - assumed - circular scatterer shape. Mesh refinement of the square case was performed to assess whether the representation of the scatterers by a greater number of elements (4 as opposed to 1) improved the accuracy of the scattering distribution. Scatterer area was kept constant between the configurations to allow direct comparison of the scattering distributions.

To measure the scattering distributions of the different configurations, a point source of acoustic pressure waves was used to insonify the target element(s) and the resulting field recorded by receiver nodes placed at points around the scatterer forming a circle of radius 15mm ($5\lambda_0$). This simulation was then repeated without the scatterer present, and the time domain difference between the pressure fields with and without

Table 4.1: Properties for the simulations described.

Property	Value
Background medium sound speed (c_0)	$1500ms^{-1}$
Scattering body sound speed (c_S)	$1497ms^{-1}$
Background medium density (ρ_0)	$1000kgm^{-3}$
Scattering body density (ρ_S)	$1000kgm^{-3}$
Courant value	0.1
Centre frequency of excitation (f_0)	$0.5MHz$
Centre Wavelength (λ_0)	$3mm$
Mesh refinement: square single (dx)	$dx = \lambda_0/50 = 60\mu m$
Mesh refinement: square four (dx)	$dx = \lambda_0/100 = 30\mu m$
Mesh refinement: triangle seven (dx)	$dx = \lambda_0/50 \times \sqrt{\frac{2}{3\sqrt{3}}} \simeq 37\mu m$

the scatterer were taken to compute the scattered pressure field. The scattered pressure at each scattering angle was then Fourier transformed, and the absolute scattered wave amplitude calculated at the centre frequency of the initial excitation (f_0), scaled by the 2D free space Green's function (equation (4.10)) and compared to the analytical model as derived by Faran[91]. The root mean square error (RMSE) between the analytical and simulation backscattering amplitudes (at the centre frequency of insonification) was used as the quality metric. This quality metric informed the choice of scatterer to use in the BSC simulation models.

4.2.2.2 Backscatter Coefficient Estimation Models

To simulate a planar reflector substitution method BSC measurement, two simulation types were required. The first is the scattering medium (the BSC of which is to be measured) and the second the planar reflector (used to compute the calibration spectrum). Measurement of the backscattered energy from the scattering medium (($S_i(\omega)$) and the planar reflector ($S_p(\omega)$) can then be used to compute the BSC using equation (4.41). Examples of these two simulation geometries are pictured in figure 4.2. For these simulations, the scattering medium was constructed by randomly selecting elements within a region of the model to be designated as 'scattering elements'. These elements were assigned material properties with a lower sound speed relative to the background, as

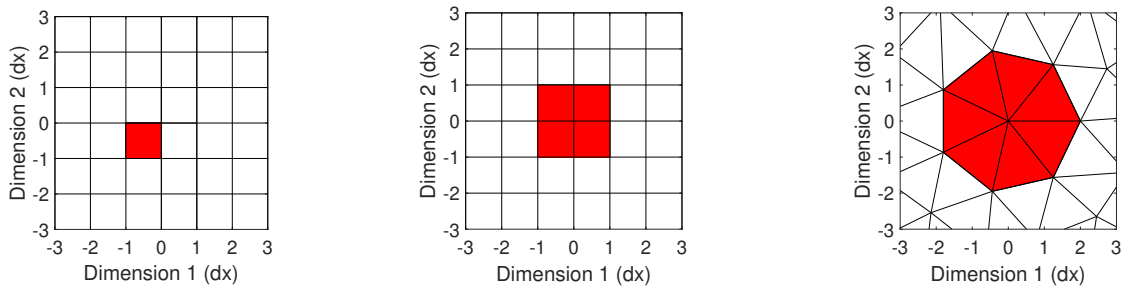

(a) (b) (c)

Figure 4.1: The three simulated single scattering models, with the background medium unshaded, and the elements with velocity fluctuation relative to background coloured in red. Black lines represent element boundaries. Figure 4.1a is the single element square case, figure 4.1b the four element square case and figure 4.1c is the triangular case. The mesh discretisation (dx) was varied between cases to maintain a constant scatterer area.

detailed in table 4.1. To prevent unwanted reflections, absorbing regions were placed adjacent to all model boundaries in the incoherent scattering model (as shown in figure 4.2). In the planar reflector model, absorbing regions were placed adjacent to all model boundaries besides that acting as the planar reflector. The absorbing boundaries attenuate wave energy by gradually increasing damping from the edge of the boundary toward the model edge, attenuating the wave energy whilst minimising the impedance mismatch between adjacent element layers. This simulates an infinite space in which only the scatterers placed in the model contribute to the measured backscattered energy.

4.2.2.3 Source Design

As described in chapter 2, focused sources were simulated through selecting a line of nodes was perpendicular to the beam axis, and applying a beam delay profile was applied to the signals from each node to simulate a curved source of pressure waves, simulating the radiated field from a single element, focused transducer (figure 2.2) or an array with a time delay profile placed on the elements. In receive mode, the backscattered pressure was recorded at each of the same nodes, time delayed with the

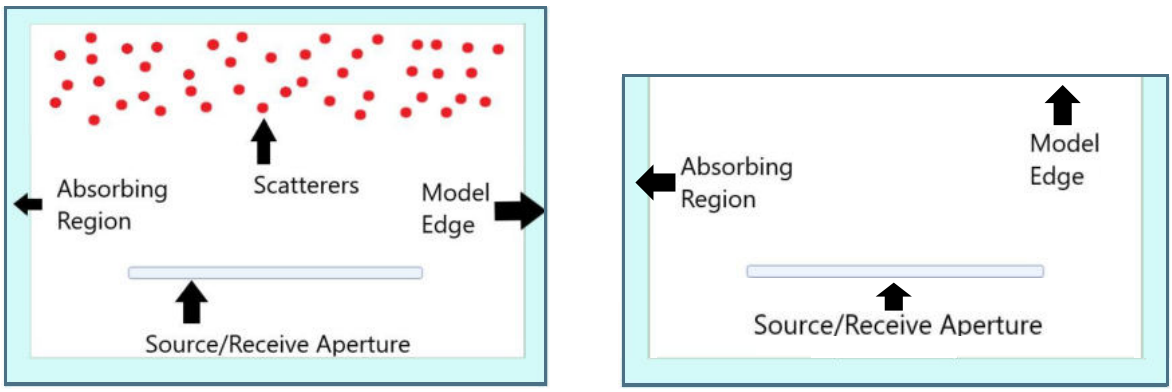

(a) (b)

Figure 4.2: Examples of the random scatterer (4.2a) and planar reflector (4.2b) simulation models. In both, the source is positioned such that the scatterer(s) of interest are positioned at the focal depth (5cm). In 4.2a, the source is positioned with the focal depth 5mm inside the region populated with scatterers so a symmetrical gate centred at the focus captured echoes scattered anterior and posterior to the focal depth. In 4.2b, the source was positioned with the model boundary at the focal depth. Absorbing regions were used to prevent unwanted reflections from model edges.

same profile used in emission and summed to generate an A-line, simulating reception across the face of a curved element (or array with a receive delay profile). In the case of the random scatterer simulation, the position of the source nodes along the beam axis was selected to ensure the focal depth was inside the region populated with scatterers, by a distance greater than half the spatial length of the emitted pulse. With a centre wavelength of 3mm (as per table 4.1), the pulse length is 9mm. In the case of the calibration spectrum, the axial position of the nodes was selected such that the focus was coincident with the depth of the planar reflector. In all cases described, the focal depth was 5cm.

The beam width of this source was also calculated to determine the number of scatterers contained within the resolution cell of the simulated sources. To measure this, a model was designed with 'field' nodes placed in the model at regular intervals to compute the incident intensity at the centre frequency for different points in the field of

view of the source. The grid of field nodes was designed with the same lateral spacing as the nodes that make up the source/receiver ($dx = \lambda_0/50$) and an axial spacing of $\lambda_0/10$. This is visualised in figure 4.3. To calculate the beam width, the data collected at nodes displaced laterally from the beam axis was analysed at the centre frequency of the excitation and the central lobe was fitted to a Gaussian beam profile, with the Gaussian width used as the measure of the beam width. The axial resolution was defined as one half the length of the imaging pulse. The imaging pulse was a 3 cycle tone burst, with a centre frequency of $3\,mm$, giving an axial resolution of $4.5\,mm$.

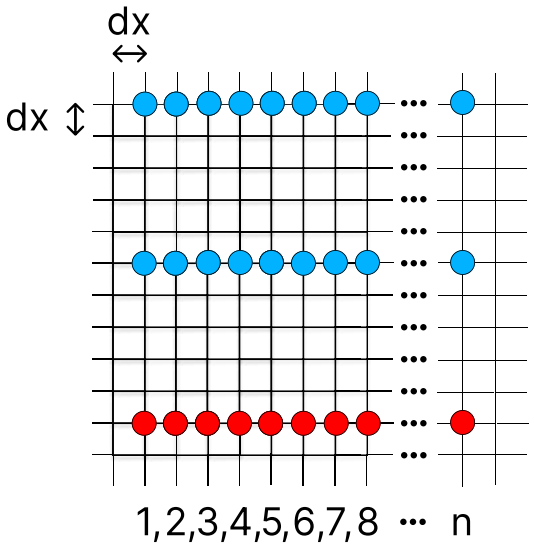

Figure 4.3: Configuration of source nodes (red) and field nodes (blue) used to measure the beam width of the simulated sources.

.

4.2.2.4 Simulation Averaging

Due to interference between scattered wavefronts, different realisations of scatterer positions will result in different backscattered power values. The theoretical BSC as described by equation (4.68) calculates a BSC value dependent on the ensemble properties (the individual scatterer strengths and scatterer number density) but the value is

independent of scatterer configuration. Therefore, to compare our theoretical value to the simulation results, it is necessary to average over statistically independent realisations of random scatterer positions with the same ensemble properties in order reduce the variation due to interference effects. To make statistically independent incoherent scattering models, multiple realisations of the random scatterer model were generated, each time with the scatterer positions selected through use of a random number generator, but the number density kept constant to maintain the ensemble properties. Convergence of the backscattered signal for the models was observed after around 10^3 ensemble realisations, so this value was used as the number of realisations in all cases.

4.2.2.5 Experimental Design: Backscatter Coefficient Estimation as a Function of Number Density of Scatterers

To quantify the accuracy of the tool over a range of BSC values, 4 sets of 10^3 scattering ensembles distinguishable by the number density of scattering bodies present were generated. These ensembles contained the same scattering bodies as described in section 4.2.2.1, hence the number density alteration constitutes a difference in the BSC between the sets of ensembles. The number density values were varied by altering the number of elements within the sample region with an impedance mismatch relative the background medium. The ratio of scattering to non-scattering elements was varied from $1 : 10^{2.5}$ to $1 : 10^4$ in a geometric progression with a multiplicative increment of $10^{0.5}$. For the apertures selected to interrogate these samples, this corresponds to around 13 scatterers per resolution cell in the highest number density case, and 0.4 per resolution cell in the lowest case. These values cover a range selected to include a fully developed speckle case (high number density) down to a condition where there are individually resolvable point scatterers (low number density). To test the accuracy of the approach, the BSC estimates from simulation were compared to the theoretical value as calculated from equation (4.68) and a linear regression was performed on the logarithm of the number density vs. the logarithm of the backscatter coefficient. This

approach was used to account for the effect of an exponentially increasing independent variable and ensure that the regression coefficients were not dictated by the data values corresponding to higher number densities. The regression coefficients were also compared to the theoretical value found from equation (4.68).

4.2.2.6 Experimental Design: Backscatter Coefficient Estimation as a Function of Aperture Width

To quantify the accuracy of the approach for different simulated sources, BSC measurement simulations were performed on the same set of 10^3 ensembles with differing f-numbers. The f-number of the source was altered by changing the aperture width whilst maintaining the same focal depth. The diameter was varied from 2.6cm to 4.0cm in increments of 0.2cm, with a focal depth of 5cm.

4.2.2.7 BSC Estimation

The A-lines formed from backscattered waves from the scattering model were exported to Matlab, where they were time gated to capture waves scattered from locations anterior and posterior to the emit/receive focal depth, with a temporal gate equal in length to the emitted pulse (3-cycles) and centred on the time step corresponding to the time of flight from the focal depth to the centre node of the receive aperture (including the time delay). This gated section was then zero padded for frequency analysis and Fourier transformed. The complex power spectra from the 10^3 independent ensemble positions were then averaged and the absolute value used as the value $S_i(\omega)$ in equation (4.41). The received A-line from the planar reflector was also zero padded and Fourier transformed to give $S_p(\omega)$ in equation (4.41). Using these two values, and the geometric properties of the aperture and gate length, an estimate of the BSC could then be produced, and compared to the theoretical value from equation (4.68), which was calculable using the number density of the scatterers and their individual reflectivity.

4.2.2.8 Quantification of Uncertainty in BSC estimate

To quantify the uncertainty in BSC estimation, an uncertainty value was defined by the standard deviation of the BSC estimates from all ensembles within a test case (be it for a single number density of scattering bodies or for a single aperture size) divided by the square root of the number of ensembles within that case. This metric was selected to scale the standard deviation expected from a set of Rayleigh-like scattering ensembles (which is of the same order as the BSC estimate) by the increased confidence in the mean BSC estimated from a large number of statistically independent ensembles with the same bulk properties.

4.2.2.9 Experimental Design: Envelope Amplitude Statistics

The variation in amplitude envelope of the backscattered signal was also compared to scattering theory to further test whether the model was behaving in a manner commensurate with a tissue like material. Using the A-lines generated from the models described previously, the mean and standard deviation of the amplitude envelope of the backscattered signal from each simulation (each of which corresponds to an independent scatterer position distribution) was computed. The probability distribution function of the collated envelope amplitudes is related to the number density of scatterers relative to the resolution cell size of the imaging device, and for more than 10 scatterers per resolution cell we expect to see a fully developed speckle with a Rayleigh distributed set of amplitude envelope values. In this case, the ratio of the mean and standard deviation of the probability distribution function will equal 1.913 [96][153][154]. Within the field of Rayleigh modelled speckle, this ratio is referred to as the signal to noise ratio (SNR), which should not be confused with the SNR as is commonly considered in pure signal processing discussions. To test whether this behaviour was observed, the SNR of the amplitude envelope was computed for the simulation models detailed in section 4.2.2.6.

4.3 Results

4.3.1 Single Scatterer Models

Figure 4.4 shows the polar scattering amplitude (SA) profiles of the single scattering bodies described in section 4.2.2.1. The relative error of the distributions as compared to the Faran scattering model[91] are shown in table 4.2. The SA and phase errors were defined as the RMS residual between the appropriate quantities for the (analytical) cylindrical model and the FE generated data between the scattering angles $\pi/4 \geq \Upsilon \geq 7\pi/4$. In the case of the SA error, this error was also calculated as a percentage of the mean SA (scaled SA error). The scaled SA error was less than 2.4% for all scatterer models. The phase error was less than 0.08 rad for all the scatterer models. Based on these results, it was determined that the single element square case was the best option to pursue, as this element shape was shown to outperform the triangular approach, and the improvement (of 0.0377%) in the accuracy of the scattering amplitude accuracy with the increased mesh refinement (four element square case) was considered little compensation for the increased simulation run time incurred. The lower accuracy with respect to the phase in the square case relative to the triangular was considered less of a concern than the scattering amplitude, as a sparse ensemble of randomly distributed scatters is expected to randomly alter the phase due to their relative incoherence. This combined with the necessity to average over many random scatterer positions to account for the statistical fluctuation in backscattered power due to interference meant that phase accuracy was of less importance than SA accuracy.

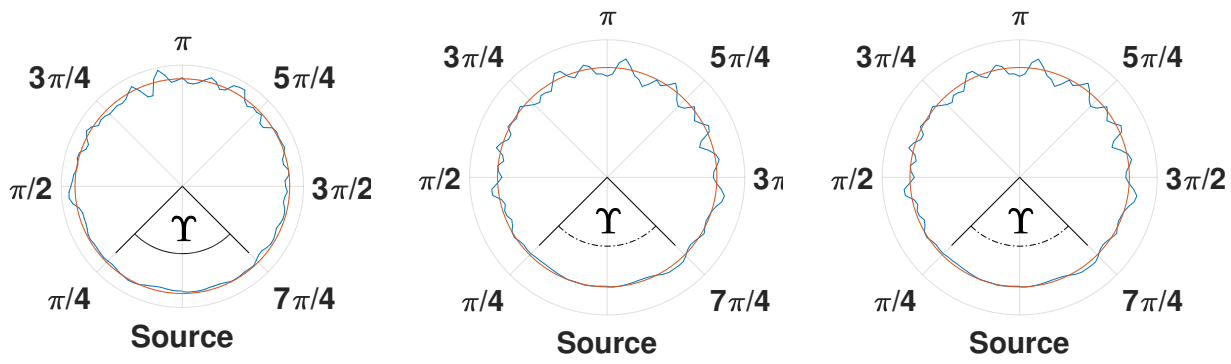

Figure 4.4: Polar scattering amplitude diagrams profiles for the single scatterer models. Pictured are the single element square case (a), the four element square case (b) and the six element triangular case (c). The blue lines are formed of data points with angular position corresponding to the position of nodes within the ring of receivers and radial position equal to the receive scattering amplitude at the centre frequency by nodes at each point on the radius of receivers. The orange line corresponds the theoretical scattering distribution for an infinite cylinder with the same properties and cross-sectional area as the meshed scatterers, immersed in a background medium with the same properties as the non-scattering elements in the FE model, computed for all points on the circle of nodes used in the FE mesh. SA values are presented without normalisation, but the value of the SA has been omitted for visual purposes.

Table 4.2: Error values associated with the single element scattering models. Error refers to the RMS residual between the simulation estimate and theoretical value for the amplitude and phase quantities over the angle subtended by Υ.

Scattering body	SA error (Pa)	scaled SA error (%)	Phase Error (rad)
single element square	4.0635×10^{-8}	1.8159	0.0574
four element square	3.9793×10^{-8}	1.7782	0.0773
six element square	5.2718×10^{-8}	2.3561	0.0245

4.3.2 Beam Width Measurements

The beam width measurements of the simulated sources produced the values in table

Aperture width (cm)	Beam width (mm)
2.6	4.2
2.8	3.9
3.0	3.5
3.2	3.4
3.4	3.2
3.6	3.0
3.8	2.9
4.0	2.7

Table 4.3: Beam width measurements

For the number density values considered with the sources, this produced a number of scatterers per resolution cell

4.3.3 BSC Estimation

Pictured in figures 4.5 and 4.6 are the pressure distributions throughout the FE models for the two simulation types. The source and receive aperture is pictured as a white bar, with the edges of the absorbing regions pictured as red lines. In figure 4.5 we can see the point at which the initial excitation is incident upon the region populated with scatterers from the scattered waves propagating back toward the source. We can also see the initial excitation propagating toward the edges of the model (highlighting the need for absorbing regions on the edge of the model), and some energy content within the absorbing regions. The values within the images have been compressed and allow the viewer to see both the initial excitation as well as the weaker backscattered signal. In figure 4.6 the excitation is propagating toward the top edge of the model, at which point it will be reflected back to the source to provide the correction spectrum. Videos of both the scattering of the field by the random medium and the reflection from the model edge are available in the supplementary content.

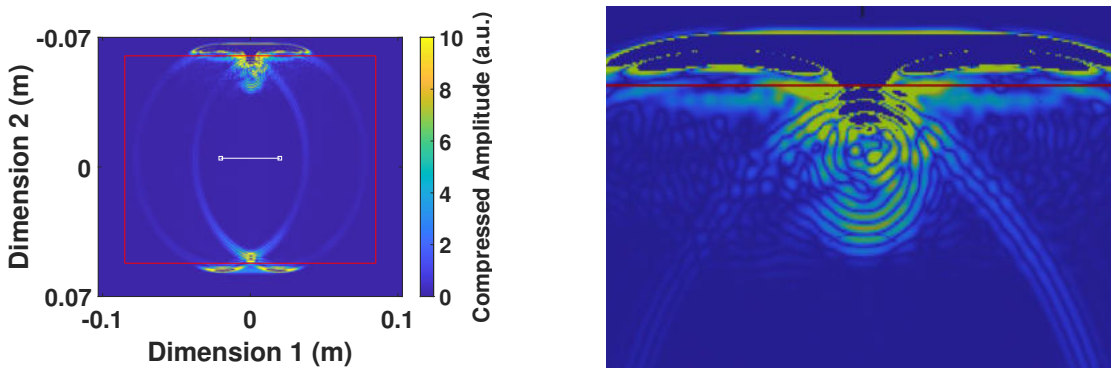

(a) (b)

Figure 4.5: Images of the wave propagation within the incoherent scattering model. Colour values correspond to the unsigned pressure amplitude at a position within the model. To allow visualisation of the incident beam and the (weakly) scattered waves, the pressure values were compressed to allow the visualisation of a greater range of propagating wave amplitude values within the model. Figure 4.5a is a view of the full model. Figure 4.5b is a zoomed in view of the scattered wave propagating away from the scatterers (not pictured).

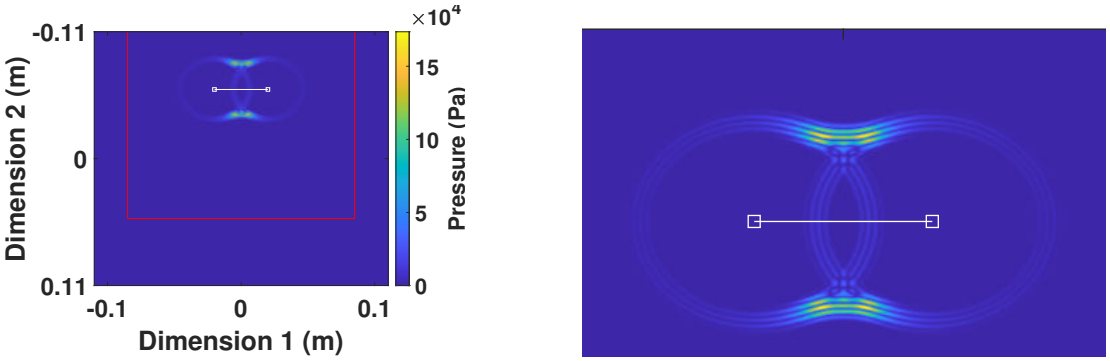

(a) (b)

Figure 4.6: Images of the wave propagation within the line reflector scattering model. As previously, figure 4.6a is a view of the full model. Figure 4.6b is a zoomed in view of the source wave propagating toward the edge of the model mimicking a line reflector.

Figure 4.7 shows the variation of the BSC estimate with number density of scatterers as measured using a 4 cm diameter aperture. The full error bar width is equal to twice the standard error of the mean for all BSC estimates. The results of the linear

regression are detailed in table 4.4.

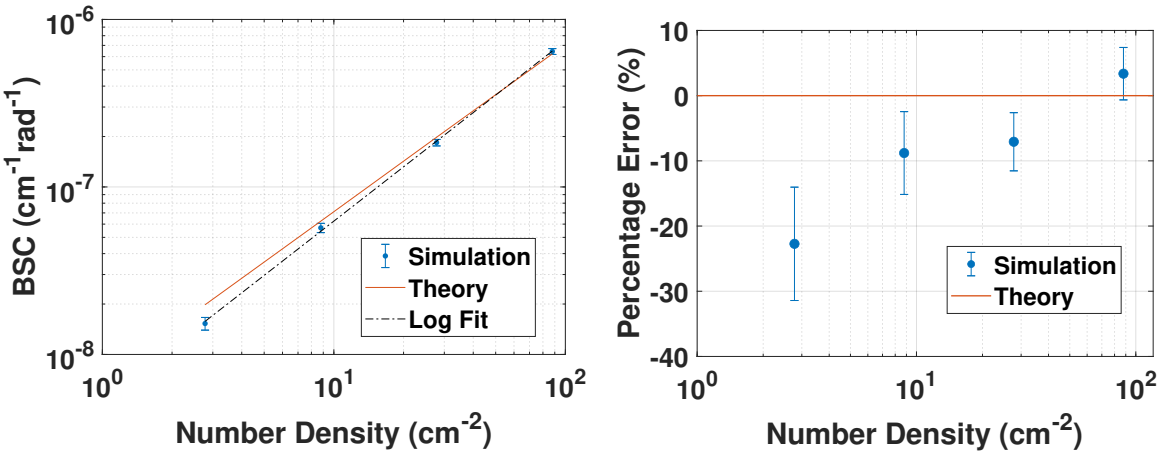

(a) (b)

Figure 4.7: BSC data for a 4 cm aperture. Variation in BSC estimate and theoretical BSC as a function of number density of scattering bodies (4.7a). Percentage error in BSC error relative to theoretical value as a function of number density of scattering bodies (4.7b). Error bars are the standard error on the mean as described in section 4.2.2.8 scaled by theoretical BSC value at each number density value in 4.7b.

Table 4.4: Linear fit parameters for the relationship between the logarithm of the number density and the logarithm of the BSC calculated from theory (Theory) and estimated from FE simulation (Simulation). Included are the 95% confidence intervals for the fit parameters.

Parameter	Theory	Simulation
slope	1	1.076 ± 0.07
intercept	-10.15	-10.28 ± 0.09

The results of the BSC estimation with varying aperture sizes are pictured in figure 4.8.

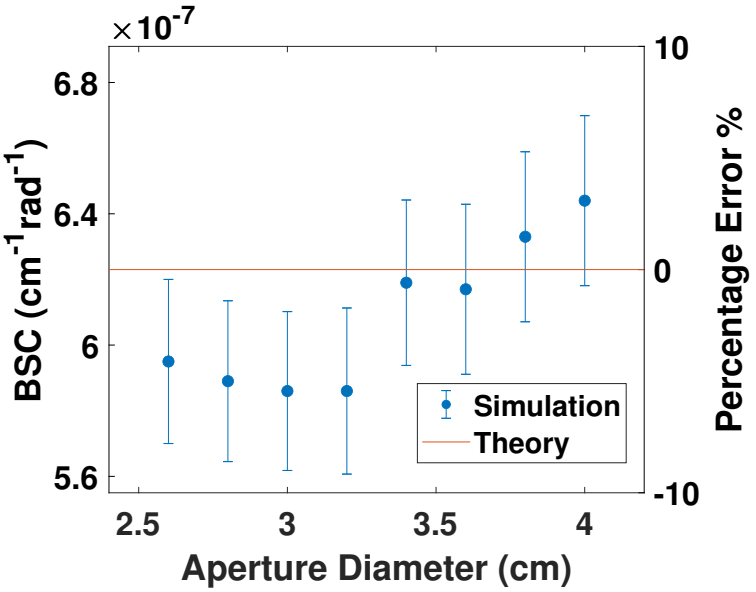

Figure 4.8: BSC estimation values (Simulation) plotted for a range of aperture sizes, with the accompanying theoretical value (Theory) calculate from the ensemble bulk properties. The BSC value is shown on the left y-axis and percentage error (relative to the theoretical value) on the right y-axis.

4.3.4 Envelope Amplitude Statistics

The results of the SNR estimation as a function of aperture size are pictured in figure 4.9.

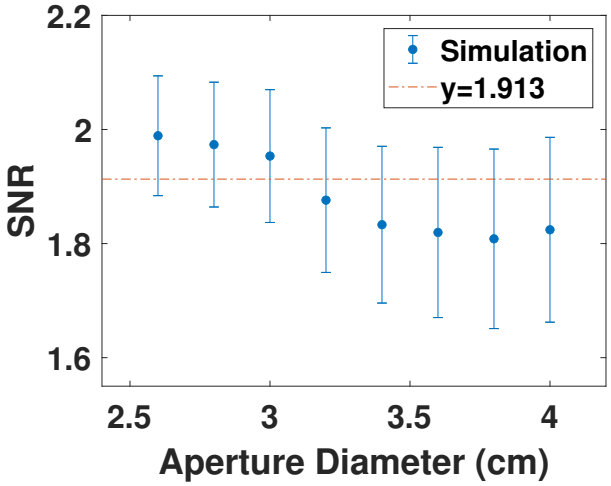

Figure 4.9: Variation in the SNR of the backscattered amplitude envelope evaluated over a set of 10^3 scattering models plotted as a function of varying aperture size. Error bars correspond to the standard deviation of the SNR estimate across all the models. Also plotted is the theoretical signal to noise ratio for a fully developed speckle pattern.

4.4 Discussion

4.4.1 BSC as a function of number density of scatterers

From figure 4.7 we can see that the simulation tool agrees well with the theoretical BSC as defined in equation (4.68). The smallest error was found to be 3.33% for the highest number density case, and the discrepancy was seen to be greater at the lower number density cases, with the lowest number density case having an error of -22.61%. To explain this reduced accuracy at lower number density values, we consider one of the assumptions involved in formulating equation (4.35): that the scatterers are incoherent relative to each other (i.e. not formed in a regular grid or plane(s)). In order to achieve such a condition we require multiple scattered wavefronts from within the scattering area (since a single, sub-wavelength, monopole scatterer will scatter a coherent wavefront at all length scales). With lower number densities this is less the case, the fewer wavefronts will not interfere to the same extent, and the backscattered profile will more closely resemble that which one would achieve with a point scatterer. The measurement of the BSC in these cases will be more sensitive to the scatterer positions within the ROI (since there is less backscattered power, individual scattering events represent a greater percentage of the backscattered energy). For a large number of scatterers, any off axis scattering (for which the receive beamformed receive pressure will be less than that for on-axis scatterers) can constructively or destructively interfere with scatterers on the opposite side of the beam axis depending on relative phase, but the contribution will be less than the on-axis scatterers. When scattering occurs from a sparse numbers of scatterers, there is less likely to be a conjugate wavefront on the opposite side of the beam axis, and hence the received wavefront for a given data point is more likely to be a scattered wave from an individual scatterer. Unless said scatterer is on the beam axis at the focal depth, the scattered wavefront will possess different curvature to the aperture, and therefore will result in a lower measured backscattered power. This could then result in an underestimate of the BSC, biasing the estimates

to be smaller than the theoretical value. The results of the linear regression as shown in table 4.4 show that the tool was able to reproduce the theoretical values with only limited accuracy, with the gradient and y-offset falling outside the 95% confidence interval, due to the underestimate of the BSC at the lower number density cases.

4.4.2 BSC as a function of aperture width

Considering now the aperture size as the independent variable, we can see that the simulations performed with a high degree of accuracy, with all simulated apertures producing results accurate to within 6.35% of the theoretical value. This compares favourably with literature results of other FE BSC simulations who found discrepancies of up to 10% [150] in BSC estimates for grain scattering simulations, and also to tissue mimicking BSC simulations where they observed discrepancies of around 6% [157] in BSC magnitude.

4.4.3 Amplitude Envelope Statistics

From figure 4.9 we can see that for all simulated apertures, the measured amplitude envelope was found to be within one standard deviation away from the theoretical, Rayleigh indicative SNR of 1.913. This is to be expected, as the number of scattering bodies per resolution cell for these simulated cases exceed the condition required (10) for a Rayleigh distributed amplitude envelope[1][96]. A parallel numerical test was run to assess the convergence of the SNR of a set of Rayleigh distributed variables, which exhibited around a 1% error on the SNR value after 10^3 generated values, indicating that the deviation in this data set can not be explained simply by convergence of the average, however the values are still all within a standard deviation of the expected value, indicating relative conformance to the scattering theory. Comparison to results found in literature showed that other simulations of the amplitude envelope [96] did not fully converge onto the theoretical value, with a slight underestimate for the highest number density case, which exceeded the number density condition for fully developed

speckle. This suggests that we cannot expect full convergence of the average onto the theoretical value even for high number densities. No adequate explanation could be found for the apparent systematic variation in the SNR with aperture width. The decrease in width (whilst maintaining a constant focal depth) will naturally increase the beam width at the focus, which should include more scatterers in the resolution cell, but given that our number density value is set to exceed the minimum for fully developed speckle, the reason for the apparent decrease in SNR with increasing aperture width is not understood.

4.4.4 Limitations

Whilst the approach of simulating a BSC measurement in reduced dimensionality has its benefits in reducing the required computational memory and time, it naturally precludes inclusion of the factors associated with the discarded dimension. Whilst it is possible to reformulate 3D scattering behaviour in 2D, we are not able to include certain effects, notably the effect of elevational beam and shape, and out of plane scattering. However, these 2D models do reduce the computational cost and run-time that would be required for an equivalent 3D investigation. For this reason we should view results from 2D simulations as both a groundwork for future investigation in 3D, as well as an opportunity to investigate similar scattering models in 2D without the aforementioned model size issues.

In the use of simulation to date, factors such as regional sound speed or density variation, or frequency dependent attenuation have not been included. Whilst this creates a simulation domain unlikely to be found in a real tissue or phantom, it is worth noting that the inclusion of both these factors are easily applicable within models of this type [116]. The reason for not including such factors in this work was to generate a test cases with known results to prove the utility of the tool.

4.5 Conclusion

This chapter has presented reformulations of BSC equations in reduced dimensionality, which will be of interest to those wishing to also simulate BSC style experiments without the time and computational memory penalties associated with a 3D simulation. Simulations of a plane reflector substitution style experiment are shown to be able to estimate the value of the BSC for digital phantoms using an FE framework in 2D. The results indicate that the tool is capable of simulating the physical scenario to a high degree of accuracy, with discrepancies of $\sim 3\%$ in the best case, and $\sim 24\%$ in the worst case, where the latter can be explained through considering the deviation of the simulated model from the theoretical assumptions used to generate the theoretical BSC. The tool is accurate across a large range of number density values, as indicated in figure 4.7 and to changes in the focusing strength of the simulated aperture, as shown in figure 4.8. In addition, the statistical nature of the backscattered signal was shown to behave in a manner commensurate with theoretical descriptions of ultrasound speckle, with the tool able to reproduce speckle-like statistical distributions that compare favourably with theoretical descriptions. SNR values of $\simeq 1.913$ were found in cases where one expects to observe a Rayleigh-like distribution of scattering amplitudes.

Chapter 5

An investigation into the effect of planar reflector positioning on the accuracy of BSC estimates using unfocused sources

5.1 Introduction

This chapter will make use of the model developed in chapter 4 to investigate the sources of variation in BSC estimates between two different methodologies are used. Unlike chapter 5, these methods will make use of unfocused sources, but the scattering models corresponding to the highest number density case presented in the previous chapter will be reused within this investigation. The factor that is to be investigated within this chapter relates to the quality of the diffraction correction applied during the BSC estimation process, and how this varies depending on the positioning of the reference scatterer. This study will attempt to perform a simulation based comparison between two methodologies for backscatter normalisation and diffraction, to investigate the quality of the BSC estimates they produce. This comparison will be made through construction of FE models, the results of which be analysed using two methodologies, with their accuracy compared to a theoretical description of the scattering as in chapter 4. The two methodologies, first adopted by Sigeleman and Reid [26] and Chen et al. [79] respectively, use a planar reflector to characterise the diffraction field of an ultrasound device in order to compute diffraction free estimates of the BSC for a sample of tissue. These methodologies differ in their positioning of the planar reflector, with Sigelman and Reid opting to place the planar reflector at the same depth as the tissue sample, whilst Chen et al. propose a new formulation whereby the planar reflector and sample do not *necessarily* need to be placed at the same depth. This approach has since been used by other authors [158][159], who placed the planar reflector at half the depth of the sample to perform their corrections. This leads to an ongoing uncertainty as to the ideal configuration of planar reflector position and sample relative to an unfocused source. The accuracies of these two diffraction correction approaches will be compared through a simulation approach to determine which provides the most accurate estimate of the BSC. The placement of the planar reflector at the same depth as the sample will be referred to as method 1, and the placement of the planar reflector at half this distance will be referred to as method 2. The use of a simulation based approach allows

a high degree of control over experimental conditions, making it a powerful tool for investigating the nature of diffraction, and its effect on the quality of BSC estimates.

The diffraction field of the source of ultrasonic waves contributes substantially to the distribution of wave energy in the emitted field for a given transmit frequency and position in the acoustic field, and hence can have a great impact on material property estimates generated using ultrasound (for example sound speed, attenuation or backscatter coefficient) [60]. Therefore, to generate material property estimates that are measurement system independent, one must correct the collected data as a function of spatial position and frequency [1]. The diffraction field of a source is a consequence of the finite source of the ultrasound device in use, and results in a spatio-spectral variation in the field emitted (and by reciprocity), the detection of scattered wave energy from a point in the field of view of the same device operating in receive mode.

This chapter will explore the particular case of the diffraction correction within a planar reflector substitution method experiment through which the sources of variability that can occur in BSC estimation methodologies will be investigated.

To explore the concept of diffraction we first consider the theoretical case of an infinite plane source and (identical) receiver of ultrasound waves with a time, frequency and amplitude independent linear acousto-mechanical transfer characteristic in both emit and receive modes. Plainly, we consider a device whereby case where the relationship between an excitation signal and the emitted pressure amplitude and the relationship between a received pressure amplitude and recorded signal is linear, and time, amplitude and frequency independent. For this theoretical, infinite device, the diffraction correction would be unity for all frequencies and positions in the field of view, since there is no bias in the emission or reception of wave energy based on spatial position or frequency characteristics: the field is diffraction free. At the other extreme, for an infinitesimal point source with the same emit and receive characteristics, the diffraction correction will now be a function of the radial distance in transmit and receive propagation directions between the position of interest and point source/receiver to account for

geometrical spreading of the wavefronts emitted from a given position. A finite sized unfocused source possesses a more complex diffraction field, as we now must consider the relationship between the wavelength of interest, the source size, and the point in the field of view. This interaction between length scales will manifest itself in the form of near and far field effects, with the diffraction field of the source being a function of both transmit frequency and position of interest. The introduction of focusing of the source/receiver results in further changes, introducing an increase in both the incident intensity and the receive sensitivity at the focal point of the source/receiver, and a reduction in both incident intensity and receive sensitivity for other points in the field. Finally, when we consider the presence of array systems, with electronic focusing, transmit and receive aperture apodisation and variable focal length, all of which will alter the diffraction field further, we begin to see the large number of variables one needs to consider when assessing the backscattered wave energy from an unknown sample due to both the incident intensity at a point in the sample, and the receiver sensitivity to a source at this point. The quality of the correction of these (frequency dependent) effects directly impacts the quality of the final BSC estimate, and has been cited as a large source of variability between measurements [2].

To compute the diffraction field for a given source and obtain measurement system independent estimates of the BSC, we can simultaneously correct for the source directivity pattern and the electromechanical characteristics of the device in emit and receive mode by placing a reference scatterer at a given position in the field of view of the source and spectrally quantifying the received echo for a given excitation. This will provide a normalisation spectrum that can be used to correct the backscattered spectrum from the sample under interrogation for device and diffraction based effects. The backscattered spectrum acquired from the reference scatterer will be a frequency dependent description of the diffraction field for that particular position and scatterer. This spectrum constitutes a quantification of the diffraction field specifically for the scatterer geometry used for the reference, since it is a manifestation of the relative ge-

ometries of the beam and the scatterer at the sampled frequencies. To universalise this to other scatterer geometries, such as the scatterers present in a section of tissue, the relative properties of the beam directivity and the scattering geometry are then required to compute a diffraction free estimate of the backscattering properties. If an identical device, with identical device settings are used for both the insonification of the unknown sample and the reference scatterer, the division of the backscattered spectrum received from the sample by the backscattered spectrum received from the reference scatterer (whilst mathematically accounting for the diffraction effects of the relative scatterer geometries) will result in the calculation of a normalised spectrum that will be more system independent than the backscattered spectrum from the sample. Whether the measurement will be entirely system independent is a point of contention, as the accuracy of the theoretical description of the beam directivity and source geometry (the diffraction term of a BSC equation such as equation (5.9) or equation (4.40)) will eventually be a factor in the accuracy of the BSC estimation. This has been shown to be a source of inconsistency in a number of inter-method and inter-device comparisons of BSC estimation variability [2][88][144][88][90]. This chapter will use FE simulation methods to explore how the description and experimental categorisation of a planar reflector impacts the quality of BSC estimates using a similar methodology as was presented in chapter 4, but using unfocused sources.

The planar reflector was the first reference scatterer used for the purpose of backscattered spectrum normalisation, by Sigelman and Reid [26], and was later used by many other authors to generate their own methods for BSC estimation [28][79][76][27][49][56]. The advantage of the planar reflector is its simple geometry. Provided its lateral extent is much greater than the beam width, we may approximate it as an infinite plane of uniform reflection coefficient at an angle normal to the beam axis. This produces a theoretical description of its scattering behaviour (as described in chapter 4) that is an integration of the source velocity potential over the full lateral dimension. This completeness of the mathematical formulation justifies the description of the reflector

as being "well categorised". This simplicity would be lost if there were spatial variation in either the geometry or the acoustic properties of the reference scatterer. To perform a planar reflector substitution normalisation experimentally, the echo power spectrum from the planar reflector is computed for use a normalisation. An illustration of the method is pictured in figure 5.1

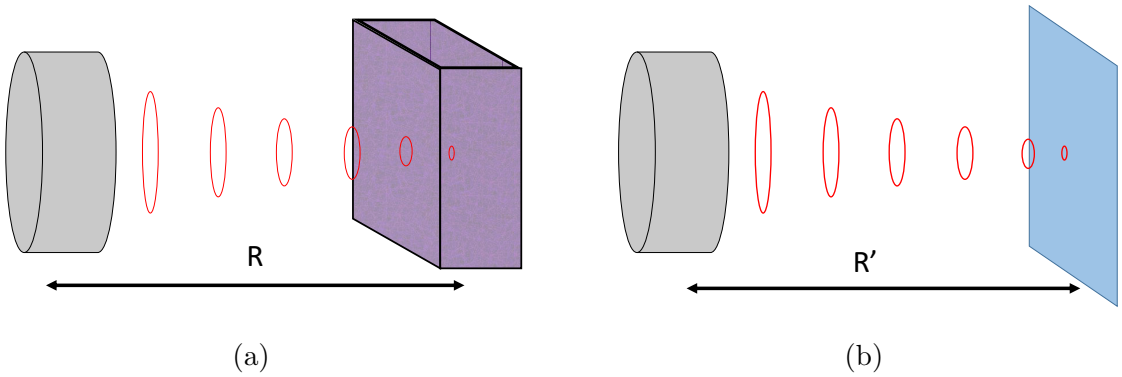

Figure 5.1: Illustration of the planar reflector reflector substitution method. The source (pictured in grey), insonifies (red) the sample (purple) and computes the backscattered spectrum. The sample is then substituted for the planar reflector (blue), and the same excitation is applied to the source, with the backscattered echoes analysed to calculate the normalisation spectrum. In the Sigelman and Reid method, the same distance is maintained for the distance between the sample ROI and planar reflector (i.e. $R = R'$). In the Chen method, the planar reflector is placed at half the distance to the sample ($R' = R/2$).

This will be specific to the device (and the associated settings) used and the depth of the planar reflector and will be used to normalise the backscattered spectrum from the sample under investigation for the depth and frequency dependent effects. The spectrum encodes information about the emit and receive characteristics of the device at the point of reception and the emit-receive characteristics of the source for a given position within the field of view. Both effects are frequency dependent. The use of a well characterised reference scatterer (as opposed one with high complexity, in terms of both the geometry and spatial variation in acoustic properties) permits formulation of expressions to describe its behaviour, and ultimately allows comparisons to be drawn

between the backscattered power from the sample and the reference reflector that are independent of the device. This normalisation hence makes the measurement more objective.

Whilst the use of the planar reflector is common for substitution experiments using single element sources, there is an unresolved question into the most ideal positioning of the reflector when imaging a diffuse, incoherent scattering medium to determine the BSC. The initial formulations placed both the incoherent scattering medium and the reference reflector at the focal plane of a focused source or in the far field of an unfocused source [56][27][28][76][27][49], but the formulation used by Chen et al. [79] generalised this, permitted placing the planar reflector at a different depth to that of the sample through use of a mirror argument. No universally agreed upon advice is found for the most accurate place for the position of the planar reflector (beyond simply 'in the far field' in the case of the former method), and hence there is an unanswered question within the literature comparing the relative merits of the two approaches, and the position of the sample in the field of the unfocused source. The expressions derived by Ozawa et al. [27] are appropriate only for expressions where the planar reflector and the region of interest within the sample are at the same depth, whereas Chen et al. [79] propose that the near field is the most convenient position. From this point onward, the method placing the planar reflector and the sample at the same depth will be referred to as method 1, and a secondary method, whereby a mirror argument is applied to allow the placement of the planar reflector at half the distance to the sample will be referred to as method 2.

This chapter will investigate the use of the planar reflector, and how its positioning within the diffraction field of the source affects BSC estimation accuracy. To do so, the relative accuracies of methods 1 and 2 will be compared in estimating the BSC from a diffuse scattering medium. This will be conducted as in chapter 4 through simulation using similar methods and mathematical descriptions of the system with comparison to the previously derived theoretical value for the BSC based on discrete

scatterer properties and their number density. These simulations will be used to assess the relative accuracy of each method, to determine the more accurate in determining the BSC for a simulated diffuse scattering medium populated by sub-wavelength scatterers.

5.2 Methods

This section will describe the testing strategy by which method 1 and method 2 for assessing the BSC are compared. To do so, two aperture widths will be considered, which for each, the sample will be positioned at three different points within the field. These simulations will represent the placement of the sample for which we want to compute the BSC at three different points within the diffraction field of the simulated source. For each of these six cases, two accompanying planar reflector spectra will be computed through simulation, one at the same depth as the sample for analysis by method 1, and one at half this distance for analysis by method 2. The estimated BSC for all 12 cases (2 apertures, 3 depths and 2 methods) can then be compared to the theoretical value for the simulated scattering medium to assess which method, aperture and position combination generates the most accurate estimate of the BSC.

5.2.1 FE Methodology

To test the relative accuracy of methods 1 and 2, simulation models were constructed of two types. The first simulates the scattering of ultrasonic waves by a random scattering medium and the second simulates the scattering by a planar reflector. The construction of each have been described in chapter 4. The focus of this chapter is on the relationship between the position of the planar reflector and the corresponding accuracy of the BSC estimates produced for different depths of sample. Within this work, we consider only a single number density case (as opposed to the multiple number density cases considered previously). The number density was selected to give a ratio of $1 : 10^{2.5}$. This value was selected as it produced the most accurate BSC estimates in chapter 4, so it was assumed that this scatterer number density produced scattering behaviour that was most similar to the derived theoretical model, and therefore provided the most ideal case in which to investigate the effect of the source on the quality of the BSC estimate. As in chapter 4, single element square scattering bodies were used, as they provided the best tradeoff between backscattering amplitude accuracy and simulation runtime. In

this chapter, two reference spectra calculations were made for each simulated aperture for each sample depth: one with the planar reflector placed at the same depth as the sample, and another with the planar reflector placed at half this distance (pictured in figure 5.2). As in chapter 4, the planar reflector is simulated by the edge of the model, which reflects all the incident wave energy back to the source. These two simulation cases were constructed by moving the source relative to the model edge. To compute a BSC estimate with the planar reflector not at the same depth as the sample, additional mathematical descriptions were developed. The simulation parameters are outlined in table 5.1.

Table 5.1: Properties for the simulations described.

Property	Value
Background medium sound speed (c_0)	$1500\,ms^{-1}$
Scattering body sound speed (c_S)	$1497\,ms^{-1}$
Background medium density (ρ_0)	$1000\,kgm^{-3}$
Scattering body density (ρ_S)	$1000\,kgm^{-3}$
Courant value	0.1
Centre frequency of excitation (f_0)	$0.5\,MHz$
Pulse length	$3/f_0 = 6 \times 10^{-6}\,s$
Centre Wavelength (λ_0)	$3\,mm$
Mesh refinement (dx)	$dx = \lambda_0/50 = 60\mu m$

For this investigation, unfocused sources were considered. Two aperture sizes were used, of widths 2.4 cm and 2.0 cm respectively. These aperture sizes were selected because – for the centre wavelength used for these simulations – their last axial maxima are in the vicinity of 5 cm, the focal depth of the simulated sources previously discussed. An advantage of this similarity is convenience: that it maintains a similar depth of interest in the focused and unfocused cases permitting a greater similarity in the models. If we were to generate apertures of the same size as the focused cases previously discussed (but without focusing) we would require both the construction of much larger models to accommodate the fact that the last axial maxima would be greatly in excess of 5 cm. This would produce simulations more expensive in time and memory and also result in the comparison between apertures with more notably different beam profiles (in terms

of the characteristic length scales). In addition, such apertures would have much larger beamwidths than the focused cases we have already considered, which would increase the number of scatterers contained within the beamwidth, and potentially take us away from the incoherent scattering cases we have been considering thus far.

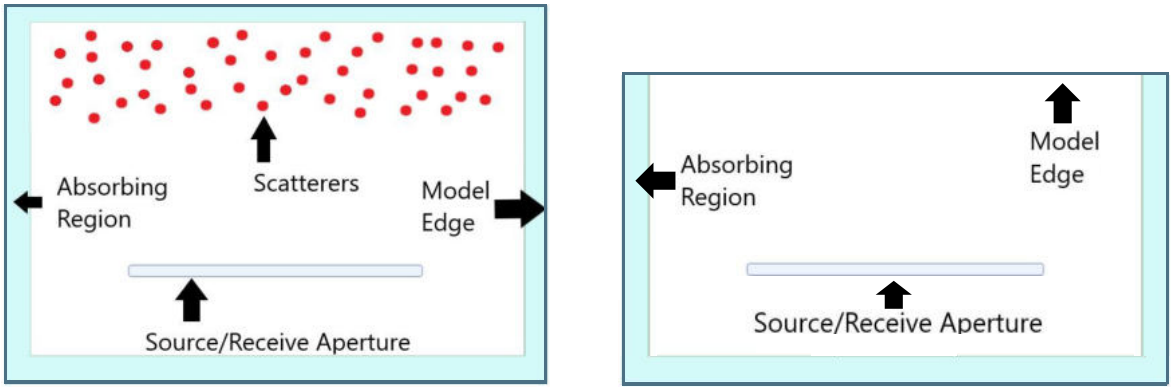

(a) (b)

Figure 5.2: Examples of the random scatterer (5.2a) and planar reflector (5.2b) simulation models. In 5.2a. The random scattering simulations were constructed as described in chapter 2 and in chapter 4, with the element positions randomised for each simulation to generate an incoherent scattering medium. Absorbing regions were used to prevent unwanted reflections from model edges. In this chapter, the source was moved relative to the region populated by scatterers to investigate the effect of this distance on the accuracy of the BSC estimate that was produced.

5.2.2 Beam measurement methods and planar reflector signal calculations

For these unfocused sources, the beam feature of interest is the last axial maximum (LAM). To determine the position of this, field plots were constructed using the same methodology as described in section 4.2.2.3. This methodology was used to both to find the position of the LAM and to assess the beam widths of the field at different depths. To construct these plots for the apertures, models were developed with 'field' nodes placed in the model at regular intervals to compute the incident intensity at

the centre frequency for different points in the field of view of the source. The grid of field nodes was designed with the same lateral spacing as the nodes that make up the source/receiver ($dx = \lambda_0/50$) and an axial spacing of $\lambda_0/10$. This is visualised in figure 5.3.

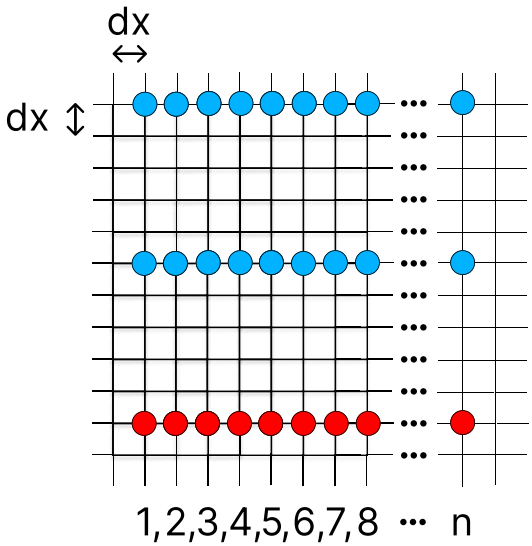

Figure 5.3: Configuration of source nodes (red) and field nodes (blue) used to measure the behaviour of the simulated apertures.

To compute the LAM for the sources, an axial beam profile was generated. This is comprised of the receive data from the previously described model using the field nodes that form a line emanating at a perpendicular angle from the centre of the aperture. The maximum of the axial beam plot was then used to find the depth of the LAM. To assess the beam width, the data collected at nodes displaced laterally from the beam axis was analysed and compared to the theoretically assumed Gaussian beam profile. In addition, the coherence of the backscattered signals corresponding to the 6 planar reflector positions were also calculated to investigate potential phase cancellation at the aperture. To do so, the coherence function of the signals at nodes separated by a wavelength (the centre wavelength of the simulation) was calculated using the normalised correlation formula:

$$R(m) = \frac{1}{N-m} \sum_{i=1}^{N-m} \frac{\sum_{n=n_1}^{n_2} s_i(n) s_{i+m}(n)}{\sqrt{\sum_{n=n_1}^{n_2} s_i^2(n) \sum_{n=n_1}^{n_2} s_{i+m}^2(n)}}. \tag{5.1}$$

This expression is used to calculate the spatial coherence of echoes [101][160] as a function of the spatial lag (m) between pressure waves (s_i) recorded by a receiver (i) for samples (n) within the analysis kernel defined from sample n_1 to n_2. This expression is typically used for array systems, where S_i represents the receive data at a transducer element. Here, we will treat nodes separated by a wavelength (laterally) across the aperture as elements, the signals received at which will be used to calculate the coherence. The sample kernel (n_1 to n_2) used in this calculation for the planar reflector echoes was positioned with its centre at the centre of the receive pulse, with a length of twice the emitted pulse. This mode and method of analysis is covered more extensively in chapter 6.

5.2.3 Mathematical Methods

To compute the BSC under the condition that the planar reflector is not at the same depth as the sample, we need to re-derive the previously derived measurement equation. The case under consideration is that for which the sample is in the far field of an unfocused source, and the planar reflector is at half this distance. Presuming that this places the planar reflector in the near field, we must now reconsider the assertion that the velocity potential at this depth can be expressed as

$$\hat{\Phi}(\omega, \bar{r}) = A_\Phi(y_0) e^{-ik(y + \frac{x^2}{2y_0})} e^{-(x/\sigma_B(y_0))^2}. \tag{5.2}$$

This hypothesis is predicated on assuming that the emitted beam possesses a Gaussian directivity function at the position of the planar reflector, the distance to the planar reflector is greater than the width of the source and that the derivative of the time independent pressure field with respect to the axial dimension is dominated by the phase change. Within the near field, these assumptions do not hold true (the most

notable being that the beam shape is not Gaussian) hence the use of this definition by Ueda and Ozawa for a focused transducer at the focal plane or an unfocused source in the far field. To maintain the use of this beam description, we must therefore reconsider our derivation of the backscattered power from the planar reflector. Using a mirror argument (as per Chen et al. [79]), we may state that the receive echo from a perfect planar reflector at a depth $y = y'$ will be equivalent to that received by an identical receiver at a depth $y = 2y'$. Using this argument we may rephrase the description of the beam at the planar reflector and instead use the description at twice the distance, avoiding the need to describe the beam in the near field and the associated mathematical difficulties. To derive the equation for the signal received at a generic distance $2y'$, we begin with the definition of the emitted pressure (P) as described as a function of local mass density (ρ_0) and velocity potential (Φ):

$$P(\bar{r}, t_0) = -\rho_0 \partial_t \Phi(\omega, t, \bar{r}), \tag{5.3}$$

Defining the velocity profile ($U(\omega)$), velocity potential field pattern ($\hat{\Phi}(\omega, \bar{r})$) and time dependencies ($\tau(t)$) as separate variables, we can express the simulated aperture's velocity potential as

$$\Phi(\omega, t, \bar{r}) = U(\omega)\hat{\Phi}(\omega, \bar{r})\tau(t), \tag{5.4}$$

where the expression $\hat{\Phi}(\omega, \bar{r})$ is a function of the position and wavenumber characteristics of the space (and not the emit receive characteristics of the source). Given that we assume the distance y_0 places us in the far field of our source, we may now use the Gaussian directivity assumption and can express $\hat{\Phi}(\omega, \bar{r})$ as per equation (5.2). We additionally assume that the time dependency of the Φ is harmonic ($\tau(t) = e^{i\omega t}$), giving a resultant pressure distribution of

$$P(x, y, y_0, t) = -i\omega\rho_0 U(\omega) A_\phi(y_0) e^{-ik(y + x^2/2y_0)} e^{-(x/\sigma_B(y_0))^2} e^{i\omega t}. \tag{5.5}$$

The mirror argument is predicated on the concept that the received echo is an image of that which would occur on the opposite axial side of the planar reflector, hence we theoretically consider that an identical receive aperture is placed at the depth y_0, with no intervening reflector. The receive echo at the single element plane receiver placed at a depth y_0 from the described source will be given by the integral of the pressure distribution in equation (5.5) over the surface of the receiver, scaled by the frequency response characteristics of the receive aperture $G(\omega)$:

$$e(\omega) = G(\omega)U(\omega)\int_{-a}^{a} dx\,(P(\bar{r},t)) = \frac{-i\omega\rho_0 A_\Phi(y_0)G(\omega)U(\omega)\sqrt{\pi}}{\sqrt{\frac{ik}{2y_0}+\frac{1}{\sigma_B(y_0)^2}}}. \tag{5.6}$$

Combining the real aperture's emit characteristics and the 'image' receiver's receive characteristics into a single variable ($T(\omega) = U(\omega)G(\omega)$) and squaring receive echo produces the receive spectrum:

$$Q(\omega,y_0) = |e(\omega)|^2 = \frac{\omega^2\rho_0^2|T(\omega)A_\Phi(y_0)|^2\pi}{\sqrt{1+\left(\frac{2y_0}{k\sigma_B(y_0)^2}\right)^2}}\left(\frac{2y_0}{k}\right). \tag{5.7}$$

Comparing this to the equation describing the backscattered power spectrum from an ensemble of discrete, sub-wavelength scatterers, imaged using a gate centred at a depth (y_0):

$$S_i(\omega) = 2\pi^2\omega^2\rho_0^2\mu_{BS}|T(\omega)A_\Phi(y_0)^2|^2 kd\sigma_B(y_0)\sqrt{\pi}, \tag{5.8}$$

we may derive a measurement equation for the BSC based on our simulated planar reflector reference ($Q(\omega,y_0)$) power spectrum and backscattered sample ($S_i(\omega,y_0)$) power spectrum:

$$\mu_{BS}(\omega) = \frac{S_i(\omega,y_0)}{Q_p(\omega,y_0)}\frac{y_0}{\pi\sqrt{\pi}|A_\Phi(y_0)|^2 dk^2\sigma_B(y_0)}\frac{1}{\sqrt{1+\left(\frac{2y_0}{k\sigma_B(y_0)^2}\right)^2}}. \tag{5.9}$$

A_Φ can be computed numerically by computing the velocity potential for the on-axis

point of the field at y_0, and this equation will give us a BSC estimate for method 2. As for method 1, we will continue to use measurement equation (4.40) as derived in chapter 4 for use in the case where the planar reflector depth is equal to the depth of the ROI:

$$\mu_{BS}(\omega) = \frac{S_i(\omega)}{S_p(\omega)} \frac{1}{2\pi\sqrt{\pi}} \frac{y_0 R_p/(d\sigma_B)}{\sqrt{(1+(\frac{2y_0}{k\sigma_B^2})^2)}}. \tag{5.10}$$

The BSC estimation produced by these equations can be compared to the previously described value as computed from the theoretical BSC equation ((4.68) derived in chapter 4:

$$\mu_{BS}(\omega) = \frac{16k^3 R_s^2 \sigma^2}{\pi} \int_0^2 d\gamma\gamma J_0(2k\gamma\sigma) \left(2cos^{-1}\left(\frac{\gamma}{2}\right) - \frac{\gamma}{2}\sqrt{4-\gamma^2}\right). \tag{5.11}$$

5.2.4 Computing A_Φ

To compute A_Φ, we consider the definition of the velocity potential field pattern (as in equation (5.4)) for a point in the far field of the source:

$$\hat{\Phi}(\omega, \bar{r}) = \frac{-i}{4}\sqrt{\frac{2}{\pi}} \int_{l'} dl' \frac{e^{i(k|\bar{r}-\bar{r}'|-\pi/4)}}{\sqrt{k|\bar{r}-\bar{r}'|}}. \tag{5.12}$$

This constitutes the integration of the wavefronts received from the set of identical, point, cylindrical sources placed on the line l' that defines the emit aperture. To compute A_ϕ, we need only consider the on-axis point at the depth of interest relative to the aperture ($\bar{r} = (0, y_0)$), and hence the integral can be expressed as:

$$\hat{\Phi}(\omega, \bar{r}) = \frac{-i}{4}\sqrt{\frac{2}{\pi}} \int_{-a}^{a} dx' \frac{e^{i(k|\sqrt{y_0^2+x'^2}|-\pi/4)}}{\sqrt{k\sqrt{y_0^2+x'^2}}}, \tag{5.13}$$

where x' represents the lateral position of a point source located on the line of the aperture. This expression can be evaluated through numerical integration.

5.2.5 Testing Strategy

To investigate the relative merits of the two approaches, simulations were performed to mimic the acquisition of a backscatter measurement from a set of 1000 scatterer distributions. Each scatterer distribution simulation took 152 s to complete, requiring 2.32 GB of memory on a GeForce GTX 1080 Ti graphics card. These scatterer distributions were the same for both aperture widths, and also the same as the highest number density case simulated in the results of chapter 4. Three relative axial positions of scattering region and source were considered, to assess how this distance affected BSC estimation accuracy. The depths were selected by analysis of the field plots generated using the model described in figure 5.3. The three depths were as follows: the last axial maximum (Y_{LAM}) of the simulated source, a distance in the far field of the source (Y_∞) and an arbitrary point between Y_{LAM} and Y_∞, which will be labelled Y_A.

The distance values selected for these three positions for each aperture were selected in an attempt to locate regions of the evolving field that were comparable between the two apertures. The LAM of each aperture was calculated from the beam profile, and the other two values were selected arbitrarily for both apertures, with the aim of capturing the source behaviour posterior to the LAM (Y_A) and deeper into the far field (Y_∞). The values of Y_A and Y_∞ were different for the two apertures simulated to reflect that the beam width and wave coherence varies at different distances depending on the size of the aperture.

Simulations with the random scattering media present were performed with the source at a distance (Y_{LAM}, Y_A or Y_∞) from a depth within the region populated by scatterers. The depth within this region was selected such that a sample gate of equal temporal length to the initial excitation could generate an ROI fully contained within the portion of the model populated by scattering bodies.

5.3 Results

5.3.1 Beam Plotting

To illustrate the shape of the emitted fields from the two simulated apertures, the model described by figure 5.3 was used to construct field plots, shown in figure 5.4 using the properties listed in table 5.2.

Table 5.2: Simulation properties for the FE model used to measure the beam properties.

Property	Value
Background medium sound speed (c_0)	$1500\,ms^{-1}$
Background medium density (ρ_0)	$1000\,kgm^{-3}$
Courant value	0.1
Centre frequency of excitation (f_0)	$0.5\,MHz$
Pulse length	$3/f_0 = 6 \times 10^{-6}\,s$
Centre Wavelength (λ_0)	$3\,mm$
Mesh refinement (dx)	$dx = \lambda_0/50 = 60\mu m$

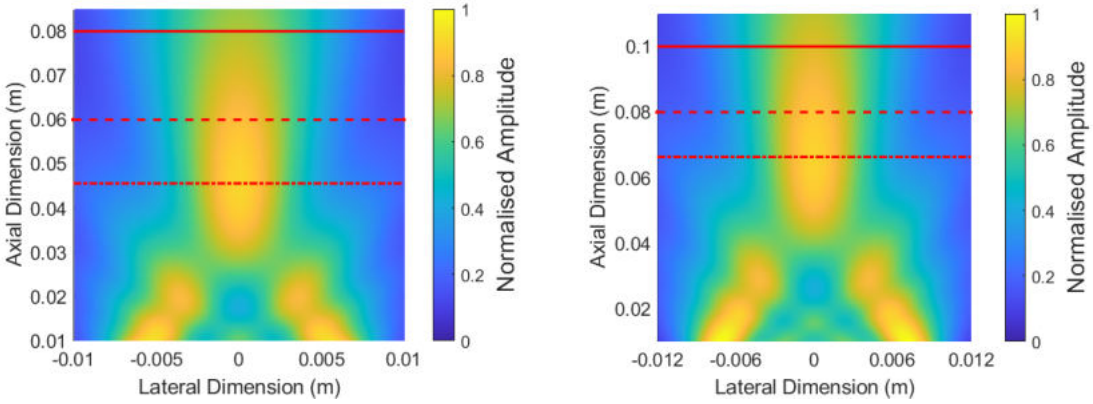

(a) (b)

Figure 5.4: Example field plots from the 2cm (5.4a) and 2.4cm 5.4b) unfocused apertures constructed using the node configuration depicted in figure 5.3. Amplitude values (at the centre frequency of the simulation) are normalised by the global maximum. Red horizontal lines correspond to the axial positions of Y_{LAM} (dot-dash), Y_A (dash) and Y_∞ (solid).

From these results, the distances from the sources to Y_{LAM} was determined, and the values of Y_A and Y_∞ were selected. These are indicated on the figure and in table

5.3. For comparison, the equivalent LAM for a circular aperture of diameter equal to the width of the simulated sources at the same frequency would be 3.3 cm and 4.8 cm respectively.

Table 5.3: Distances of interest for the simulated apertures

	Distance (m)		
Aperture Width (m)	Y_{LAM}	Y_A	Y_∞
0.020	4.56×10^{-2}	6.0×10^{-2}	8.00×10^{-2}
0.024	6.63×10^{-2}	8.00×10^{-2}	1.00×10^{-1}

5.3.2 Beam Width measurements

From the results highlighted in figure 5.4, beam width measurements were performed for both aperture widths at the three depths of interest. This was done by squaring the recorded amplitude field and fitting the lateral intensity distribution to a Gaussian function and computing the Gaussian RMS width (σ_B in equation (5.5)). The results of this investigation are shown in table 5.4. The corresponding number of scattering elements contained per resolution cell (SpRC) is included in table 5.5.

Table 5.4: Results of beam width fitting for both aperture widths at the depths of interest.

	Beam width (m)		
Aperture Width (m)	Y_{LAM}	Y_A	Y_∞
2.0×10^{-2}	5.37×10^{-3}	6.92×10^{-3}	9.48×10^{-3}
2.4×10^{-2}	6.43×10^{-3}	7.58×10^{-3}	9.74×10^{-3}

Table 5.5: Calculation of number of scatterers per resolution cell based on the beamwidth (table 5.4) and pulse properties (table 5.1)

	SpRC		
Aperture Width (m)	Y_{LAM}	Y_A	Y_∞
2.0×10^{-2}	21.2	27.4	37.5
2.4×10^{-2}	25.4	30.0	38.5

5.3.3 Planar Reflector Receive Signals

Figure 5.5 contains time trace plots of the normalised (to the maximum absolute amplitude) receive pressure signals for the 2.0 cm aperture for the 6 different planar reflector positions. Two features are of particular interest within these figures: the coherence of the wave and the lateral spread of beam energy. The former will dictate the phase cancellation losses at the planar receiver, and the latter will dictate the beam divergence. Phase cancellation losses and beam divergence losses are not computed for within the derivations of the BSC as presented, and hence, if they are present, they would constitute an unaccounted for reduction in the measured reference power spectrum from

the planar reflector. This constitutes the reference power spectrum underestimating of the value as described by the derived coupling equations between the source and planar reflector (equations (4.39) and (5.7)), which could then result in overestimates of the BSC. Indications of potential phase cancellation within the time traces would be wavefront curvature, indications of beam divergence would be a lack of lateral containment of the beam energy. We would anticipate that beam divergence would constitute a greater underestimation of the reference power spectrum since all divergence beyond the lateral width of the receiver would constitute entirely 'lost' energy, whereas phase cancellation effects would only result in a partial loss of receive energy, particularly given that the coupling of an unfocused source with a planar reflector should behave in a highly planar (and therefore coherent) manner.

From figs. 5.5a to 5.5f we can see the development of the receive wavefront as the distance between the source and the planar reflector is changed. With the planar reflector at half the distance to the last axial maximum (figure 5.5b) we observe potential for phase cancellation due to edge effects (seen posterior to the main arriving wave close to the lateral extrema of the aperture) owing to the fact the image of the receiver is on the edge of the near field of the source. However, the phase appears to be highly uniform within the main pulse , so we anticipate that the coherence of this wave would be close to unity across all lags.

As the distance increases (going from figure 5.5b to 5.5d), the potential for edge effects reduces, the wavefront curvature increases (which will result in greater phase cancellation, and an underestimation in the acoustic power) and the beam energy appears to be more laterally confined within the pulse. As we move the planar reflector from $Y_A/2$ to $Y_\infty/2$ (going from figure 5.5d to 5.5f), the beam width increases, and the beam energy becomes more diffusely spread across the aperture (which will result in a reduced value in receive power due to beam divergence). The level of wavefront curvature visually appears to remain constant between figures 5.5d and 5.5f.

As the planar reflector is moved to the LAM (figure 5.5a), the wavefront becomes

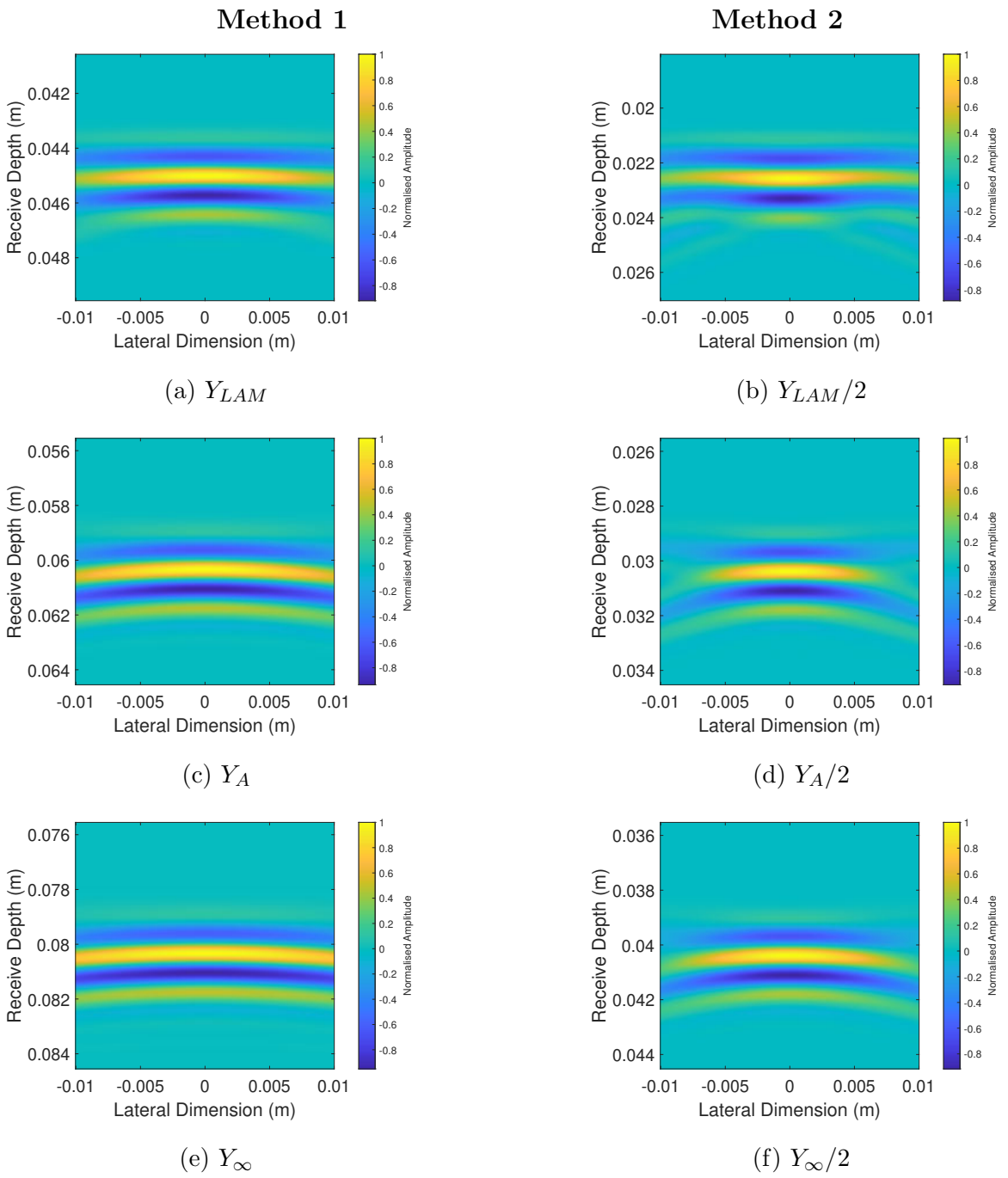

(a) Y_{LAM}

(b) $Y_{LAM}/2$

(c) Y_A

(d) $Y_A/2$

(e) Y_∞

(f) $Y_\infty/2$

Figure 5.5: Images of the receive signals at the 2 cm aperture for the 6 distances used for BSC estimation, with column 1 and 2 representing the signals used for methods 1 and 2 respectively. The figures for planar reflector depths Y_{LAM}, Y_A and Y_∞ are 5.5a, 5.5c and 5.5e respectively. The figures for planar reflector depths $Y_{LAM}/2$, $Y_A/2$ and $Y_\infty/2$ are 5.5b, 5.5d and 5.5f respectively. In all cases the y-axis is zeroed on the time sample at which the centre of the pulse is emitted before converting to a distance value through multiplication by the sound speed.

highly coherent, with the wavefront curvature decreasing from figure 5.5f and the lateral spread of beam energy also becoming more uniform. As the planar reflector is moved to Y_A (figure 5.5c), the beam energy continues to broaden, and the wavefront curvature returns. At Y_∞, the beam energy can be seen to broaden even further, but the wavefront curvature also appears to reduce as the planar reflector is moved further into the far field.

To quantify the shape of these wavefronts relative to the shape of the receive aperture (to give an indication of any potential phase cancellation) we can compute the coherence of these receive signals using equation (5.1), which we can plot for the three depth pairs in figure 5.5 as a function of spatial distance (lag) between receivers, where the minimum lag is set to be the centre wavelength (see table 5.1) of the transmitted pulse. These results are included in figure 5.6.

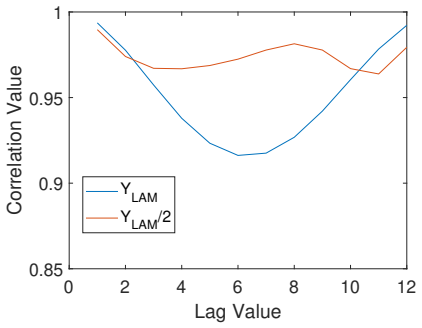

(a)

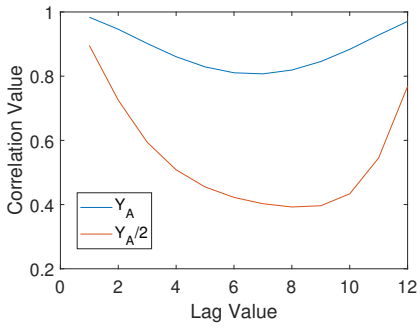

(b)

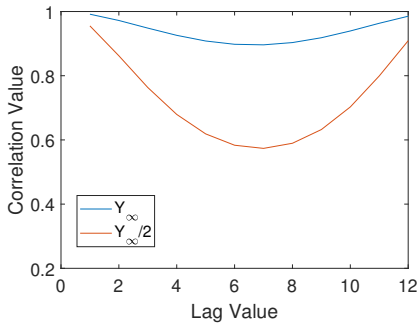

(c)

Figure 5.6: Coherence function calculations for the 6 receive signals pictured in figs. 5.5a to 5.5f. The legend label corresponds to the depth of planar reflector that generates the backscattered data. In all cases, the blue line corresponds to the receive signal that will be used for 'method 1', and the orange line corresponds to the receive signal that will be used for 'method 2'.

As predicted from time traces in figures 5.5a and 5.5b, the visual absence of notable wave curvature presents itself as highly coherent measurements in figure 5.6a, where the coherence is close to unity across all the spatial lags for both planar reflector positions. The observation of increased curvature as the planar reflector is moved from $Y_{LAM}/2$ (figure 5.5b) to $Y_G/2$ (figure 5.5d) to $Y_\infty/2$ (figure 5.5f) is apparent when we compare the method 2 coherence functions in figures figs. 5.6a to 5.6c, where the coherence function decreases, particularly for lags of 6-8, which correspond to comparisons of receive echoes separated by around half the width of the aperture. The observations of high wavefront coherence where the planar reflector is placed at Y_{LAM} or at Y_∞ (figures

5.5a and 5.5e respectively) are also reproduced in figures 5.6a and 5.6c respectively, where the coherence value is close to unity across the width of the aperture. The appearance of slight wavefront curvature with the planar reflector placed at Y_G (figure 5.5c) is also seen in figure 5.6b, which is seen to be the least coherent of the method 1 planar reflector measurements.

Comparing the results with the $2\,cm$ aperture to those with the $2.4\,cm$ aperture, we can compute the same coherence functions for the 6 planar reflector positions (illustrated in figure 5.7).

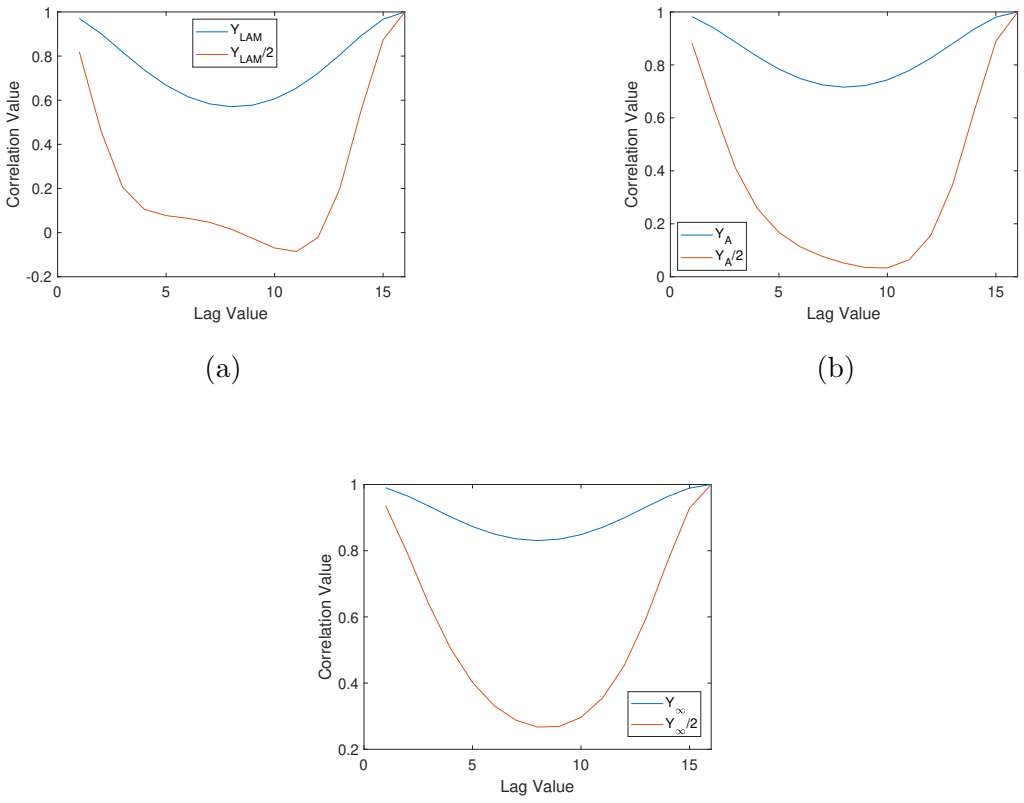

(a) (b)

(c)

Figure 5.7: Coherence functions for the $2.4\,cm$ aperture, using the same notation convention as in figure 5.6.

Notable in this case are the lower coherence values across all the positions, most notably the depths $Y_{LAM}/2$, $Y_A/2$ and $Y_\infty/2$, which all correspond to planar reflectors placed in the near field of the source, anterior to the LAM. To illustrate this point more

clearly, the average value of the coherence functions pictured in figures 5.6 and 5.7 was calculated. This provides a single measure of the coherence at each of the planar reflector depths, for both apertures, which are recorded in table 5.6.

Table 5.6: Coherence measurements for the estimation of phase curvature, to assess sources of potential phase cancellation on reception of the planar reflector echoes. The summation of the coherence function (R_m) was performed over spatial lags covering the extent of the aperture width. For the 2.0 cm aperture, $N = 12$, for the 2.4 cm aperture $N = 16$

	$\sum_{m=1}^{N} R(m)/N$					
Aperture size (cm)	$Y_{LAM}/2$	$Y_A/2$	$Y_\infty/2$	Y_{LAM}	Y_A	Y_∞
2.0	0.97	0.55	0.77	0.95	0.88	0.94
2.4	0.26	0.36	0.55	0.76	0.84	0.91

5.3.4 Diffraction correction functions

Based on the derived diffraction corrections and beam width measurements, we can compute the value of the diffraction correction for methods 1 and 2 to investigate their respective behaviours. Expressing equations (5.9) and (5.10) in the form

$$\mu_{BS}(\omega) = \frac{S_i(\omega)}{S_p(\omega)} D_i(\omega, y, \sigma_B), \tag{5.14}$$

where $D_i(\omega, y, \sigma_B)$ is the diffraction correction for method i. Interpolation of the beam width values over the axial distance was used to generate diffraction correction functions over the range $Y_{LAM} \leq y \leq Y_\infty$.

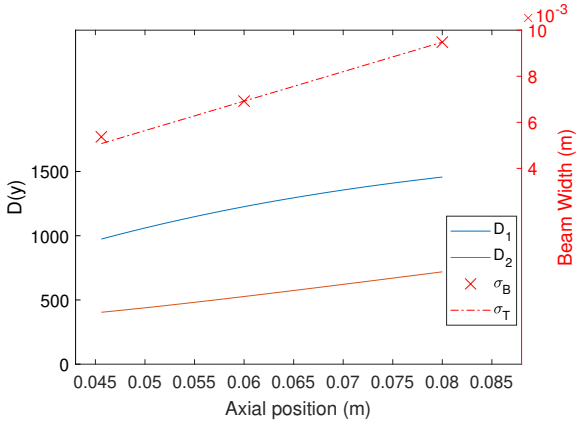

Figure 5.8: Diffraction correction functions for methods 1 (D_1) and 2 (D_2) for the $2\,cm$ aperture based on linear interpolation (σ_T) of the beamwidth of the simulated source (σ_B) for sample distances corresponding to Y_{LAM}, Y_A and Y_∞. The linear interpolation approach clearly underestimates the beam width at Y_{LAM} ($0.045\,m$), but is only used for illustrative purposes to visualise the potential value of the diffraction correction between the depths of interest.

Table 5.7

	$D(\omega, y, \sigma_B)$					
	Method 1 ($\times 10^3$)			**Method 2**		
Aperture size (cm)	Y_{LAM}	Y_A	Y_∞	Y_{LAM}	Y_A	Y_∞
2.0	1.0447	1.2134	1.4416	414.17	526.65	718.89
2.4	1.2590	1.3840	1.6228	498.59	582.44	738.17

5.3.5 BSC estimates

The results of the incoherent scattering simulations were used to compute the backscattered sample power spectrum $S_i(\omega)$ and the planar reflector power spectrum for methods 1 ($S_p(\omega)$) and 2 ($Q_p(\omega)$), and the BSC estimation performed using equations (5.10) and (5.9) respectively. The results of this analysis for both aperture widths at the three sample depths are shown in figure 5.9.

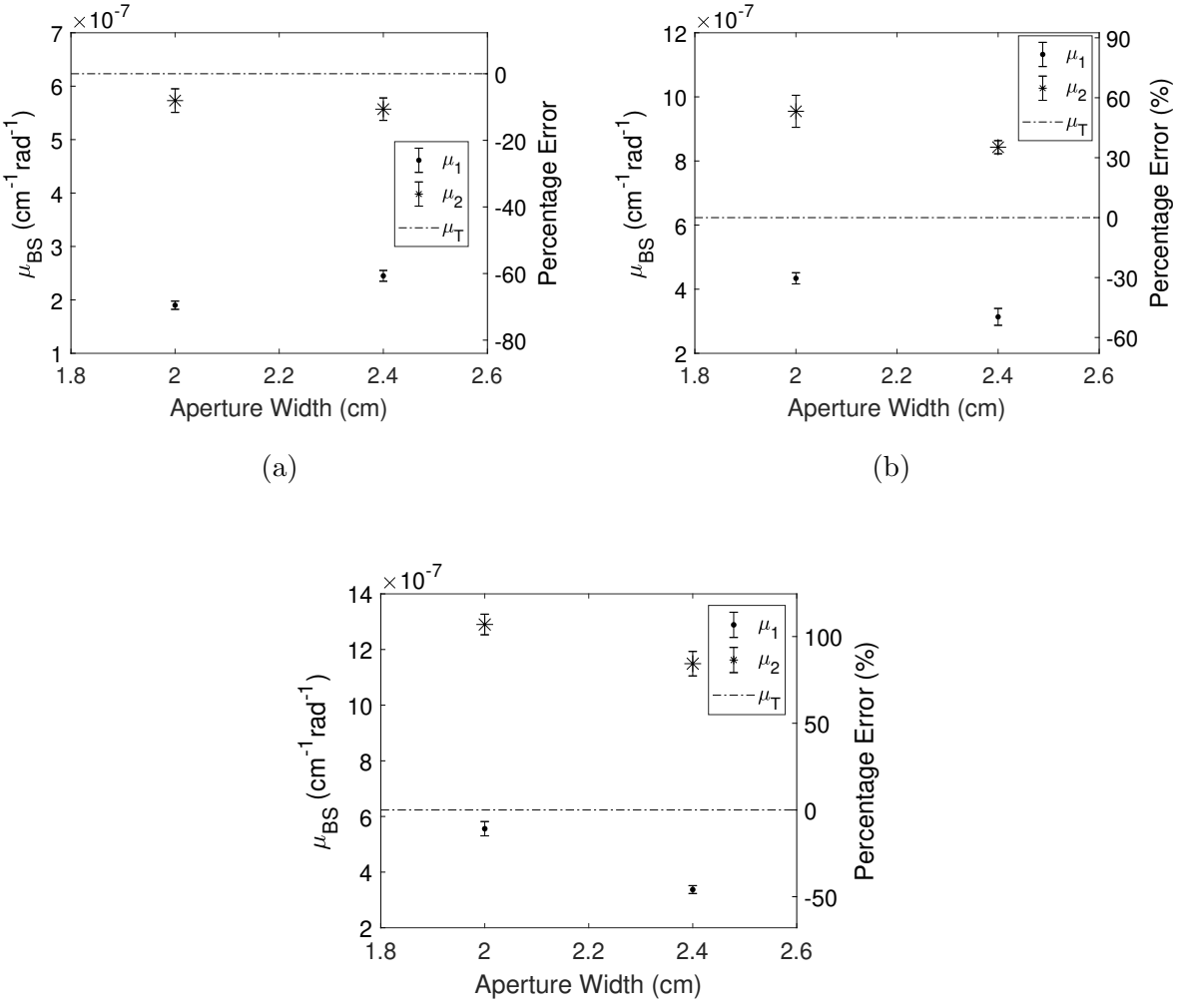

Figure 5.9: BSC estimation results for sample positions Y_{LAM} (5.9a), Y_A (5.9b) and Y_∞ (5.9c) respectively. BSC estimations are plotted for methods one (μ_1) and two (μ_2) with the accompanying theoretical value (μ_T) computed using equation (4.68). Percentage error in BSC estimates is measured relative to μ_T, with error bars corresponding to the standard error on the mean.

From figure 5.9a, we see that method 1 substantially underestimates the BSC when the sample is placed at the last axial maximum for both aperture sizes (68.18% and 60.65% respectively). A significant improvement (errors of 8.10% and 10.59%) was found through use of method 2 at this depth. Both methodologies tended to underestimate the BSC at this sample position for both aperture sizes. Placing the sample at the depth Y_G produces figure 5.9b in which the percentage error in the estimates reduced from figure 5.9a for method 1 (-30.34% and -49.67%), but increased for method 2 (53.25% and 35.27%). With the sample at Y_∞, the error using method 1 was reduced from the Y_A data set for the 2cm aperture (to -10.87%) but increased for the 2.4cm aperture (to -40.19%). Using method 2, the results continued to decrease in accuracy, producing large overestimates in the BSC for both apertures (106.34% and 84.36%).

Averaging the absolute percentage error across the two apertures produces the results shown in figure 5.10.

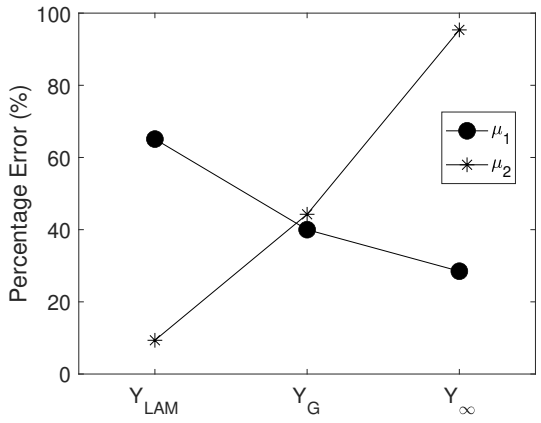

Figure 5.10: Average (absolute) error across both aperture sizes for the three depths of interest for method 1 (μ_1) and method 2 (μ_2).

Grouping these by aperture instead of sample depth produces figure 5.11. Method 1 is shown to be most accurate for the 2.0cm aperture when the sample is furthest into the far field ($Y_\infty = 8\,cm$), and the most accurate for the $2.4\,cm$ aperture for the arbitrary far field depth posterior to the last axial maximum ($Y_A = 8\,cm$). In the case of method 2, the error was shown to increase the further the sample was placed in the

far field, with the smallest errors observed when the sample was placed at the last axial maximum of the source. A tabular representation of all the results as described by their percentage error is shown in table 5.8.

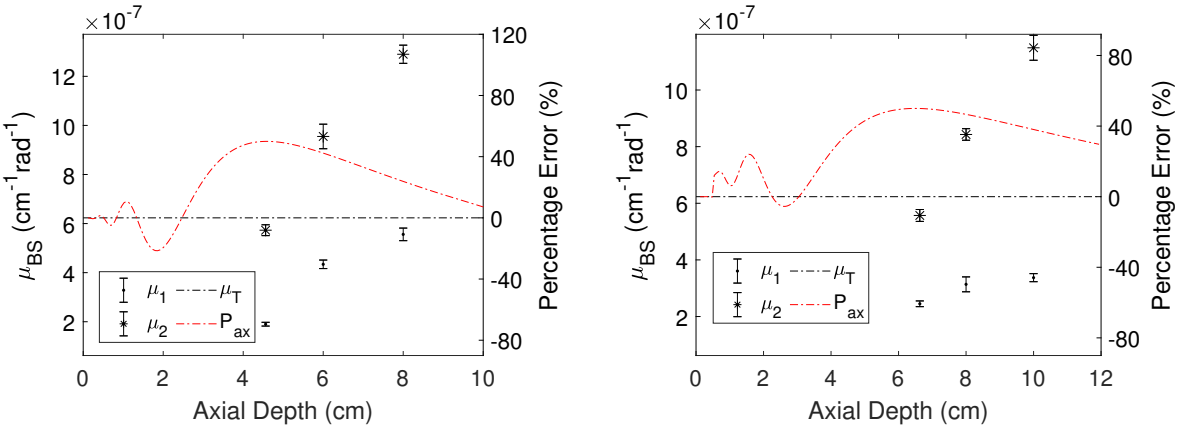

Figure 5.11: BSC estimation accuracy as a function of the sample depth for both methods for apertures measuring 2 cm (5.11a) and 2.4 cm (5.11b). A normalised plot of the on-axis amplitude (P_{ax}) is included to give spatial reference to the field position. This line is set such that the first data point is aligned to the 0% error line, and the LAM value is normalised to the 50% error line within the figure. Error bars correspond to the standard error on the mean.

Table 5.8: Percentage error values for BSC estimates produced by a given aperture and method. The sign convention is such that a minus percentage corresponds to a BSC underestimate (as compared to the theoretical value) and a positive percentage corresponds to an overestimate. The absolute value of the error was used in the averaging to prevent an overestimate/underestimate combination giving the impression of accuracy in a case of symmetrical variability about 0% error.

	Percentage Error (%)					
	Method 1			**Method 2**		
Aperture size (cm)	Y_{LAM}	Y_A	Y_∞	Y_{LAM}	Y_A	Y_∞
2.0	-68.18	-30.34	-10.87	-8.10	53.25	106.34
2.4	-60.65	-49.67	-40.19	-10.59	35.27	84.36
Average absolute error	65.10	40.01	28.49	9.35	44.26	95.35

5.4 Discussion

We will now consider the relative accuracies of the two BSC estimation methods for the different planar reflector positions. The two beam characteristics discussed within the results section: wavefront curvature and beam divergence will be used to explain this. Two general points regarding this can be made to aid in this discussion. Firstly, these factors will cause underestimates in both the planar reflector power spectrum and the sample power spectrum, since they correspond to lost energy. The effect of underestimating the planar reflector power spectrum will be to increase the BSC estimate. The effect of underestimating the sample power spectrum will be to reduce the BSC estimate. Secondly, it would be expected that the beam divergence will have more of an effect on method 2 than method 1. This is due to the fact that in method 1, the wavefront curvature and lateral confinement of the beam energy is common between the pulse incident on the sample and reference reflector. Based on these observations, we will now discuss the BSC estimation accuracy, firstly by method, followed by a comparison of the two methods.

5.4.1 Method 1

Considering first method 1 and the $2.0\,cm$ aperture, it is noted that the BSC value is underestimated in all cases. The largest underestimate (-68.18%) is found with the planar reflector and sample placed at the last axial maximum, with the underestimation reducing as the planar reflector and sample is moved to Y_A (-30%) and to Y_∞ (-10.87%) into the far field. From figures 5.5 and 5.6, we may note that the three receive echoes are similar in wavefront curvature, so losses due to phase cancellation for the reference power spectra should be minimal, and vary slowly as the reference reflector distance is increased, since all receive echoes appear to be highly planar. From figure 5.8 and table 5.4, we see that the beamwidth increases by a factor of $\sim 29\%$ from Y_LAM to Y_A and then 37% from Y_A to Y_∞. This beamwidth increase should increase the divergence losses, as less of the beam energy is laterally contained within

the width of the aperture, leading to an underestimate of the reference power spectrum, particularly given the increase in distance to the reflector.

Considering now the diffraction correction terms (see figure 5.8 and table 5.7) the analysis reveals that the correction term is shown to increase by a factor of $\sim 20\%$ between the three successive depths, indicating that the geometrical considerations are attempting to correct the normalised spectrum ($S_i(\omega)/S_p(\omega)$), but do not solely account for the difference in percentage error in estimate. To fully explain the observed behaviour, it is therefore hypothesised that the differing factor between the three depths is that of the phase cancellation losses in the sample power spectrum. By the van Cittert-Zernike theorem, we can state that with the sample centred at a depth of Y_{LAM}, the phase cancellation losses at the receiver will be at their greatest of the three cases (since this is the smallest distance between the incoherent scattering medium and the receiver). As the distance from the sample and the receiver is increased, these phase cancellations will be reduced, and the scattered wavefront will become more planar. This effect will then reduce with increasing distance until the receiver is effectively sampling a point on a cylindrically (or spherically in 3D) spreading wave. Whilst this hypothesis appears to provide a mechanism by which the reduction in underestimation is observed for the $2.0\,cm$ aperture, it does not adequately explain the results for method 1 using the $2.4\,cm$ aperture. In this set, underestimation is also observed at all three sample depths, which, whilst it does appear to improve as the sample is moved into the far field, still produces significant ($\sim 40\%$) underestimates in the BSC. A notable difference in this data set as compared to the $2.0\,cm$ data set is that the coherence appears to be lower (see 5.7 and table 5.6). Based on the previous statements and observations, we would expect that the reduction in coherence in the planar reflector echoes would result in an underestimation of the planar reflector power spectrum, which would result in greater BSC estimates, but despite this, underestimates were still observed. Since it is assumed that the incoherent scattering medium scrambles the phase of the incident pulse, it is not assumed that this reduction in coherence of

the incident wave should have a notable effect on the phase cancellation at the receiver for the echoes received from the sample.

5.4.2 Method 2

Considering now the results using method 2, we notice that a more consistent behaviour is to be found when the different source sizes are used. For both, the smallest error (-8.10% and -10.59% for the $2.0\,cm$ and $2.4\,cm$ sources respectively) were observed where the sample was placed at Y_{LAM} and the planar reflector was placed at $Y_{LAM}/2$, with both aperture sizes underestimating the value of the BSC when compared to the theoretical value. Increasing the sample distance and planar reflector distance resulted in increases in BSC estimate, with errors of 53.25% and 35.27% observed at Y_A and errors of 106.34% and 84.36% observed at Y_∞ for the $2.0\,cm$ and $2.4\,cm$ sources respectively. Using method 2, we note the factor of 2 difference in distance from the source to the planar reflector and source to sample. The effect of this will be to minimise beam divergence losses when measuring the planar reflector power spectrum. This will result in more accurate estimation of this factor, but will remove an element of self-correction in beam divergence effects, as the angle subtended by the receiver at the planar reflector depth is now larger than that at the sample depth. This effect will manifest itself more as the distance to the sample is increased, as the difference in depth between the planar reflector and the sample will also increase. This is a possible explanation for the decreasing accuracy (and increased overestimation) of the BSC as the sample distance increases. The point at which this effect is minimised would be with the sample placed at Y_{LAM}, at which the error is minimised. As mentioned, the beam divergence effects are expected to dominate the effect of phase cancellation that are stronger when the incoherent scattering medium is closer to the receiving aperture. For method 1, it was hypothesised that more accurate estimates of the sample scattered power spectrum were acquired through moving the sample further into the far field, which led to a reduction in BSC overestimate. This factor will also be present in

the data presented for method 2 (since the same sample spectra are used for both calculations), but in this case, the increase in the accuracy of estimation of the sample scattered power spectrum will be combined with increasing underestimation of the reference power spectrum, which could explain the distinct increase in BSC estimation.

5.4.3 General Discussion

Firstly, to present an overview of the behaviour of the two models, the analysis presented here appears to suggest that the use of method 1 is limited by phase cancellation effects. This reduces the measured value of the sample power spectrum, particularly when the sample is placed at the LAM, and produces underestimates of the BSC. When the sample and planar reflector are moved beyond the LAM, the phase cancellation effects will reduce, which is matched by observations of reduced underestimation in the BSC. The observation that the accuracy increases with the source to sample distance is an indication that it is phase cancellation limited. The method performs relatively poorly, producing consistently large underestimates of the BSC as compared to the results of chapter 4 which could be an implication that the beam divergence effects that are also manifest lead to a poor methodology for BSC estimation using unfocused sources. Method 2 behaves in much the opposite way, and appears to be limited by the beam divergence factors associated with the reference reflector power spectrum. The evidence for this is that it tends to produce the most accurate BSC estimations at the point at which beam divergence effects will be minimised, and appears to overestimate the BSC at the point at which the beam divergence effects will be maximised. As previously stated, the phase cancellation for the sample power spectrum will be greatest with the sample placed at the LAM, and as such, the results appear to indicate that these two effects happen to cancel for these aperture sizes as presented here. Whilst this may appear coincidental, the results produced from method 2 at the LAM are notable in that they are the most constant across all of the depths and methods considered, indicating the potential for a physical significance in this approach.

Considering the average behaviour of the methods and aperture widths in figure 5.10, we can see that the best performing method and distance combination is the use of method 2, with the sample placed at the last axial maximum of the source, as this produced the lowest absolute percentage error, and the least variable BSC estimate. From a practical standpoint, implementation of this approach has the benefit that the incident intensity on the region of interest is maximised by placing the sample at this point, maximising the signal to noise ratio. The disadvantage is that determining the position of the last axial maximum would require an extra (minor) experimental step. Further experimental benefits of method 2 over method 1 are that the requirements for greater source to sample distance will result in a greater loss of signal due to attenuation, and the increase in beam width will reduce spatial resolution. Going deeper into the far field negates some of the phase cancellation effects (as indicated by figure 5.6), but the accompanying increase in the beamwidth reduces lateral resolution, which is of detriment to the resulting BSC image generated. In addition, this increases the total path attenuation and - from the results presented here - potential issues could be found in assessing the incoherent backscattered spectrum from a diffuse scattering medium.

5.4.4 Limitations

The limitations of this study are as follows. Firstly, (as in chapter 4) these simulations investigate scattering behaviour in reduced dimensionality. As such, the effects of elevational beam width on the scattering behaviour at the point of incidence on the discrete scattering bodies or the planar reflector are not representative of same situation one would encounter with a real transducer and scattering medium. The conclusions drawn from these simulations must be contextualised into three dimensions for application onto real world examples, particularly given that the beam divergence and phase cancellation arguments presented here will be altered by the inclusion of a third dimension. Whilst the general physical principles will remain the same, certain observations - particularly those pertaining to the mutual annulment of phase cancellation

and beam divergence effects behave with a different dependence on radial distance in three dimensions as opposed to two, which may alter the final results. Secondly, whilst the use of the same set of scattering media for all the investigations presents benefits in reproducibility, the disadvantage of this in investigating the physics of scattering is that the changing beamwidth (see table 5.4) results in differing numbers of scatterers per resolution cell as the sample is moved (see table 5.5). As a result, the relative properties of the beam and the scattering medium are changing as the sample is moved, which could have an effect on the ability of the simulated source to compute accurate BSC estimates under the assumptions detailed in the derivation of the measurement equation(s). This limitation could also be rephrased to suggest that the use of only one simulated scattering medium (despite it being comprised of many independent ensembles) is a limitation to the applicability of the results, and that simulating a range of scattering media with differing properties would be more insightful. A third limitation is the discrete nature of the results with respect to the positions of sample and reflector investigated. Ideally, further investigation would be performed that would investigate a greater number of sample and reflector distances, to further probe the relationship between the wave field as it evolves with distance from the source. In this investigation only three sample distances were considered, due to the time taken to complete a full compliment of simulations. This factor limits the breadth of knowledge that can be interpreted from the results. Fourthly, only two sources were considered, which limits the power of the conclusions that can be drawn from the results. For example, it is hypothesised from the results presented that the beam divergence and phase cancellation cancel one another when using method 2 with the sample placed at the LAM. This result is constant across the two simulated sources, but more source sizes would be need to be investigated in order to have confidence that this result is universal enough to be applied elsewhere.

5.5 Conclusion

To conclude, this chapter has explored the construction of mathematical and finite element models to describe and model the coupling between a planar reflector and an unfocused source. The investigation has focused on the nature of the diffraction correction, and the effects of the accuracy of this correction on producing estimates of the BSC.

The findings of this investigation were as follows: the most accurate method for BSC estimation using a planar reflector and unfocused source was shown to be using the method developed by Chen et al. (method 2), whereby the sample is placed at the LAM, and the planar reflector is placed at half the distance to the LAM. Based on the analysis presented here, this depth of sample and planar reflector was hypothesised to minimise the beam divergence effects that the method is sensitive to. The investigation revealed that the Sigelman and Reid method (method 1) of BSC estimation was shown to be more accurate when the sample and planar reflector were placed further into the far field of the source. The explanation drawn from this result was that this approach was more sensitive to phase cancellation effects across the aperture when the sample is placed closer to the LAM.

Whilst the results presented here are limited in their specificity to both the simulated aperture sizes, the dimensionality and the design of the scattering sample, it is hoped that this work does provide a framework on which similar experiments could be conducted into the investigation into the nature of diffraction corrections for BSC estimation. If this were to be performed in the correct dimensionality and with a range of aperture sizes and sample depths, it could provide valuable information in terms of both informing future practices in performing accurate measurements of the BSC and also provide the required information to investigate previously reported tissue properties to ascertain the reasons for differing tissue characterisation measurement results observed by authors who use different methods for BSC estimation.

Chapter 6

An investigation into the effect of coherence on the accuracy of BSC estimation

6.1 Introduction

This chapter will evaluate methods to improve upon BSC estimates, and investigate factors that degrade their quality through investigation into the effects of scattered wave coherence on BSC estimates. Chapter 5 investigated the potential effects of coherence in the reference reflector echo, and elucidated on the potential for phase cancellation of echoes causing an underestimation in the backscattered power. As a continuation of this work, this chapter will investigate how coherence impacts upon BSC estimates from the sample and present a method by which they can be improved through coherence based segmentation.

Soft tissue is modelled as an incoherent, speckle producing medium, and it is assumed that it is populated by randomly distributed scattering bodies much smaller than the wavelength of an ultrasound imaging pulse [55][57][161][25]. The description of the medium as incoherent refers to the assumption that the phasors from each scattering event within the scattering volume are randomly distributed throughout the range of potential phase angles. Their random positioning results in a lack of correlation between the phases of the waves scattered from inside the scattering volume, which ultimately leads to interference effects when the scattered waves are incident on the receive aperture. To reduce the impact of interference effects on backscatter coefficient (BSC) estimates, BSC values are averaged over multiple scan lines, to produce BSC estimates over regions of tissue. The reduction in spatial resolution by increasing the voxel size is compensated for by the fact that the resulting data blocks are partially denoised from the interference effects. This chapter will investigate how coherence properties of tissue backscatter can be used to predict the interference effects, and whether the measured coherence of backscatter data could be used to select the optimal tissue regions for averaging to generate increased accuracy in BSC estimates. This investigation will be comprised of three parts. Firstly, the properties of the coherence of an incoherent scattering medium will be investigated. Secondly, the coherence will be investigated as an imaging metric for soft tissue target segmentation. Finally, coherence

properties will be used to design a segmentation algorithm for BSC data.

The assumption that soft tissue can be modelled as an incoherent scattering medium is implicit in the derivation of the BSC estimation equation, both in published literature [27][25][1] and the derivation presented in chapter 4. It is for this reason that the BSC equations *estimate* the backscattered power from a tissue using a formulation based on the describing the average properties of the medium, since the actual backscattered power measured from sections of incoherent medium will be dependent on the particular scatterer configuration in the scattering volume. Since the BSC equations are formulated on the assumptions of incoherence, deviations from this assumed behaviour within a tissue would be expected to generate unpredicted variance in the estimated BSC value. As a simple result highlighting how the coherence impacts the estimation of backscattered power, consider a situation where the coherence of backscatter is predicated solely on the geometrical shape of the scatterer. To observe how the the geometry of the scattering media changes the estimated backscattered power, we can consider the planar reflector substitution method as described in chapter 4. If we compare the presented equations describing the backscattered power expected from the incoherent scattering medium (S_i):

$$S_i(\omega) = 2\pi^2\omega^2\rho_0^2\mu_{BS}|T(\omega)A_\Phi^2|^2 kd\sigma_B\sqrt{\pi}, \tag{6.1}$$

and the planar reflector (S_p):

$$S_p(\omega) = \frac{ky_0\omega^2\rho_0^2|T(\omega)A_\Phi^2|^2 R_p\pi}{\sqrt{(1+(\frac{2y_0}{k\sigma_B^2})^2)}}, \tag{6.2}$$

we can see how the the difference in the scatterer geometry results in a different functional form in the two equations (see chapter 4 for an explanation of the derivation and terms). In the case of the planar reflector, its planar geometry gives rise to coherence in reflection: exemplifying how the geometry affects the functional form of the estimation of the backscattered power. This result directly relates to the BSC estimate equation,

which is formed by dividing equation (6.1) by (6.2) and rearranging for μ_{BS}. Since the BSC estimate is dependent on the relative geometries of the reference scatterer and the sample, we can therefore state that the accuracy by which the reference scatterer and sample scatterer distributions are described will have a direct impact on the accuracy of the result. It is for this reason that the reference scatterer is selected to either possess a simple geometry (such as a planar reflector) so that it can be described with simplicity, or it is designed to possess a scatterer distribution similar to that of the sample (such as a reference phantom) so that the geometrical considerations are presumed to cancel when the ratio of the respective power spectra is computed. This chapter will investigate how BSC estimates are affected when the sample scattering medium deviates from the assumptions in the derivation of the estimation equation. In particular, it will focus on how the violation of the incoherent scattering assumption affects BSC estimates. The spatial coherence of a field produced by an incoherent source (such as a diffuse scattering medium) is described by the van Cittert-Zernike theorem. This theorem describes the spatial evolution of the coherence properties of a wave field propagating from an incoherent source [162][163] as a function of the source geometry and the distance from the source to the point at which the coherence is measured. A key result of the theorem predicts that the wave field of an incoherent source becomes more coherent as the distance from the source increases. Application of this theorem to backscatter imaging by Mallart and Fink [163] and Bamber et al. [164][165] showed that the spatial dependence of the spatial coherence of an incoherently scattered wave field should be proportional to the autocorrelation of the transmit aperture function. For a 1-D array, the aperture function is rectangular, for which the autocorrelation is a triangular function, so a measure of the coherence in the far field of an idealised incoherent scattering medium should be triangular in shape. This result was also shown to be independent of the source focal length and source f-number [163]. An illustration of the vCZ theorem in practice appears earlier in this thesis, in figure 4.5a, where an image is presented of the scattered wavefronts emanating from the simulated incoher-

ent scattering medium. This figure is reproduced in figure 6.1, where one can observe the increase in spatial coherence of the scattered field from an incoherent scattering medium as the wave propagates from the source of the scattering. In relation to the vCZ theorem, this constitutes analysing the wave field at a greater distance from the incoherent source.

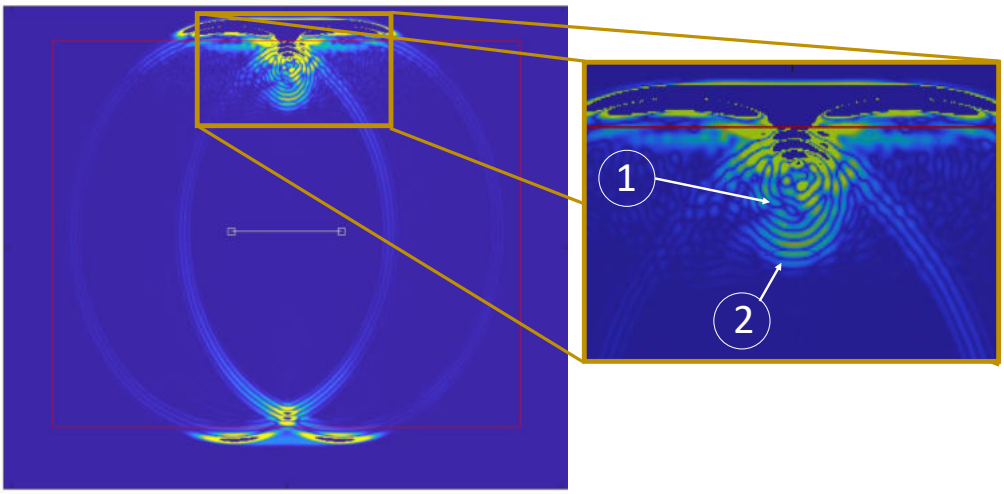

Figure 6.1: Illustration of the evolution of the coherence behaviour of the wave field scattered by an incoherent, diffuse scattering medium. The phase scrambling effect of the randomly positioned scatterers allows us to treat the scattering medium as an incoherent source, and thus apply the vCZ theorem. In the zoomed part of the figure, we can see the low spatial coherence close to the source of the scattering (1), and the increase in spatial coherence as the scattered wave propagates into the far field. Note that this wave field is produced by a focused source, so the curved wavefront will appear planar only after the receiver delay profile is applied. For the details of this result, consult figure 4.5a.

To quantify the coherence of the wavefront, Mallart and Fink [163] and Bamber et al. [165] computed the coherence function, a normalised cross-correlation of the echo received at separate points along the aperture. Expressing the echo recorded by a receiver i as s_i, and the spatial lag between two receivers as m, the coherence function of a wavefront received across a set of N receivers can be calculated using the equation:

$$R(m) = \frac{1}{N-m} \sum_{i=1}^{N-m} \frac{\sum_{n=n_1}^{n_2} s_i(n) s_{i+m}(n)}{\sqrt{\sum_{n=n_1}^{n_2} s_i^2(n) \sum_{n=n_1}^{n_2} s_{i+m}^2(n)}}, \tag{6.3}$$

where $n_1 \rightarrow n_2$ represents the axial analysis kernel over which the coherence is calculated. This expression has been applied in the analysis backscatter imaging characteristics by a number of authors [163][164][165][101]. An illustration of the apperance of such a function for four different scatterer sites is shown in figure 6.2. The coherence characteristics of an incoherent scattering medium measured by a 1D aperture (red) is pictured as perfectly triangular. A coherence function is also plotted for a planar reflector imaged at the focal depth of the source (which we assume to be close to unity irrespective of the spatial lag, since the reflector is a coherent scatterer). Additionally we consider two media that are not perfect representations of incoherent media. This first is a highly incoherent medium whereby measured coherence is lower than the incoherent case. This may be caused by strong off-axis scattering, or may simply be a result of a section of the random scattering medium being arranged in a highly incoherent manner. The second is labelled as the 'relatively incoherent medium', a name which is proposed to suggest that the echoes may possess greater coherence than the incoherent medium due to either weakened off-axis scattering, or through the presence of structure within the scattering medium, either by design, or by chance. To apply a phasor description to these models, we would say that scattererd wave phasors from the planar reflector are aligned at one phase angle (corresponding to coherent reflection). The phasors from the incoherent medium would be uniformly distributed through the potential phase angles. The relatively incoherent medium is a combination of the first two, in that the medium produces scattered phasors with a partially random distribution, but with a bias toward certain phase angles. The highly incoherent medium can be considered to be a combination of pairs of anti-aligned phasors (producing negative coherence), combined with some random distribution of phasors. These cancel to produce low (close to zero) coherence.

An illustration of the potential structural scattering configurations that would

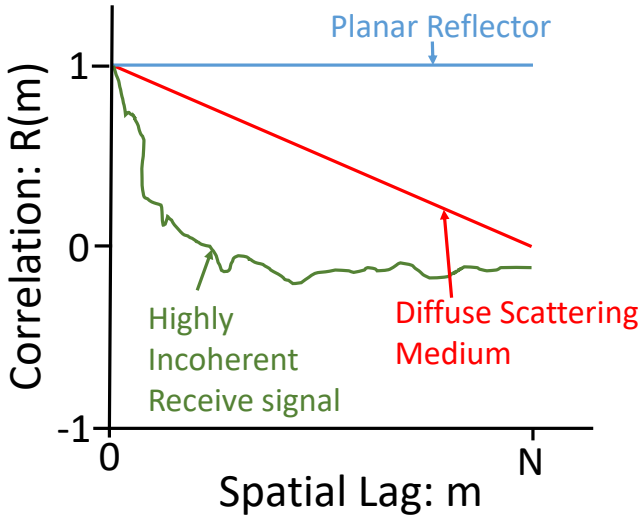

Figure 6.2: Example coherence functions for 4 cases. For each of the lines, the coherence function would be calculated for each spatial lag (m). Identically, the coherence function will be unity for $m = 0$. Credit to Lediju et al. for the original image on which this is based [101].

cause noticeable changes to the coherence of the scattered wavefronts are pictured in figure 6.3. In figure 6.3a, two scatterer types are pictured. The relative strength of scatterer type 1 (on the beam axis) compared to scatterer type 2 (off the beam axis) will cause an increase or decrease in the coherence of the echoes produced by this section of the sample. In the second example (figure 6.3b), the presence of structure in the positioning of the scatterers could result in non-random phase cancellation due to the periodicity of the scattering sites, producing Bragg diffraction effects. In this case, the backscattered power from the structured region will be dependent on the relative length scales of the scatterer spacing and the wavelength.

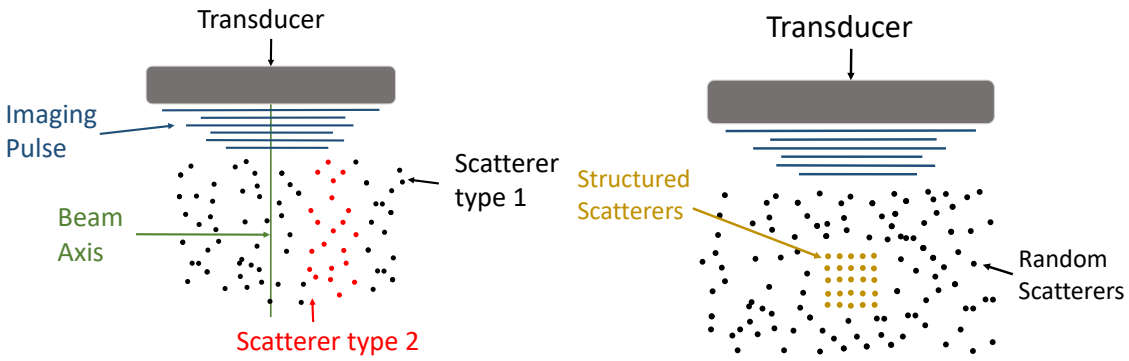

(a) (b)

Figure 6.3: Illustration of causes of increases and decreases in the coherence within a diffuse scattering medium through local variation in the scatterer distribution. In figure 6.3a, pictured are two scattering populations (type 1, black and type 2, red) in a uniform background medium. The influence of the off-axis scatterers (red) will either increase or diminish the measured coherence for the given sample-transducer position when compared to the case where the red and black scatterers are indistinguishable. If scatterer type 2 has a greater impedance mismatch relative to the background medium than type 1, the increase in off axis backscatter will reduce the measured coherence. If scatterer type 2 has a smaller impedance mismatch relative to the background medium than type 1, the reduction in off axis backscatter will increase the measured coherence. In figure 6.3b, the correlation of the structured scatterer positions will result in a measure of coherence greater than the surrounding randomly regions, due to the coherent nature of scattering from a region possessing periodicity. The structured scatterers are colour coded for delineation, and need not possess different acoustic properties to cause a change in coherence in the backscatter.

We would expect to observe spatial fluctuations in the measured coherence even from a medium populated by identical random scatterers. In a random configuration, some configurations of scatterer position will present with greater or lower scattering coherence than others. We would expect the average coherence function to resemble the triangular function pictured in figure 6.2. The random fluctuation in backscatter coherence is partially manifest in the interference effects that generate noise in BSC

estimates, although the relationship between wave coherence and backscattered power is not monotonic. Regions which backscatter more strongly would be expected to be coherent, as constructive interference across the receive aperture will increase the measure of the backscattered power. By contrast, high measures of coherence will not necessarily equate to high measures of backscattered power. As a hypothetical example, if a scattering volume contained a configuration of scatterers that happened to cancel from the off-axis directions but constructively interfere on-axis, this could result in a received wave packet from the centre of the resolution cell that is both highly coherent and low in power.

In the work of Verhoeven et al. [166], it is stated that the speckle statistics become independent of the number density of the scatterers once the fully developed speckle case is reached (10 scatterer per imaging resolution cell volume). From this autocorrelation argument, one can hypothesise that the coherence behaviour of the speckle also becomes uncorrelated from the exact number density once the condition for fully developed speckle is reached. If this is the case, then one fully developed speckle producing medium should have the same statistical coherence properties as another fully developed speckle producing medium, provided the same emit and receive apertures were used in subsequent investigations. Therefore, one fully developed speckle producing medium could be used to generate a 'universal' speckle reference data set which can be used to investigate another unseen speckle producing medium using the same ultrasound device. Investigation of the reference phantom's coherence properties could then be used as a segmentation blueprint for other samples. Due to the amplitude normalised nature of the coherence function, test samples would not need to be populated by the same strength scatterers as the reference phantom, provided that their strength did not invoke substantial multiple scattering, as this would violate the weak scattering assumption made in the derivation of the BSC. Due to the autocorrelation argument presented above, the test sample would also not be required to possess the same number density as the reference speckle producing material. Based on these two arguments,

coherence based segmentation could represent a highly flexible analysis tool with which to segment backscattered data for BSC calculation.

This chapter will investigate the use of coherence metrics for the analysis of backscatter data to improve BSC estimates. To do so, coherence of backscatter will be measured to assess how well a simulated tissue section matches the assumptions of incoherence made in the BSC derivation. To perform this investigation, the simulation methods outlined in chapters 4 and 5 will be developed to incorporate spatial variation in both coherence and BSC. Through simulation of a set of backscatter experiments and the analysis of the coherence and BSC characteristics, a segmentation approach will be presented to improve BSC estimates by coherence segmentation of tissue regions.

6.2 Methods

To investigate the effect of coherence on the quality of BSC estimates, models simulating incoherent scattering media, and models simulating an incoherent medium interspersed with local variations in coherence were developed. The former were constructed through random positioning of the scatterers (as per chapter 4 and 5). The latter contained target regions deliberately designed to violate the assumptions of the BSC estimation equation. Coherence was then used to identify the properties of the model to assess the impact of coherence on the backscattered power. Analysis methodology was designed to calculate the contrast of the targets, to assess coherence as a metric for direct segmentation of the target regions. The relationship between the coherence and backscattered power was then investigated to determine sources of variability in both the random, incoherent media and in the regions populated by coherence targets.

The assumed hypothesis is that the regions not matching the incoherence assumptions made in the derivation of the BSC estimation equation lead to increased variability in backscattered power and errors in the final BSC estimate. Whilst variability due to interference is inherent for backscattering analysis, it is hypothesised that identification of these regions using coherence will allow segmentation of the non-conformant regions to produce a more accurate BSC estimate.

6.2.1 FE Model Parameters and Methods

This subsection will discuss the construction of the FE models simulating the incoherent media, and the models containing the coherence targets. The background medium (within which the scatterers were distributed) properties, the centre frequency of excitation, the mesh refinement value and the Courant value used for the investigation in chapters 4 and 5 were reused here to maintain some of the conditions under which the results are generated within the different chapters. The properties are listed in in table 6.1.

Table 6.1: Properties for the mesh construction, time step and background medium.

Property	Value
Background medium sound speed (c_0)	$1500\,ms^{-1}$
Background medium density (ρ_0)	$1000\,kg\,m^{-3}$
Courant value	0.1
Centre frequency of excitation (f_0)	$0.5MHz$
Centre Wavelength (λ_0)	$3mm$
Mesh refinement: square single (dx)	$dx = \lambda_0/50 = 60\mu m$

6.2.1.1 Source Design

For this chapter, a $4\,cm$ line aperture focused at a depth of $5\,cm$ was used in all cases. The method by which this source was designed is described in chapter 2, and BSC estimates produced using this source are detailed in chapter 4. The reason for the selection of this aperture were twofold. Firstly, the simulations using this aperture size as described in chapter 4 were shown to possess the highest agreement with the theoretically calculated value of the BSC in the simulated cases of a fully developed speckle, implying that the diffraction correction for this combination of scattering medium and source was accurate, and that the BSC estimates could be relied upon. Secondly, selecting the widest source of those already considered allows us to investigate the coherence properties over the greatest length scale (simply due to the greater lateral extent of the aperture). This allows greater freedom in parameterisation of the coherence function. The beam width of this aperture was assessed using the methodology described in sections 4.2.2.3 and 5.2.2. The value computed for the Gaussian RMS beam width for the $4\,cm$ source was found to be $2.7\,mm$.

6.2.1.2 Lateral Scanning

To assess spatial variation in the coherence in the axis normal to the beam, the FE models listed within this chapter were designed to simulate the lateral scanning of a source across a region populated by scatterers. Between consecutive simulations, the position of scatterers was translated laterally by 10 element widths ($\lambda_0/5$) relative

to the source, simulating the movement of the source relative to the scatterers. The positions of the scatterers were generated before simulation, within a Boolean matrix. The matrix contained columns dictating lateral position and rows corresponding to axial position within the mesh, with a value of 1 corresponding to a scatterer position, and 0 corresponding to background medium. Sections of the matrix were then applied to the mesh to dictate the positions of scatterers. Each successive simulation partitioned a different part of the scatterer position matrix and applied the Boolean value to the mesh elements to mimic the scatterers being moved relative to the source.

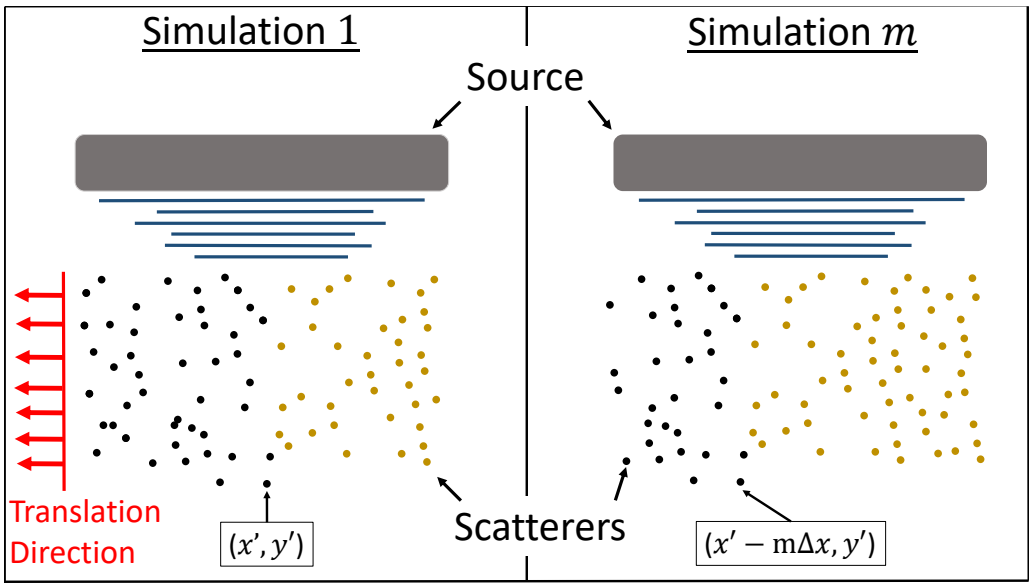

Figure 6.4: The lateral scanning method shifts the scatterer positions by Δx after each simulation, which simulates the scanning of the source over an area of a sample. The diagram depicts a population of scatterers which are displaced in the lateral dimension by $m\Delta x$ between the first and 'm'th simulation. Two scatterer populations are pictured in different colours, to aid visualisation of the movement.

Unlike the models described in chapters 4 and 5 - where the scatterer positions were randomised for each simulation - the scatterer positions are now correlated between simulations. This allows us to construct images of the simulated models and analyse the lateral variation in the backscattered wave properties such as BSC, backscattered amplitude and coherence. To ensure that the simulation included a significant enough number of scattering ensemble positions to present a reasonable estimates of the BSC,

and so that the coherence targets could be spaced out laterally through the model, 600 scan lines were simulated using the lateral scanning approach.

6.2.2 Scattering Model Design

To investigate the relation between coherence and BSC estimate accuracy, models were designed with a background speckle that matched the criteria for an incoherent scattering medium. This was achieved using the methods presented in chapter 4, where weak, monopole scattering elements were generated in random positions throughout the model. The manner in which this speckle pattern was confirmed to be accurately matching the description made in the BSC will be discussed later. As outlined in chapter 4, the monopole scattering behaviour was achieved through applying sound speed fluctuations to the scattering elements, whilst keeping the mass density constant throughout the model. The sound speed used for the background scatterers is labelled in tables 6.2 and 6.3 as 'speckle'. Spatial variation in expected backscattered power was then introduced by replacing regions of the incoherent scattering medium with scatterers of different properties to the background speckle. These target regions were designed to introduce BSC outliers into the models. An average of the backscattered power over the whole of these models (both the background speckle and the target regions) would therefore change the BSC estimate that would have been made if only the incoherent scattering medium regions were used in the BSC estimation process. The ability to identify these regions based on their coherence characteristics could then be used to assess the performance of coherence as a segmentation metric.

Hypoechoic and hyperechoic target regions were designed to produce regions with lower and higher expected backscattered power than the power as measured from the background speckle. This was performed to assess the ability of coherence metric to identify regions that could generate BSC under or overestimates. In addition, a region populated by identical, randomly positioned scatterers identical to those in the background speckle regions of the model was also included.

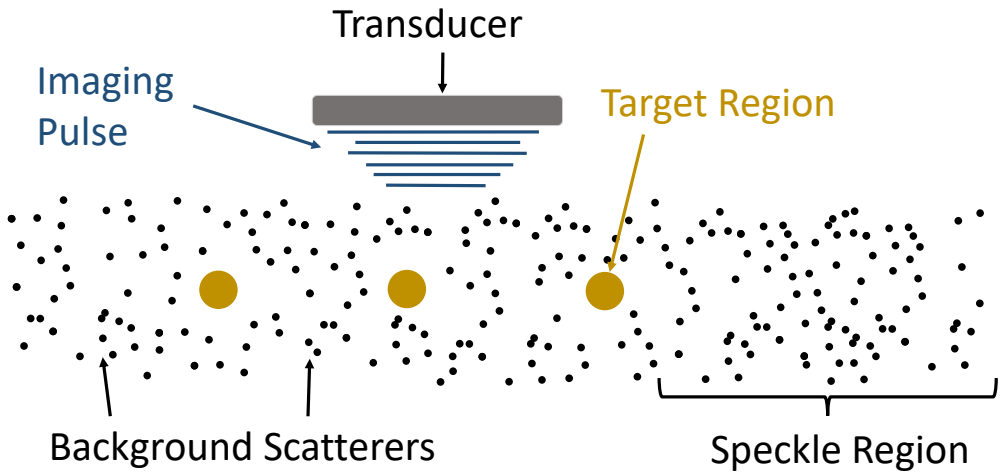

Figure 6.5: Schematic outlining the design of the test models. The background scatterers generate the background speckle, the speckle region is included as a region expected to generated backscattered power values that match the incoherency assumption in the derivation of the BSC. The target regions are designed *not* to match this assumption, and are the targets which we aim to identify using coherence analysis. The incoherent scattering models were populated solely with 'background' scatterers, with no target regions included.

In addition to the models with imposed BSC variation, incoherent scattering models were also produced with identical, randomly positioned scatterers. Four models of this type were produced, which differed in the number density of the scatterers populating the model. Analysis of the coherence behaviour of these models was performed to assess whether coherence based analysis could improve the BSC estimates of models that statistically match the presumed incoherence conditions, but may have local random fluctuations in coherence, and also to estimate the number density values at which the medium ceases to act like an incoherent scattering medium and violates the assumptions in the derivation of the BSC estimation equation.

6.2.2.1 Hypoechoic Models

To generate the hypoechoic targets, regions of the model were populated by weaker scatterers than the background speckle. The hypoechoic targets took two forms. The first were circles of radius $4\,mm$, centred at the focal depth of the source, and separated laterally across the simulated sample by $4\,cm$. The second type were rectangles of length $1.2\,cm$, centred at the focal depth and separated laterally by $4\,cm$. The reason for the size selections will be apparent when the predicted coherence characteristics of the targets are described.

Since these regions contained weaker scatterers than the background speckle, the estimated power from the regions would be expected to be lower than the background. Their inclusion in any spatial averaging of BSC estimates could therefore generate an underestimate in their vicinity. If the whole model were to be averaged - under the assumption of homogeneity - then the result would be an underestimation of the BSC.

We also expect an effect on the local spatial coherence. When two different scatterer populations, distinguishable by their scattering strength) are contained within distinct regions that are straddled by the beamwidth, the result on the backscattered wave is a reduction in the measured coherence that would have been observed if the scatterers were all identical. This is due to the fact that the scattered wavefront received at the aperture will contain an imbalanced contribution of off-axis scattering from one side of the beam axis. Off-axis scattering will - on average - cancel where the scatterers are identical on either side of the beam axis, but the increase in scattering strength from one side will generate an imbalance. Since the wavefronts received from off-axis scatterers will not match the aperture shape, they will cause a reduction in measured coherence. This effect is expected to be at its most powerful when the target region boundary lies on the beam axis. Once the beam width is scanned past the boundary, one scattering population will begin to occupy a greater area within the resolution cell, and the effect will continue to diminish as the area within the beamwidth becomes more dominated by one scatterer type. This process is known as coherence recovery[101]. The circular

targets (measuring $8\,mm$ in diameter) are similar in size to the full RMS width of the beam produced by our simulated source ($5.4\,mm$) at this depth. Therefore we would expect only a little, or no coherence recovery as the targets are laterally scanned, and they should appear as low coherence circular regions in a coherence image. By contrast, the rectangular targets are bigger (measuring $12\,mm$ in width) than the beam width, so we would expect to observe coherence recovery in the centre, once the beam width is fully contained within the target region.

The circular targets were designed to be of comparable size to the beamwidth in an attempt to generate targets that did not exhibit coherence recovery, and therefore present a simpler structure to analyse using the coherence. The rectangular targets were - by contrast - designed to test the sensitivity of the coherence based analysis to larger regions and assess how the coherence recovery might impact the quality of the coherence analysis.

Schematics of the circular and rectangular targets are shown in figures 6.6 and 6.7. The properties of the background speckle scatterers, and the scatterers populating the three circular targets (labelled 'One','Two' and 'Three') are listed in table 6.2.

Table 6.2: Model Category One Circular Target properties. Sound speed corresponds to the sound speed of the elements designated as scatterers that are located within the circular target regions. Reflection coefficient corresponds to the linear reflection coefficient of the individual scatterers relative to the background, the sound speed of which was $1500\,ms^{-1}$.

Target	Sound Speed (ms^{-1})	Reflection Coefficient
Speckle	1497.0	1.0×10^{-3}
One	1499.7	1.0×10^{-4}
Two	1499.5	1.8×10^{-4}
Three	1499.1	3.2×10^{-4}

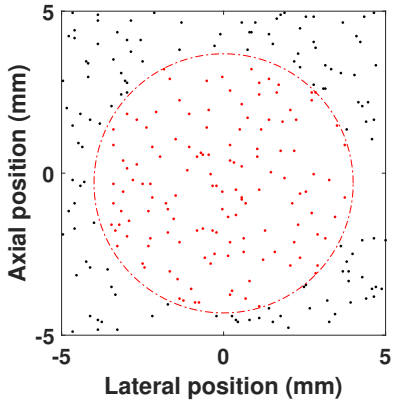

Figure 6.6: Hypoechoic circular Target Design. The black dots correspond to the background, speckle producing elements. The red dots correspond to the - weaker - scatterers located within the circular region, the boundary of which is indicated by the dashed line. These target regions were located such that the centre of the circular region was located at the focal depth of the source.

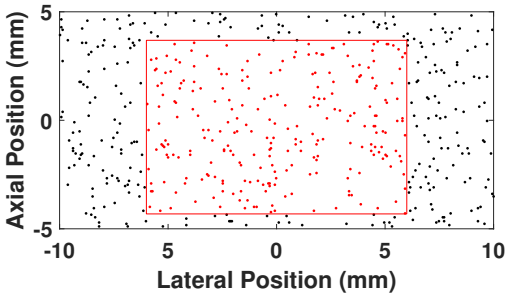

Figure 6.7: Hypoechoic rectangular Target Design. The design of the rectangular target was the same as was used for the circular hypoechoic target, with the only change being the shape delineated by the regions of weak scatterers. The centre of the rectangle was designed to be at the focal depth of the source.

6.2.2.2 Hyperechoic Model

Inverting the previous approach, small circular hyperechoic regions were generated to simulate regions of higher expected backscattered power than the background speckle. Their inclusion in any spatial averaging of BSC estimates could therefore generate an

overestimate in their vicinity. If the whole model were to be averaged - under the assumption of homogeneity - then the result would be an overestimation of the BSC.

We expect these regions to exhibit greater coherence than the background speckle when the beam is centred on the hyperechoic region due to the fact the on-axis scattering (from the hypoechoic region) will be from stronger scatterers than the off-axis scattering (from the background speckle region). As such, off-axis scattering – which decreases coherence - will contribute less to the reduction of coherence than would be the case if there were only one type of scatterer within the beamwidth. This will result in greater coherence values when the hypoechoic region is situated on the beam axis. This concept is tractable to the work of Li and Li [167], who used coherence analysis to suppress off-axis scattering for the improvement of image quality.

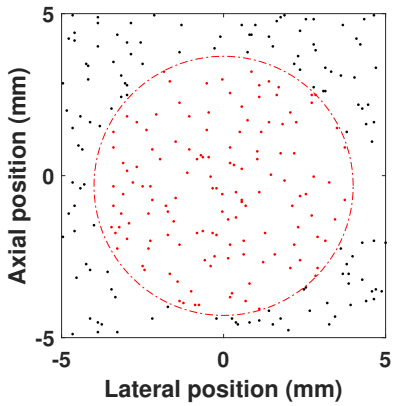

Figure 6.8: Hyperechoic circular Target Design. The design here was as for the circular hypoechoic target, with the only change being that the scatterers populating the circular region possessed a greater impedance mismatch relative to the background medium.

Table 6.3: Hyperechoic model properties. As before, the sound speed and reflection coefficients correspond to the scatterer properties found within the target region.

Target	Sound Speed	Reflection Coefficient
Speckle	1497.0	1.0×10^{-3}
One	1496.2	1.3×10^{-3}
Two	1494.0	2.0×10^{-3}
Three	1490.5	3.2×10^{-3}

6.2.2.3 Speckle Models

To generate speckle producing, incoherent scattering media, random elements were selected within the scattering region of the model. The properties of these scatterers were the same as the background speckle producing scatterers described in the other models. The elements selected within the scattering region were designated as scattering elements, and their acoustic properties were altered relative to the background elements to generate an acoustic impedance. The number of elements selected within the region dictated the number density of the scattering bodies. The number density values selected are included in table 6.4. The resolution cell size is computed from the Gaussian RMS beam width and the pulse length as per section 6.2.1.1.

Table 6.4: Incoherent scattering model properties. The scatterers used in each model were identical, with the only distinguishing feature between models being the number density of scatterers. The theoretical BSC was computed using the individual scatterer properties and their number density using equation (4.68).

	Number density		Theoretical BSC ($cm^{-1}rad^{-1}$)
Model	per unit area (cm^{-2})	per Resolution cell	
One	278	41	1.958×10^{-6}
Two	87.8	13	6.23×10^{-7}
Three	27.8	4.1	1.958×10^{-7}

Table 6.5: Model design Descriptions and hypotheses for the BSC and coherence characteristics. Model categories one and two feature an incoherent media forming a background speckle, within which the targets are placed. The scatterers populating the targets are described relative to those forming the background speckle.

Model Category	**BSC Characteristics**	**Coherence Characteristics**
Hypoechoic	BSC estimates within the hypoechoic scattering targets will be lower than the surrounding speckle.	The spatial variation in backscattering amplitude will reduce the measurement of the coherence when the beam straddles the target boundary. Coherence recovery will be expected for the rectangular target but not for the circular model.
Hyperechoic	BSC estimates within the hyperechoic scattering targets will be higher than the surrounding speckle.	Coherence reduction will be expected on the target boundary. Coherence will be greater than the surrounding speckle when the beamwidth is fully contained within the target. No coherence recovery expected.
Speckle	The backscatter behaviour will fluctuate spatially based on interference between scattered wavefronts.	On average, we expect the coherence function to be triangular in the cases of fully developed speckle.

6.2.3 Analysis Methodology

This subsection will explain the design of the algorithms used to examine the results of the FE simulations. The results of these algorithms constitute the final measured values of BSC, coherence, and RF envelope amplitude.

6.2.3.1 Computing the Correlation Function

To compute the spatial coherence of backscattered waves, the normalised correlation between signals received at different points on the face of the receiver (as reported in sections6.1) was used. The equation is reproduced here:

$$R(m) = \frac{1}{N-m} \sum_{i=1}^{N-m} \frac{\sum_{n=n_1}^{n_2} s_i(n) s_{i+m}(n)}{\sqrt{\sum_{n=n_1}^{n_2} s_i^2(n) \sum_{n=n_1}^{n_2} s_{i+m}^2(n)}}, \tag{6.4}$$

where s_j corresponds to the signal measured by the j'th receive element across the aperture, $n_2 - n_1$ defines the analysis kernel, and N is the maximum lag, corresponding to comparison of elements on the extremes of the receive aperture. Whilst this computation is normally performed through comparison between the transducer elements of an array, this simulated case models the emitting and receiving apertures as lines of point sources and receivers, each separated by an element width. The result of this is that there is a finer spatial sampling of the backscattered waves than would be observed with an array transducer. We are hence able to compute the correlation function for a range of length scales from the point source separation (the mesh discretisation length) up to the full width of the aperture. If this approach were to be taken for an aperture of width w, the correlation function would be evaluated for a range of lags corresponding to length scales (let us refer to them as spatial lags) ranging from $\lambda_0/50$ up to $4\,cm$ (the width of the source) in increments of $\lambda_0/50$. The two issues with this approach are redundancy and time. To address the first point, we expect the coherence of the backscattered waves to vary slowly on length scales much smaller than the wavelength, so we do not require such a fine discretisation of spatial lags. Considering now the

time required to perform the analysis, the number of calculations per lag value and the number of lags we consider are proportional to the number of calculations required, and therefore the time taken for computation of the correlation function. If the spatial separation of the minimum lag distance is reduced, the number of calculations increases exponentially. For this reason, increasing the minimum spatial lag and discretisation of the spatial lag values results in a reduction in the time taken to compute the correlation function for each set of results. It is therefore, advantageous to downsample the matrix of receive signals in the lateral dimension (across the receive aperture). To ensure that the downsampling did not affect the computation of the correlation function, a test case was composed where the correlation function was computed under three different sampling approaches.

1. **Full sampling**: The minimum spatial lag is the length of an element. The wavefront similarity is compared on a sub-wavelength ($\lambda_0/50$) scale across the aperture using all the receiver nodes following application of the receive time-delay profile to the echo data.

2. **Transducer element sampling**: A sub-aperture grouped delay-and-sum operation is performed on the receiver to simulate reception at finite width receivers (receiver width and kerf were set at $\lambda/4$) formed into an array. This approach performs a spatial averaging of the backscattered wave over a small range, and compares these averages across the aperture. Data received from nodes within the 'kerf' region is discarded.

3. **Under sampling**: Following application of the time delay receive profile, the receive aperture is undersampled, considering only individual nodes separated by $\lambda_0/2$. Data received by other nodes is discarded.

To perform the comparison, simulations were performed with an incoherent scattering medium was constructed using the same scatterer properties and number density as was selected for the background speckle producing regions of the models in category

1 and 2. The scattering medium was insonified as described in the previous section, and the backscattered wavefronts received at the source. The coherence function was then calculated using the three sampling methods described above and the results compared over 100 simulations corresponding to different sections of the simulated speckle producing model.

6.2.3.2 Parameterisation of the Correlation Function

On completion of the FE simulation of the wave scattering from each model, the correlation function can be computed for a given receive depth using equation (6.4). In all the cases described here, the correlation kernel length ($(n_1$ to $n_2)$ in equation (6.4)) was set to be one period of the centre frequency of the simulation. Using the minimum spatial lag of $\lambda_0/2$ and the aperture of with $4\,cm$, this results in a correlation function comprised of 26 values (or lags). To parameterise this function, we can adopt the approach developed by Lediju et al. [101], and compute the summation of the correlation function over a given number of lags to generate a single metric of coherence for a given spatial position within the model. The number of lags summed over as a percentage of the receive aperture width is described as the Q value within the work of Lediju et al., who consider only the shorter lags to develop their 'short lag coherence' (SLC) imaging metric. Within this work we will consider the Q value as a parameter by which we assess the performance of coherence as a basis for BSC segmentation, considering larger lag values as well as the short lag values. For this reason, the summation over the correlation coefficient will be referred to as the summed correlation value (SCV), to generalise the parameterisation to the use of higher spatial lag values. The coherence calculation was performed over a range of sample depths, from $1.0\,cm$ anterior to the focal depth up to $0.5\,cm$ posterior to the focal depth, separated by an axial increment of $\lambda_0/50$, equal to the element width dx. The lateral separation of the simulations was $10\,dx$ as described in section 6.2.1.2.

6.2.3.3 BSC and Amplitude Envelope Calculations

In addition to computation of the coherence properties, the BSC for each individual scan line was also computed using equation (6.5) as derived in section 4.2.1.5:

$$\mu_{BS}(\omega) = \frac{S_i(\omega)}{S_p(\omega)} \frac{1}{2\pi\sqrt{8\pi}} \frac{ka/d}{\sqrt{(1 + (\frac{ka^2}{4y_0})^2)}}. \tag{6.5}$$

where S_i corresponds to the backscattered power spectrum from an individual scatterer configuration, S_p to the planar reflector normalisation power spectrum for a 4cm aperture coupled to a line reflector placed at the focal depth y_0, a as the half width of the source aperture, d as the spatial gate length, ω as the angular frequency and k is the wavenumber. The normalisation power spectrum S_p was the same as was determined for the results in chapter 4. The analysis kernel for BSC estimation was set to be 6 periods of the centre frequency of the pulse: equal to twice the length of the excitation signal. This is the same approach as used in chapters 4 and 5. The theoretical BSC was calculated for each model based on the background speckle properties using the equation derived in section 4.2.1.6. This equation is reproduced here:

$$\mu_{BS}^{T}(\omega) = \frac{16k^3 R_s^2 \sigma^2}{\pi} \int_0^2 d\gamma\gamma J_0(2k\gamma\sigma) \left(2cos^{-1}\left(\frac{\gamma}{2}\right) - \frac{\gamma}{2}\sqrt{4-\gamma^2}\right). \tag{6.6}$$

μ_{BS}^{T} is the theoretical BSC value, R_s is the standard deviation of the reflection coefficient of the scattering medium, σ is the scatterer size and k is the wavenumber.

The amplitude envelopes of the backscattered signals were also computed from the generated simulations by calculating the absolute value of the Hilbert transform of the delay-and-sum beamformed receive data. In all cases, the full receive aperture width was used to compute the receive envelope.

6.2.3.4 Target contrast measurements

To assess the contrast of the target regions as assessed by the different imaging modalities, we can calculate the contrast of the targets using the mean pixel value within

target regions and compare this to speckle regions. We can express this as:

$$C = 20\, log_{10}\left(\frac{p_t}{p_s}\right). \tag{6.7}$$

Where p_t corresponds to the mean pixel value in a target region, and p_s the mean value of the speckle region. For all the models, a speckle region was selected that was laterally separated from the targets to compute the speckle mean.

6.2.3.5 The Effect of Noise on Coherence

Since the coherence measures the correlation between two signals, the presence of random noise will affect the coherence value. Unlike physical experiments, the FE simulations presented here do not contain the random electrical noise that one would expect from a real transducer and sample. The presence of random noise will typically decrease the coherence of a signal that itself is not random, due to the introduction of additional, random phase shifts that are unique to each signal. This will reduce the similarity of the two receive signals under comparison, reducing the value of the cross-correlation, and hence the measured coherence. Whilst random noise (as opposed to deterministic speckle noise) typically reduces image quality and complicates segmentation, we would expect the coherence reduction effect to be more pronounced for lower amplitude signals than higher, provided we have a fixed absolute power of noise added to the noiseless signals. As a result, one would expect the contrast of targets which are hypoechogenic to increase relative to the speckle background.

By the inverse argument, for models with hyperechogenic targets (of size on the order of the beamwidth), the addition of noise will result in a smaller coherence reduction for backscattered data from the hyperechogenic regions than the surrounding speckle, which would result in a greater increase in the hyperechogenic target coherence contrast, and a greater reduction in coherence when the target boundary is on the beam axis.

To investigate how noise impacts coherence measurements, noise was added to

the receive data corresponding to each of the simulation results. This generated three version of the simulation results, the original, noiseless data set, and two other version with $-10\,dB$ and $-20\,dB$ zero mean, white Gaussian noise added to the receive data matrix across all receive nodes and sample depths. The noise power was calculated relative to the mean backscattered node power from the speckle region of each model.

6.2.3.6 Coherence Segmentation Algorithm

To perform the coherence segmentation, an understanding is required of the coherence characteristics of a desirable incoherent scattering medium. To do so, a 'ground truth' speckle pattern was computed. This was achieved through simulating the scattering from a incoherent scattering medium over many lateral positions. The properties of this model were the same as the incoherent scattering medium labelled 'One' in the table 6.4. This model was selected as it represents a model that we would expect to produce a fully developed speckle. From the description of speckle as developed by Bamber [165], Mallart and Fink [163] and Verhoeven [166], we state that the backscattering coherence properties of a fully developed speckle pattern should depend on the autocorrelation function of the emit aperture and not on the specific number density of scatterers. For this reason, the selection of a fully developed speckle producing medium as a reference provides the most useful ground truth for application onto other data sets.

In the same manner that many multiple scan lines are required to reduce the dependence of the BSC average on interference effects, representing a convergence of the final estimate onto the value predicted by the number density and individual scattering strength. It was hypothesised that once a sufficient number of scatterer configurations were averaged over, the average BSC value would then converge onto the expected average, and the coherence characteristics would be indicative of the full range of possible backscattered coherence values. Within chapters 4 and 5, 1000 simulations of independent scattering ensembles were generated to produce the BSC estimates quoted. In this investigation, 2000 were generated using the lateral scanning method described

in section 6.2.1.2. The reason for the increased number of simulations was two-fold. Firstly, the lateral scanning approach reduces the statistical independence between the scattering areas in consecutive simulations (due to spatial proximity) when compared to randomly generating the scatterer positions for each simulation. For this reason, an increased number was hypothesised as being needed to ensure that enough statistically independent scan lines were included in the average of the coherence and BSC values. It should be noted that this number is dictated solely by observation of the convergence behaviour of these simulations, and is not a generalisable result, although published results of simulations of this type have employed a similar number of scatterer position configurations in their investigations [99]. On completion of the 2000 simulations, the analysis of the backscattered waves was performed.

Firstly, the BSC, amplitude envelope and coherence function were computed for each simulation, with the coherence value computed by summing the values of the coherence function up to Q% of the aperture for each simulation. Coherence values were computed for a range of depths posterior and anterior to the focal depth, and a mean value was computed for the range of depths, weighted by a Hanning window to place a greater dependence of the average on the coherence values acquired at the focal depth.

On computation of the BSC and coherence value for the ground truth speckle across all the simulation lines, the data set was then segmented using upper and lower thresholds for coherence to establish the contribution of scan lines with different coherence values to the final estimate of the BSC. The upper and lower thresholds were varied between the maximum and minimum lag available for the given Q-value, in increments of 0.1, with the data set segmented by coherence value based on these parameters. Following the segmentation, the remaining data was used to compute a BSC estimate for each pair of threshold values. Repeating this for all the combinations of the upper and lower threshold generated a matrix of BSC estimates for the ground truth speckle data for each coherence threshold pair.

The coherence threshold pairs that minimised the error in the BSC (as compared to the theoretical value based on the statistical estimation of the BSC from the number density and scatterer strengths) were then computed. These values were arranged to form an error minimising line (EML). Since stronger segmentation results in greater losses of data, the points on the EML were categorised by the percentage of data segmented out they represented. The line was only sampled at 9 points corresponding to integer multiples of 10% segmentation strength. Thus, the 'i'th threshold pair stored in the line corresponds to 'i x 10%' segmentation. A number of EMLs were generated under a variety of conditions, using different powers of added noise, a different number of axial kernels over which the coherence function was evaluated, and a set of Q-values.

The threshold value pairs were then used to segment the data sets produced from the FE models described in section 6.2.2. The unsegmented scan lines were then used to compute a BSC average for the whole model, and this was compared to a theoretical value computed from the properties of the background speckle. Application of the coherence segmentation threshold to the incoherent scattering models was hypothesised to remove the coherence outliers that are observed when we analyse the backscatter from a randomly distributed set of identical scatterers. For the hyperechoic and hypoechoic models, it was hypothesised that coherence segmentation would segment both the target regions and coherence outliers in the speckle regions. For all model types, it was hypothesised that discarding regions defined as coherence outliers would improve the final BSC estimate.

To summarise, the analysis methodology for the ground truth speckle pattern was as follows:

1. Ground truth speckle model generated through randomly distributing weak scatterers throughout a section of the simulation domain.

2. FE simulations performed to calculate the backscatter characteristic of the ground truth speckle model.

3. Previous step iterated using the lateral scanning method to capture different sections of the ground truth speckle model.

4. Coherence function calculated for simulation results using equation (6.4). Coherence function parameterised through summation over Q% of the possible lags.

5. BSC computed for all simulations using equation (6.5)).

6. Full data set segmented based on upper/lower threshold pairs of coherence, and BSC computed for remaining data

7. Error minimising line (EML) computed in coherence space.

8. Point on EML applied to unseen data set to segment based on coherence.

These steps are also illustrated in figure 6.9.

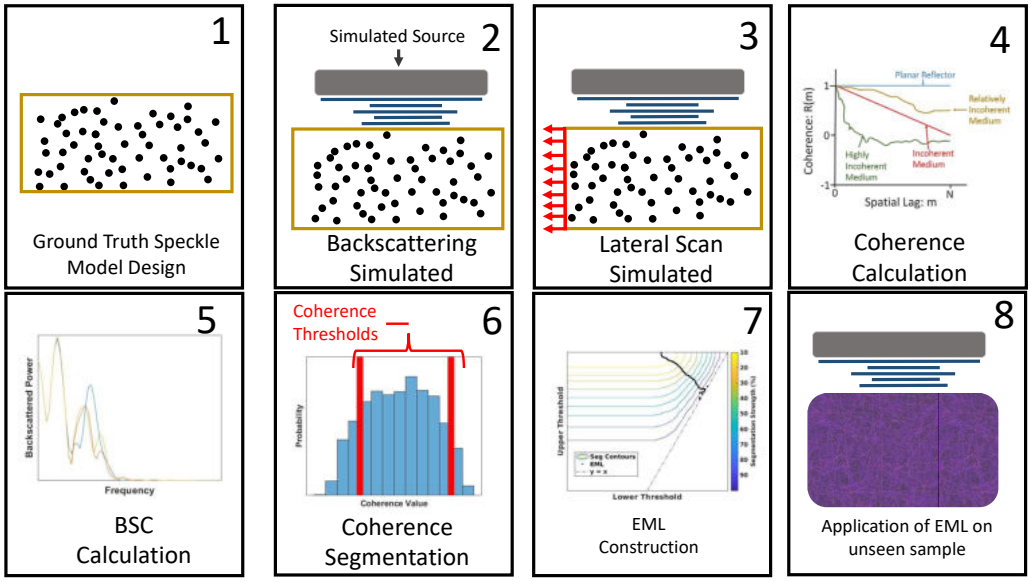

Figure 6.9: Illustration of the calculation and construction of the EML. First, the ground truth speckle model is constructed (1), which backscatter simulations are performed on (2), laterally scanned over a range of the model (3). The backscattered data is then analysed to calculate the coherence (4) and bakcscatter properties (5). Segmenting the data based on the coherence properties (6) and assessing the resulting BSC estimates produced post segmentation allows construction of an EML that generates the best BSC estimates for the ground truth speckle model (7). This line can then be applied to an unseen sample to segment the the data based on its coherence properties.

6.2.3.7 Coherence Algorithm Testing Parameters

As mentioned, a number of test parameters were used to investigate how the segmentation approach varied with parameter selection. These parameters were as follows:

- **Segmentation strength** : The EMLs were sampled at points corresponding to different percentages of segmentation, this approach was taken to assess the effect on the final estimate of the BSC when more or less data was segmented out of the model.

- **Number of axial kernels** : The number of kernels used axially to compute the coherence characteristics was varied to take values of 1, 10, 20, 25 and 50. The axial separation of these kernels is described in section 6.2.3.2. The central axial kernel was at the focal depth in all cases. Including kernels anterior and posterior to the focal depth was used in an attempt to reduce the potential variability in coherence value with depth.

- **Q-Value** : The Q-value was varied to assess how the inclusion of higher spatial lags affected the quantification of speckle texture. EML lines were only reliably generated when larger Q-values were used, so only values of 50% and 100% were considered.

- **Noise** : As mentioned in section 6.2.3.5, random noise plays a part in the measurement of coherence. To test this, three conditions were considered, a noiseless case, a case with $-20dB$ noise added to the simulation results, and a case with $-10dB$ noise added to the simulation results. BSC values were computed before the addition of noise, to prevent the noise confounding the estimate of the backscattered power and isolate the effect on the coherence.

6.3 Results

The results presented here will comprised of two main parts, the first computing the image contrast of the targets using b-mode and coherence based metrics. The second section will analyse the result of the coherence based segmentation on the final BSC estimate.

6.3.1 Results of aperture sampling investigation

A comparison between the computed coherence function at the focus of the source for the three methodologies is shown in figure 6.10. Whilst the single ensemble behaviour was seen to be different between the different methodologies, the average behaviour over 100 iterations was shown to converge, giving an approximately equal mean and standard deviation at all spatial lags. For this reason, the undersampling (method 3) approach was selected: to undersample the aperture and select only the nodes corresponding to integer multiples of $\lambda_0/4$ from the first node of the aperture. We can also note that the three results all converge onto the prediction of the VCZ theorem as interpreted by Mallart and Fink [163] and Bamber [165]: that the coherence function for a rectangular aperture in the far field of an incoherent scattering medium should be a linear function decreasing from 1 at 0 lag down to 0 at the maximum available lag the aperture is able to measure.

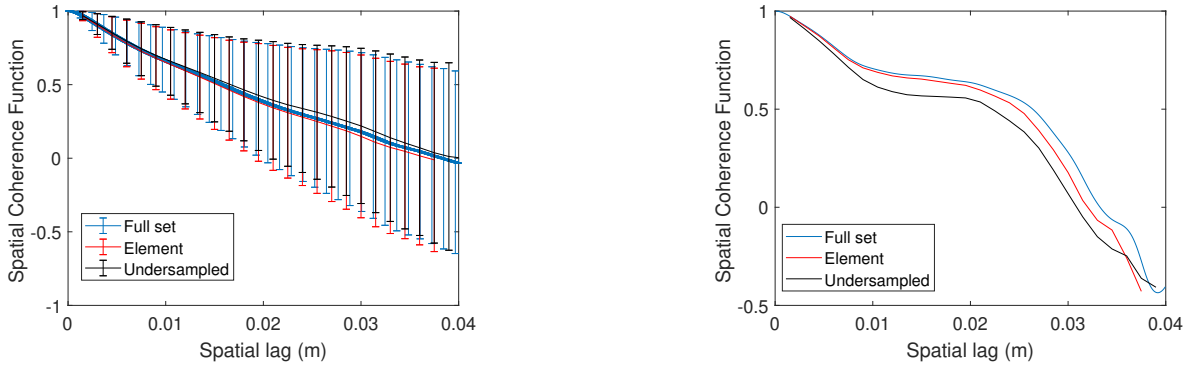

(a) (b)

Figure 6.10: Comparison of the effect of aperture sampling on the coherence function for a single (6.10a) and 100 (6.10b) simulations.

6.3.2 Target Segmentation

6.3.2.1 Example Coherence Images

Considering first hypoechoic circular target 1 (the most hypoechoic), figure 6.11 contains coherence images across three Q-values. A minimum Q-value of 35% was selected as it was the minimum Q-value that provided enough information within the speckle regions for the coherence based segmentation to compute EMLs for all the simulated models. From the images we can see the dark region corresponding to the incoherence generated by the hypoechoic region. The measured coherence value inside the hypoechoic region appears to be close in value to the speckle coherence nulls, but is distinguishable by the fact that the target is more homogeneously incoherent than the speckle region.

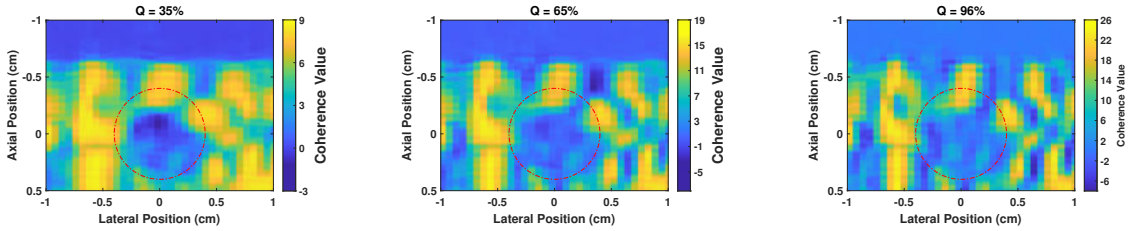

(a) (b) (c)

Figure 6.11: Example coherence images for circular hypoechoic target 1 (circled in red) over a range of Q values. Pixel values correspond to measured coherence by a kernel (of length equal to one period at the centre frequency of the simulation) centred on the pixel position.

The hypoechoic rectangular target results are shown in figure 6.12. Figure 6.12a appears to show a large coherence null throughout the target region, with higher coherence value consistently observed in the surrounding speckle. Over the lags considered in this image, the coherence appears to be maintained on the model boundary, and only decreases when the beam moves past the boundary into the target. Increasing the Q-value to 65% of the aperture width, the coherence on the model boundary appears decrease, with texture starting to appear in the surrounding background speckle. Further increase of the Q-value to 96% increases the speckle texture further, with no

obvious improvement in target delineation.

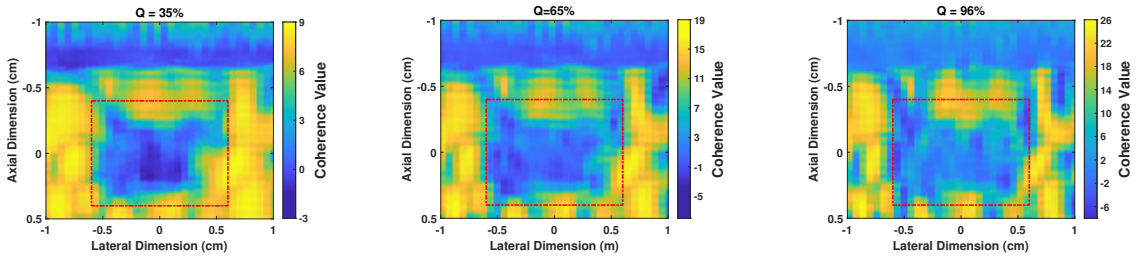

(a) (b) (c)

Figure 6.12: Example coherence images for a rectangular hypoechoic target (red) over a range of Q values. Pixel values correspond to measured coherence by a kernel (of length equal to one period at the centre frequency of the simulation) centred on the pixel position.

Figure 6.13, contains the coherence measurements of the third hyperechoic target. Here the target is not as clearly visible as the hypoechoic targets, with the strongest imaging characteristic appearing to be the regions of high coherence measured on the periphery of the target at the focal depth. The target appears to be slightly more coherent than the background, if only in the absence of the same coherence nulls as observed in the background speckle. This observation matches with the hypothesis presented earlier, that the high amplitude on axis scattering could generate high coherence values when a hyperechoic target is placed amidst a weaker, speckle producing region, but of note is the fact that the high coherence is not maintained as consistently across the diameter of the target as the hypoechoic targets. This suggests that the coherence recovery is quicker in the case of on-axis high scattering than on-axis weak scattering. With respect to the effect of the Q-value, no value delineates the target with notable accuracy, with the most appreciable difference between the images being the increase in background speckle texture.

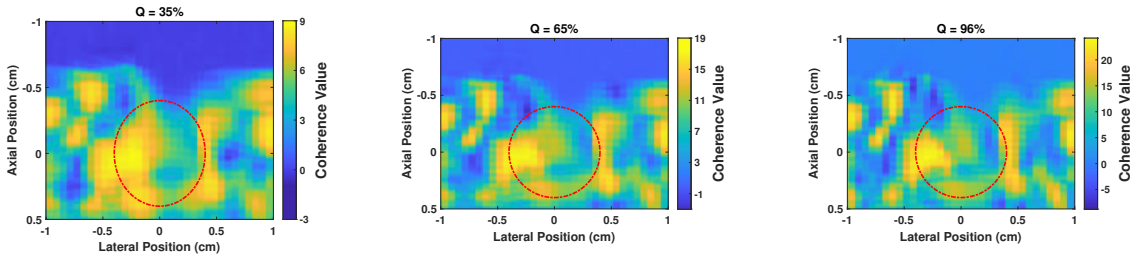

(a) (b) (c)

Figure 6.13: Example coherence images for the third hyperechoic target (circled in red) over a range of Q values. Pixel values correspond to measured coherence by a kernel (of length equal to one period at the centre frequency of the simulation) centred on the pixel position.

To investigate the effect of Q-value on the speckle regions texture, included are results taken from the ground truth speckle data set in figure 6.14. At the lower Q-values, the speckle texture is minimal, with regions of high coherence interspersed with smaller regions of low coherence. The coherence values are mainly concentrated at the higher lags, indicating that the backscattered echoes are very similar on the short length scales considered. Increasing the Q-value, to incorporate higher spatial lags reveals more texture in the images, with the incoherent regions between the coherent patches increasing in size. The greater Q-values incorporated could be seen as analogous to increasing the f-number of the receive aperture.

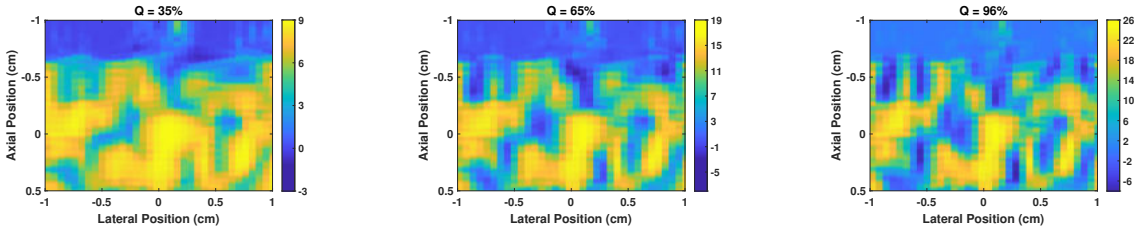

(a) (b) (c)

Figure 6.14: Coherence image texture for a randomly positioned scattering model over a range of Q values%. The colour bar corresponds to the coherence value calculated through summation over Q% of the aperture.

6.3.2.2 Example B-mode images

The B-mode images in figure 6.15 illustrate the backscattering amplitude of the waves from the three targets. We can see the dark and bright regions that correspond to the hypoechoic and hyperechoic targets. It can be noted that there is more visible speckle texture produced from within the hyperechoic target than the hypoechoic – which appears relatively constant within the target boundary, but no further observations can be drawn from this.

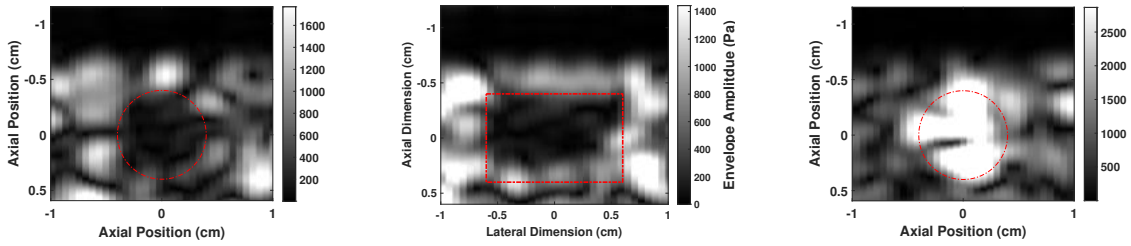

(a) (b) (c)

Figure 6.15: Example b-mode images of the hypoechoic circular (6.15a), hypoechoic rectangular(6.15b) and hyperechoic (6.15c) circular target.

6.3.2.3 Hypoechoic Circle Model: Contrast Measurements

Figure 6.16 illustrates the contrast measurements of the hypoechoic circular target using coherence and backscattered amplitude envelope (which will be referred to as B-mode contrast) measurements. For all the target regions, a greater imaging contrast (more negative) was calculated using the B-mode value as opposed to the coherence value. Of the three coherence Q-values considered, the greater Q-values appeared to result in greater imaging contrast. The effect of noise addition was seen to reduce the imaging contrast (less negative) for the B-mode analysis, but for target 1, was seen to increase the imaging contrast of the coherence imaging for the three Q-values. The observation that only the contrast of target 1 was reliably improved with increased power of added noise did not match the predictions, as it was expected that increased noise should increase the imaging contrast of these targets provided they were hypoechogenic (darker on the

B-mode image) relative to the speckle background.

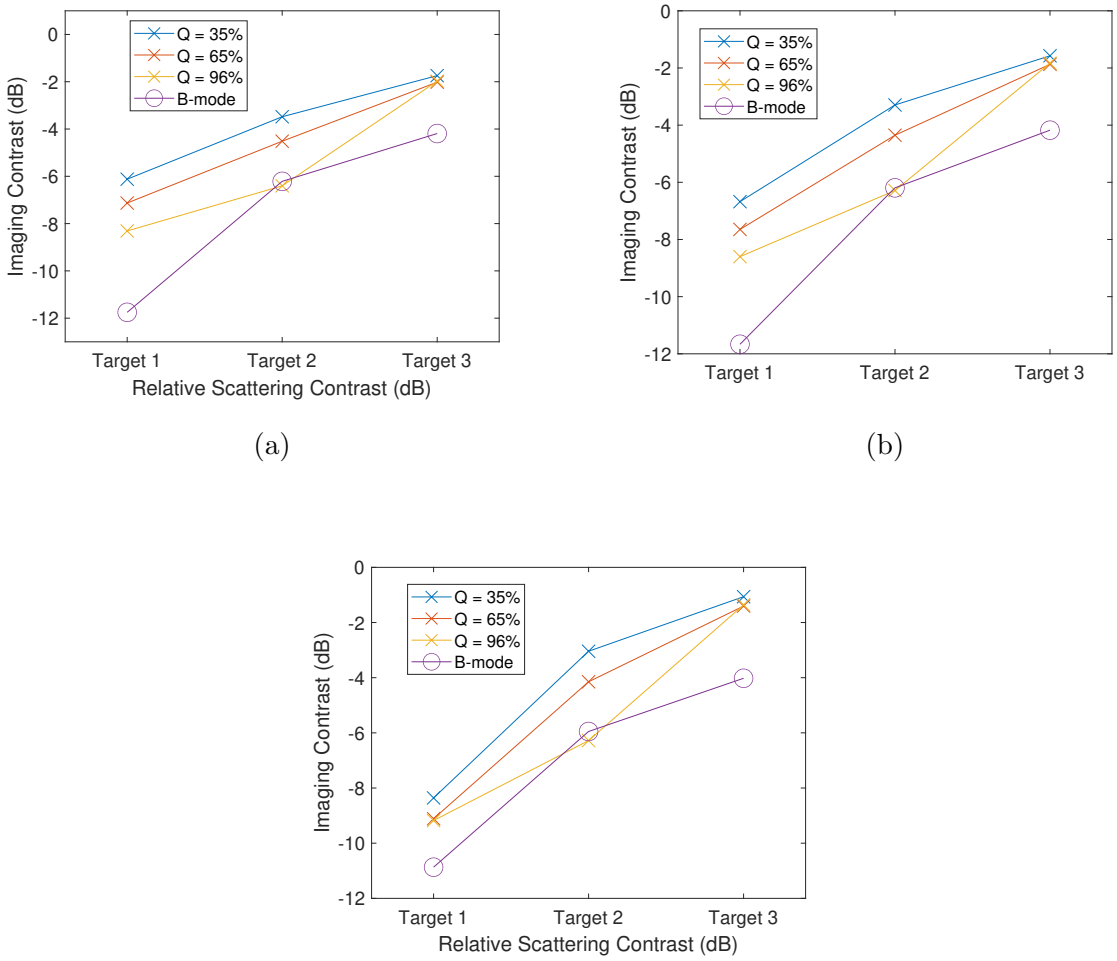

(a) (b)

(c)

Figure 6.16: Illustration of the imaging contrast of the three hypoechoic circular targets in the noiseless (6.16a), -20dB (6.16b) and -10dB (6.16c) noise cases, using coherence image and B-mode image pixel data.

In figure 6.17, the same data set for the hypoechoic circular targets is shown as a function of Q-value for the three noise conditions. Increasing the Q-value was seen to improve the imaging contrast for targets 2 and 3 monotonically, whilst a local minima was observed for target 1 at a Q-value of around 50%. The effect of the addition of noise on the contrast measurement of target 1 is apparent in this figure, and the lack of effect of noise addition on the measured contrast of the other targets also becomes clearer.

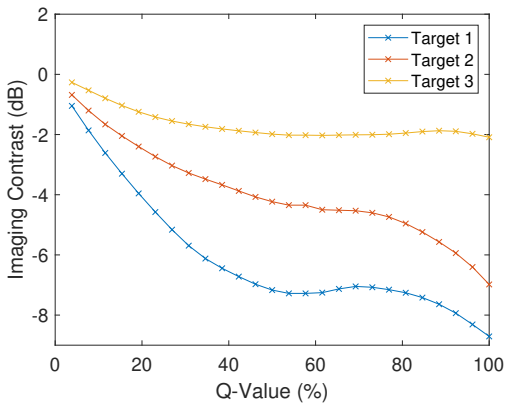

(a)

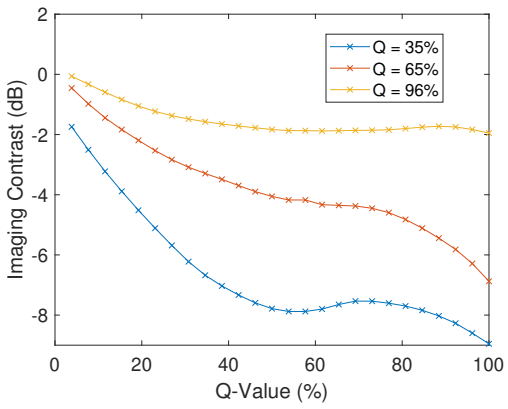

(b)

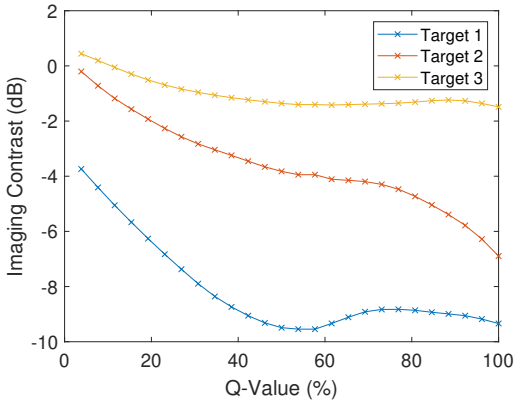

(c)

Figure 6.17: Illustration of the effect of Q-value on the coherence contrast for the three hypoechoic circular targets for the noiseless (6.17a), -20dB (6.17b) and -10dB (6.17c) cases.

Table 6.6 contains the mean and standard deviation of the pixel values within the three targets for the two imaging modalities across the three noise conditions with a Q-value of 96%. This value was selected as it provided the greatest coherence contrast. Firstly, the effect of the target region scattering strength on the coherence within the target regions can be noted: the mean and the standard deviation of the coherence value is lowest within the scattering target that was most hypoechogenic (target 1), and higher for the less hypoechogenic targets (2 and 3). This can be observed by scanning down the table from target 1 to target 3 in any column: the coherence value in the region increases,

and the standard deviation also increases. The speckle regions recorded higher mean and standard deviation in measured coherence than the targets, confirming that low coherence targets (relative to the speckle background) had been constructed. Scanning across the table to assess the effect of noise, it was observed that increasing the power of added noise reduces both the mean and standard deviation of the coherence in the region. With the respect to the B-mode measurements, it was observed that the most hypoechogenic targets produced both the lowest mean backscattered amplitude (as expected), and the smallest standard deviation in this value. The addition of noise increased the measured amplitude envelope, and increased the standard deviation of the pixel value.

Table 6.6: Mean and standard deviation of the pixel values in the target and speckle regions for the hypoechoic circular model. Coherence values (C) were computed through summation over the coherence function using $Q = 96\%$, and are unitless The standard deviation is calculated for the pixels within the target region. The B-mode pixel values (BM) have units of Pa. T. i corresponds to the 'i'th target within the model.

	Noiseless		-20dB		-10dB	
	C	BM (Pa)	C	BM (Pa)	C	BM (Pa)
T. 1	3.98 ± 6.57	222 ± 137	3.70 ± 6.28	224 ± 138	2.93 ± 5.27	248 ± 146
T. 2	4.85 ± 7.34	420 ± 364	4.70 ± 7.10	421 ± 364	3.89 ± 5.82	437 ± 366
T. 3	8.52 ± 8.20	530 ± 385	8.29 ± 8.05	533 ± 385	7.24 ± 7.44	545 ± 384
Speckle	10.83 ± 8.31	859 ± 475	10.38 ± 8.09	860 ± 475	8.60 ± 7.31	866 ± 478

6.3.2.4 Hypoechoic Rectangular Model: Contrast Measurements

Figures 6.18 and 6.19 illustrate the variation in imaging contrast for the three hypoechoic rectangular targets for the 3 noise conditions over a range of Q-values. Here, the contrast of the coherence based imaging was noticeably poorer (less negative) than the B-mode contrast, and also worse than for the hypoechoic circular targets, indicating that the approach is more effective in segmenting targets that are closer in lateral size

to the beamwidth. In the noiseless case, target 3 - which was populated by scatterers of the most similar properties to the background speckle - was segmented particularly poorly. This target was virtually unresolvable from the background speckle by coherence by any Q-value. As with the hypoechoic circular case, the addition of noise was seen to increase the contrast of the targets.

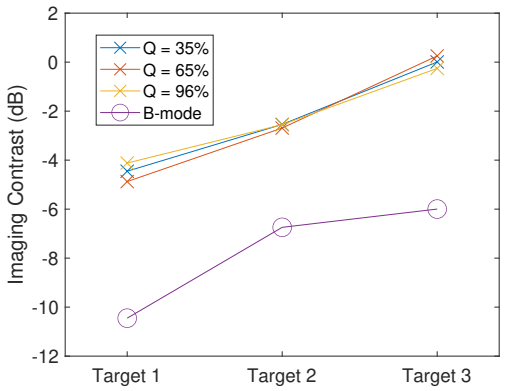

(a)

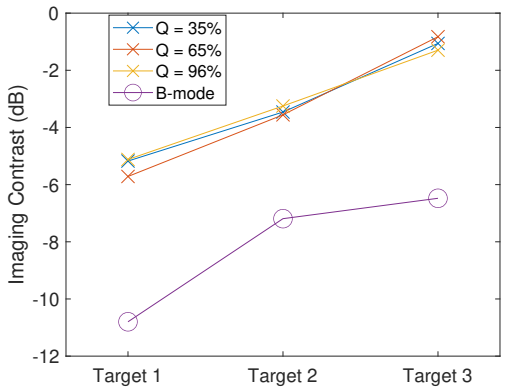

(b)

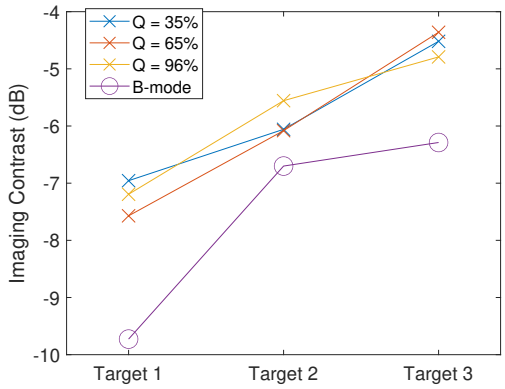

(c)

Figure 6.18: Illustration of the imaging contrast of the three hypoechoic rectangular targets in the noiseless (6.18a), -20dB (6.18b) and -10dB (6.18c) noise cases, using coherence image and B-mode image pixel data.

Figure 6.19 illustrates the contrast behaviour for the rectangular targets over a finer range of Q-values. Within this data set, a lack of contrast across all the Q-values was observed for target 3 in the noiseless case. With the addition of noise, negative contrast

was observed. Targets 1 and 2 produced results more similar to the results in figure 6.17, and both possessed a local minima in imaging contrast at a Q-value of 50%. In both these cases, the contrast was also seen to slightly improve in the $-20\,dB$ noise case, and more noticeably improve in the $-10\,dB$ noise case.

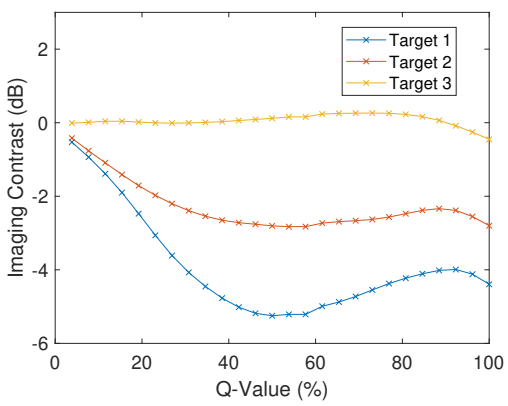

(a)

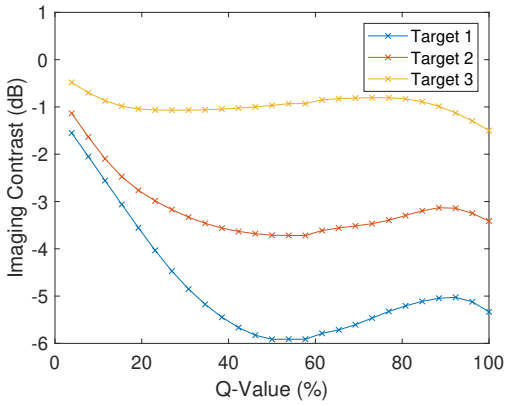

(b)

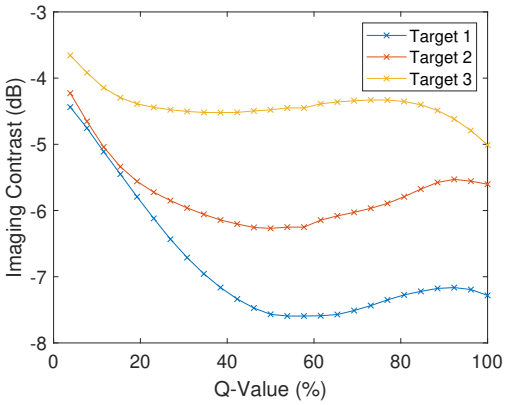

(c)

Figure 6.19: Illustrations of the effect of Q-value on imaging contrast for the three hypoechoic circular targets for the noiseless (6.19a), -20dB (6.19b) and -10dB (6.19c) cases.

Table 6.7 details the mean and standard deviation of the pixel regions used to compute the contrast measurements for the hypoechoic rectangular model. The same observations regarding the effect of the scattering strength of the target relative to the speckle background can be made here. In this test example, the background speckle possessed

a slightly lower average coherence value as compared to the hypoechoic circular model, which may partially explain the reduction in observed coherence contrast in the model.

Table 6.7: Mean and standard deviation of the pixel values in the target and speckle regions for the hypoechoic rectangular model.

	Noiseless		-20dB		-10dB	
	C	BM (Pa)	C	BM (Pa)	C	BM (Pa)
T. 1	5.50 ± 6.96	220 ± 204	4.53 ± 6.25	223 ± 207	2.47 ± 3.8	255 ± 210
T. 2	6.61 ± 7.71	335 ± 331	5.65 ± 6.80	337 ± 331	3.00 ± 4.11	361 ± 330
T. 3	8.66 ± 7.15	364 ± 189	7.05 ± 6.08	367 ± 191	3.21 ± 4.12	378 ± 201
Speckle	9.12 ± 8.37	727 ± 430	8.38 ± 7.93	771 ± 445	5.72 ± 6.00	781 ± 445

6.3.3 Hyperechoic Circular Model: Contrast Measurements

Figure 6.20 illustrates the imaging contrast measured from the hyperechoic targets for the three targets across the three noise conditions. The first target (the least hyperechoic) does not register a positive imaging contrast for any of the coherence or B-mode imaging analysis routines. This indicates that despite the region being populated by stronger scatterers than the background speckle, the variation in pixel value (coherence or brightness value) due to interference effects (speckle) from the random position of scatterers within the region dominated the effects associated with the absolute strength of the scatterers. When the scattering strength in the region was increased (targets 2 and 3), the imaging contrast of all the metrics was seen to increase (more positive). The B-mode image contrast increased most noticeably, suggesting that the absolute backscattering amplitude is more effective at identifying hyperechoic targets than the coherence values. The coherence metrics reported a positive contrast in imaging target 2, indicating that the increased strength (as compared to target 1) of on-axis scattering relative to the speckle background was significant enough to affect the coherence contrast of the speckle and target regions. Target 3 reported the highest imaging contrast

within the B-mode analysis, increasing significantly relative to target 2. The coherence metrics however did not increases universally, only increasing in the noiseless case, and decreasing in the two cases where noise was added to the results. The relationship between the noise and the coherence imaging contrast was more complex than observed with the hypoechoic target regions. The imaging contrast of target 1 registered a slight increase (more positive) in contrast with increased power of noise. This is most noticeable for the $-10\,dB$ noise case, for which the coherence contrast was greater than the B-mode contrast. However, the effect of increased noise was seen to decrease the imaging contrast for targets 2 and 3.

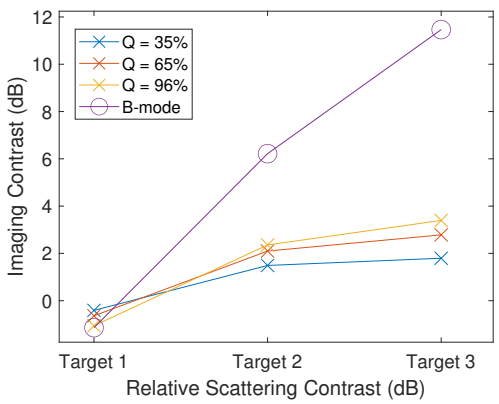

(a)

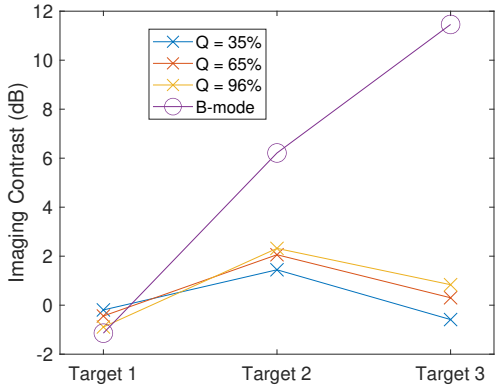

(b)

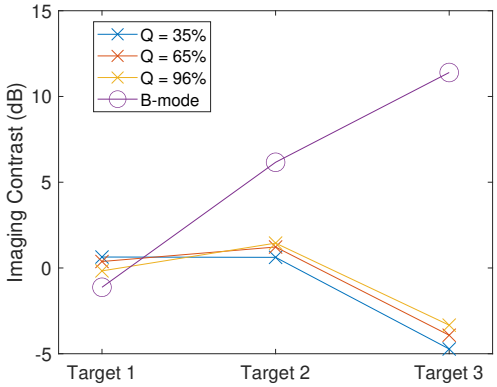

(c)

Figure 6.20: Illustration of the imaging contrast of the three hyperechoic rectangular targets in the noiseless (6.20a), -20dB (6.20b) and -10dB (6.20c) noise cases, using coherence image and B-mode image pixel data.

Considering now the finer discretised Q-value results, it was observed that effect of increasing the Q-value resulted in a reduction (less positive) in the imaging contrast for target 1, whilst it appeared to increase (more positive) the imaging contrast for the other targets. As noticed previously, the effect of noise addition had the greatest impact on the contrast estimation of target 3, which was shown to reduce in imaging contrast as the power of the added noise was increased.

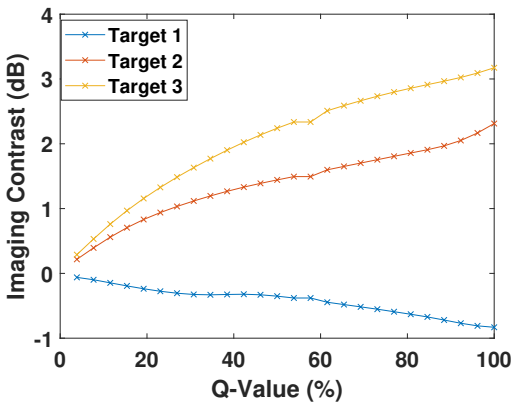

(a)

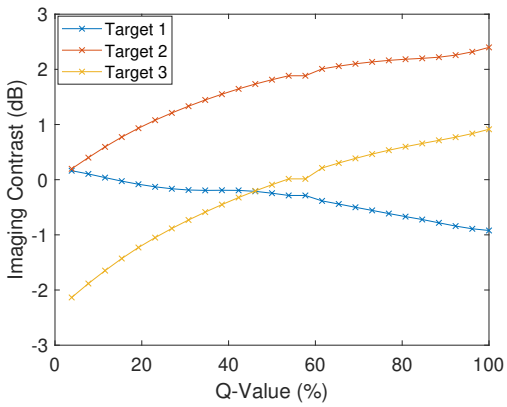

(b)

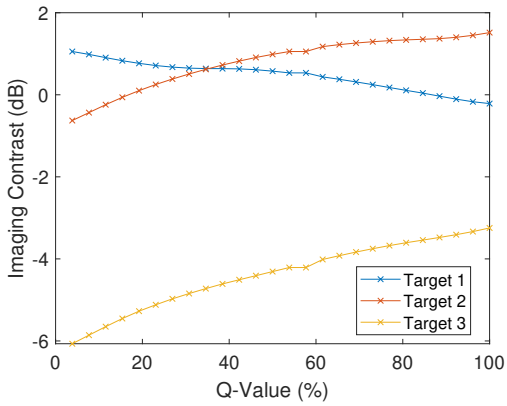

(c)

Figure 6.21: Figures showing the range in contrast detectability for the three hyperechoic circular targets for the noiseless (6.21a), -20dB (6.21b) and -10dB (6.21c) cases.

Table 6.8 contains the pixel values for the measurement of the contrast for the hyerechoic model. Analysis of the Target 1 coherence behaviour across the noise conditions confirms the observations of above: the coherence values registered within the target are not statistically distant enough from those of the background speckle to result in effective delineation, producing low (close to 0) contrast. In all cases, the increase in target scattering strength was shown to increase the coherence value for the pixels within the target region. This matched the design of the model, whereby increased on axis scattering was hypothesised to generate high coherence outliers. The results of this study suggest that these high coherence values are challenging to separate from

background speckle. The addition of random noise (with constant power) across the image was hypothesised to reduce the coherence of the speckle background more than the target regions, and therefore result in an increase in the coherence contrast of the hyperechoic regions. There were no observed results that consistently supported this hypothesis.

Table 6.8: Mean and standard deviation of the pixel values in the target and speckle regions for the hyperechoic circular model.

	Noiseless		-20dB	
Region	C	BM (Pa)	C	BM (Pa)
T. 1	9.7 ± 7.89	732 ± 380	9.48 ± 7.76	733 ± 377
T. 2	14.56 ± 8.34	1709 ± 935	13.90 ± 8.21	1.709 ± 935
T. 3	16.42 ± 6.92	3127 ± 1311	11.71 ± 6.08	3127 ± 1311
Speckle	11.00 ± 8.20	835 ± 448	10.54 ± 7.96	836 ± 448

	-10dB	
	C	BM (Pa)
T. 1	8.09 ± 6.90	740 ± 382
T. 2	9.87 ± 6.58	1712 ± 936
T. 3	5.71 ± 5.56	3127 ± 1313
Speckle	8.29 ± 6.97	842 ± 451

6.3.4 Coherence Segmentation for BSC estimation

Within this section, details related to the behaviour of the ground truth speckle model are first presented, with an illustration of one of the EMLs. Following on from this, the results from the hypoechoic, hyperechoic and speckle models will be presented. Due to the high number of parameters considered within this investigation, the effect of the segmentation was presented in the results section for a set of results with a fixed

Q-value of 100%, and with 50 axial kernels used to compute the average coherence for each lateral scanning position. The error bars presented were calculated through averaging 15 adjacent simulation lines to mimic the construction of BSC estimation kernels across the simulation model. The standard error across the kernels was then calculated and quoted as the uncertainty of the individual segmentation results. In addition to the coherence segmentation, a manual segmentation of the coherence targets for the hypoechoic and hyperechoic models was performed to investigate the contribution of the designed coherence outliers on the average BSC value over the whole model. In the case of the circular targets, this resulted in the manual segmentation of 7% of the lateral area of the model. In the case of the rectangular targets, this resulted in the manual segmentation of 10% of the lateral area of the model.

6.3.4.1 Ground Truth Speckle Model

Results taken from the ground truth speckle model were used to plot the spatial coherence value (SCV) for each simulation using a Q-value of 100% against the estimated backscatter coefficient. This result is plotted for the three noise cases in figure 6.22, as well as histograms to illustrate the distribution of measured coherence values. The results indicate how the addition of noise alters the spread of coherence values. The theoretical coherence value is computed through the summation of the triangular coherence function from a lag of 1 up to the maximum for this aperture size and Q-value (26). From the histograms, we can see that the noiseless model has an average coherence value closest to the theoretical coherence. As the power of added noise is increased, the coherence values reduce and the average moves further away from the theoretical value.

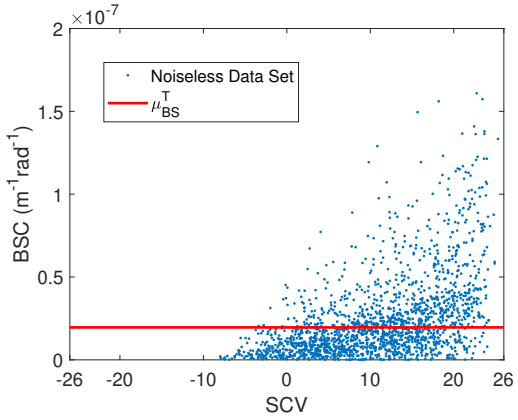

(a)

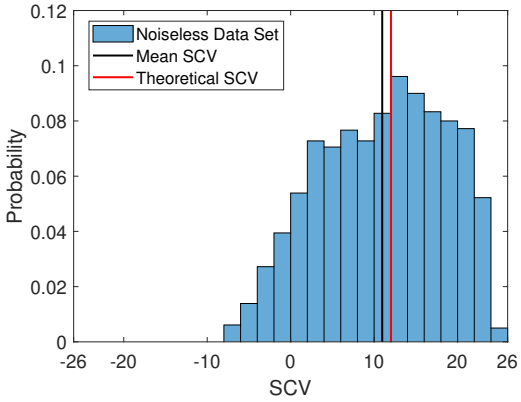

(b)

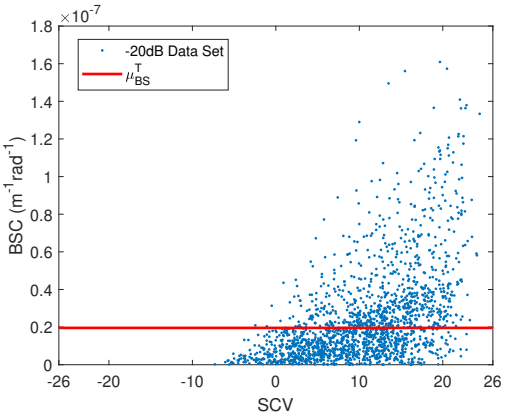

(c)

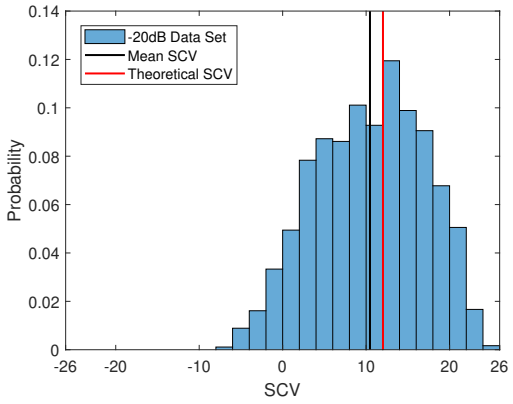

(d)

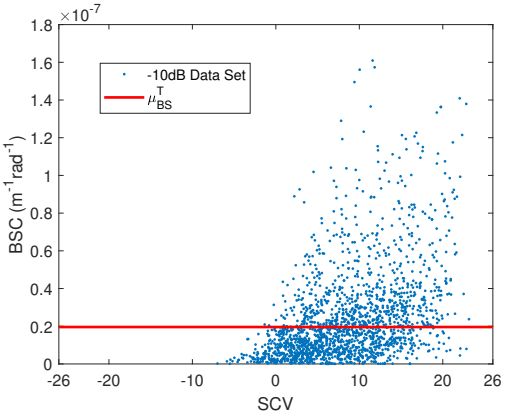

(e)

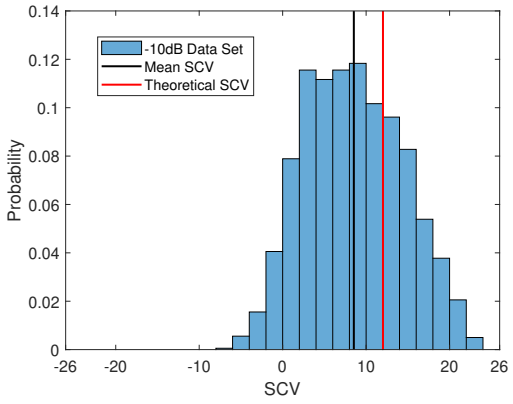

(f)

Figure 6.22: BSC estimate plotted against spatial coherence value (SCV) for the noiseless (6.22a), $-20dB$ (6.22c) and $-10dB$ (6.22e) cases, with the theoretical BSC value for the whole model (μ_{BS}^{T}). Histogram plots for the coherence data sets are plotted in figures 6.22b, 6.22d and 6.22f, with the theoretical and mean SCV value.

From the results presented in figure 6.22, the correlation coefficient between the coherence and BSC value was computed, and recorded in table 6.9. The correlation between the coherence and the BSC value for the speckle data set appears to be maximised under the conditions of $-20\,dB$ noise. Since the segmentation algorithm is attempting to relate the coherence to the BSC, this result would suggest that segmentation of pure speckle regions would be most optimal under this noise condition. For non-speckle regions, due to the relationship between coherence contrast and noise, other noise conditions may result in better segmentation of the data, and better estimates of the BSC. For example in sections 6.3.2.3 and 6.3.2.4, increased noise was shown to result in improved hypoechogenic target contrast. Combining the coherence probability distributions for the three noise conditions produces figure 6.23. The noiseless probability distribution function is seen to be highly right skewed, which becomes more normally distributed as the power of added noise is increased. The reduction in the right skew can be explained by the reduction in the coherence of the echoes due to the added (incoherent noise). This effect will be most prominent for the echoes corresponding to a low backscattered amplitude but a high coherence value (the data points occupying the bottom left quadrants of figures 6.22a, 6.22c and 6.22e). For the data points recorded as possessing a negative coherence value, the addition of incoherent noise has the opposite effect to the positive coherence data points, and will increase their coherence value towards zero.

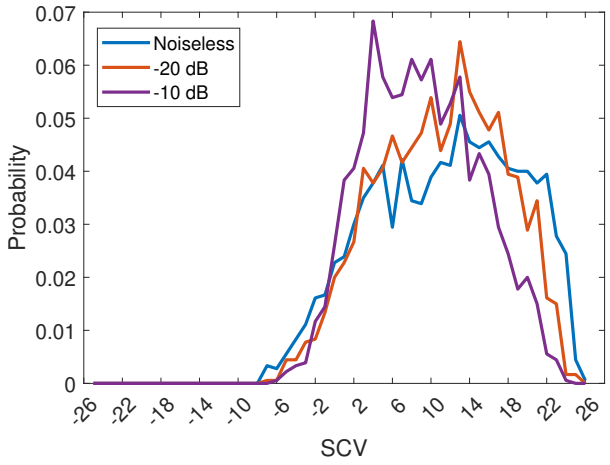

Figure 6.23: Coherence probability distribution functions for the three noise conditions.

Table 6.9: Correlation coefficient calculation for the ground truth speckle data set under the three noise conditions.

Model	Correlation Coefficient
Noiseless	0.4965
$-20\,dB$	0.5088
$-10\,dB$	0.4329

The results of the backscatter analysis of the ground truth speckle model are included in table 6.10. The BSC estimate and the theoretical value were calculated using the methods outlined in section 6.2.3.3. The uncertainty in the BSC estimate was calculated from the standard error on the mean from the estimate, as in chapters 4 and 5. The difference between the BSC estimate and the theoretical value constitutes a 1.4565% underestimate in the BSC as compared to the theoretically derived value. This underestimate is equal to 51.245% of the standard error on the mean.

Table 6.10: Calculation of the BSC properties of the ground truth speckle model

Quantity	μ_{BS} $(m^{-1}rad^{-1})$
Ground Truth BSC estimate	$(1.9290 \pm 0.0564) \times 10^{-8}$
Theoretical BSC	1.9575×10^{-8}

From the ground truth speckle pattern, an EML example is shown in figure 6.24. This example was taken for a Q-value of 100%, which gives a potential range of -26 to +26 from the summation of coherence function.

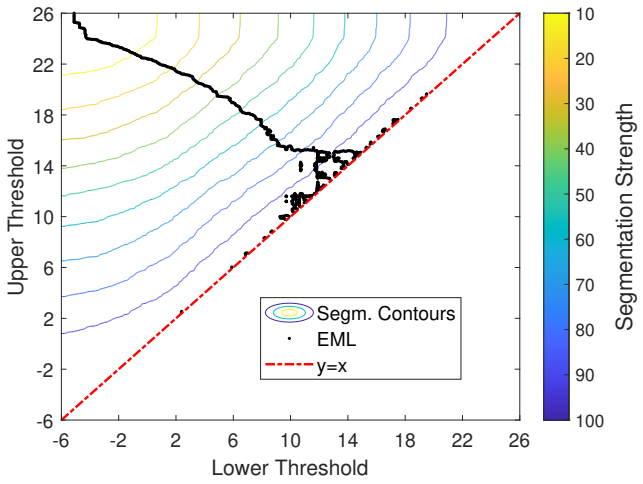

Figure 6.24: EML example pictured as a black line, representing segmentation values minimising the error in BSC estimation of the ground truth speckle model as compared to the theoretical value. The coloured lines represent segmentation contours indicating the amount of data segmented for a given upper and lower segmentation thresholds. Any point for which the lower threshold exceeds the upper threshold results in segmentation of all the data, so the line $y = x$ is included as a visual reference.

The ground truth speckle probability distribution function for the BSC estimates of individual simulation lines is shown in figure 6.25. The left skew of this distribution is indicative of the fact that the incoherent scattering medium is prone to produce values of backscattered power that are relatively small, due to loss in estimated backscattered power from interference effects.

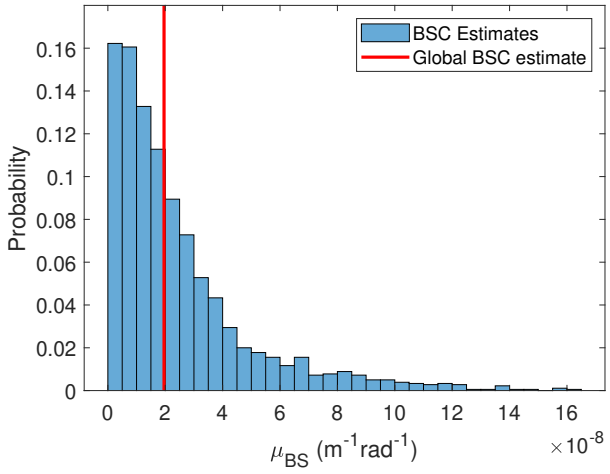

Figure 6.25: Probability distribution function for the ground truth speckle pattern. The BSC is computed for each line, individually using equation (6.5), and the global BSC estimate is computed using the same equation, after averaging the complex power spectra computed from the receive data from each simulation.

6.3.4.2 Hypoechoic Circular and Rectangular Models : Segmentation Results

Figure 6.26 illustrates the effect of the coherence segmentation algorithm for the hypoechoic circular model for the three noise conditions. In the noise-free case (figure 6.26a), a reduction in the error was observed for all segmentation strengths below 70%. For a segmentation percentage above 70%, the estimates were observed to diverge, and the error increased relative to the unsegmented result. In the $-20\,dB$ case, the segmentation was also shown to improve the BSC estimation for segmentation percentages below 30%. Increasing the segmentation percentage above 30% was shown to increase the error relative to the unsegmented result. For the $-10\,dB$ noise case, the results were observed to be more similar to the noise-free case: the segmentation was shown to increase the accuracy of the final BSC estimates for segmentation percentages up to 70% segmentation. Manual segmentation of this data set to remove backscattered data for which the beam axis intersected with the coherence target produced a BSC estimate of $1.99 \times 10^{-8}\,m^{-1}rad^{-1}$, which corresponds to an overestimate in the BSC

by 1.83%. This indicates that the hypoechoic regions reduced the global BSC estimate (across the whole model) by 6%.

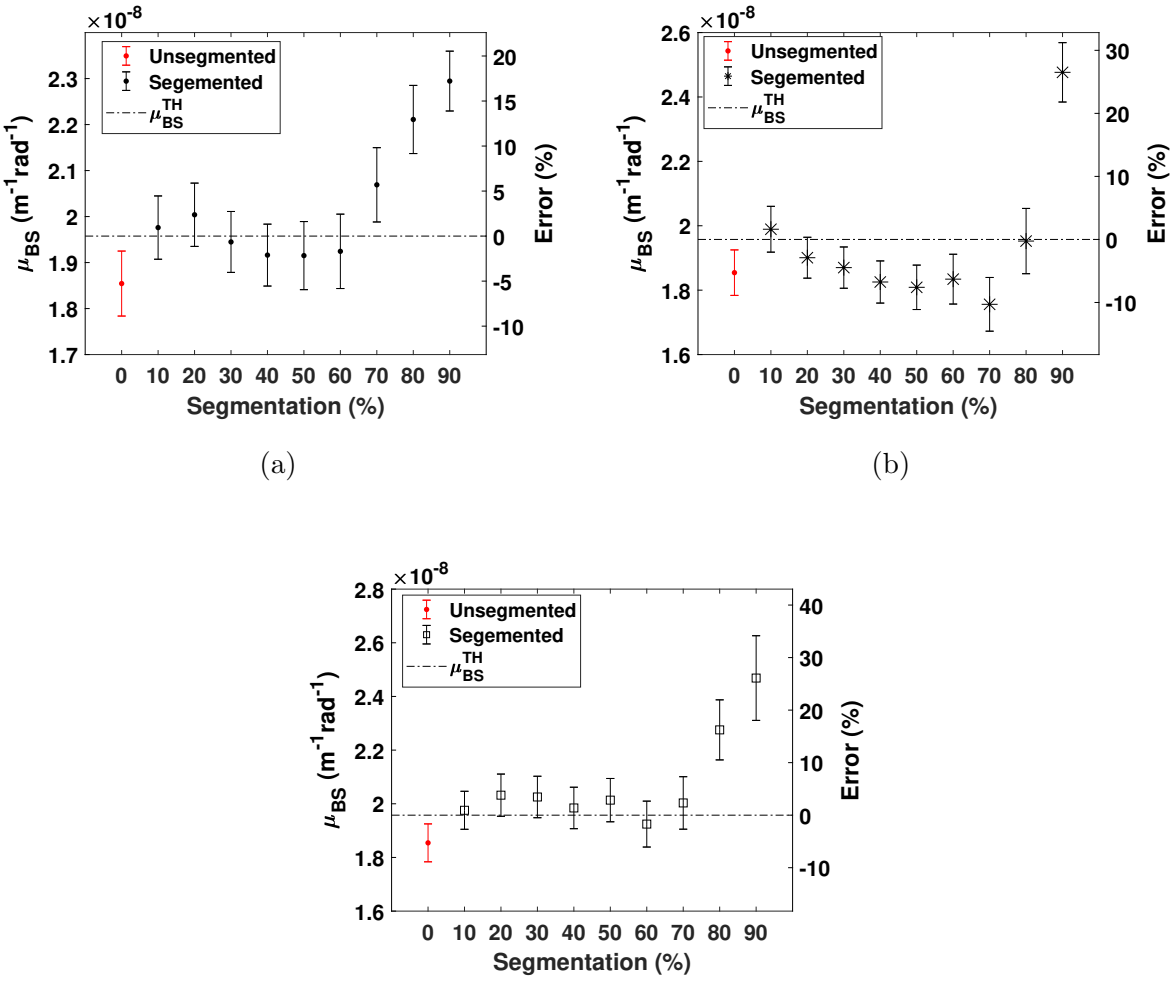

Figure 6.26: Segmentation results for the Hypoechoic circular model. Figures correspond to the noiseless (6.26a), -20dB (6.26b) and -10dB (6.26c) cases. The theoretical BSC value (μ_{BS}^{TH}) is computed from the background speckle properties.

The result of the application of the segmentation approach to the rectangular hypoechoic model is shown in figure 6.27. The noiseless case (figure 6.27a) did not show any improvement in BSC estimate for the calculated segmentation percentages, with the results all shown to exhibit an error of around 25%. Segmentation of the $-20\,dB$ case revealed improvement in the BSC estimate for all segmentation percentages, with the error being reduced to around 15% between segmentation percentages of 10% and

60%, and reducing further with increased segmentation percentage. In the $-10\,dB$ noise case, the error reduced significantly for percentages of 10% to 40%, after which the BSC estimate was seen to continue to increase, producing overestimates of the BSC greater in error than the unsegmented data set for segmentation percentages greater than 70%. The manual segmentation of this data set produced a BSC estimate of $1.74 \times 10^{-8}\,m^{-1}rad^{-1}$, which corresponds to a 10.3% underestimate in the BSC as calculated from the background speckle properties. This indicates that the hypoechoic regions reduced the global BSC estimate (across the whole model), by 13.3%

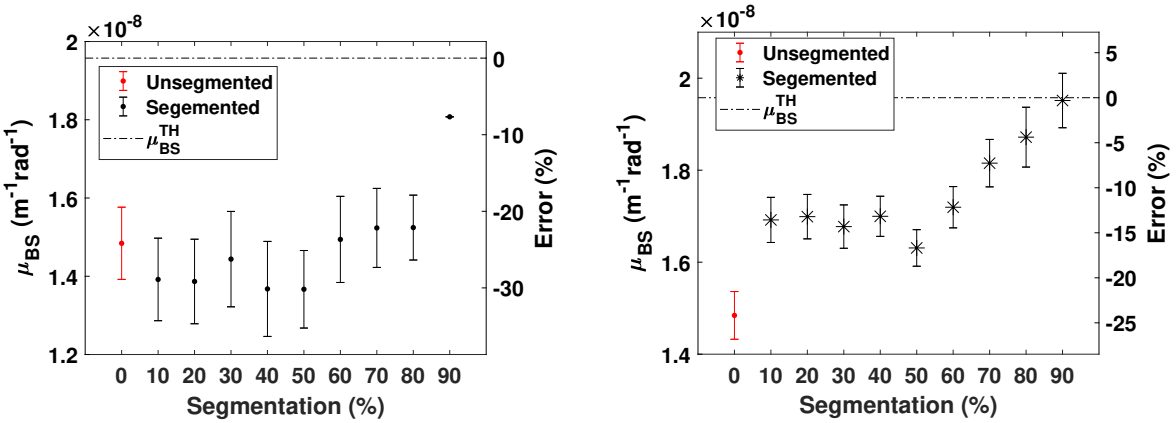

(a) (b)

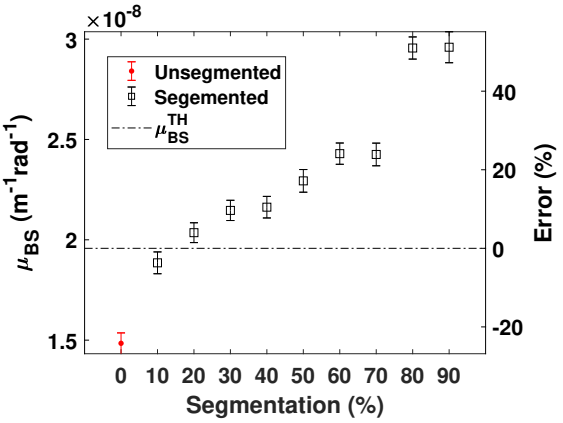

(c)

Figure 6.27: Segmentation results for the Hypoechoic rectangular model. Figures correspond to the noiseless (6.27a), -20dB (6.27b) and -10dB (6.27c) cases. The background speckle was once again used to compute the theoretical BSC value (μ_{BS}^{TH}), which is the same as in figure 6.26.

To illustrates the effect of the segmentation, images were constructed illustrating the points within the model that were segmented for target 1 (the least echogenic) of the hypoechoic circle (figure 6.28a) and hypoechoic rectangular (figure 6.28b) models. These images were created using the results of the algorithm at 10% segmentation strength. They contained the original coherence image, overlaid with the boundary of the coherence target and dark blocks indicating regions segmented by the coherence algorithm. In figure 6.28a, incoherent regions in the centre of the hypoechoic circle were

segmented, as well as a region of high coherence at a lateral position of $-0.5\,cm$ and an incoherent speckle region at $-0.8\,cm$. In figure 6.28b, the segmentation algorithm segmented only four simulation lines within the rectangular region (two at a lateral position of around $0.2\,cm$, and two at around $-0.6\,cm$). A region of high coherence was also segmented at a position of $-0.8\,cm$.

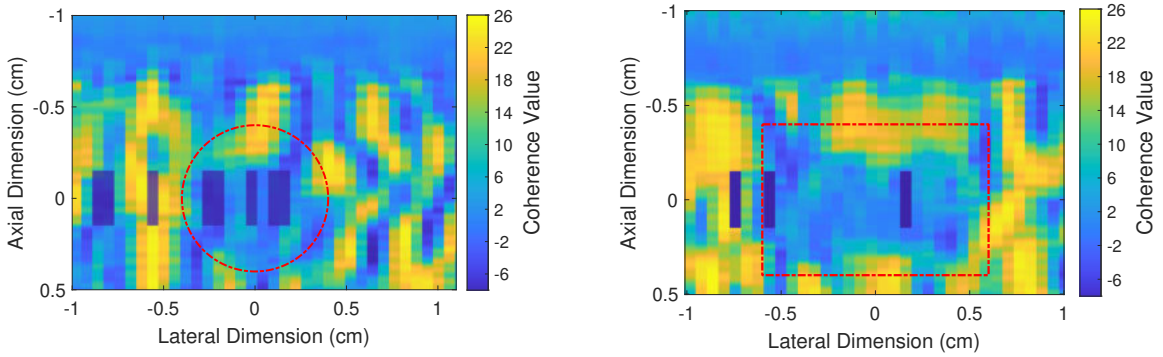

(a) (b)

Figure 6.28: Coherence plots for target 1 of the hypoechoic circular (6.28a) and rectangular (6.28b) simulation models. The target boundaries are outlined in red, with the segmented regions of the model indicated by the dark blocks. The blocks are equal to the coherence pixel width, and measure 50 pixels axially, to reflect the dimensions of the number of kernels used in computation for the segmentation.

6.3.4.3 Hyperechoic Model : Segmentation Results

Figure 6.29 illustrates the segmentation results for the hyperechoic model. In the noiseless case, no significant improvement is observed for any segmentation percentage, with a slight reduction in the overestimation observed at segmentation percentages of 50%-70%. The $-20\,dB$ case was not observed to produce any improvement on this behaviour. The $-10\,dB$ case did show improvement, with a 10% reduction in the BSC estimation error observed for segmentation percentages between 40% and 80%. Manual segmentation of the hypoechoic scattering regions produced a BSC estimate of $1.97 \times 10^{-8}\,m^{-1}rad^{-1}$, which represents an overestimate in the BSC of 0.50%. This indicates that the hypoechoic regions increased the global BSC estimate by 20.9%.

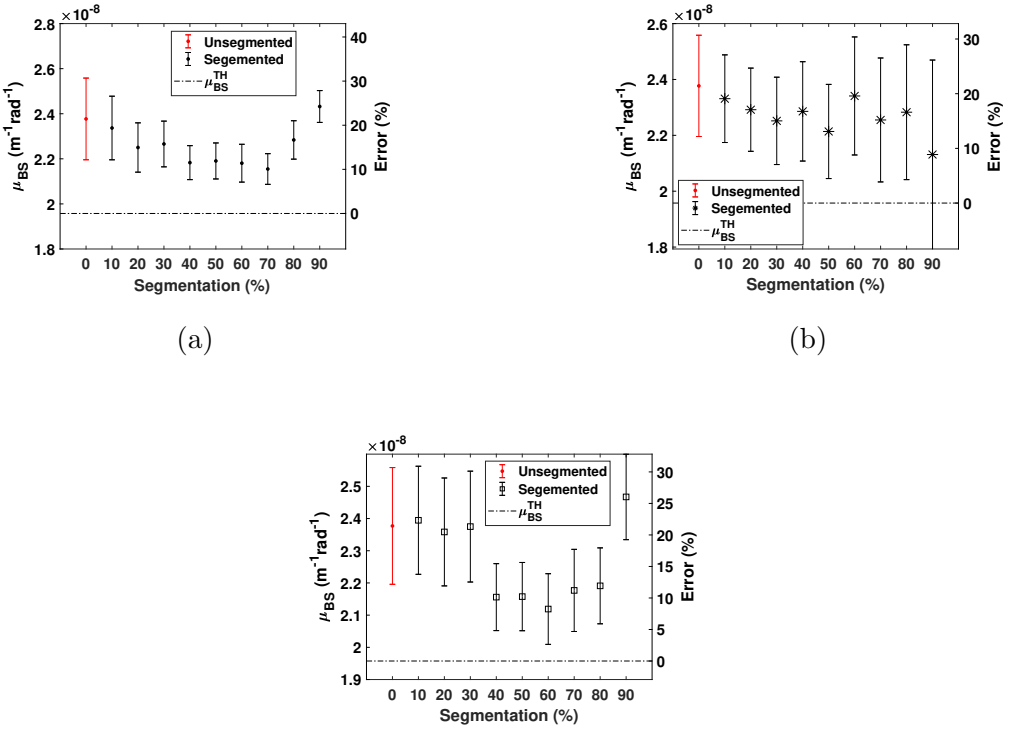

Figure 6.29: Segmentation results for the Hyperechoic circular model. Figures correspond to the noiseless (6.29a), -20dB (6.29b) and -10dB (6.29c) cases. The theoretical BSC value (mu_{BS}^{TH}) as calculated from the background speckle properties was the same as for figures 6.26 and 6.27.

As in figure 6.28, an image was constructed to illustrate the effect of the segmen-

tation algorithm for the hyperechoic model. Once again, a segmentation strength of 10% was used to construct the image. The effect of the segmentation in the vicinity of target 3 (the most echogenic) of the hyperechoic model is shown in figure 6.30. Higher coherence values are expected from the hyperechoic targets, which is reflected in these results, where two regions of higher coherence are segmented from the centre and lateral edge of the target (at $0\,cm$ and $-0.4\,cm$ respectively). In addition, an incoherent region positioned at $-0.7\,cm$ was also segmented.

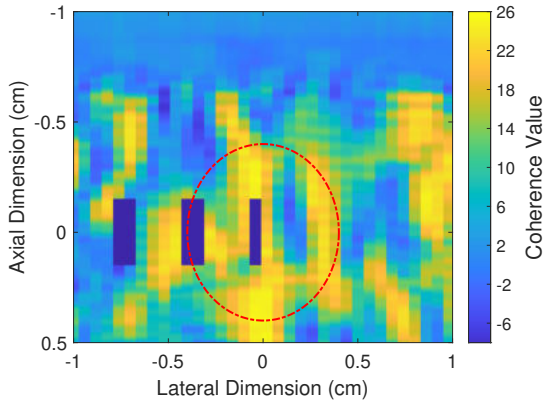

Figure 6.30: Coherence plot for target 3 of the hyperechoic circular simulation model.

6.3.4.4 Speckle Model Results

The final set of results present the analysis of the pure speckle producing regions, in absence of coherence targets. The first case, pictured in figure 6.31, corresponds to a speckle producing region with the same scatterer properties and number density as the ground truth speckle pattern. This result produced highly variable results between the different noise conditions. In the noiseless case, there is a little change in the BSC estimate below a segmentation amount of 40%, at which point the segmentation algorithm produced increased overestimates of the BSC. In the $-20\,dB$ noise case, a consistent decrease in the estimate is observed across all segmentation percentages besides 90%. The effect of the segmentation was to reduce the overestimation in the BSC provided by the raw data, which, between segmentation percentages of 10% and 50%, produced BSC estimates within one standard error of the theoretical value. For

segmentation percentages greater than 60%, the segmentation approach was seen to increase the absolute error on the final BSC estimate. In the $-10\,dB$ case, the coherence segmentation resulted in an initial improvement in BSC estimate between segmentation percentages of 10% and 20%. For segmentation percentages greater than this, the absolute error appeared to increase relative to the unsegmented case.

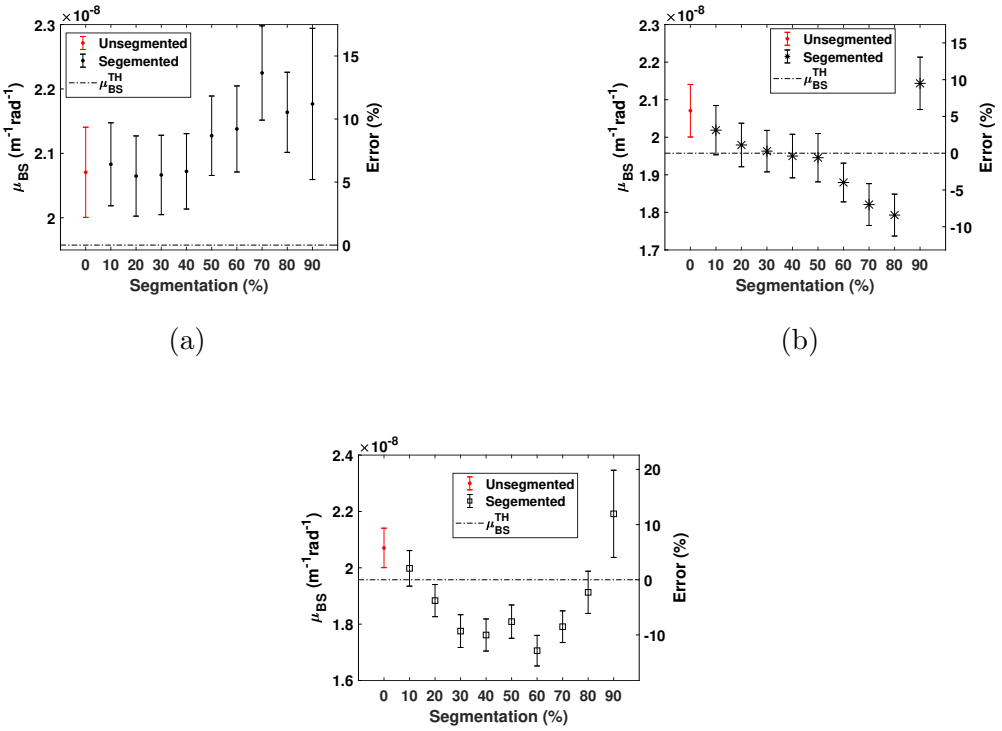

(a) (b)

(c)

Figure 6.31: Segmentation results for speckle model 1. Figures correspond to the noiseless (6.31a), -20dB (6.31b) and -10dB (6.31c) cases.

Figure 6.32 (speckle data set 2) corresponds to a speckle data set we expect to produce a fully developed speckle (14 scatterers per resolution cell), but with a lower number density than the previously discussed case. The unsegmented value for this data set was found to be within a standard error on the theoretical value, presenting a greater challenge to produce an improvement with the segmentation approach. In the noiseless case, little change was observed through the segmentation process being applied, with a stable absolute error observed for segmentation percentages below 70%, maintaining the relatively small error observed in the absence of segmentation, with

divergence in the estimated BSC for higher segmentation values. In the $-20\,dB$ and $-10\,dB$ cases, application of the segmentation algorithm produced relatively consistent decreases in the estimated BSC value for all segmentation percentages, with some oscillation observed at the very high segmentation values.

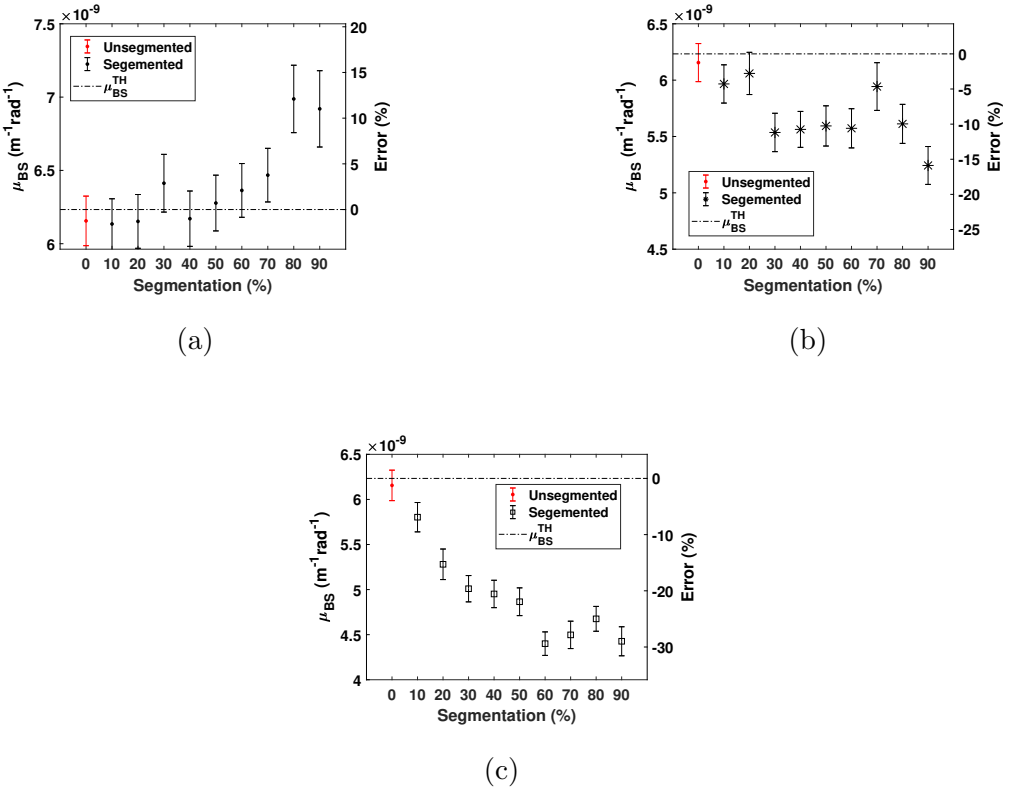

Figure 6.32: Segmentation results for speckle model 2. Figures correspond to the noiseless (6.32a), -20dB (6.32b) and -10dB (6.32c) cases.

Speckle test model 3 was the lowest number density case of the three speckle models, representing an underdeveloped speckle pattern. This data set produced a BSC estimate that underestimated the theoretical value in the unsegmented case. In the noiseless simulation model (figure 6.33a), the segmentation approach was not seen to change the resulting BSC estimate for segmentation percentages between 10% and 40%. A slight improvement was observed when the segmentation percentage was increased above 50%, with small error observed at segmentation percentages of 60% and 70%. Increasing the segmentation percentage beyond 70% was seen to decrease the quality of the BSC estimation. In the $-20\,dB$ (figure 6.33b) and $-10\,dB$ (figure 6.33c) noise

cases, the application of the coherence segmentation was seen to decrease the quality of the BSC estimate in almost all cases.

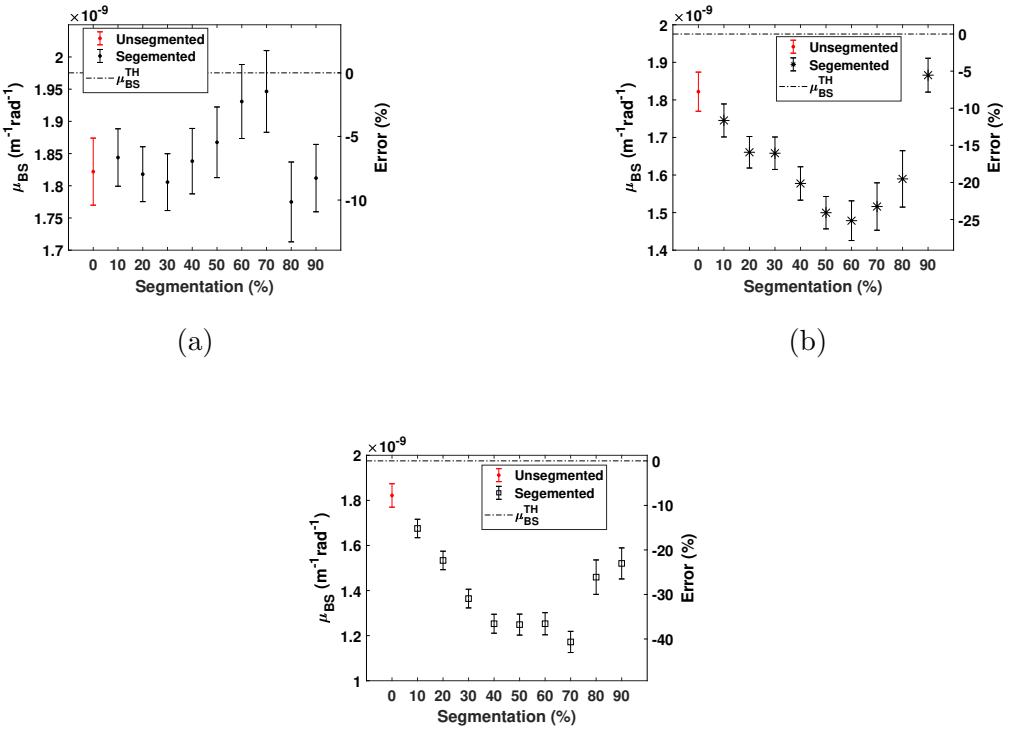

(a) (b)

(c)

Figure 6.33: Segmentation results for speckle model 3. Figures correspond to the noiseless (6.33a), -20dB (6.33b) and -10dB (6.33c) cases.

6.4 Discussion

6.4.1 Contrast Measurements

From the analysis of the segmentation of coherence inhomogeneities, the following observations were made.

Firstly, it was observed that the low coherence targets (the hypoechogenic circle and rectangle targets) possessed greater coherence contrast than the high coherence targets (the hyperechogenic circle targets) relative to the speckle background. Of the low coherence targets simulated, the coherence based approach appeared to be more adept at segmenting the smaller circular targets (that were closer in size to the beamwidth) than the larger, rectangular targets, although it was noted that the background speckle in the hypoechogenic rectangle model was on average less coherent, which will have reduced the contrast measurement. In future work, the use of the same speckle background to compare different coherence targets would provide greater assurance in the results of such a contrast investigation. The Q-values corresponding to the highest contrast for these models was found at 100% in the case of the circular models, and at either 50% or 100% in the rectangular models, depending on the target. The increased ability of the higher Q-values to identify the targets implies that the backscatter of the speckle and the target were similar on the length scale of a few lags, and that higher spatial lags are required to identify targets of this size (on the order of the beamwidth).

Secondly, it was found that the addition of noise improved the coherence contrast in the low coherence models, which was hypothesised to be due to the effect of increasing the incoherence in low backscatter areas (the targets) more substantially than the higher backscatter areas (the background speckle). This result suggests both that the qualitative results of coherence based evaluation of tissue should be categorised by the noise condition. This could present a limitation to coherence based segmentation for BSC estimation, as it introduces another factor (the noise level) that is required to be normalised for in comparing quantitative results. The promising result of this

observation is that it suggests that noise could be added to backscattered data for the delineation of low coherence regions of tissue, which could aid the segmentation of two hypothetical regions differentiated solely by their coherence characteristic.

Thirdly, the high coherence targets were shown to possess a lower coherence contrast relative to the speckle background. This result suggests that an increase in off-axis scattering contributions (as per the incoherent models) results in a greater reduction in measured coherence than reduction in off-axis scattering results in coherence increase. This result is limitation of the coherence based segmentation presented, as it implies that the approach is more sensitive to regions of low coherence than high coherence. The counter-argument to this point is that the only tested conditions involved increased coherence through the design of strong off-axis scatterers, and that the methodology may be as adept at identifying high coherence regions not formed of highly echogenic scatterers. Such a region could represent a high backscattering strength purely due to the structure of the associated scatterers.

Fourthly, it was observed that the backscattered amplitude provided a greater measure of contrast between the background speckle and target regions where the target and background speckle pixels were manually selected. This result may have been expected, since the coherence targets were generated through altering the strength of scattering. This represents a limitation of the design of this study. Future work should consider the construction of scattering regions that generate high levels of coherence through structure as opposed to the scattering strength of the individual scatters. Structures such as these may prove as echogenic as surrounding speckle in a B-mode image, but differ in coherence characteristics.

6.4.2 Coherence Segmentation of Low Coherence Targets

From the segmentation of the hypoechoic models based on their coherence properties, the coherence based segmentation was seen to increase the accuracy of BSC estimates most effectively where low percentage segmentation was implemented. Application of

the segmentation algorithm to implement a 10% reduction in the number of averaged simulation lines was shown to reduce the error in BSC estimation measured in the hypoechoic circular and rectangular models under all three noise conditions, and reduce the error for the rectangular model in the cases where noise was added to the simulation. The reason for the greater accuracy of segmented BSC estimates at the lower segmentation percentage can be hypothesised to be due to the size and backscattering properties of the coherence targets. In the hypoechoic circular and rectangular models, the coherence targets accounted for 7% and 10% of the model area respectively, and - through manual segmentation of the targets - accounted for most of the discrepancy between the theoretical BSC and the unsegmented BSC estimate. This implies that the simulated background speckle was in high agreement with the theoretical model of the incoherent BSC, or else the error contribution from the background speckle regions would have been greater. This resulted in the accuracy of the segmentation process being dictated by the efficacy with which the coherence targets were segmented. This observation is an indication of why the post-segmentation estimates of the BSC from the hypoechoic rectangular models were found to be poorer than the circular models: the unsegmented results represented a greater underestimate of the BSC due to the greater spatial extent of the coherence targets (as indicated by the quoted error from the manual segmentation and unsegmented BSC estimate) and the targets themselves had reduced contrast relative to the speckle background (as shown from the evaluation of the rectangular target contrast). The aim of the segmentation algorithm was to present a tool to segment regions based on their coherence, irrespective of whether the region was speckle or coherence target in its design, and the outcome bias towards segmentation of the target regions (due to their high inhomogeneity in BSC), is a limitation of this study. Future work should consider attempts to model tissues based on measured tissue structures to assess whether the models here represent realistic inhomogenieties.

6.4.3 Coherence Segmentation of High Coherence Targets

Considering now the hyperechoic circular model, it was observed that the coherence segmentation either maintained, or slightly improved the quality of the final BSC estimate across all the considered noise cases. As identified with the previous models, the main constituent of the error was the coherence target, from which it may be observed that, once again, the theoretical value of the BSC as computed was accurate to the simulation model. In addition, if we assume that the segmentation algorithm was sub-optimal in segmenting the high coherence regions (an assumption based on the low contrast measurements), then it would be logical that the maintenance of the BSC esimtates observed for this model corresponds to a segmentation of the background speckle based on the ground truth speckle characteristics that did not substantially change the BSC. The relatively small changes in the BSC estimation error (even at high segmentation percentages) would suggest in that case that the background speckle was - to an extent - tracing the path of the EML, maintaining the same contribution to the global BSC estimate whilst being segmented. If this were to be true, it would suggest that the background speckle was behaving with the same coherence-BSC characteristics as the ground truth speckle. This would imply that the ground truth speckle model characteristics could be applied to other, speckle based models.

6.4.4 Coherence Segmentation of Speckle Models

6.4.4.1 Speckle Model 1

We first consider speckle model 1. This model was comprised of scatterers with the same properties and number density (41 scatterers per resolution cell) as the ground truth speckle model and produced an unsegmented BSC estimate that was an overestimate of the theoretically predicted value by 5%. Unlike the coherence target models, this overestimate must be attributed to interference effects generated by the random positioning of the scattering elements. The aim of the coherence segmentation algorithm in this case is to segment the naturally occurring coherence fluctuations to improve the

final BSC estimate.

Turning our attention to the noiseless simulation, it was observed that the unsegmented overestimate in BSC was not noticeably changed by the application of the coherence segmentation. The BSC estimation error remained constant up to a segmentation percentage of 50%, at which point the error absolute value of the error was seen to diverge. Using the arguments presented earlier, we can hypothesise that the relative stability at low segmentation percentages corresponds to the scattering model moving along the EML as developed from the ground truth speckle model. The divergence in the estimate for higher values can then be attributed to the variability associated to the relationship between the coherence and BSC. Divergence at higher segmentation percentages in the models with coherence targets could have been attributed to the segmentation of regions within the target that represented large BSC outliers, but in the case of the speckle models, we assume the model is statistically homogeneous. In this cases, it is hypothesised that the relatively fewer data points make the final BSC estimate more sensitive to individual outliers in BSC that occur naturally. Since the relationship between coherence and BSC is not monotonic (as seen in figure 6.22), individual outliers with median coherence but extreme (relative to the distribution of values) measures of BSC can be hypothesised to have a larger effect on the eventual BSC estimate. This is most apparent when we consider the probability distribution of the ground truth speckle pattern in figure 6.25. The right skew of the distribution indicates that the majority of the BSC values from the simulation lines are low in value, with few large estimates. As the segmentation reaches higher percentages, the addition of one of these higher values will have a greater effect on the overall BSC estimate. Considering now the $-20\,dB$ case, the segmentation algorith was seen to improve the BSC estimation accuracy consistently up to segmentation percentages of around 50%. Further segmentation resulted in divergence of the BSC estimate. The $-10\,dB$ case also improved the absolute BSC estimate error for a segmentation of 10%, but the results diminished in quality with further segmentation.

Considering the three noise cases together, it is not immediately apparent why the 10% segmentation resulted in improvements for the noisy cases but not for the noiseless case, but a potential hypothesis may be presented. Firstly, it is noted that the EML that dictates the segmentation thresholds is based on a larger data set than the test cases. In addition, the threshold values divined from the EML are computed on a mean basis, i.e. how the effect of the segmentation affects the mean BSC produced. Thirdly, we note that the BSC probability distribution is highly left skewed. To explain the observation that the application of the coherence segmentation algorithm to these data sets in the presence of noises causes reduction in BSC estimate, it is therefore hypothesised that the BSC estimate produced from the ground truth speckle pattern is less sensitive to high BSC data points than the test data sets. This hypothesis is predicated on the fact that the EML that dictates the segmentation parameters is a reflection of the mean BSC estimate from the ground truth data set. As we have noted, the left skewed nature of the probability distribution means that the segmentation of one high BSC data point will have less of an effect on the BSC estimate than the equivalent segmentation applied to a smaller data set. In the noiseless case, segmentation of high coherence data points is performed on a slower basis for a given segmentation percentage, due to the right skew of the coherence probability distribution function (figure 6.23), but for the noisier cases, the upper threshold of coherence segmentation will be lower for a given segmentation percentage, and the effect of segmenting high BSC data points will be more pronounced. If this effect were manifest in this data set, it would represent a limitation of the segmentation approach, as identical sized data sets would be required for the ground truth data set and the test sample. This would be in contradiction to the design of the approach, whereby a large test data set is used to cover a wide range of potential backscattered coherence values. The obvious limitation to this presented hypothesis is that a similar effect is not observed in the aforementioned models where coherence outliers are included in the simulation domain.

6.4.4.2 Speckle Model 2

Whilst speckle model 1 could be considered as a sub population of the speckle producing medium from which the ground truth data set and the EMLs were computed, speckle model 2 represents the first application of the segmentation approach on an incoherent scattering medium possessing different statistical properties. Both speckle models 1 and 2 were expected to produce fully developed speckle characteristics. For this reason, the testing of speckle model 2 using the coherence characteristics the ground truth speckle model constitutes a test of the theory that fully developed speckle patterns should exhibit coherence characteristics dependent on the emitted beam auto-correlation function and the receive aperture characteristics.

The results of this investigation possessed similar characteristics to those observed for speckle model 1. In the noiseless case, the absolute error was shown to be maintained up to around 50% segmentation, at which point the result was observed to diverge. This divergence was attributed to the same mechanisms as were outlined to describe the divergence of the speckle model 1 results. When noise was added to the simulated data, the result was observed to reduce the efficacy of the segmentation appraoch. In the $-20\,dB$ case, the estimation accuracy in the BSC was observed to reduce for all segmentation percentatges, particularly after 20% segmentation. In the $-10\,dB$ case the reduction in accuracy was even more apparent, with the estimation accuracy decreasing with increased segmentation percentage. As with speckle model 1, the discrepancy in the accuracy between the noiseless and noisy cases is not understood.

6.4.4.3 Speckle Model 3

Speckle model 3 represented an underdeveloped speckle case, with fewer than 10 scatterers per resolution cell. The backscattered coherence characteristics were therefore not expected to match those of the fully developed speckle cases presented in speckle models 1 and 2. With fewer scatterers contained within the resolution cell, the echoes were expected to be more coherent in nature, which one would expect to result in a

different response to the application of the segmentation algorithm. Despite this, the behaviour of this model was notably similar to the previously discussed. In the noiseless case, the segmentation algorithm maintained a constant estimate in BSC, before segmentation percentages above 50% caused divergence in results (once again attributed to the relationship linking coherence and BSC value). In the $-20\,dB$ and $-10\,dB$ cases, the results resembled that of speckle model 2, whereby increased segmentation resulted in increasing underestimates of the BSC.

6.4.5 Future Work

Future work that could improve the contrast as measured by the coherence characteristics would be to employ a more regional based approach to the segmentation. Within the coherence images of the simulated models, the coherence targets were visible, and yet the ability of the algorithm to segment them effectively (as shown by figures 6.28a 6.28b and 6.28b) appeared low. The design of the algorithm was such as to allow the segmentation of both speckle regions of high/low coherence as well as the target regions, but in the simulated models, the high dependence of the accuracy of the final result on target segmentation indicates that prioritising segmentation of the target regions would have produced more accurate outcomes. To this end, an approach that attempted to connect regions of high or low coherence found in proximity to one another may have improved the final result. In future work, the adaptation of the algorithm to connect local coherence features that could be indicative of structure might provide better target segmentation, improving the final BSC estimate.

As an extension of this, the segmentation algorithm could be redesigned to - instead of axially averaging coherence values to generate one average per simulation line - to perform the segmentation to generate confidence values for pixels within the coherence image based on their coherence value. The combined confidence of the pixels within an axial line could then be used to produce a weighted average of the values to generate the BSC estimate. This approach would result in discarding of data, and would generate

a regional map of values displaying confidence in the BSC estimate acquired from the region.

As previously mentioned, future investigation into the applicability of this approach should be concerned with ensuring that the modelled coherence or BSC outliers are representative of those that would be found in soft tissue. Since the motivation for developing this approach is to improve BSC estimates for tissue characterisation, it is imperative that the algorithm be tested against structures that be expected to occur in the proposed sample to be analysed.

To increase confidence in the utility of this approach, it should also be compared against other segmentation approaches. In this work, the coherence contrast of the targets was compared to the B-mode image contrast through the averaging of the pixel values within target regions. To provide a measure of the utility of this approach, the effect of segmentation by other such metrics should be performed, in order to establish confidence that the coherence is a viable metric for the segmentation of the BSC data.

Whilst maintaining within the sphere of simulation based investigation, it would be useful to repeat the described experiments with different emit and receive apertures, to assess how the f-number of the simulated source (in both emit and receive mode) affects the results.

To apply this approach to real samples and transducers, a primary investigation should be conducted to test the viability of the segmentation algorithm to a test sample such as a phantom. The EMLs generated for the data sets presented within this chapter will be specific to the emit and receive aperture of the simulated source, and - to an unknown degree - the ground truth speckle data set, so application of this concept will require significant investigation to assess its feasibility in a non-simulation based experiment.

Lastly, given the large number of parameters considered within this investigation, including - but not limited to - the Q-value, the number of axial kernels used in averaging, the noise condition and the segmentation strength, it would present an interesting

challenge to assess using a multi-variate approach. Robust PCA has been proposed for the analysis of coherence imaging over short lags[168], and the high dimensionality of the parameter space suggests that such an approach could provide greater insight into the observed variability of the results.

6.5 Conclusion

To conclude, this chapter has presented simulation models with spatially imposed variation in coherence and BSC value, which was then used to test the feasibility of BSC data segmentation based on echo coherence.

To investigate this, tests were performed to investigate the coherence contrast of simulated targets. This was performed through the simulation of a backscatter experiment of a sample containing a speckle producing background region and regions with altered coherence and BSC contrast. The contrast of these regions was measured using coherence and B-mode image brightness metrics. The three contrast regions were as follows: a circular, low coherence and backscatter region of similar size to the beam width; a rectangular low coherence and backscatter region larger than the beam width; a circular high coherence and backscatter region of size similar to the beamwidth. The investigation revealed that the coherence was most adept at segmenting the circular, low coherence target of size similar to the beam width. The measured contrast was observed to increase in the presence of noise, and with the number of spatial lags used to calculate the coherence value for a given position. Reduced contrast was observed in the segmentation of the larger, rectangular incoherent target, indicating that the spatial extent of the coherence target had a detrimental effect on the ability of the coherence metric to segment this region. Once again, target contrast was improved through the addition of white, Gaussian noise, and through the incorporation of higher spatial lags in the coherence evaluation. The contrast was poorest for the high coherence target, where the target exhibited little contrast in the coherence image. For this case, the addition of noise or higher spatial lags did not result in an improvement in the results.

Following this investigation, an algorithm was described by which the model would be segmented based on the coherence characteristics of a ground truth data set that was designed to be representative of an ideal speckle pattern for BSC estimation. Through calculation of segmentation thresholds that minimised the error between the BSC estimate of the ground truth data set and a theoretically determined BSC value, an error

minimising set of coherence segmentation parameters were developed for application on unseen data sets.

The segmentation parameters from the ground truth data set were then applied to results acquired from backscatter simulations of a set of models. Three of the models contained background speckle producing regions and coherence outliers which represented targets for segmentation. Three more models were produced of speckle producing media, to test the ability of the model to segment the echoes produced from an incoherent scattering media and improve the associated BSC estimate produced. These three models were distinguishable by their number density, which was hypothesised to alter their coherence characteristics, thereby testing the ability of the algorithm to improve the BSC estimate for an unseen speckle region.

Implementation of the segmentation algorithm on the six data sets produced a mix of results. BSC estimates calculated from models containing low coherence targets were mainly shown to be improved through the application of the segmentation routine in cases where the segmentation percentage was set to segment around 10% of the input data. This result was observed for all bar one of the simulated cases. The results of the application of the segmentation algorithm was noted to be most effective in conditions where noise was included in the simulated data, for which consistent improvement was observed in all cases using the 10% segmentation. The BSC estimates calculated from models containing high coherence targets was shown to perform more poorly, with higher levels of segmentation required to register improvements in the BSC estimates. Unlike the low coherence models, the addition of noise did not appear to improve the quality of the BSC estimates. The results of the speckle models were the least promising of the three, with the application of the segmentation approach appearing to either maintain the current BSC estimate in the noise free simulations, or result in immediate reduction in BSC estimate in the simulations with added noise.

Future work within this field should seek to analyse further the relationship between the BSC and coherence to refine the algorithm for segmentation of speckle patterns,

and to simulate coherence structures based on soft-tissue like structures for application in the improvement of BSC estimates for tissue characterisation. Additionally, the considerations for different source apertures should be considered in both emit and receive modes. Finally a suggestion of multivariate analysis is proposed, to deal with the high dimensionality of the parameter space considered.

Chapter 7

Discussion

Chapter 3 contains results simulating the attenuation of a plane wave ultrasound pulse by layers of attenuating material. In one simulation case, impedance-matched models were used to investigate the effect of attenuation in the absence of boundary reflections between attenuating and non-attenuating layers. In the second case, a model was simulated with geometric and acoustic properties mimicking human skin, fat and muscle, to assess the ability of the simulation method to calculate the attenuation of an ultrasound pulse attenuated by materials modelled on tissue properties.

The aim of chapter 3 was to provide proof of concept results for two potential end goals. The first was the concept of patient specific attenuation correction. Whilst the simple models presented in chapter 3 do not represent the full complexity of the human anatomy, the construction of wave propagation simulation models through delineating tissue regions and assigning acoustic properties to them based on published data has recently been applied by other authors such as Kumar et al.[169]. Although they were modelling therapeutic ultrasound beam propagation, this required attenuation calculation and their approach applying published attenuation coefficients to segmented tissue regions was similar to that in chapter 3. To extend these models towards a patient-specific attenuation correction, many further steps would be required, but the findings presented provide a positive first step towards this goal.

The second aim of chapter 3: of generating a simulation tool within which attenu-

ation correction algorithms could be tested, the combination of the results of chapters 3 and 4 present a strong case for this. The accurate reproduction of the total, frequency dependent attenuation in the former and the theoretical backscatter properties in the latter suggest that a model combining these two approaches could be used to generate test data against which methods for correcting BSC estimates for attenuation in both the intervening tissue and within the scattering volume could be tested with known ground truths for both the attenuation and backscatter properties.

Two observations were made from this study. The first observation was that the attenuation measured from the simulation was shown to be numerically closest to the theoretically calculated value in cases where the domain was discretised to produce a mesh comprised of elements of length equal to 1/50th of the central wavelength of the simulation. This condition for mesh refinement was stricter than other results from the literature. The most comparable study was performed by Egerton et al. [130], who considered mesh discretisation values of 20 elements per wavelength and 40 elements per central wavelength for their application of the multi-band Finite element (FE) method. Since the analysis approach was different in this study, direct comparison of the attenuation errors relative to the theoretical value are not directly comparable between the studies. However, the conclusions were that increased accuracy relative to the theoretical model for the wave propagation was observed when the mesh discretisation was increased from 20 elements to 40 elements per wavelength, in alignment with the observations made within chapter 3. The second observation made was that variation in the time step over the range of values considered (corresponding to Courant values from 0.01 to 0.5 in increments of 0.01) resulted in a smaller variation in the computed attenuation than variation in the mesh discretisation was also noted by Egerton et al.[130]. The largest error (of 1.4%) in the measured attenuation relative to the theoretical value was observed where a mesh discretisation of 10 elements per wavelength and a Courant value of 0.5. Using a mesh discretisation of 50 elements per wavelength produced errors no greater than 0.15% relative to the theoretical value. The optimal time step of the

considered values was found to be 0.5.

These mesh discretisation observation take on increased importance when considered in relation the results of chapter 4 . In section 4.2.2.1, the scatterers that mimic the soft tissue scatterers were designed using a mesh discretisation of 50 elements per wavelength, which produced both accurate modelling of an isotropic sub-wavelength scatterer (as required by the definition of the BSC) and good agreement between simulated BSC estimates using the focused sources in chapter 4 and the known (theoretical) values of the BSC. The fact that the most accurate attenuation characteristics were observed for the properties that also produced accurate representation of the scattering behaviour suggests that attenuation could be incorporated into the scattering simulations without a need to consider the trade-off between the attenuation and scattering behaviours. The parameters used with respect to the time step (i.e. a Courant value of 0.5 for the attenuation simulations and 0.1 for the scattering simulations) does represent a need to identify a trade off between these factors. However, as seen in chapter 3, the time step appeared to be a much smaller factor in attenuation modelling accuracy than the mesh refinement. Investigations into the effect of the time step on the BSC estimation accuracy were not considered, and cannot be commented on.

A limitation of the study presented in this chapter was that sound speed dispersion effects were not considered. Soft-tissue materials are shown to exhibit low dispersion across clinical frequencies, and mathematical models of wave propagation typically do not consider this effect. For this reason, a confirmation that the correct degree of dispersion effects were produced by the multi-band approach should be considered in future work.

In chapters 4 and 5, it is noted that the unfocused sources in chapter 5 produced BSC estimates that deviated from the theoretical BSC more strongly than the focused source simulations of chapter 4 (seen through comparing the results presented in figures 4.8 and 5.11). Consultation of table 5.8 confirms that the most accurate results acquired (using method two with the sample placed at the last axial maximum) were underes-

timates of the theoretical BSC value by 8.10% and 10.59% for the 2.0 cm and 2.4 cm apertures respectively. By contrast, the largest discrepancy between the estimated and theoretical BSC found in figure 4.8 was 6.35%, and the smallest 3.04%. These two figures correspond to the estimation of the BSC over the same set of 1000 scattering ensembles, and hence the accuracy of the two estimation accuracies can be directly compared. Whilst comparison between focused transducers of different types (single element comparisons against array transducers, or the comparison of single element transducers with different f-numbers) are found in the literature [2][92][90][88][89][92], a search of the relevant literature did not reveal any comparisons between the accuracy of BSC estimates as measured by focused or unfocused sources. The comparison of the results from these chapters could therefore be considered as a result in itself. Use of the method 1 approach with the unfocused sources in chapter 5 resulted in significant underestimates at the last axial maximum, with decreasing underestimation as the sample and planar reflector were moved into the far-field. Even with the reduction in error, the results deviated from the theoretical value more substantially in the case of the unfocused source than the results presented for all the focused sources in chapter 4. These two compared cases (the unfocused cases with method 1 and the focused cases) employed the same measurement equation and were analysing the same set of scattering models, from which we may conclude that – for the considered cases – that focused sources provide better BSC estimates than unfocused sources. One could hypothesise that use of method 1 with the sample and planar reflector further into the far-field could generate BSC estimates that are closer to the theoretical model than the estimates provided by the focused source, but – as argued previously – the effective increase in the beamwidth and source sample distance would result in reduced spatial resolution in the BSC estimates, and would also reduce the signal strength due to reduction in solid angle of reception. The best results using method 2 and the unfocused source were found to be for sample positions nearer to the source, which was hypothesised to be due to a coincidental cancellation of the error between sample echo phase cancellation

and reference reflection beam divergence.

Common to the results of chapters 4, 5 and 6 was the use of individual mesh elements to represent sub-wavelength discrete scattering bodies. Using the mesh discretisation of 50 elements per centre wavelength ($3\,mm$ at $0.5\,MHz$), this results in a scatterer size of $60\,\mu m$. The effective diameter of scatterers that populate a medium can be estimated from the backscatter coefficient estimate made from the region through the application of analysis on the frequency dependence of the BSC. This analysis was not performed on the backscattered data within this thesis, and yet: from the accuracy observed in the backscatter coefficient estimates, one could hypothesise that these data sets could produce good estimates of the scatterer size. To apply such an analysis to the results presented would constitute a sanity check of the scattering diameter estimation algorithm, since the scatterer diameter is already used in computation of the theoretical BSC value against which the BSC estimates were computed with high accuracy. Nevertheless, the ability to reliably produce accurate estimates of the BSC does imply that these simulation models could be capable of testing scatterer diameter estimation algorithms. Of interest within this field of research is the development of algorithms to generate scatterer diameter estimates where a range of scattering sizes are present within the scatterer population [170][171]. An example study by Nordberg et al. [170] artificially generated BSC data values before application of the scatterer diameter estimation algorithm. Their approach provided a highly idealised data set for the analysis. The results presented within this thesis could be argued to present an opportunity to analyse BSC data generated from time domain simulations of wave scattering, which would represent a more realistic method of analysing scatterer diameter. An extension of this idea could be to consider the simulation of an inhomogeneous continuum model (see section 1.3.3) using an adaptation of the approaches presented in this thesis to model the scattering due to bulk modulus and/or density fluctuations over multiple elements within the FE mesh.

Chapter 8

Conclusion

Chapter 3 described an investigation into the attenuation characteristics of soft tissue like materials through Finite Element (FE) simulations. This investigation found that the representation of simulated models that produced the most accurate and reliable attenuation modelling was achieved where the simulation domain was discretised spatially to produce 50 finite elements per centre wavelength of the simulation. The optimal results were shown to be where the wave propagation was modelled using a time step of Courant value 0.5. The results of this chapter indicated that a multi-band finite element modelling approach was able to generate linear and power-law frequency dependencies of attenuation coefficient, with the analysis of the measured attenuation reproducing the input attenuation coefficient parameters reliably and to a high degree of accuracy. A human tissue mimicking model containing layers of human skin, fat and muscle was developed, which was shown to accurately reproduce attenuation and interface reflection of the simulated materials based on published tissue properties. The aim of the work presented in this chapter was to highlight the potential for the re-purposing of a tool to show its applicability in modelling wave attenuation by soft tissue like materials. The work reported in this chapter achieved this through demonstrating the capability of an FE simulation tool to simulate a measurement of the attenuation of an infinite plane wave through a region imitating a section of tissue. This work provides a proof of concept for the concept of calculating the attenuation correction for a BSC

measurement through use of FE methods.

Chapter 4 outlined mathematical reformulations of equations for calculation of the backscatter coefficient (BSC) and FE simulations of a tissue backscatter experiment. The resulting estimates of the incoherent scattering BSC for a tissue-mimicking sample created within the FE model using focused sources of ultrasound. The results were shown to produce accurate BSC estimates within 6% of the theoretically calculated BSC value in the case of models simulating speckle producing tissue samples, across a range of source f-numbers, and were also shown to exhibit speckle statistics expected of a fully developed speckle model. The simulations were also shown to produce good estimates of the BSC across a range of simulated number densities of scatterers present, with results within 24% of the theoretical value. The aim of this chapter was to simulate the backscattering behaviour from a tissue mimicking sample comprised of scattering bodies that mimicked the speckle producing scatterers found in soft tissues. The agreement between the simulation and the developed mathematics indicated that this had been achieved. The value of this result is in developing a tool by which BSC estimation approaches could be investigated using simulations with relatively low computational cost. For example, this tool could be applied to investigate into factors related to the test sample or the simulated source, to determine where sources of error occur in estimations of the BSC, and help to improve experimental and analysis techniques through interrogation of these factors.

Chapter 5 detailed an investigation into the effect of planar reflector positioning on the quality of BSC estimates measured using unfocused sources. Through adaptation of the simulation and mathematical methods developed in chapter 4, a set of planar reflector and sample distances were considered. The BSC was estimated for the simulated tissue samples used in chapter 3 using two unfocused sources.

This investigation revealed that BSC accuracy maximisation was achieved through placing the sample at the last axial maximum of the source and the planar reflector at half this distance. This combination of sample and planar reflector position was

hypothesised to minimise the error in the estimation of the backscattered powers from the two scattering materials considered, and as a results provide the most accurate BSC estimate. The investigation also revealed that when the sample was placed at an on-axis point in the the far field of the unfocused source, BSC estimation inaccuracy was minimised through placing the planar reflector at the same depth as the sample. Using the developed tool, the effect of diffraction correction accuracy and applicability was assessed through the positioning of the reference reflector. This result was an indication of how the developed simulation may be used to improve the accuracy of BSC estimates, and make the BSC a more clinically useful metric for tissue characterisation.

Chapter 6 contains descriptions of an investigation into the relationship between the spatial wave coherence of received echoes and the measurement of the BSC. BSC data sets were simulated using the methods developed in chapters 3 and 4, and the backscatter characteristics were analysed relative to the coherence of the backscattered waves. Within this chapter, a coherence based segmentation algorithm was developed to remove coherence outliers from BSC data sets, with the aim of improving the final BSC estimate. This investigation revealed that coherence based approaches were able to improve the BSC estimate of the simulation model through segmentation of high and low coherence regions in certain cases. It was found that the coherence based approach developed was most adept at improving BSC estimations where low coherence targets were embedded in a speckle background, and that the addition of noise to such models was necessary to improve coherence contrast of the targets. The investigation found that the high coherence targets modelled were less easily segmented using coherence, and that improvement in the BSC estimation was not as reliably found, and not influenced through the addition of noise. Finally, a coherence based segmentation approach was applied to test speckle patterns, which did not alter BSC estimate in noiseless cases, and caused underestimation of the BSC when noise was added to the RF echo data sets. Whilst chapter 5 considered the effect of the measurement approach on the accuracy of the BSC estimation, this chapter investigated how the structural and acoustic prop-

erties of a sample affect the resulting BSC estimate. This work provided both insight into the effect of spatial variation in coherence on BSC estimation and contributed to the investigation into spatial wave coherence through analysis of simulated coherence targets. In addition this chapter contributed a novel method for the segmentation of BSC data.

The limitations of the results presented in this thesis are in their applicability to real world examples, particularly in terms of dimensionality. Whilst chapter 3 presented results using tissue properties taken from published data, the design of the scattering media, and of the coherence targets in chapters 4, 5 and 6 were constructed theoretically in order to generate certain effects: the impact of which on the BSC were then evaluated. To improve on the applicability of these results, the first step for future work should be to develop and improve on the similarity between the simulated models and the soft tissue structures they represent. An obvious example of this is to reconstruct the models in 3D. A limitation of the results presented lies in their dimensionality.

This thesis has presented methods for and results from investigating BSC measurement methods, with the aim of improving their accuracy. With future work, application of these approaches and findings should contribute to further research that will increase the clinical applicability of BSC estimation, particularly for tissue characterisation in assessment of tumour state. If developed and applied in this way, BSC measurement holds potential to provide biomarkers that are early indicators of response, which would make treatment more adaptable and personalised. This could allow early selection of treatments that are most effective, reduction of suffering of patients throught earlier cessation of treatments that otherwise prove eventually ineffective.

Bibliography

[1] Goutam Ghoshal, Michael L. Oelze, and William D. O'Brien Jr. *Quantitative Ultrasound in Soft tissues*. Ed. by Jonathan Mamou and Michael L. Oelze. Dordrecht: Springer, 2013. Chap. 2, pp. 21–42.

[2] Roberto Lavarello and Michael L. Oelze. "Quantitative ultrasound estimates from populations of scatterers with continuous size distributions". In: *IEEE Transactions on Ultrasonics, Ferroelectrics and Frequency Control* 58.4 (Apr. 2011), pp. 744–753. DOI: 10.1109/tuffc.2011.1867.

[3] Gloria H. Heppner and Fred R. Miller. "The Cellular Basis of Tumor Progression". In: *International Review of Cytology*. 1997, pp. 1–56. DOI: 10.1016/s0074-7696(08)62230-5.

[4] Patrick Therasse et al. "New Guidelines to Evaluate the Response to Treatment in Solid Tumors". In: *JNCI: Journal of the National Cancer Institute* 92.3 (Feb. 2000), pp. 205–216. DOI: 10.1093/jnci/92.3.205.

[5] Martin D. Pickles et al. "Diffusion changes precede size reduction in neoadjuvant treatment of breast cancer". In: *Magnetic Resonance Imaging* 24.7 (Sept. 2006), pp. 843–847. DOI: 10.1016/j.mri.2005.11.005.

[6] A.R Padhani. "Functional MRI for anticancer therapy assessment". In: *European Journal of Cancer* 38.16 (Nov. 2002), pp. 2116–2127. DOI: 10.1016/s0959-8049(02)00388-x.

[7] Vanessa N Harry et al. “Use of new imaging techniques to predict tumour response to therapy”. In: *The Lancet Oncology* 11.1 (Jan. 2010), pp. 92–102. DOI: 10.1016/s1470-2045(09)70190-1.

[8] Robert A. Gatenby et al. “Adaptive Therapy”. In: *Cancer Research* 69.11 (June 2009), pp. 4894–4903. DOI: 10.1158/0008-5472.can-08-3658.

[9] Martin D. Pickles et al. “Role of dynamic contrast enhanced MRI in monitoring early response of locally advanced breast cancer to neoadjuvant chemotherapy”. In: *Breast Cancer Research and Treatment* 91.1 (May 2005), pp. 1–10. DOI: 10.1007/s10549-004-5819-2.

[10] T. L. Chenevert. “Diffusion Magnetic Resonance Imaging: an Early Surrogate Marker of Therapeutic Efficacy in Brain Tumors”. In: *Journal of the National Cancer Institute* 92.24 (Dec. 2000), pp. 2029–2036. DOI: 10.1093/jnci/92.24.2029.

[11] Daniel A Hamstra, Alnawaz Rehemtulla, and Brian D Ross. “Diffusion magnetic resonance imaging: a biomarker for treatment response in oncology”. In: *Journal of clinical oncology* 25.26 (2007), pp. 4104–4109.

[12] Martin D Pickles et al. “Role of dynamic contrast enhanced MRI in monitoring early response of locally advanced breast cancer to neoadjuvant chemotherapy”. In: *Breast cancer research and treatment* 91 (2005), pp. 1–10.

[13] ML George et al. “Non-invasive methods of assessing angiogenesis and their value in predicting response to treatment in colorectal cancer”. In: *British Journal of Surgery* 88.12 (2001), pp. 1628–1636.

[14] Mark C Preul et al. “Using proton magnetic resonance spectroscopic imaging to predict in vivo the response of recurrent malignant gliomas to tamoxifen chemotherapy”. In: *Neurosurgery* 46.2 (2000), p. 306.

[15] Amita Shukla-Dave et al. “Prediction of treatment response of head and neck cancers with P-31 MR spectroscopy from pretreatment relative phosphomonoester levels”. In: *Academic radiology* 9.6 (2002), pp. 688–694.

[16] Wolfgang A Weber et al. “Positron emission tomography in non–small-cell lung cancer: prediction of response to chemotherapy by quantitative assessment of glucose use”. In: *Journal of Clinical Oncology* 21.14 (2003), pp. 2651–2657.

[17] Jian-Wei Wang et al. “Ultrasound elastography as an imaging biomarker for detection of early tumor response to chemotherapy in a murine breast cancer model: a feasibility study”. In: *The British Journal of Radiology* (Feb. 2018), p. 20170698. DOI: 10.1259/bjr.20170698.

[18] Jason Fernandes et al. “Monitoring Breast Cancer Response to Neoadjuvant Chemotherapy Using Ultrasound Strain Elastography”. In: *Translational Oncology* 12.9 (Sept. 2019), pp. 1177–1184. DOI: 10.1016/j.tranon.2019.05.004.

[19] JC Bamber and CR Hill. “Acoustic properties of normal and cancerous human liver—I. Dependence on pathological condition”. In: *Ultrasound in medicine & biology* 7.2 (1981), pp. 121–133.

[20] Kibo Nam et al. “Ultrasonic Attenuation and Backscatter Coefficient Estimates of Rodent-Tumor-Mimicking Structures: Comparison of Results among Clinical Scanners”. In: *Ultrasonic Imaging* 33.4 (Oct. 2011), pp. 233–250. DOI: 10.1177/016173461103300403.

[21] Roxana M. Vlad et al. “Quantitative Ultrasound Characterization of Responses to Radiotherapy in Cancer Mouse Models”. In: *Clinical Cancer Research* 15.6 (Mar. 2009), pp. 2067–2075. DOI: 10.1158/1078-0432.ccr-08-1970.

[22] Jonathan Mamou et al. “Three-Dimensional High-Frequency Backscatter and Envelope Quantification of Cancerous Human Lymph Nodes”. In: *Ultrasound in Medicine and Biology* 37.3 (Mar. 2011), pp. 345–357. DOI: 10.1016/j.ultrasmedbio.2010.11.020.

[23] Sandeep K Kasoji et al. “Early assessment of tumor response to radiation therapy using high-resolution quantitative microvascular ultrasound imaging”. In: *Theranostics* 8.1 (2018), p. 156.

[24] François Destrempes and Guy Cloutier. “A Critical Review and Uniformized Representation of Statistical Distributions Modeling the Ultrasound Echo Envelope”. In: *Ultrasound in Medicine and Biology* 36.7 (July 2010), pp. 1037–1051. DOI: 10.1016/j.ultrasmedbio.2010.04.001.

[25] Frederic L. Lizzi et al. “Theoretical framework for spectrum analysis in ultrasonic tissue characterization”. In: *The Journal of the Acoustical Society of America* 73.4 (Apr. 1983), pp. 1366–1373. DOI: 10.1121/1.389241.

[26] Rubens A. Sigelmann and John M. Reid. “Analysis and measurement of ultrasound backscattering from an ensemble of scatterers excited by sine-wave bursts”. In: *The Journal of the Acoustical Society of America* 53.5 (May 1973), pp. 1351–1355. DOI: 10.1121/1.1913479.

[27] Mitsuhiro Ueda and Yasuhiko Ozawa. “Spectral analysis of echoes for backscattering coefficient measurement”. In: *The Journal of the Acoustical Society of America* 77.1 (1985), pp. 38–47. DOI: 10.1121/1.391898.

[28] Jeffrey Bamber et al. “Ultrasonic propagation through fixed and unfixed tissues”. In: *Ultrasound in Medicine & Biology* 5.2 (1979), pp. 159–165. DOI: 10.1016/0301-5629(79)90084-x.

[29] Cuiping Li et al. “In vivo Breast Sound-Speed Imaging with Ultrasound Tomography”. In: *Ultrasound in Medicine and Biology* 35.10 (Oct. 2009), pp. 1615–1628. DOI: 10.1016/j.ultrasmedbio.2009.05.011.

[30] Jakob Nebeker and Thomas R. Nelson. “Imaging of Sound Speed Using Reflection Ultrasound Tomography”. In: *Journal of Ultrasound in Medicine* 31.9 (Sept. 2012), pp. 1389–1404. DOI: 10.7863/jum.2012.31.9.1389.

[31] James F Greenleaf et al. “Algebraic reconstruction of spatial distributions of acoustic velocities in tissue from their time-of-flight profiles”. In: *Acoustical Holography: Volume 6* (1975), pp. 71–90.

[32] CM Sehgal et al. “Measurement and use of acoustic nonlinearity and sound speed to estimate composition of excised livers”. In: *Ultrasound in medicine & biology* 12.11 (1986), pp. 865–874.

[33] T Lin, J Ophir, and G Potter. “Correlations of sound speed with tissue constituents in normal and diffuse liver disease”. In: *Ultrasonic imaging* 9.1 (1987), pp. 29–40.

[34] Jeffrey Bamber, Christopher Hill, and John A. King. “Acoustic properties of normal and cancerous human liver—II Dependence on tissue structure”. In: *Ultrasound in medicine & biology* 7.2 (1981), pp. 135–144.

[35] Marko Jakovljevic et al. “Local speed of sound estimation in tissue using pulse-echo ultrasound: Model-based approach”. In: *The Journal of the Acoustical Society of America* 144.1 (July 2018), pp. 254–266. DOI: 10.1121/1.5043402.

[36] P. Huthwaite and F. Simonetti. “High-resolution imaging without iteration: a fast and robust method for breast ultrasound tomography”. In: *The Journal of the Acoustical Society of America* 130.3 (Sept. 2011), pp. 1721–1734. DOI: 10.1121/1.3613936.

[37] Chris D Madsen et al. “Hypoxia and loss of PHD 2 inactivate stromal fibroblasts to decrease tumour stiffness and metastasis”. In: *EMBO reports* 16.10 (2015), pp. 1394–1408.

[38] Jiacheng Huang et al. “Extracellular matrix and its therapeutic potential for cancer treatment”. In: *Signal Transduction and Targeted Therapy* 6.1 (Apr. 2021). DOI: 10.1038/s41392-021-00544-0.

[39] Norman F. Boyd et al. “Evidence That Breast Tissue Stiffness Is Associated with Risk of Breast Cancer”. In: *PLoS ONE* 9.7 (July 2014). Ed. by Judy R. Rees, e100937. DOI: 10.1371/journal.pone.0100937.

[40] Eun Jee Song, Yu-Mee Sohn, and Mirinae Seo. “Tumor stiffness measured by quantitative and qualitative shear wave elastography of breast cancer”. In: *The British Journal of Radiology* (Apr. 2018), p. 20170830. DOI: 10.1259/bjr.20170830.

[41] Kyung Hee Ko et al. “Potential role of shear-wave ultrasound elastography for the differential diagnosis of breast non-mass lesions: preliminary report”. In: *European Radiology* 24.2 (Oct. 2013), pp. 305–311. DOI: 10.1007/s00330-013-3034-4.

[42] Huisuo Hong et al. “Performance of Real-Time Elastography for the Staging of Hepatic Fibrosis: A Meta-Analysis”. In: *PLoS ONE* 9.12 (Dec. 2014). Ed. by Seung Up Kim, e115702. DOI: 10.1371/journal.pone.0115702.

[43] Norihisa Yada et al. “Diagnosis of Fibrosis and Activity by a Combined Use of Strain and Shear Wave Imaging in Patients with Liver Disease”. In: *Digestive Diseases* 35.6 (2017), pp. 515–520. DOI: 10.1159/000480140.

[44] Cheng Fang et al. “Strain elastography for noninvasive assessment of liver fibrosis: A prospective study with histological comparison”. In: *Ultrasound* 27.4 (July 2019), pp. 262–271. DOI: 10.1177/1742271x19862836.

[45] Daniel Jesper et al. “Ultrasound-Based Attenuation Imaging for the Non-Invasive Quantification of Liver Fat - A Pilot Study on Feasibility and Inter-Observer Variability”. In: *IEEE Journal of Translational Engineering in Health and Medicine* 8 (2020), pp. 1–9. DOI: 10.1109/jtehm.2020.3001488.

[46] Yu Ogino et al. “The ultrasound-guided attenuation parameter is useful in quantification of hepatic steatosis in non-alcoholic fatty liver disease”. In: *JGH Open* 5.8 (July 2021), pp. 947–952. DOI: 10.1002/jgh3.12615.

[47] P.A. Narayana and J. Ophir. "On the Frequency Dependence of Attenuation in Normal and Fatty Liver". In: *IEEE Transactions on Sonics and Ultrasonics* 30.6 (Nov. 1983), pp. 379–382. DOI: 10.1109/t-su.1983.31444.

[48] Kibo Nam, James A. Zagzebski, and Timothy J. Hall. "Quantitative Assessment of In Vivo Breast Masses Using Ultrasound Attenuation and Backscatter". In: *Ultrasonic Imaging* 35.2 (Mar. 2013), pp. 146–161. DOI: 10.1177/0161734613480281.

[49] F.T. D'Astous and F.S. Foster. "Frequency dependence of ultrasound attenuation and backscatter in breast tissue". In: *Ultrasound in Medicine and Biology* 12.10 (Oct. 1986), pp. 795–808. DOI: 10.1016/0301-5629(86)90077-3.

[50] Nikolaos Liasis et al. "The use of Speckle Reduction Imaging (SRI) Ultrasound in the characterization of carotid artery plaques". In: *European Journal of Radiology* 65.3 (Mar. 2008), pp. 427–433. DOI: 10.1016/j.ejrad.2007.05.004.

[51] C. P. Loizou et al. "Quality evaluation of ultrasound imaging in the carotid artery based on normalization and speckle reduction filtering". In: *Medical and Biological Engineering and Computing* 44.5 (Apr. 2006), pp. 414–426. DOI: 10.1007/s11517-006-0045-1.

[52] Sergio Mondillo et al. "Speckle-Tracking Echocardiography". In: *Journal of Ultrasound in Medicine* 30.1 (Jan. 2011), pp. 71–83. DOI: 10.7863/jum.2011.30.1.71.

[53] Brage H. Amundsen et al. "Noninvasive Myocardial Strain Measurement by Speckle Tracking Echocardiography". In: *Journal of the American College of Cardiology* 47.4 (Feb. 2006), pp. 789–793. DOI: 10.1016/j.jacc.2005.10.040.

[54] Arco J Teske et al. "Echocardiographic quantification of myocardial function using tissue deformation imaging, a guide to image acquisition and analysis using tissue Doppler and speckle tracking". In: *Cardiovascular Ultrasound* 5.1 (Aug. 2007). DOI: 10.1186/1476-7120-5-27.

[55] K J Parker. "Shapes and distributions of soft tissue scatterers". In: *Physics in Medicine and Biology* 64.17 (Sept. 2019), p. 175022. DOI: 10.1088/1361-6560/ab2485.

[56] Michael F. Insana et al. "Describing small-scale structure in random media using pulse-echo ultrasound". In: *The Journal of the Acoustical Society of America* 87.1 (Jan. 1990), pp. 179–192. DOI: 10.1121/1.399283.

[57] Mitsuhiro Ueda and Yasuhiko Ozawa. "Spectral analysis of echoes for backscattering coefficient measurement". In: *The Journal of the Acoustical Society of America* 77.1 (Jan. 1985), pp. 38–47. DOI: 10.1121/1.391898.

[58] D. K. Nassiri and C. R. Hill. "The use of angular acoustic scattering measurements to estimate structural parameters of human and animal tissues". In: *The Journal of the Acoustical Society of America* 79.6 (June 1986), pp. 2048–2054. DOI: 10.1121/1.393213.

[59] D. Nicholas. "Evaluation of backscattering coefficients for excised human tissues: results, interpretation and associated measurements". In: *Ultrasound in Medicine and Biology* 8.1 (Jan. 1982), pp. 17–28. DOI: 10.1016/0301-5629(82)90065-5.

[60] Malcolm J. Crocker and Jeffrey Bamber. *Encyclopedia of acoustics*. Nashville, TN: John Wiley Sons, May 1997. Chap. 141, pp. 1703–1727.

[61] Roxana M. Vlad et al. "Quantitative Ultrasound Characterization of Cancer Radiotherapy Effects In Vitro". In: *International Journal of Radiation Oncology Biology Physics* 72.4 (Nov. 2008), pp. 1236–1243. DOI: 10.1016/j.ijrobp.2008.07.027.

[62] Maurice M. Pasternak et al. "High-frequency ultrasound detection of cell death: Spectral differentiation of different forms of cell death in vitro". In: *Oncoscience* 3.9-10 (Sept. 2016), pp. 275–287. DOI: 10.18632/oncoscience.319.

[63] Ali Sadeghi-Naini et al. “Quantitative evaluation of cell death response in vitro and in vivo using conventional-frequency ultrasound”. In: *Oncoscience* 2.8 (Sept. 2015), pp. 716–726. DOI: 10.18632/oncoscience.235.

[64] M.C Kolios et al. “Ultrasonic spectral parameter characterization of apoptosis”. In: *Ultrasound in Medicine and Biology* 28.5 (May 2002), pp. 589–597. DOI: 10.1016/s0301-5629(02)00492-1.

[65] G J Czarnota et al. “Ultrasound imaging of apoptosis: high-resolution non-invasive monitoring of programmed cell death in vitro, in situ and in vivo”. In: *British Journal of Cancer* 81.3 (Sept. 1999), pp. 520–527. DOI: 10.1038/sj.bjc.6690724.

[66] E.J. Feleppa et al. “Diagnostic spectrum analysis in ophthalmology: A physical perspective”. In: *Ultrasound in Medicine and Biology* 12.8 (Aug. 1986), pp. 623–631. DOI: 10.1016/0301-5629(86)90183-3.

[67] R M Golub et al. “Differentiation of breast tumors by ultrasonic tissue characterization”. In: *Journal of Ultrasound in Medicine* 12.10 (Oct. 1993), pp. 601–608. DOI: 10.7863/jum.1993.12.10.601.

[68] P Mohana Shankar et al. “Classification of ultrasonic B-mode images of breast masses using Nakagami distribution”. In: *IEEE transactions on ultrasonics, ferroelectrics, and frequency control* 48.2 (2001), pp. 569–580.

[69] Emi Saegusa-Beecroft et al. “Three-dimensional quantitative ultrasound for detecting lymph node metastases”. In: *Journal of Surgical Research* 183.1 (July 2013), pp. 258–269. DOI: 10.1016/j.jss.2012.12.017.

[70] W. Fraser Symmans et al. “Paclitaxel-induced Apoptosis and Mitotic Arrest Assessed by Serial Fine-Needle Aspiration: Implications for Early Prediction of Breast Cancer Response to Neoadjuvant Treatment1”. In: *Clinical Cancer Research* 6.12 (Dec. 2000), pp. 4610–4617. ISSN: 1078-0432.

[71] Ali Sadeghi-Naini et al. "Quantitative Ultrasound Evaluation of Tumor Cell Death Response in Locally Advanced Breast Cancer Patients Receiving Chemotherapy". In: *Clinical Cancer Research* 19.8 (Apr. 2013), pp. 2163–2174. DOI: 10.1158/1078-0432.ccr-12-2965.

[72] Hamidreza Taleghamar et al. "Deep learning of quantitative ultrasound multiparametric images at pre-treatment to predict breast cancer response to chemotherapy". In: *Scientific Reports* 12.1 (Feb. 2022). DOI: 10.1038/s41598-022-06100-2.

[73] Daniel DiCenzo et al. "Quantitative ultrasound radiomics in predicting response to neoadjuvant chemotherapy in patients with locally advanced breast cancer: Results from multi-institutional study". In: *Cancer Medicine* 9.16 (June 2020), pp. 5798–5806. DOI: 10.1002/cam4.3255.

[74] Trong N. Nguyen et al. "Estimation of Backscatter Coefficients Using an in situ calibration Source". In: *IEEE Transactions on Ultrasonics, Ferroelectrics, and Frequency Control* 67.2 (Feb. 2020), pp. 308–317. DOI: 10.1109/tuffc.2019.2944305.

[75] Xucai Chen, Karl Q. Schwarz, and Kevin J. Parker. "Radiation pattern of a focused transducer: A numerically convergent solution". In: *The Journal of the Acoustical Society of America* 94.5 (Nov. 1993), pp. 2979–2991. DOI: 10.1121/1.407329.

[76] D. Nicholas, C.R. Hill, and D.K. Nassiri. "Evaluation of backscattering coefficients for excised human tissues: Principles and techniques". In: *Ultrasound in Medicine and Biology* 8.1 (Jan. 1982), pp. 7–15. DOI: 10.1016/0301-5629(82)90064-3.

[77] Mitsuhiro Ueda and Hiroshi Ichikawa. "Analysis of an echo signal reflected from a weakly scattering volume by a discrete model of the medium". In: *The Journal*

of the Acoustical Society of America 70.6 (Dec. 1981), pp. 1768–1775. DOI: 10.1121/1.387196.

[78] M.F. Insana, T.J. Hall, and L.T. Cook. "Backscatter coefficient estimation using array transducers". In: *IEEE Transactions on Ultrasonics, Ferroelectrics and Frequency Control* 41.5 (1994), pp. 714–723. DOI: 10.1109/58.308508.

[79] Xucai Chen et al. "The measurement of backscatter coefficient from a broadband pulse-echo system: a new formulation". In: *IEEE Transactions on Ultrasonics, Ferroelectrics and Frequency Control* 44.2 (1997), pp. 515–525. DOI: 10.1109/58.585136.

[80] Kibo Nam, James A. Zagzebski, and Timothy J. Hall. "Simultaneous Backscatter and Attenuation Estimation Using a Least Squares Method with Constraints". In: *Ultrasound in Medicine and Biology* 37.12 (Dec. 2011), pp. 2096–2104. DOI: 10.1016/j.ultrasmedbio.2011.08.008.

[81] Andres Ruland, James M. Hill, and Gordon G. Wallace. "Reference Phantom Method for Ultrasonic Imaging of Thin Dynamic Constructs". In: *Ultrasound in Medicine and Biology* 47.8 (Aug. 2021), pp. 2388–2403. DOI: 10.1016/j.ultrasmedbio.2021.04.014.

[82] Timothy J Hall et al. "Ultrasonic measurement of glomerular diameters in normal adult humans". In: *Ultrasound in medicine & biology* 22.8 (1996), pp. 987–997.

[83] E. Holasek et al. "A method for spectra-color B-scan ultrasonography". In: *Journal of Clinical Ultrasound* 3.3 (Sept. 1975), pp. 175–178. DOI: 10.1002/jcu.1870030305.

[84] F.S. Foster, M. Strban, and G. Austin. "The Ultrasound Macroscope: Initial Studies of Breast Tissue". In: *Ultrasonic Imaging* 6.3 (July 1984), pp. 243–261. DOI: 10.1177/016173468400600301.

[85] M Insana. “Parametric ultrasound imaging from backscatter coefficient measurements: Image formation and interpretation”. In: *Ultrasonic Imaging* 12.4 (Oct. 1990), pp. 245–267. DOI: 10.1016/0161-7346(90)90002-f.

[86] L Yao. “Backscatter coefficient measurements using a reference phantom to extract depth-dependent instrumentation factors”. In: *Ultrasonic Imaging* 12.1 (1990), pp. 58–70. DOI: 10.1016/0161-7346(90)90221-i.

[87] Keith A. Wear and Brian S. Garra. “Assessment of bone density using ultrasonic backscatter”. In: *Ultrasound in Medicine and Biology* 24.5 (June 1998), pp. 689–695. DOI: 10.1016/s0301-5629(98)00040-4.

[88] E L Madsen et al. “Interlaboratory comparison of ultrasonic backscatter, attenuation, and speed measurements.” In: *Journal of Ultrasound in Medicine* 18.9 (1999), pp. 615–631. DOI: 10.7863/jum.1999.18.9.615.

[89] Janelle J. Anderson et al. “Interlaboratory Comparison of Backscatter Coefficient Estimates for Tissue-Mimicking Phantoms”. In: *Ultrasonic Imaging* 32.1 (Jan. 2010), pp. 48–64. DOI: 10.1177/016173461003200104.

[90] Keith A. Wear et al. “Interlaboratory Comparison of Ultrasonic Backscatter Coefficient Measurements From 2 to 9 MHz”. In: *Journal of Ultrasound in Medicine* 24.9 (2005), pp. 1235–1250. DOI: 10.7863/jum.2005.24.9.1235.

[91] James J. Faran. “Sound Scattering by Solid Cylinders and Spheres”. In: *The Journal of the Acoustical Society of America* 23.4 (July 1951), pp. 405–418. DOI: 10.1121/1.1906780.

[92] Kibo Nam et al. “Cross-imaging system comparison of backscatter coefficient estimates from a tissue-mimicking material”. In: *The Journal of the Acoustical Society of America* 132.3 (Sept. 2012), pp. 1319–1324. DOI: 10.1121/1.4742725.

[93] Michael R. King et al. “Ultrasonic backscatter coefficients for weakly scattering, agar spheres in agar phantoms”. In: *The Journal of the Acoustical Society of America* 128.2 (Aug. 2010), pp. 903–908. DOI: 10.1121/1.3460109.

[94] Lauren A. Wirtzfeld et al. "Cross-Imaging Platform Comparison of Ultrasonic Backscatter Coefficient Measurements of Live Rat Tumors". In: *Journal of Ultrasound in Medicine* 29.7 (July 2010), pp. 1117–1123. DOI: 10.7863/jum.2010.29.7.1117.

[95] J C Bamber and R J Dickinson. "Ultrasonic B-scanning: a computer simulation". In: *Physics in Medicine and Biology* 25.3 (May 1980), pp. 463–479. DOI: 10.1088/0031-9155/25/3/006.

[96] B Oosterveld. "Texture of B-mode echograms: 3-D simulations and experiments of the effects of diffraction and scatterer density". In: *Ultrasonic Imaging* 7.2 (Apr. 1985), pp. 142–160. DOI: 10.1016/0161-7346(85)90073-2.

[97] Jørgen Arendt Jensen. "Field: A program for simulating ultrasound systems". In: *Medical & Biological Engineering & Computing* 34.sup. 1 (1997), pp. 351–353.

[98] J.A. Jensen and N.B. Svendsen. "Calculation of pressure fields from arbitrarily shaped, apodized, and excited ultrasound transducers". In: *IEEE Transactions on Ultrasonics, Ferroelectrics and Frequency Control* 39.2 (Mar. 1992), pp. 262–267. DOI: 10.1109/58.139123.

[99] Bernard Shieh, F. Levent Degertekin, and Karim Sabra. "Simulation of absolute backscattering coefficient in Field II". In: *2014 IEEE International Ultrasonics Symposium*. IEEE, Sept. 2014. DOI: 10.1109/ultsym.2014.0604.

[100] Alfonso Rodriguez-Molares et al. "The Generalized Contrast-to-Noise Ratio: A Formal Definition for Lesion Detectability". In: *IEEE Transactions on Ultrasonics, Ferroelectrics, and Frequency Control* 67.4 (2020), pp. 745–759. DOI: 10.1109/TUFFC.2019.2956855.

[101] M. A. Lediju et al. "Short-lag spatial coherence of backscattered echoes: imaging characteristics". In: *IEEE Transactions on Ultrasonics, Ferroelectrics and Fre-*

quency Control 58.7 (July 2011), pp. 1377–1388. DOI: 10.1109/tuffc.2011.1957.

[102] Bradley E. Treeby and B. T. Cox. "Modeling power law absorption and dispersion for acoustic propagation using the fractional Laplacian". In: *The Journal of the Acoustical Society of America* 127.5 (May 2010), pp. 2741–2748. DOI: 10.1121/1.3377056.

[103] Samuel W. Key and Raymond D. Krieg. "Comparison of Finite-Element and Finite-Difference Methods." In: *Numerical and Computer Methods in Structural Mechanics*. Elsevier, 1973, pp. 337–352. DOI: 10.1016/b978-0-12-253250-4.50019-1.

[104] Peter Huthwaite. "Accelerated finite element elastodynamic simulations using the GPU". In: *Journal of Computational Physics* 257 (Jan. 2014), pp. 687–707. DOI: 10.1016/j.jcp.2013.10.017.

[105] Robert D Cook et al. *Concepts and applications of finite element analysis*. en. 4th ed. Nashville, TN: John Wiley & Sons, Oct. 2001.

[106] Adrian I. Nachman, James F. Smith, and Robert C. Waag. "An equation for acoustic propagation in inhomogeneous media with relaxation losses". In: *The Journal of the Acoustical Society of America* 88.3 (Sept. 1990), pp. 1584–1595. DOI: 10.1121/1.400317.

[107] RC Chivers. "The scattering of ultrasound by human tissues—Some theoretical models". In: *Ultrasound in medicine and biology* 3.1 (1977), pp. 1–13.

[108] S. A. Goss, R. L. Johnston, and F. Dunn. "Comprehensive compilation of empirical ultrasonic properties of mammalian tissues". In: *The Journal of the Acoustical Society of America* 64.2 (Aug. 1978), pp. 423–457. DOI: 10.1121/1.382016.

[109] L.L. Fellingham and F.G. Sommer. "Ultrasonic Characterization of Tissue Structure in the In Vivo Human Liver and Spleen". In: *IEEE Transactions on Sonics and Ultrasonics* 31.4 (July 1984), pp. 418–428. DOI: 10.1109/t-su.1984.31522.

[110] Martin F. Schiffner and Georg Schmitz. "On the separate recovery of spatial fluctuations in compressibility and mass density in pulse-echo ultrasound imaging using linear inverse scattering". In: *The Journal of the Acoustical Society of America* 135.4 (Apr. 2014), pp. 2179–2179. DOI: 10.1121/1.4877088.

[111] F.L. Lizzi et al. "Relationship of Ultrasonic Spectral Parameters to Features of Tissue Microstructure". In: *IEEE Transactions on Ultrasonics, Ferroelectrics and Frequency Control* 34.3 (May 1987), pp. 319–329. DOI: 10.1109/t-uffc.1987.26950.

[112] The MathWorks Inc. *MATLAB version: 9.13.0 (R2022b)*. Natick, Massachusetts, United States, 2022.

[113] J.R. Pettit et al. "A Stiffness Reduction Method for efficient absorption of waves at boundaries for use in commercial Finite Element codes". In: *Ultrasonics* 54.7 (2014), pp. 1868–1879. ISSN: 0041-624X. DOI: https://doi.org/10.1016/j.ultras.2013.11.013.

[114] A. Van Pamel et al. "Numerical and analytic modelling of elastodynamic scattering within polycrystalline materials". In: *The Journal of the Acoustical Society of America* 143.4 (Apr. 2018), pp. 2394–2408. DOI: 10.1121/1.5031008.

[115] Peter Huthwaite. "Accelerated finite element elastodynamic simulations using the GPU". In: *Journal of Computational Physics* 257 (2014), pp. 687–707. ISSN: 0021-9991. DOI: https://doi.org/10.1016/j.jcp.2013.10.017.

[116] George West et al. "Multi-band finite element simulation of ultrasound attenuation by soft tissue". In: *2021 IEEE International Ultrasonics Symposium (IUS)*. 2021, pp. 1–5. DOI: 10.1109/IUS52206.2021.9593686.

[117] Jong Keon Jang et al. "Accuracy of the ultrasound attenuation coefficient for the evaluation of hepatic steatosis: a systematic review and meta-analysis of prospective studies". In: *Ultrasonography* 41.1 (Jan. 2022), pp. 83–92. DOI: 10.14366/usg.21076.

[118] Yasutomo Fujii et al. “A New Method for Attenuation Coefficient Measurement in the Liver”. In: *Journal of Ultrasound in Medicine* 21.7 (July 2002), pp. 783–788. DOI: 10.7863/jum.2002.21.7.783.

[119] L. Landini, R. Sarnelli, and F. Squartini. “Frequency-dependent attenuation in breast tissue characterization”. In: *Ultrasound in Medicine and Biology* 11.4 (1985), pp. 599–603. ISSN: 0301-5629. DOI: https://doi.org/10.1016/0301-5629(85)90031-6.

[120] S Flax. “Spectral characterization and attenuation measurements in ultrasound”. In: *Ultrasonic Imaging* 5.2 (Apr. 1983), pp. 95–116. DOI: 10.1016/0161-7346(83)90013-5.

[121] M.E. Lyons and K.J. Parker. “Absorption and attenuation in soft tissues. II. Experimental results”. In: *IEEE Transactions on Ultrasonics, Ferroelectrics and Frequency Control* 35.4 (July 1988), pp. 511–521. DOI: 10.1109/58.4189.

[122] Andrew Gray. *Atlas of ultrasound-guided regional anesthesia*. Elsevier, 2019. Chap. 3, p. 5.

[123] P.N.T. Wells. “Absorption and dispersion of ultrasound in biological tissue”. In: *Ultrasound in Medicine and Biology* 1.4 (1975), pp. 369–376. ISSN: 0301-5629. DOI: https://doi.org/10.1016/0301-5629(75)90124-6.

[124] Francis A. Duck. “Acoustic Properties of Tissue at Ultrasonic Frequencies”. In: *Physical Properties of Tissues*. Elsevier, 1990, pp. 73–135. DOI: 10.1016/b978-0-12-222800-1.50008-5.

[125] R. Kuc and M. Schwartz. “Estimating the Acoustic Attenuation Coefficient Slope for Liver from Reflected Ultrasound Signals”. In: *IEEE Transactions on Sonics and Ultrasonics* 26.5 (1979), pp. 353–361. DOI: 10.1109/T-SU.1979.31116.

[126] R. Kuc. “Estimating acoustic attenuation from reflected ultrasound signals: Comparison of spectral-shift and spectral-difference approaches”. In: *IEEE Trans-*

actions on Acoustics, Speech, and Signal Processing 32.1 (1984), pp. 1–6. DOI: 10.1109/TASSP.1984.1164282.

[127] Timothy A. Bigelow et al. "Comparison of algorithms for estimating ultrasound attenuation when predicting cervical remodeling in a rat model". In: *2011 IEEE International Symposium on Biomedical Imaging: From Nano to Macro*. 2011, pp. 883–886. DOI: 10.1109/ISBI.2011.5872545.

[128] J Ophir. "Elimination of diffraction error in acoustic attenuation estimation via axial beam translation". In: *Ultrasonic Imaging* 10.2 (Apr. 1988), pp. 139–152. DOI: 10.1016/0161-7346(88)90055-7.

[129] Yassin Labyed and Timothy A. Bigelow. "A theoretical comparison of attenuation measurement techniques from backscattered ultrasound echoes". In: *The Journal of the Acoustical Society of America* 129.4 (Apr. 2011), pp. 2316–2324. DOI: 10.1121/1.3559677.

[130] J. S. Egerton et al. "Ultrasonic attenuation and phase velocity of high-density polyethylene pipe material". In: *The Journal of the Acoustical Society of America* 141.3 (2017), pp. 1535–1545. DOI: 10.1121/1.4976689. eprint: https://doi.org/10.1121/1.4976689.

[131] J.R. Pettit et al. "A Stiffness Reduction Method for efficient absorption of waves at boundaries for use in commercial Finite Element codes". In: *Ultrasonics* 54.7 (2014), pp. 1868–1879.

[132] Mickael Brice Drozdz. "Efficient finite element modelling of ultrasound waves in elastic media". PhD thesis. Imperial College London, 2008.

[133] Karan Chopra et al. "A Comprehensive Examination of Topographic Thickness of Skin in the Human Face". In: *Aesthetic Surgery Journal* 35.8 (Oct. 2015), pp. 1007–1013.

[134] Paul Störchle et al. "Measurement of mean subcutaneous fat thickness: eight standardised ultrasound sites compared to 216 randomly selected sites". In: *Scientific Reports* 8.1 (Nov. 2018). DOI: 10.1038/s41598-018-34213-0.

[135] *ITIS Foundation: Tissue Acoustic Properties Database.* "https://itis.swiss/virtual-population/tissue-properties/database/acoustic-properties/". Accessed: 2021-04-20.

[136] Robert L. McIntosh and Vitas Anderson. "A Comprehensive Tissue Properties Database Provided For The Thermal Assessment Of A Human At Rest". In: *Biophysical Reviews and Letters* 05.03 (Sept. 2010), pp. 129–151. DOI: 10.1142/s1793048010001184.

[137] Kyriakou, Adamos. "Multi-Physics Computational Modeling of Focused Ultrasound Therapies". en. PhD thesis. 2015. DOI: 10.3929/ETHZ-A-010469577.

[138] D.E. Collins. "Tissues Substitutes, Phantoms and Computation Modelling in Medical Ultrasound". In: *International Commission on Radiation Units and Measurements* 61 (2009).

[139] R. C. Chivers and R. J. Parry. "Ultrasonic velocity and attenuation in mammalian tissues". In: *The Journal of the Acoustical Society of America* 63.3 (Mar. 1978), pp. 940–953. DOI: 10.1121/1.381774.

[140] M. A. El-Brawany et al. "Measurement of thermal and ultrasonic properties of some biological tissues". In: *Journal of Medical Engineering and Technology* 33.3 (Jan. 2009), pp. 249–256. DOI: 10.1080/03091900802451265.

[141] Dinah Maria Brandner et al. "Estimation of Tissue Attenuation from Ultrasonic B-Mode Images: Spectral-Log-Difference and Method-of-Moments Algorithms Compared". In: *Sensors* 21.7 (Apr. 2021), p. 2548. DOI: 10.3390/s21072548.

[142] Francis A Duck. "Nonlinear acoustics in diagnostic ultrasound". In: *Ultrasound in Medicine and Biology* 28.1 (Jan. 2002), pp. 1–18. DOI: 10.1016/s0301-

5629(01)00463-x. URL: https://doi.org/10.1016/s0301-5629(01)00463-x.

[143] Eenas Omari, Heichang Lee, and Tomy Varghese. "Theoretical and phantom based investigation of the impact of sound speed and backscatter variations on attenuation slope estimation". In: *Ultrasonics* 51.6 (Aug. 2011), pp. 758–767. DOI: 10.1016/j.ultras.2011.03.004.

[144] Masaaki Omura et al. "Validation of differences in backscatter coefficients among four ultrasound scanners with different beamforming methods". In: *Journal of Medical Ultrasonics* 47.1 (Oct. 2019), pp. 35–46. DOI: 10.1007/s10396-019-00984-w.

[145] Prerna Singh, Ramakrishnan Mukundan, and Rex De Ryke. "Texture Based Quality Analysis of Simulated Synthetic Ultrasound Images Using Local Binary Patterns". In: *Journal of Imaging* 4.1 (Dec. 2017), p. 3. DOI: 10.3390/jimaging4010003.

[146] Michael L. Oelze and William D. O'Brien. "Defining optimal axial and lateral resolution for estimating scatterer properties from volumes using ultrasound backscatter". In: *The Journal of the Acoustical Society of America* 115.6 (June 2004), pp. 3226–3234. DOI: 10.1121/1.1739484.

[147] Isabelle Fontaine, Michel Bertrand, and Guy Cloutier. "A System-Based Approach to Modeling the Ultrasound Signal Backscattered by Red Blood Cells". In: *Biophysical Journal* 77.5 (Oct. 1999), pp. 2387–2399. DOI: 10.1016/s0006-3495(99)77076-1.

[148] Isabelle Fontaine, David Savéry, and Guy Cloutier. "Simulation of Ultrasound Backscattering by Red Cell Aggregates:Effect of Shear Rate and Anisotropy". In: *Biophysical Journal* 82.4 (Apr. 2002), pp. 1696–1710. DOI: 10.1016/s0006-3495(02)75522-7.

[149] Shih-Jeh Wu, Ihyuan Kuo, and K.Kirk Shung. "Boundary element simulation of backscattering properties for red blood with high frequency ultrasonic transducers". In: *Ultrasonics* 43.3 (Jan. 2005), pp. 145–151. DOI: 10.1016/j.ultras.2004.06.001.

[150] Yuan Liu et al. "Investigation of ultrasonic backscatter using three-dimensional finite element simulations". In: *The Journal of the Acoustical Society of America* 145.3 (Mar. 2019), pp. 1584–1595. DOI: 10.1121/1.5094783.

[151] X. Bai et al. "Finite element modeling of grain size effects on the ultrasonic microstructural noise backscattering in polycrystalline materials". In: *Ultrasonics* 87 (2018), pp. 182–202. DOI: 10.1016/j.ultras.2018.02.008.

[152] Jørgen Arendt Jensen. "FIELD: A Program for Simulating Ultrasound Systems". In: *10TH NORDICBALTIC CONFERENCE ON BIOMEDICAL IMAGING, VOL. 4, SUPPLEMENT 1, PART 1:351–353*. 1996, pp. 351–353.

[153] R.F. Wagner et al. "Statistics of Speckle in Ultrasound B-Scans". In: *IEEE Transactions on Sonics and Ultrasonics* 30.3 (1983), pp. 156–163. DOI: 10.1109/T-SU.1983.31404.

[154] Christoph B. Burckhardt. "Speckle in ultrasound B-mode scans". In: *IEEE Transactions on Sonics and Ultrasonics* 25.1 (1978), pp. 1–6. DOI: 10.1109/T-SU.1978.30978.

[155] Mitsuhiro Ueda and Hiroshi Ichikawa. "Analysis of an echo signal reflected from a weakly scattering volume by a discrete model of the medium". In: *The Journal of the Acoustical Society of America* 70.6 (1981), pp. 1768–1775. DOI: 10.1121/1.387196.

[156] Max Born and Emil Wolf. *Principles of optics*. 7th ed. Cambridge, England: Cambridge University Press, 2019.

[157] Timothy A. Bigelow and William D. O'Brien. "Scatterer size estimation in pulse-echo ultrasound using focused sources: Theoretical approximations and simulation analysis". In: *The Journal of the Acoustical Society of America* 116.1 (July 2004), pp. 578–593. DOI: 10.1121/1.1757452.

[158] C.M. Moran, N.L. Bush, and J.C. Bamber. "Ultrasonic propagation properties of excised human skin". In: *Ultrasound in Medicine and Biology* 21.9 (Jan. 1995), pp. 1177–1190. DOI: 10.1016/0301-5629(95)00049-6. URL: https://doi.org/10.1016/0301-5629(95)00049-6.

[159] Nesrine Houhat and Tarek Boutkedjirt. "Frequency and concentration dependence of the ultrasonic backscatter coefficient in a soft tissue mimicking material". In: 2012. URL: https://api.semanticscholar.org/CorpusID:113397887.

[160] R.J. Fedewa et al. "Spatial coherence of the nonlinearly generated second harmonic portion of backscatter for a clinical imaging system". In: *IEEE Transactions on Ultrasonics, Ferroelectrics and Frequency Control* 50.8 (Aug. 2003), pp. 1010–1022. DOI: 10.1109/tuffc.2003.1226545.

[161] Jeffrey C. Bamber et al. "B-Mode Speckle Texture: The Effect of Spatial Coherence". In: *Acoustical Imaging*. Kluwer Academic Publishers, pp. 141–146. DOI: 10.1007/0-306-47108-6_20.

[162] Joseph W Goodman. *Statistical optics*. John Wiley & Sons, 2015.

[163] Raoul Mallart and Mathias Fink. "The van Cittert–Zernike theorem in pulse echo measurements". In: *The Journal of the Acoustical Society of America* 90.5 (Nov. 1991), pp. 2718–2727. DOI: 10.1121/1.401867.

[164] Jeffrey C. Bamber, Ronald A. Mucci, and Donald P. Orofino. "Spatial Coherence and Beamformer Gain". In: *Acoustical Imaging*. Kluwer Academic Publishers, pp. 43–48. DOI: 10.1007/0-306-47108-6_6.

[165] Jeffrey C. Bamber et al. "B-Mode Speckle Texture: The Effect of Spatial Coherence". In: *Acoustical Imaging*. Kluwer Academic Publishers, pp. 141–146. DOI: 10.1007/0-306-47108-6_20.

[166] J Verhoeven. "Improvement of lesion detection by echographic image processing: Signal-to-noise-ratio imaging". In: *Ultrasonic Imaging* 13.3 (July 1991), pp. 238–251. DOI: 10.1016/0161-7346(91)90074-r.

[167] Pai-Chi Li and Meng-Lin Li. "Adaptive imaging using the generalized coherence factor". In: *IEEE Transactions on Ultrasonics, Ferroelectrics and Frequency Control* 50.2 (Feb. 2003), pp. 128–141. DOI: 10.1109/tuffc.2003.1182117.

[168] Arun Asokan Nair, Trac Duy Tran, and Muyinatu A. Lediju Bell. "Robust Short-Lag Spatial Coherence Imaging". In: *IEEE Transactions on Ultrasonics, Ferroelectrics, and Frequency Control* 65.3 (Mar. 2018), pp. 366–377. DOI: 10.1109/tuffc.2017.2780084.

[169] Avisha Kumar et al. "Computational modeling towards focused ultrasound therapy for spinal cord injury: visualization of beam propagation through patient-specific anatomy". In: *Medical Imaging 2023: Image-Guided Procedures, Robotic Interventions, and Modeling*. Ed. by Cristian A. Linte and Jeffrey H. Siewerdsen. SPIE, Apr. 2023. DOI: 10.1117/12.2654357.

[170] Eric P. Nordberg and Timothy J. Hall. "Effective Scatterer Diameter Estimates for Broad Scatterer Size Distributions". In: *Ultrasonic Imaging* 37.1 (May 2014), pp. 3–21. DOI: 10.1177/0161734614534399.

[171] Noushin Jafarpisheh et al. "Estimation of the Scatterer Size Distributions in Quantitative Ultrasound Using Constrained Optimization". In: *2021 IEEE International Ultrasonics Symposium (IUS)*. IEEE. 2021, pp. 1–4.